Development of a Complex Flow Phantom for Diagnostic Imaging

Simone Ambrogio

Medical Physics Group
Mathematical Modelling in Medicine
Infection Immunity and Cardiovascular Disease
Faculty of Medicine, Dentistry and Health
The University of Sheffield

Thesis submitted for the degree of PhD
August 2019

Abstract

Literature and market analysis have highlighted the lack of flow phantom technologies able to challenge innovative medical imaging devices, such as Ultrasound and Magnetic Resonance. A novel, cost-effective, compact and robust Complex Flow Phantom prototype was proposed. The design relies on the generation of stable, reproducible, predictable and controllable vortex rings. Vortex rings were chosen because bring together high stability and physiological relevance. The design was tested with multiple and independent measurement methods under challenging working conditions. Overall, it demonstrated to produce reproducible flows with variability always lower than +/- 10 %. This variability was assessed with regards to translational velocity, however, macro-flow reproducibility implies micro-flow stability. Computational Fluid Dynamics (CFD) and optical/video acquisitions were used as first methods to independently validate two early prototypes operating in air and water. CFD overall well approximate theoretical predictions but accuracy was insufficient to provide a reference standard. Overall, the early prototypes demonstrated encouraging stability and a Vortex Ring based Complex Flow Phantom prototype was manufactured. Laser PIV acquisitions were performed to establish flow reference standard values. Optical/video acquisitions were performed and results were compared with Laser PIV to assess the rigour of the methods. Results obtained by the two different measurement methods on two identically manufactured but different systems showed credible consistency. Conventional and advanced (Vector Flow Imaging) Ultrasound acquisitions were also performed on the design. An instrumentation pack was designed and is provided as tool for self-calibrating the phantom and for estimating flow reference values under different generating conditions. An MRI compatible version of the phantom was manufactured and was tested in laboratory. Design and experiments are supported by journal article and conference proceeding publications, poster and oral presentation in international conferences. The phantom is purchasable from Leeds Test Objects Ltd or can be manufactured in laboratory following the specifications provided.

“Be less curious about people and more curious about ideas.”

Marie Skłodowska Curie

Publications

The work presented in this thesis is complimented by a series of publications which are listed below:

Ambrogio, S., Walker, A., Narracott, A., Ferrari, S., Verma, P. & Fenner J.W. (2019). A Complex Flow Phantom for Medical Imaging: Ring Vortex Phantom Design and Technical Specification. *Journal of Medical Engineering and Technology.*

Badescu, E., Ambrogio, S., Fenner, J., Liebgott, H., Friboulet, D. & Garcia, D. (2018). Vortex Ring Phantom for Investigation of Ultrasound Vector Flow Imaging, in: *IEEE International Ultrasonics Symposium, IUS*.

Ferrari*, S., Ambrogio*, S., Walker, A., Verma, P., Narracott, A. J., Wilkinson, I. & Fenner, J. W. (2017). The Ring Vortex: Concepts for a Novel Complex Flow Phantom for Medical Imaging. *Open Journal of Medical Imaging*.

Ferrari*, S., Ambrogio*, S., Walker, A., Narracott, A. J. & Fenner, J. W. (2018). The Ring Vortex: A Candidate for a Liquid-Based Complex Flow Phantom for Medical Imaging. *Lecture Notes in Computational Vision and Biomechanics*.

* authors contributed equally to the preparation of the manuscript

Awards

Results illustrated in this thesis have been presented in international conferences and have been awarded with:

- "Invest in the Youth" at "The Annual Meeting of the European Society of Radiology 2019" (ESR 2019, Vienna, Austria, February 27 – March 3)
- the "Best Scientific Poster Prize 2018" at "The 50th Annual Scientific Meeting of the British Medical Ultrasound Society" (BMUS, Manchester, United Kingdom, 4-6 of December 2018)

Statement of work performed

I would like to confirm that all the work presented in this thesis is my own with the exception of the following:

1) CFD simulation results (Figure 3.4, Figure 3.5, Figure 3.6, Figure 3.7, Figure 3.13, Figure 3.17, Figure 3.18, Chapter 3) were provided by Simone Ferrari, Early Stage Researcher of the VPH-CaSE consortium (http://www.vph-case.eu/) within the European Union's Horizon 2020 research and innovation programme (Marie Skłodowska-Curie grant agreement No 642612)

2) Echo-PIV and 3D Doppler images (Figure 5.16, Figure 5.17, Figure 5.18, Figure 5.19, Figure 5.20, – Chapter 5) were provided by Emilia Badescu, Early Stage Researcher of the VPH-CaSE consortium (http://www.vph-case.eu/) within the European Union's Horizon 2020 research and innovation programme (Marie Skłodowska-Curie grant agreement No 642612)

Contents

Chapter 6 – Design improvements and instrumentation pack

Chapter 7 – Instrumentation Pack – Experimental Analysis

Chapter 8 – magnetic Resonance Compatible Vortex Ring based Complex Flow Phantom design – Proof of Concept

Chapter 9 – Conclusion and Future Work

Table of Figures

List of Tables

CHAPTER 1

1.1 Introduction and Motivation

Cardiovascular diseases (CVDs) are the biggest cause of death in the modern world (Mendis et al 2011). More than 17 million people die each year (31% global death) and arguably the majority of deaths due to premature heart disease (people under the age of 60) could have largely been prevented (Institute for Health Metrics and Evaluation 2010). In the United Kingdom, 7 million people live with CVDs and the related healthcare costs are estimated to be around GBP 9 billion per year (British Heart Foundation 2018). The early prediction of CVDs is crucial to support diagnosis and to improve surgical outcomes and the evaluation of potential therapies. Consequently, diagnostic techniques are constantly being developed. The tendency is to combine information derived from mechanical, electrical and fluid dynamics tests for more accurate examinations. Pedrizzetti et al (2014) observed that fluid dynamics analysis can reflect the presence of abnormalities before noticeable structural (mechanical or electrical) changes occur and can be an early indicator of CVDs.

Medical imaging techniques, such as Doppler Ultrasound (acoustic waves) and Phase Contrast Magnetic Resonance Imaging (magnetic fields), have been developed for the assessment of the cardiovascular system. The ability of medical imaging techniques to accurately quantify specific physics parameters is assessed periodically as part of the Quality Control process. Quality Control (QC) aims to uncover non-conformities or to identify anomalies from product performance specification. It is not mandatory but it is good practice in every hospital and it is recommended within the principle of Quality Management described by the International Organization for Standardization (ISO 9000:2015 - Quality Management System). QC is commonly performed through the acquisition of images on dedicated test objects, namely medical imaging phantoms, and the evaluation of specific parameters of interests (i.e. spatial resolution, contrast resolution, etc.). If a parameter differs greatly from reference values (exceeding pre-defined tolerances), machine performance may be compromised and, corrective actions may be undertaken. Medical imaging phantoms are specifically designed test objects, manufactured according to rigorous specifications to ensure consistent measurements for medical device evaluation/calibration and for the validation of new techniques at research level.

Currently, there are not many flow phantoms available in literature or on the market; the few that are available are expensive, they lack accuracy of specification and they fail to capture the complexity of flow features present in the cardiovascular system. Consequently, the calibration of medical flow imaging technologies and the definition of standards for routine QC checks is challenging. An innovative, stable, reproducible, complex flow phantom design will enable more effective calibration to clarify the capacity of current technologies to quantify pathological flows.

1.2 Aim of the thesis

It is this context that justifies the work of this thesis. Its aim is the design, construction, development and testing of a novel, cost-effective, robust, compact, multimodal complex flow phantom compatible with medical diagnostic imaging techniques for blood flow analysis. Since the main techniques for the evaluation of blood velocity flow fields are Doppler ultrasound and Magnetic Resonance, the ambition is to develop a phantom design compatible with both technologies. However, the construction and the validation of an advanced multimodal complex flow phantom design is challenging, and therefore, the phantom is first constructed and validated for Doppler ultrasound modalities. Subsequently, the design is adapted for operating in the Magnetic Resonance environment.

Ideally, a medical imaging flow phantom (or test object) provides a flow benchmark that is stable and mimics anthropomorphic conditions. A flow benchmark for medical imaging technologies is important in several ways, including:

- calibration of medical imaging scanners;
- clarification of the capacity of scanners to quantify pathological flows;
- validation of improved quantitative flow algorithms at research level;
- research and development of innovative scanning techniques.

Medical imaging phantoms have the main advantage of providing consistent and reliable performance over time. This allows the carrying out of repeated experiments under the same experimental conditions, avoiding the use of human or animal subjects and the biological variability of tissues. A flow phantom allows investigation of the flow field velocities and supports analysis of the relationship between flow and biological functions.

The fluid dynamics of the cardiovascular system shows complexities both in pathological and healthy conditions. Quantification of these complexities can be crucial for the early prediction of pathologies and more perceptive diagnosis. Although materials must be chosen to be compatible with medical imaging technologies of interest, the key element for the development of the phantom is the flow itself. The phantom provides a flow that offers complex flow patterns that resemble physiological flow conditions. The test object needs to provide reliable and consistent measurements over time. The flow must be stable (resistant to disturbances), reproducible (repeatable over time, within defined tolerances), predictable (within specified tolerances, known fluid dynamics at every point in space and time) and controllable (relevant flow features can be varied in a controlled manner). The ultimate aim of this work is to develop a complex flow phantom compatible with both Doppler ultrasound and Magnetic Resonance Imaging in order to enable comparative studies.

1.3 Structure of the Thesis

The structure of this thesis is as follows:

Chapter 1: basic concepts of medical imaging technologies for blood flow assessment, basic concepts of Quality Control for medical imaging (with focus on flow phantoms), literature and market analysis on flow phantoms for Doppler ultrasound and MRI.

Chapter 2: identification of the candidate complex flow for the phantom (Ring Vortex). Literature review and implications for the development of a complex flow phantom for medical imaging (physiological relevance, stability, predictability, reproducibility, controllability).

Chapter 3: construction of an Air-based Vortex Ring Generator (proof of concept) and a Liquid-based Vortex Ring Generator for characterising flow performance.

Chapter 4: construction of a Vortex Ring based Complex Flow Phantom prototype (technical drawing and specifications).

Chapter 5: testing and validation of three Vortex Ring based Complex Flow Phantom prototypes through independent measurement methods (Laser PIV vs Optical/video, Ultrasound vs Laser PIV).

Chapter 6: design improvements including piston, design and construction of an instrumentation pack tool for supporting testing and characterisation of the complex flow phantom.

Chapter 7: experimental exercise demonstrating the value of the instrumentation pack and to further characterise features of the phantom and flow.

Chapter 8: Magnetic Resonance Compatible Vortex Ring based Complex Flow Phantom design (Proof of concept, design specification and testing in laboratory environment).

Chapter 9: Conclusions, design limitations, study limitations and future work.

1.4 Medical Imaging Technologies for blood flow assessment - Overview

The remainder of this introductory chapter is divided in to three main sections. The first section describes the main medical imaging techniques (and basic physics principles) commonly used to obtain quantitative information on blood fluid dynamics within the cardiovascular system. The second section provides a description of Quality Control in medical imaging and medical imaging phantoms, with an emphasis placed on flow phantoms. The third section provides an analysis of relevant flow phantoms for Magnetic Resonance and Doppler ultrasound developed at research level and available on the market.

1.4.1 Introduction to Medical Imaging for Blood Flow Assessment

Medical Imaging is a critical technology that is used to view the human body in order to obtain information about structures (structural imaging) and physiological functions (functional imaging). The information it provides is used for diagnosis, monitoring and treatment of medical conditions. Medical imaging techniques include use of X-rays (X-ray imaging), acoustic waves (Ultrasound Imaging), magnetic and radiofrequency fields (Magnetic Resonance Imaging), or radioactive tracers (Nuclear Medicine imaging). Doppler ultrasound and Magnetic Resonance Imaging are the most frequently used techniques for blood flow assessment. Examinations are performed with or without the injection of specific contrast agents. The basic principles of these techniques are described in the following sub-sections. Please note that state-of-the art technologies described within this chapter are up to date at the time of writing this manuscript (2019).

1.4.2 Doppler Ultrasound – Basic Principles

Ultrasound imaging is a non-invasive medical imaging technique that uses high-frequency sound waves (between 2-15 MHz) to obtain real-time information about anatomical and functional properties of an organ or tissue. The amplitude and the frequency of the echo, produced by scattering from tissue and red blood cells, and reflections from boundaries between structures with different acoustic impedance, is detected and post-processed to produce an image. Ultrasound imaging relies on the piezoelectric effect of an array of piezo-crystals assembled on a scanning probe (ultrasound transducer). Due to crystal deformation, kinetic (or mechanical) energy is converted into an electrical signal and vice versa (inverse piezoelectric effect).

Ultrasound imaging is a powerful medical imaging diagnostic technique and has a number of advantages, including that it is:

- non-invasive;
- relatively inexpensive;
- universally available;
- mobile (can be performed almost in any venue);
- it requires short scanning time and short post-processing time;
- it provides real time images;
- it provides qualitative and quantitative data;
- non-ionising;
- safe (at diagnostic power output);
- it has higher temporal resolution than MRI (Hong et al 2013; Pellikka et al 2013).

The blood is itself echo-lucent and, for specific applications, can be visualised using contrast agents (typically microbubbles encapsulated in perfluorocarbon lipid shell). However, the basic principle of blood motion detection with ultrasound systems relies on the Doppler effect. The Doppler effect is the change in the observed frequency of the sound wave (f_r) compared to the emitted frequency (f_t) which occurs due to the relative motion between the observer and the source (Hoskins et al 2019).
In a theoretical model:

- if the source and the observer are stationary: the observed sound has the same frequency of the emitted sound;
- if the source is moving towards the observer: the observer witnesses a higher frequency wave than that emitted;
- if the source is moving away from the observer: the observer witnesses a lower frequency wave than that emitted.

The difference in frequency between the sound wave emitted by the transducer (f_t) and the returning wave (f_r) reflected from the targets, is known as Doppler shift ($f_d = f_t$-f_r). The magnitude of the Doppler shift frequency is proportional to the relative velocity between the source and the observer. To assess the flow velocity, clinical ultrasound scanners measure the change in frequency of the sound wave scattered from the red cells in the moving blood. The Doppler shift frequency (f_d) depends on the frequency of the transmitted wave, the speed of sound in the tissue (c) the wave is passing through, the velocity of the scatterers in the blood (v) and the cosine of the angle of insonation (Θ). The angle of insonation is defined as the angle between the path of the ultrasound beam and the direction of the blood flow. This relationship can be expressed by the Doppler equation (1.1) (Quinones et al 2002):

$$f_d = f_r - f_t = \frac{2\, f_t\, v\, \cos\theta}{c} \quad (1.1)$$

In medical ultrasound imaging, a transducer is held stationary and the blood moves with respect to the transducer. The transducer emits the ultrasound wave which is scattered by the moving blood cells. Part of the scattered ultrasound beam returns to the transducer and is detected. The detected signal is shifted in frequency because of the motion of the blood cells. The velocity of the moving scatterers (blood cells) can be derived from equation (1.1), as shown in Figure 1.1.

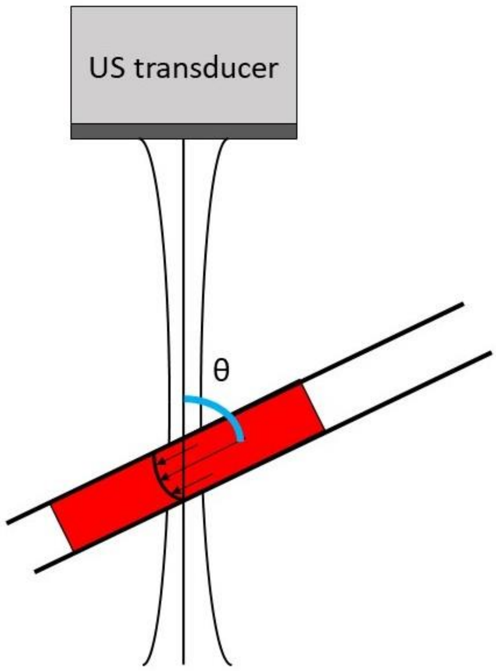

$$v = \frac{c\, f_d}{2\, f_t \cos\theta}$$

v = velocity of the moving targets (blood cells)
f_d = Doppler shift
f_t = frequency of the transducer
θ = angle of insonation
c = speed of sound of the medium

Figure 1.1: Blood velocity estimation – Doppler Effect

The estimation of velocity relies on knowing the angle between the beam and flow direction (angle of insonation). The highest Doppler frequency shift occurs when the beam is aligned with the flow direction, thus, the angle of insonation is 0 degrees ($\cos\theta = 1$). The least desirable situation occurs when the angle approaches 90 degrees ($\cos\theta = 0$) and then the theoretical frequency shift is zero. However, in clinical practice it can be difficult to align the beam and the vessel. As a rule, the angle of insonation should be less than 60 degrees. Significant errors occur when the angle of insonation is greater than 60 degrees (Logason et al 2011).

1.4.3 Conventional Doppler Ultrasound techniques

In conventional Doppler, the Doppler shift data are displayed in real time as Doppler frequency versus time or as a colour-map. The first representation, Spectral Doppler is essentially a time-velocity waveform. The second representation, which is named Colour Doppler, depicts flow toward and away from the transducer as red or blue for individual pixels in a region of interest (ROI) superimposed on the B-Mode image. Conventional ultrasound Doppler techniques for blood flow estimation include three main modalities: Continuous Wave Doppler (CW), Pulsed Wave Doppler (PW) and Colour Doppler Imaging.

In ***Continuous Wave Doppler (CW)*** the ultrasonic transducer continuously transmits and receives ultrasonic signals. Typically, separate piezoelectric elements in the transducer are positioned to allow simultaneous transmission and reception of the ultrasound wave. The main advantage of this technique is that very high velocities can be measured as the sampling rate is not limited by the pulse repetition frequency (PRF). However, the CW Doppler signal combines velocity information from all depths along the beam and cannot be used to select a specific sample depth. CW Doppler tends to ve more sensitive to non-haemodynamic movements along the beam (i.e. moving cardiac structures or vessel walls), which may mask blood flow and information of interest (Maulik 2005).

In ***Pulsed Wave (PW) Doppler***, the same crystals of the ultrasonic transducer emit and receive pulses of ultrasound. Since the speed of sound in soft tissues can be assumed to be approximately constant, velocity information from a specified depths (or sample volume) can be selected based on echo time. PW Doppler works essentially as a sampling tool for the Doppler frequencies generated by the blood flow. The maximum pulse repetition frequency that can be achieved by the system (PRF ~ KHz) depends on the depth of insonation. If the PRF is insufficient for adequate sampling, the Doppler signal may be misrepresented (known as aliasing). To be adequately sampled, Nyquist's theorem suggests that the PRF should be at least twice the Doppler shift frequency ($2\ f_d\ max$). PW Doppler ultrasound is a valuable tool because provides quantitative estimation of blood flow velocity, however, its accuracy depends on a number of setting parameters such as, Doppler sample volume, PRF, angle of insonation, gain and tissue depth.

The Doppler shift detected in continuous (CW) and pulsed (PW) wave is displayed on the screen in a ***spectral form (Spectral Doppler)***. The horizontal axis shows evolution of the velocity while Doppler shift frequency (or velocity) is represented on the vertical axis. The greyscale of the spectral waveform is related to the intensity of the Doppler shift signal. The Doppler shift signal (variation over time) is processed through spectral analysis (typically, Fast Fourier Transform analysis) and velocity plotted as a pixel whose intensity approximately represents the number of scatterers travelling at a given speed (the number of red blood cells at each velocity). This signal is known as power of spectrum. A full spectral processing that represents both frequency and average power content is called power spectrum analysis. The Fast Fourier Transform (FFT) analysis is a highly effective tool for power spectrum analysis because it can be implemented with reduced computational time.

Colour Doppler (CD) is a form of PW Doppler where velocity information and flow patterns are visualised in real time with the use of a colour-coded map. Typically, red is used to denote flow directed toward the probe and blue away from the probe. Different shades of red and blue colour indicate the blood flow velocity scale. CD displays the direction and component of the velocity in the direction of the beam, which allows identification of abnormal haemodynamic, stenosis, occlusion, valvular regurgitation, increased velocities through valve orifices and thrombus formation. Being a PW Doppler modality, the velocity scale and PRF must be optimised to avoid aliasing. The baseline and colour scale range should be kept low enough to obtain meaningful directional flow data and high enough to avoid aliasing. High speeds can be estimated using a high *PRF*, but the sensitivity to low flow is then significantly reduced. At low *PRFs* the system is sensitive to low velocities, but aliasing can occur, and high velocities are falsely interpreted. Other important parameters, such as beam steering, gate size and gain should be optimised to obtain reliable measurements. A detailed review about the optimisation of Doppler parameters in US scanners is provided by Kruskal et al (2004).

1.4.4 Angle independent Doppler Ultrasound techniques (Vector Flow Imaging)

Conventional Doppler ultrasound techniques have the main limitation that only the components along the beam can be estimated (Jensen, 1996). Although angle corrections tools are available, it is still challenging to judge the angle in respect of complex geometries such as valves, bifurcations or tortuous vessels. Furthermore, in cardiac applications the angle can vary during the cardiac cycle and can significantly affect the estimation of the velocity. The analysis of complex flows, such as vortex within the left ventricle, is not possible using conventional Doppler techniques. Velocity components not parallel to the beam are wrongly estimated and velocity components orthogonal to the beam do not generate a Doppler shift. Inaccuracies in velocity estimation, limited haemodynamic information and operator variability (as the measurements are dependent on angle correction by the user) have highlighted the need for angle independent Doppler techniques. Recent developments in Doppler ultrasound include Vector Flow Imaging (VFI), which allows visualisation of blood flow velocity patterns as vectors that indicate direction and magnitude (Hansen et al 2017-a). VFI overcomes the main limitation of conventional Doppler ultrasound techniques by providing angle independent measurements. The true flow vector and the velocity magnitude are calculated from the measurement of at least two of the three components of a velocity vector. Spatial and temporal information are provided without manually performing an angle correction. Generally, the flow is displayed with coloured arrows that indicate the velocity magnitude (colour and length) and flow direction.

The cross-beam (or multibeam, or Vector Doppler) method was one of the first methods for finding the flow vector (Peronneau et al 1974; Dunmire et al 2000). This approach uses multiple beams from different angles to derive the 2-D (or 3-D) velocity vector. The cross-beam method has also been combined with plane waves, where crossing beams are replaced by overlapping regions of steered plane waves. This increases the frame rate and the field of view compared to single beam acquisitions.

The main VFI techniques are the Cross-Beam method, Plane Wave Imaging (PWI), Speckle Tracking, Conventional Transverse Oscillation (TO) and Colour-Doppler-based Vector Flow Mapping (VFM). The complete description of VFI algorithms is beyond the scope of this manuscript and a complete review is provided by Jensen et al (2016). However, basic principles are briefly described for better comprehension, since they represent cutting edge technologies that would benefit from the presence of a complex flow phantom.

The Cross-Beam method employs multiple beams from different angles to estimate the velocity vector. This approach can be combined with Plane Wave Imaging to increase the frame rate and field of view. However, it is used primarily for research and is not implemented on any clinical scanner.

In Plane Wave Imaging (PWI), a plane wave is commonly generated by applying flat delays to the transmit elements of a linear transducer. The wave insonifies a large area of interest and backscattered echoes are recorded and processed. Several image lines are beamformed in parallel by ultrafast scanners (Fast Plane Wave Imaging). PWI is implemented in commercial Mindray (Mindray Medical International Limited, Shenzen, China) clinical scanners.

Speckle tracking can be performed with (traditionally called echo-PIV) or without (Blood Speckle Tracking) the use of contrast agents. Microbubbles are used to increase the backscattered echoes from blood flow in echo-PIV while the speckles emerging naturally from the red cells are tracked in blood speckle tracking. Speckle movements are tracked from one frame to the next using block-matching algorithms and the velocity vectors are estimated. Blood Speckle Tracking (or Blood Speckle Imaging) is implemented on GE Healthcare (GE Healthcare, Illinois, USA) VIVID™ scanners.

Transverse Oscillation (TO) employs a single array transducer and two received beamformers to estimate axial and transverse components of the velocity vector. The TO technique was FDA approved in 2013 and is available on BK Ultrasound (BK Ultrasound, Nova Scotia, Canada) and Carestream (Carestream Health, Ontario, Canada) scanners for phased array, convex and linear probes (Jensen et al 2013).

Colour-Doppler-based Vector Flow Mapping (also known as VFM) is based on post processing of colour Doppler images. Since it provides streamline distribution and quantitative information about the strength and the direction of vorticity distribution fields, this method has been mostly developed for the clinical evaluation of complex flows within the left ventricle chamber. VFM is commercially available on Hitachi (Hitachi Ltd., Tokyo, Japan), GE Healthcare (GE Healthcare, Illinois, USA) and Mindray (Mindray Medical International Limited, Shenzen, China) clinical scanners.

1.4.5 Magnetic Resonance Imaging – Basic Principles

A competing technology for measuring flows, and therefore relevant for the development of a complex flow phantom, is Magnetic Resonance Imaging (MRI). In MRI, the combination of strong magnetic fields and radio frequency signals is used to excite hydrogen nuclei in the body. When nuclei with half-integer spin are placed into a magnetic field with intensity B_0, their magnetic moment precesses around the axis field with frequency ω_0 (resonance frequency or Larmor frequency). The Larmor frequency is given by (1.2) (Kwong et al 2008):

$$\omega_0 = \gamma B_0 \quad (1.2)$$

where Υ is the gyro magnetic ratio. Fields with linear varying intensity (gradients) are commonly applied to vary the rate at which the spins precess. Three different gradient magnetic fields can be applied: G_x, G_y, and G_z. Depending on the location in space of the region of interest, the gradients add or subtract from the main static magnetic field B_0 an amount of field strength. Applying gradients $G_{x,y,z}$ to the field, the resonance frequency of the spins varies according to (1.3) (Kwong et al 2008):

$$\omega_0 = \gamma(B_0 + G_X x + G_Y y + G_Z z) \quad (1.3)$$

After the excitation radio-frequency signals are removed, the nuclei relax sending decaying signals that are measured by receiver coils. The procedure is repeated multiple times and different gradients and pulse sequences are applied. Several acquisition techniques are used to obtain 2-D or 3-D information about anatomy, motion, functioning and perfusion of organs or tissues (Haacke et al 1999). MRI has requirements for a complex flow phantom because imaging reconstruction algorithms are very elaborate. Many assumptions are made in the image reconstruction process, which may hide errors or provide false quantitative information. Flow-sensitive MRI techniques, based on intrinsic motion sensitivity of phase images (Phase Contrast MRI), have been developed, tested and validated both *in vitro* and *in vivo* since the 1980s (Bryant et al 1984; Moran, 1985; O'Donnel 1985; Firmin et al 1987; Maier et al 1989; Pelc et al 1991; Kraft et al 1992; Rebergen et al 1993; Pelc et al 1994; Frayne & Rutt 1995; Lotz et al 2002; Kwong et al 2008). Basic principles of Phase Contrast MRI technique are described in the following sections.

1.4.6 Flow-sensitive MRI technique – Phase Contrast MRI

Phase Contrast (PC) MRI is a non-invasive medical imaging technique that can be used to visualise and quantify tissue motion or blood flow. The MR signal is a function of longitudinal (M_z) and transverse (M_{xy}) components of spin magnetization in blood or tissue (Figure 1.2). Magnitude and phase images are influenced by the length and orientation of the transverse component (M_{xy}). Phase images are motion sensitive, therefore, these can be used, in combination with specific magnetic gradients, to measure local velocities of moving spins.

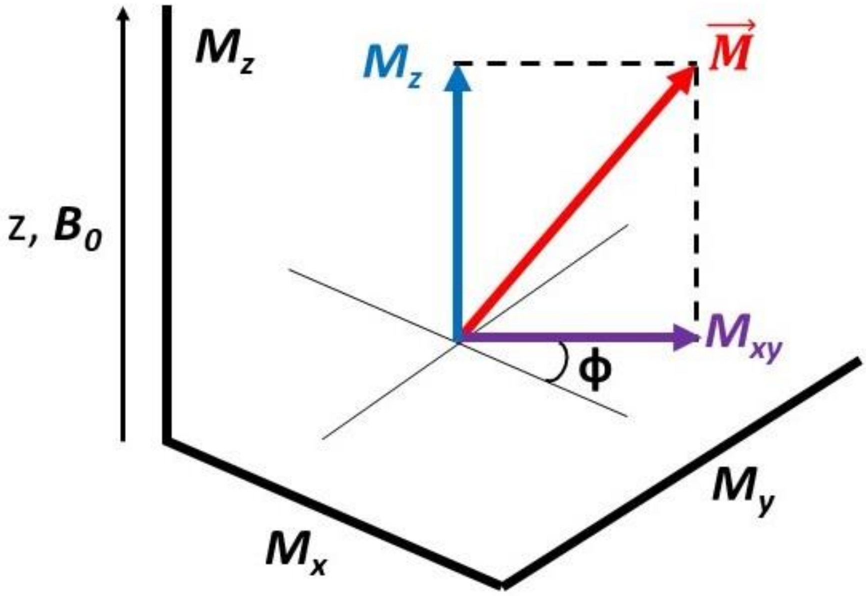

Figure 1.2: Longitudinal (*Mz*) and transverse (M_{xy}) spin magnetization in blood or tissue. Magnitude and phase images can be derived from the length and the orientation of M_{xy}. ϕ = phase.

Magnetic moments (spins) moving along a magnetic field gradient experience a phase shift which, for linear field gradients, is proportional to the velocity of the moving spin (Lotz et al 2002). If constant velocity motion is assumed and no refocusing radio frequency pulses are used, the phase shift at the time (*t*) (after the transverse magnetization is created) is proportional to the velocity (*v*) and to the first moment of the gradient waveform (Pelc et al 1991):

$$\emptyset\ (\mathrm{t}) = \gamma v \int_0^t G(t)\ t\ dt \qquad (1.4)$$

Therefore, the transverse magnetization of spins that move in the presence of a magnetic field gradient acquire a different phase than static spins. The diagram in Figure 1.3 shows the effect of an external magnetic field gradient applied to static and moving spins.

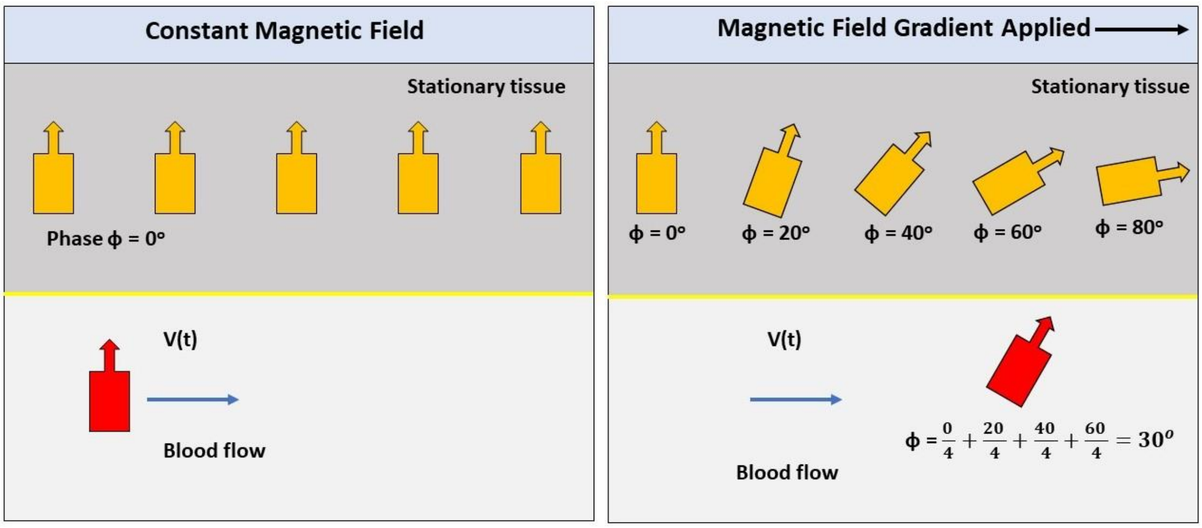

Figure 1.3: External magnetic field gradient applied to static and moving spins. The amount of phase difference is proportional to the velocity *v(t)* of the moving spin and to the amplitude and timing of the gradient. ϕ= phase, t=time, v= velocity.

Unfortunately, the phase change of the spins can be affected by many other phenomena, such as B_0 inhomogeneity, magnetic field eddy currents and motion in other directions. Consequently, it is not possible to image flow from a single data acquisition and from the assumption the change in phase is only due to motion in the direction of interest (Bryant et al 1984). In order to quantify flow or motion velocities, PC MRI methods do not rely on absolute phase images but on relative phase shifts. Multiple measurements are performed using identical acquisition parameters and varying the velocity encoding gradients. Subtraction of the resulting phase images allows elimination of phase shifts induced by the sequence of parameters and quantitative assessment of the velocities of the underlying flow or motion. The simplest PC MRI pulse sequence, known as the "two-point method", requires two measurements, each made with a different magnetic field gradient along one direction to examine motion in that direction (O'Donnel 1985). Two bipolar gradients with equal magnitude but opposite polarities are applied, as shown in a schematic representation in Figure 1.4. Stationary spins do not experience any phase change after the two gradients are applied. Moving spins have a different spatial position and experience a different magnitude of the second gradient compared to the first. Thus, moving spins undergo phase change proportional to the blood flow velocity and to the amplitude and timing of the gradient.

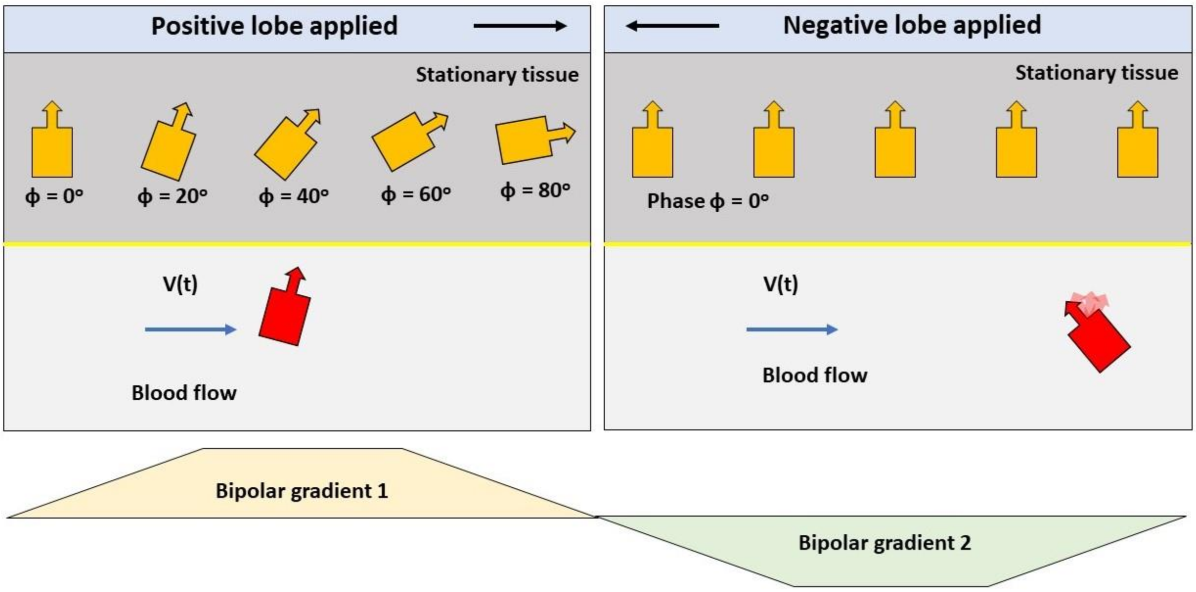

Figure 1.4: Two acquisitions are performed with identical parameters except for the flow-sensitising bipolar gradients. Subtraction of the two resulting phase images allows quantification of the flow or motion velocities. Stationary spins undergo no net change in phase after the two gradients are applied while moving spins experience a phase shift. ϕ= phase, t=time, v= velocity.

Three pairs of measurements ("six-point method"), each pair sampling along one Cartesian direction, are needed to measure motion along all directions (*X, Y, Z*) (Pelc et al 1991). The "six-point method" uses an independent phase reference for each direction *X*, *Y* and *Z*. Alternatively, a single-phase reference can be measured and used to encode the other directions. In this case, one measurement provides the phase reference (ϕ_0) and other three points are needed to encode differentially in each direction ("four-point method") (Pelc et al 1991). A PC MRI measurement also requires prior knowledge of the magnitude of the velocities that have to be quantified. The velocity dependent phase shift has to be within a range of +/-180° (+/-π) to avoid wraparound. The velocity encoding (V_{enc}), which is given in centimeters per seconds (*cm/s*), determines the highest and lowest detectable velocity (or the velocity that produces a phase shift of 180°) that can be encoded by a phase-contrast sequence. Velocity sensitivity is defined as the velocity that produces a phase shift ($\Delta\phi$) of π radians, and is determined by the difference of the first gradient moments used for the velocity encoding (1.5) (Kwong et al 2008, p. 207):

$$V_{enc} = \frac{\pi}{\gamma \Delta M} \quad (1.5)$$

where Υ is the gyro magnetic ratio and ΔM denotes the difference of the first moment of the gradient time curve. For velocities larger than the velocity encoding (V_{enc}), the velocity induced phase shift will exceed +/-π and phase wrapping (aliasing) occurs. Unfortunately, the velocity encoding (V_{enc}) cannot be set arbitrarily high because that incurs a signal-to-noise ratio (SNR) penalty. The better the encoding velocity matches the peak velocity of the region of interest, the more precise the measurement will be.

1.4.7 Phase Contrast MRI – from 2D to 4D

Phase Contrast Magnetic Resonance Imaging has seen clinical acceptance for the visualisation and quantitative assessment in the heart, aorta and large vessels (Nayak et al 2015). Traditionally, electrocardiography-gated time-resolved (CINE) 2D phase-contrast MRI sequences were used in clinical practice for quantifying blood flow and peak flow velocities (Bollache et al 2016). Velocity was encoded in single direction through a 2D plane (2D-1dir) during a breath-holding. Instantaneous flow rate and total forward and backward flow during a cardiac cycle were derived, basing on the area of the vessel cross-section and the average velocity within the defined region (van der Geest and Garg, 2016). However, placement of the 2D acquisition plane is challenging and peak velocities can be underestimated if misplaced or not orthogonal to the flow direction. In common cases involving complex intra-cardiac patterns, flow quantification accuracy of 2D PC MRI is limited. This limitation can be improved by taking into account all flow directions, which can be achieved by three-directional encoding of all three principal velocity directions inside a slice of interest (2D-3dir) (Bollache et al 2016). Alternatively, flow-encoding can applied to all the three spatial directions to obtain data in all the three dimensions of space and to the dimension of time along the cardiac cycles (4D flow MRI = 3D MRI + time) (Dyverfeldt et al 2015). Velocity is encoded along the three spatial dimensions providing a time-resolved 3D velocity field. 4D flow MRI has great potential for quantifying intra-cardiac parameters of the blood flow, such as vortex ring formation or vector flow components. The image provides full volumetric coverage of the structure of interest with comprehensive spatial and temporal information on the 3D blood flow dynamics (Markl et al 2014). Several visualization techniques, such as color-coding, streamlines or vectors display, are used for visual data interpretation in 2D or 3D (van der Geest and Garg, 2016). By way of example, streamline display of intra-cardiac vortex ring flow is shown in Figure 1.5. Quantitative analysis can be performed in post-processing from a single 4D flow MRI acquisition. The scanned 3D volume can be retrospectively reformatted in 2D images planes and through-plane velocity encoding can be applied for flow quantification, similar to conventional 2D phase contrast imaging (van der Geest and Garg, 2016).

Main advantages are that:

- measurements are derived from a single scan, therefore, heart rate variability does not degrade measurement consistency;
- position and orientation of the reformat planes can be adjusted at any location inside the 3D data volume;
- multiple measurement planes can be defined from a single acquisition.
-

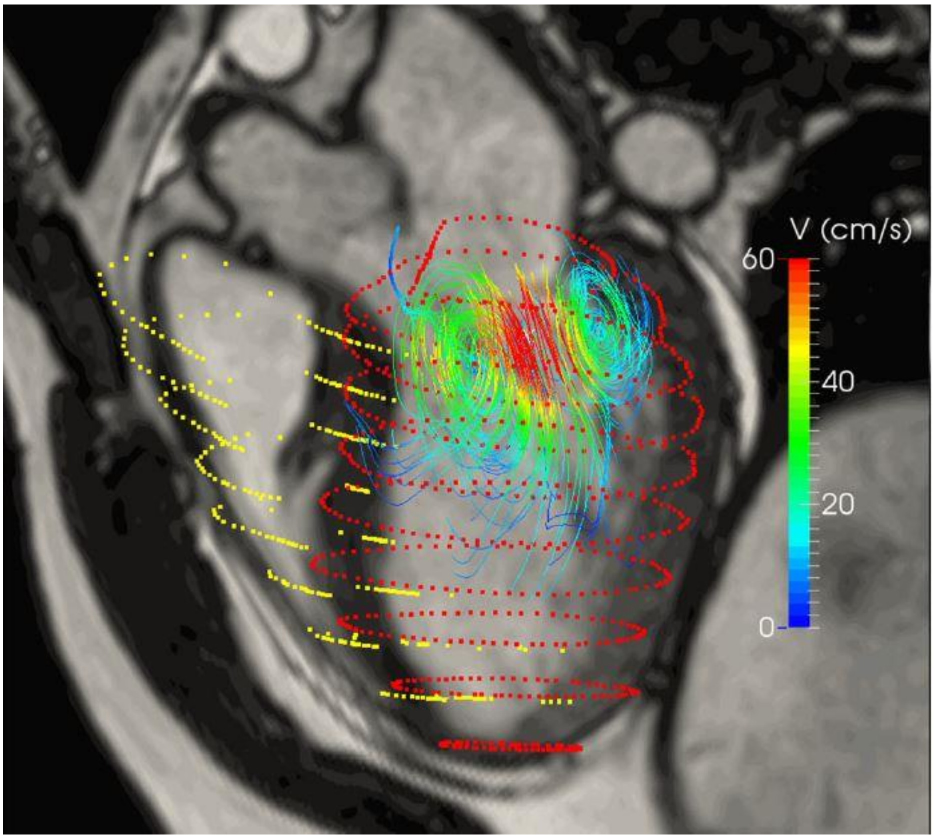

Figure 1.5: Streamline display of intra-cardiac vortex ring following a 4D Flow MRI acquisition. Left ventricle and right ventricle endocardial surfaces are displayed with red and yellow dots, respectively.

Figure 4: van der Geest, R.J. & Garg, P. (2016). Advanced analysis techniques for Intra-cardiac Flow evaluation from 4D Flow MRI. *Cur Radiol Rep,* 4:38.

1.4.8 Summary

In general, there is no such thing as a perfect imaging system. The medical imaging modality is chosen to match the clinical need or the research question. Doppler ultrasound and Phase Contrast (PC) Magnetic Resonance Imaging are currently the preferred technologies for quantitative analysis of intravascular complex (i.e. turbulent, vortical) flows. Both techniques can provide 2D and 3D blood flow field imaging as a function of time (4D flow MRI and Ultrasound VFI). Since no ionising radiations are involved, Ultrasound and MRI scanning are suitable for repeated follow up studies. Although there are short-term hazards for MRI, they are well known and well managed in clinical practice (Hoskins 2017).

Phase Contrast MRI is a powerful and well-established technique for obtaining (non-invasively) quantitative information on the blood flow or tissue motion. It is widely considered the gold standard for blood flow assessments of the cardiovascular system (Brown et al 2014). 2D PC MRI is not suitable for the quantification of complex flow patterns: underestimation of peak velocities occurs when the 2D acquisition plane is misplaced or not placed orthogonal to the flow direction. As an alternative, 4D Flow MRI has developed to obtain more comprehensive information on blood flow through the heart and large vessel. However, 4D Flow imaging requires the acquisition of a large amount of data. Long scan times, ranging from 10 to 20 min, initially limited the application of the technology to research (Markl et al 2014). Recent developments have reduced scan times to a range of 2-8 min (Garg et al 2018; Zhang et al 2018; Garcia et al 2019) and a consensus statement on the clinical utility of the technology has been published (Dyverfeldt et al 2015). Current implementations in 4D flow MRI are quickly approaching clinically feasible scan times, however, the technology is still not routinely accepted in clinical practice. In addition, MRI is not compatible with all patients. Implantable devices, such as stents, cardiac valves or pacemakers, produce artefacts in the image or rules out Magnetic Resonance scanning (Segupta 2012). Apart from technical issues, such as motion artefacts due to patient breathing, MRI can prove to be a problem for hospitals because it is time-consuming with implications for long patients waiting lists. Moreover, a Magnetic Resonance device (and compatible Magnetic Resonance room) can cost over 1 million GBP and its presence is limited to specific departments of a high budget hospital.

An effective diagnostic alternative is Doppler ultrasound, which is a non-invasive, non-ionising, cost-effective, portable and fast medical imaging technique that provides real-time quantitative and qualitative information about the fluid dynamics of the blood flow. The use of Doppler ultrasound can significantly reduce waiting lists with comparable diagnostic results to MRI. This has clinical impact, providing rapid diagnosis and improved outcomes. The accuracy, the precision and the clinical efficacy of several Doppler ultrasound techniques have been widely demonstrated and constant effort is put into research, aiming to make ultrasound diagnostic imaging the first method of choice for real-time analysis of blood fluid dynamics (Jensen et al 2016; Hansen et al 2017-a).

Transverse Oscillation (Ultrasound Vector Flow Imaging technique) has been FDA approved (2013) and it is recommended as the first choice for real-time assessment of cardiovascular complex flows (Jensen et al 2013). 2D and 3D velocity VFI algorithms are currently available on research scanners manufactured by Verasonics (Verasonics Inc, Washington, USA) and on clinical scanners manufactured by GE Healthcare (GE Healthcare, Illinois, USA), BK Ultrasound (BK Ultrasound, Nova Scotia, Canada), Mindray (Mindray Medical International Limited, Shenzen, China), Carestream (Carestream Health, Ontario, Canada) and Hitachi (Hitachi Ltd., Tokyo, Japan).

Currently, there is little in the way of cost-effective phantom technologies on the market able to challenge clinical ultrasound scanners incorporating these innovative modalities. Validated complex flows are desirable to support calibration of equipment and drafting of new QC protocols for these devices. A test object that provides a known (with well-defined tolerances) complex flow field would be advantageous to support calibration, validation, research and development of quantitative blood flow velocity algorithms for both Ultrasound and MRI modalities.

1.5 Quality Control in Medical Imaging

The scope of this thesis is the development of a phantom to test the ability of advanced medical flow imaging scanners to quantify complex flow patterns. The aim is to provide a flow benchmark for comparative studies, Quality Control and calibration of clinical scanners, which is suitable for testing and validating advanced velocity estimation algorithms at a research level.

As described in the previous section 1.4, Ultrasound Vector Flow Imaging is already available on a number of clinical scanners while Phase Contrast Magnetic Resonance Imaging is still not fully clinically accepted due to expense and long scanning times. Consequently, the phantom prototype described in this thesis is initially designed to challenge clinically available ultrasound technologies. Design adaptation for Magnetic Resonance environment compatibility and for comparative studies (Ultrasound vs MRI) is described in Chapter 8.

Basics concepts of Quality Assurance and Quality Control in medical imaging are described in this section. Definition, classification, use, and relevance of phantoms in medical imaging are described in detail.

1.5.1 Introduction

The International Organization for Standardization (ISO) defines Quality Assurance (QA) and Quality Control (QC) as follows (ISO 9000:2015):

Clause 3.3.4 - Quality Assurance: "part of quality management focused on providing confidence that quality requirements will be fulfilled".

Clause 3.3.7 – Quality Control: "part of quality management focused on fulfilling quality requirements".

In other words, Quality Assurance (QA) is a proactive process whose purpose is to prevent nonconformities (defects) in products from the beginning of the manufacturing process, while Quality Control (QC) is a reactive process that seeks to eliminate nonconformities in the finished product. They are both part of the Quality Management System (ISO 9000:2015) and they include activities such as inspecting, monitoring, checking, testing and recording. QA analyses the process and the product while the QC identifies flaws in the finished product. Quality Control in medical imaging can be described as a series of regular (daily, weekly, monthly or yearly), detailed evaluations of medical imaging equipment by qualified personnel (e.g. a medical physicist, engineer, clinical scientist, qualified technician). QC is desirable and aims to obtain an optimal image through the evaluation of specific parameters. If the specific parameters differ greatly (with values exceeding defined tolerances) from the reference values, corrective actions must be taken and may stop the device from being used. Commonly, the assessment is made through the acquisition of images on dedicated test objects (medical imaging phantoms) and the subsequent evaluation of the main physical parameters of the image. Phantoms play a basic role both at research and clinical level and ideally they should develop in step with new technologies.

1.5.2 Medical Imaging Phantoms

Medical imaging phantoms are specific test objects designed to provide consistent, reliable, qualitative and quantitative information when scanned or imaged in the field of medical imaging. Results should be consistent over time and (ideally) measurements should be traceable to national or international standards. Phantoms are widely used for calibration, Quality Assurance, training, validation, research and development of new imaging techniques both at commercial, hospital and research levels.

The use of test objects has four main advantages (Hoskins 2017):

- ***Reproducibility of results***: a test object is designed to provide reliable and consistent results over a defined time. This allows repeated experiments under the same (within specified tolerances) experimental conditions, avoiding measurement problems associated with biological variability.
- ***Control***: test objects are designed to provide a high degree of control including geometries, dimensions, flow rates, pressures etc.
- ***Ethics***: test objects allow the undertaking of experiments without the use of human or animal subjects, biological tissues and hazardous materials. This avoids all the ethical issues associated with licensing and health and safety regulation.
- ***Idealisation***: medical imaging phantoms can be broadly categorised as anthropomorphic, semi-anthropomorphic and non-anthropomorphic.

Anthropomorphic phantoms mimic as closely as possible the anatomy and/or the physiology of a human subject in pathological and/or healthy conditions. The design aims to be a useful “substitute” for human body parts. By way of example, a whole body anthropomorphic phantom manufactured from Kyoto Kagaku (Kyoto Kagaku Co., Ltd, Kyoto, Japan) is shown in Figure 1.6.

Figure 1.6: Anthropomorphic whole-body phantom PBU-60 manufactured by Kyoto Kagaku (Kyoto Kagaku Co., Ltd, Kyoto, Japan)
Figure 1: Kyoto Kagaku catalogue (https://www.kyotokagaku.com/lineup/pdf/ph-2_catalog.pdf)

Semi-anthropomorphic phantoms provide a simplified version of human body parts, which aims to conserve the key aspects of interest that the user wants to investigate. An example of a semi-anthropomorphic phantom is the PETIQ phantom (Figure 1.7) developed by Leeds Test Objects Ltd (Boroughbridge, United Kingdom). This phantom meets the standards NEMA-NU2 (2007) and IEC

61675-1 (2013) for Quality Control of image quality in Positron Emission Tomography (PET). The design simulates the trunk of the human body in terms of average dimensions and shape.

Figure 1.7: Semi-anthropomorphic PETIQ phantom designed by Leeds Test Objects Ltd for Positron-emission Tomography quality control (Leeds Test Objects Ltd, Boroughbridge, United Kingdom).
Figure 1: https://www.leedstestobjects.com/wp-content/uploads/PET-IQ-product-specifications13.pdf

Finally, non-anthropomorphic phantoms are designed with high precision machined (tolerances typically of +/- 0.1 mm) test targets to allow the calibration of medical devices at clinical and research level. Non-anthropomorphic phantoms usually contain line pairs per mm (LP/mm) resolution targets and simple geometric structures, such as circular- or square-shaped targets, with different contrast levels. These targets support quantitative measurements of fundamental imaging parameters, such as low contrast resolution, spatial resolution, geometric distortion, Modulation Transfer Function (MTF), Point Spread Function, etc. As an example, non-anthropomorphic phantoms manufactured by Leeds Test Objects Ltd (Leeds Test Objects Ltd, Boroughbridge, United Kingdom) for Fluoroscopy and Magnetic Resonance modalities are shown in Figure 1.8.

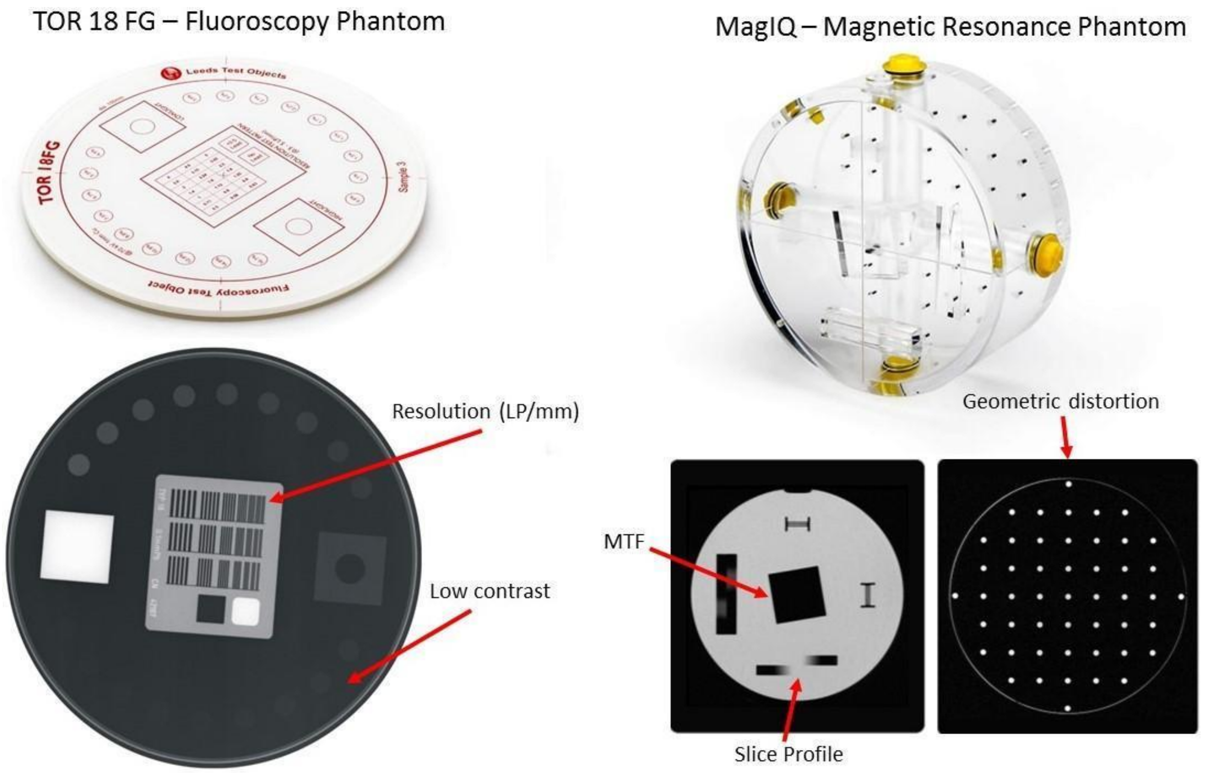

Figure 1.8: Non-anthropomorphic phantoms TOR 18FG and MagIQ manufactured from Leeds Test Objects Ltd (Leeds Test Objects Ltd, Boroughbridge, United Kingdom).
Figure: Images adapted from Leeds Test Objects Ltd brochures (https://www.leedstestobjects.com/).

1.5.3 Flow Phantoms

Flow phantoms are a challenging area of phantom design since they must invoke motion, produce a known field (within pre-defined tolerances) and mimic in vivo conditions. Depending on the application, flow phantoms can be designed with anthropomorphic, semi-anthropomorphic or non-anthropomorphic considerations. In general, a flow phantom consists of a conduit which mimics geometries of interest of the cardiovascular system through which a fluid (blood mimic) is pumped. The conduit is embedded in a material that mimics human tissues (Tissue Mimicking Material) and it is compatible with the medical imaging modalities of interest. When appropriate, the simplest Tissue Mimicking Material (TMM) is deionised water because it has well known physical properties. The blood mimicking fluid usually consists of a mixture of deionised water and chemical components (or particles). The chemical components are chosen to provide viscosity and density comparable to the blood, and signals that can be detected by the imaging system of interest. The pump is usually computer controlled and (ideally) provides pulsatile flow with known waveforms and tolerances. Information and quantities of interest, recorded by the imaging system, are compared with the reference values provided by the phantom specifications (hopefully well established). Basic components constituting a standard flow phantom are shown, with a schematic representation, in Figure 1.9.

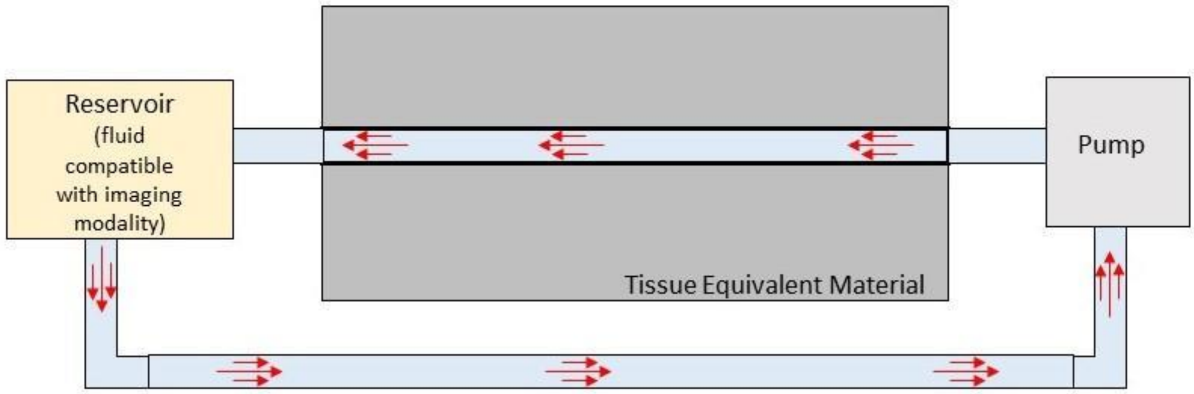

Figure 1.9: Basic components of a flow phantom

Such phantoms allow the calibration of clinical medical imaging systems by permitting repeated experiments in the laboratory, which would be difficult (or impossible) in living subjects.

A flow phantom is commonly used for (Hoskins 2017):

- investigation of flow field velocities: phantoms can be built with optical transparent materials that allow the undertaking of measurements with optical imaging systems, such as Laser-PIV (Particle Imaging Velocimetry) or LDA (Laser Doppler Anemometry). These technologies have high temporal and spatial resolution and allow reconstruction of the flow field velocity data and associated phenomena;
- cross-validation of flow-field data obtained using different medical imaging modalities and optical imaging systems: medical imaging systems, such as MRI and Ultrasound, can be used to measure blood velocity flow fields and associated quantities. Comparative studies can be carried out (even using optical imaging systems data) and validation of new techniques for blood flow velocity estimation can be undertaken;
- investigation of the relationship between flow and biological functions: flow phantoms can be built with materials and geometries that mimic specific physical properties (i.e. elasticity and dimensions) of sections of the cardiovascular system. Relationships between the physical properties of interest and biological function can be studied.

A flow phantom cannot mimic in detail all the aspects of the cardiovascular system, but needs to be sufficiently complex to allow specific research questions to be answered (Hoskins 2017). The phantom design should not be over complicated, but should provide a simplified version of reality and mimic key aspects of interest in a reproducible and controllable way. The research question comes first. The flow phantom design follows the research question, trying to satisfy all the main aspects that characterise a test object (i.e. reproducibility, controllability, stability).

1.5.4 Steps for the development of a medical imaging phantom

No single test object, tissue mimicking material or geometrical shape will be optimal for all the applications and modalities available on a single medical device. However, a few basic requirements for the development of a test object can be identified.

An ideal test object should be:

- simple;
- usable;
- informative;
- discriminative (between several images);
- reliable (consistent results);
- robust;
- safe (i.e. transport, delivery);
- provided with well-defined accuracy specification.

Quality Control checks are often performed within tight schedules so that they do not interfere with clinical workflows, therefore, a test object should be simple, to set up and use and should provide results that are easy to interpret. The phantom design should be informative and usable for the purpose for which it has been developed. It should enable discrimination between different images and different image techniques. It should be robust to provide consistent results within a reasonable amount of time. The phantom should be easy and safe to ship, and testing materials (i.e. imaging compatible solutions) should be accurately contained. Open source packages or software tools for consistent and quick analysis of imaging data should be encouraged.

Typically, the development of a new phantom design involves cooperation between manufacturers and clinical scientists (i.e. medical physicist, biomedical engineers) (Figure 1.10). Clinical scientists identify needs, project objectives and goals. Manufacturers define what is doable (in practice), identify the most cost-effective solution and pursue market opportunities. Within this process, the scope of the project is defined, and usually a non-disclosure agreement is signed between parties. The manufacturers are responsible for the development of prototypes and for the modification (if needed) until the design is validated. Prototypes are tested by clinical scientists in a clinical setting, such as a hospital, a university, or a private clinic. Suitability for the task, reliability and accuracy of the results are the features most evaluated. Eventually, if sufficient evidence of test results is observed the design is validated. Clinical scientists (may) use the results to write protocols (e.g. IPEM, ACR standards) and scientific articles while manufacturers (may) launch a product on the market that is supported by valuable scientific evidence.

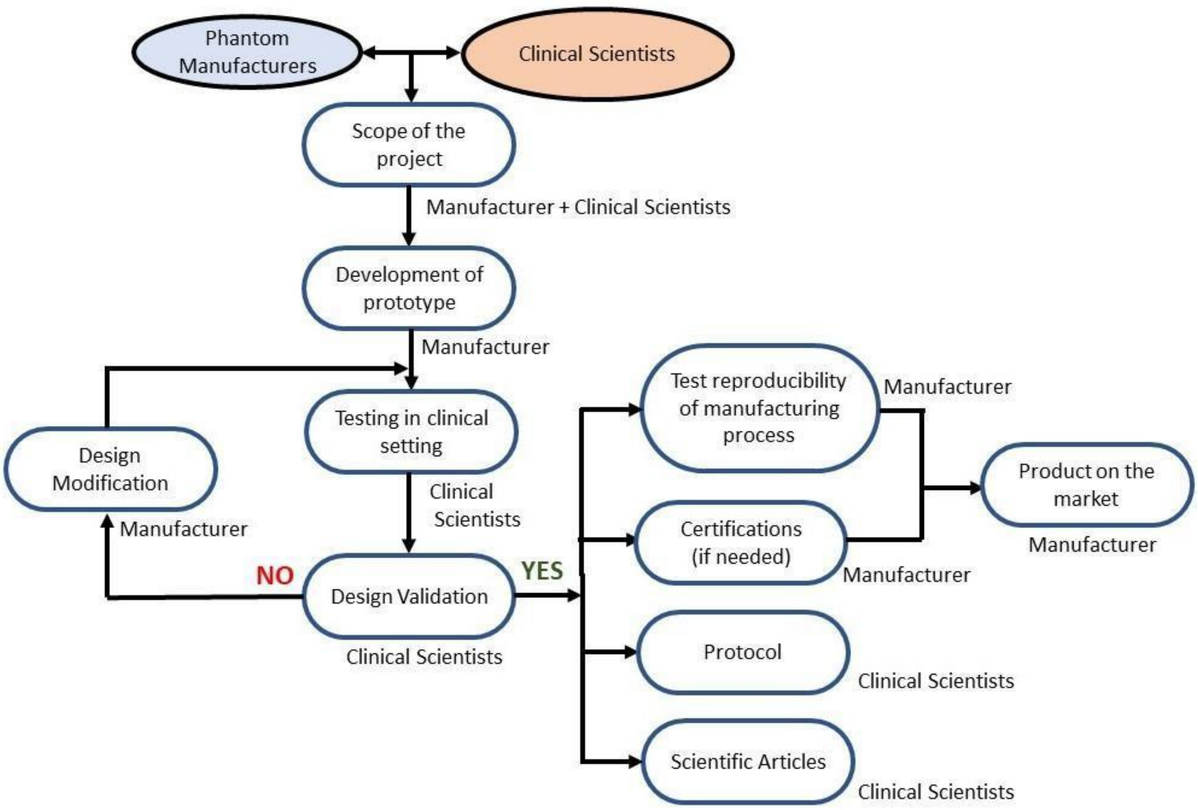

Figure 1.10: typical workflow for the development of new protocols and test objects

1.5.5 Summary

Quality Assurance and Quality Control in medical imaging are advisable to maintain optimal diagnostic image quality with minimum hazard to patients. Device performance is evaluated with the acquisition of images on specifically designed test objects (phantoms). Test objects have the main advantage of providing reliable and consistent results over time, avoiding the use of human or animal subjects. Depending on the application, medical imaging phantoms are designed with anthropomorphic, semi-anthropomorphic or non-anthropomorphic shapes. Key requirements and steps for the development of a medical imaging phantom have been listed. Cooperation between manufacturers and clinical scientists is desirable for the development of harmonised standards and for the designs of effective test objects.

A market analysis is conducted in the next section of this chapter, in order to identify which technologies are currently proposed/available for flow phantom design. Relevant technologies proposed in literature have been also quoted.

1.6 Relevant Flow Phantom technologies available in the literature and on the market

1.6.1 Flow Phantoms and their Design – An introduction

From an analysis of the literature and of the phantom market it is noticeable that there are not many flow phantoms available. They tend to be expensive, fail to mimic relevant physiological conditions and accuracy specifications are not clearly provided. Consequently, calibration and Quality Control checks of medical imaging systems for blood flow assessment are challenging or not feasible. In addition, the lack of appropriate equipment makes the creation of well-defined Quality Control guidelines difficult to establish.

This section describes relevant flow phantoms that have been developed at a commercial and research level, for Doppler ultrasound and Magnetic Resonance Imaging flow modalities (at the time of writing this manuscript, 2018). Doppler ultrasound and Magnetic Resonance modalities have been selected over X-ray modalities because these are the main medical imaging technologies used for quantitative blood flow velocity estimation (as described in Section 1.4).

1.6.2 Phantoms for Doppler ultrasound

The choice of ultrasound compatible materials is an important challenge in the construction of a flow phantoms for Doppler modalities. The choice of conduits and surrounding materials has important implications for acoustic wave propagation and for velocity Doppler estimation. For simplicity the phantom proposed in this thesis is designed to work in the free field (deionised water), although it does offer some possibility for embedding of tissue mimicking materials (TMMs). Nonetheless, the latter is not the focus of this work and analysis of tissue and vessel mimicking materials for ultrasound compatibility would be outside the scope of this study. However, relevant studies of Doppler ultrasound flow phantoms are acknowledged and the main technologies proposed for ultrasound Vector Flow Imaging evaluation are also reported.

1.6.3 Doppler ultrasound flow phantoms proposed in literature

A C-Flex pipe surrounded by an Agar-based TMM is the design suggested by the BS EN 61685:2002 – IEC 61685:2001, a current International standard (stability date: 2020) for the development of a flow Doppler test object (BS EN 61685:2002, IEC 61685:2001). However, C-Flex tubing (Cole-Parmer, IL, USA) has attenuation values that are five to ten times higher than vessel tissues and even thin wall thickness (0.2 mm) produces substantial Doppler Spectral distortion (Hoskins 2008). A large number of alternative materials have been characterised and tested as vessel mimicking material including PVA-c, Norprene, Perspex and Polyethylene (Hoskins 2008).

As an alternative to phantom designs embedding pipes, wall-less phantoms have been widely proposed and tested in the literature (Rickey et al 1995; Ramnarine et al 2001; Pye & Ellis 2002; Meagher et al 2007; Weir et al 2015; Kenwright et al 2015-b; Ho et al 2017; Zhou et al 2017). Tissue

Mimicking Materials are used to form channels, which mimic soft tissues properties in terms of characteristic acoustic impedance, acoustic attenuation, speed of sound and acoustic backscatter coefficient (BS EN 61685:2002, IEC 61685:2001). Agar-based (Teirlinck et al 1998) and gelatine-based (Madsen et al 1982) TMMs have been extensively studied and fully characterised (Brewin et al 2008; Sun et al 2012; Rajagopal et al 2015). However, these materials are brittle and lack mechanical strength (they break if the flow speed is set higher than certain limits), therefore, they have been widely used in research studies but are not commonly used in commercial ultrasound phantoms. Another material widely used is Polyvinyl Alcohol (PVA). PVA is prepared as a gel and exposed to different freeze-thawing cycles to produce an elastic material called PVA-cryogel. Several studies have been conducted on different PVA-based recipes (Chu & Rutt 1997; Surry et al 2004; Dineley et al 2006; Cournane 2010; Cannon et al 2011; Ramnarine et al 2013; Kokkalis et al 2014; Zhou et al 2017) but the physical properties of the final cryogel are strictly dependent on the evaporation during the mixing (typically performed at temperatures higher than 90 degrees), freezing temperature, freezing holding time, thawing rate and number of freezing/thawing stages (Peppas and Scott 1991; Stauffer and Peppas 1992). In addition, the reproduction of certain shapes is challenging because it is not possible to fully control the gel swelling process during the freezing stages. All these variables make the repeatability of the manufacturing process challenging. The intra- and inter-variability of the PVA manufacturing process, which significantly affect the acoustic and mechanical properties of the final TMM, makes comparative studies challenging.

As an alternative to flow phantoms, rotating test objects have been used for mean velocity accuracy and spatial resolution estimation. The rotating block, consisting of reticulated foam (Mc Dicken et al 1983), block of gelatine (Fleming et al 1994) or agar-based TMM (Kripfgans et al 2006; Ressner et al 2006; Yang et al 2013; Kenwright et al 2015; Badescu et al 2017; Ketterling et al 2017), can simulate blood flow and tissue motion. The Rotating Cylinder Phantom has the main advantage of providing known axial and lateral velocities over a wide range of Doppler angles. Vector Flow Imaging techniques have been successfully applied among others by Kripfgans et al (2006), Badescu et al (2017) and Ketterling et al (2017), amongst others. Unfortunately, the Rotating Cylinder phantom is not commercially available and does not provide complex flow features. Images of the phantom developed by Kripfgans et al (2009) and examples of VFI results obtained by Ketterling et al (2017) are shown in Figure 1.8a and Figure 1.11b, respectively. Typically, a block of TMM is immersed in water and rotated at known velocity through the connection to a stepper motor (Figure 1.11a).

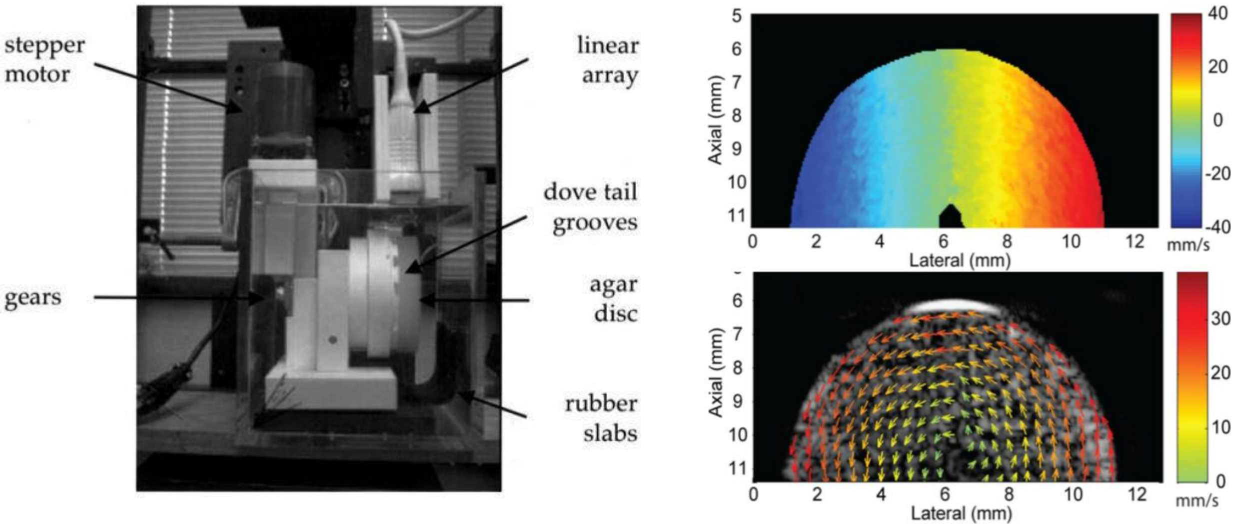

(a) (b)

Figure 1.11: Rotating Cylinder Phantom (a) developed by Walker et al (2009) and VFI results (b) obtained by Ketterling et al (2017) used as examples. Colour encoded map Figure 18b (top) and vector flow mapping imaging Figure 18 (bottom).

Figure 1.10a: Adaptation of Figure 1: Kripfgans, O. D., Rubin, J. M., Hall, A. L. & Fowlkes, J. B. (2006). Vector Doppler Imaging of a Spinning Disc Ultrasound Doppler Phantom. Ultrasound in Medicine and Biology.

Figure 1.10b: Adaptation of Figure 1 and Figure 3: Ketterling, J. A., Aristizabal, O., Yu, A. C. H., Yiu, B. Y. S., Turnbull, D. H., Phoon, C. K. L. & Silverman, R. H. (2017). High-Speed, High-Frequency, Vector-Flow Imaging of in Utero Mouse Embryos, in: IEEE International Ultrasonics Symposium, IUS.

An innovative phantom, designed to challenge VFI Ultrasound Doppler techniques, has been proposed by Yiu et al (2017). The so-called Spiral Flow Phantom (Yiu et al 2017) comprised a 3D printed spiral lumen of polylactic acid embedded within an ultrasound compatible TMM. The spiral lumen is later dissolved, leaving a wall-less phantom structure of TMM. The geometric structure is intended to mimic a tortuous vessel and offers multi-directional flow over all angles (0-360 degrees). It is a great tool for estimating the accuracy of flow estimation algorithms, but it is not commercially available, as it is challenging to manufacture (it is a PVA-based TMM) and chloroform (which is toxic) is used to dissolve the vascular structure. The Spiral Flow Phantom proposed by Yiu et al (2017) and VFI acquisitions results are shown in Figure 1.12. Similar technology has been used by Ho et al (2017) for the construction of a wall-less flow phantom with tortuous vascular geometries.

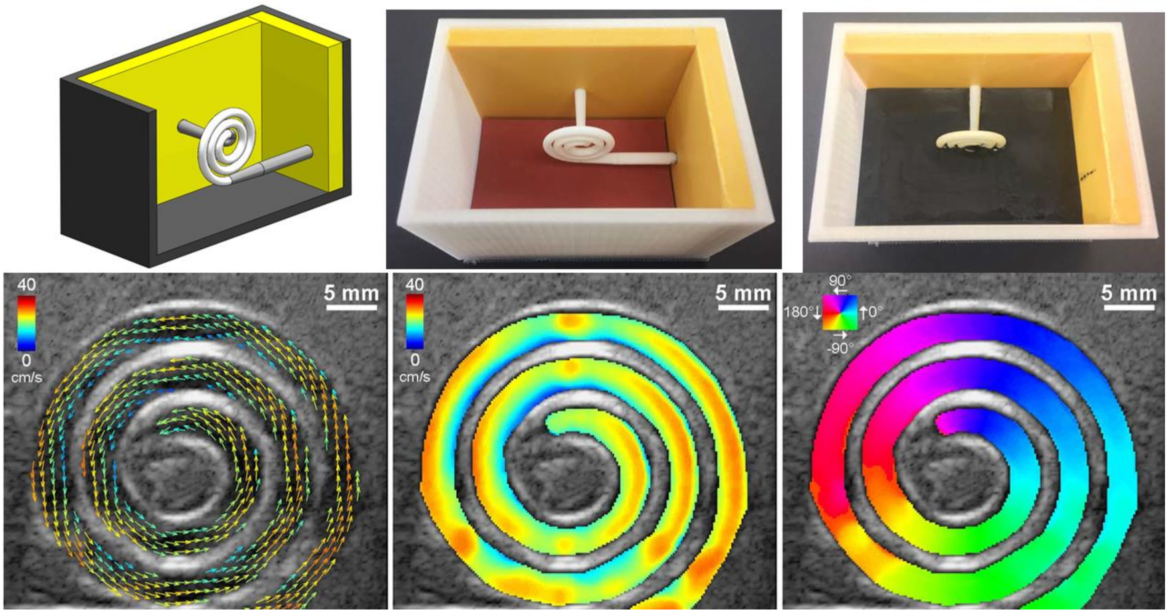

Figure 1.12: Spiral Flow phantom developed by Yiu et al (2017). Top images: Cad drawing (top left), assembled box (top middle), box with TMM poured (top right). Bottom images: vector flow imaging (Bottom left), estimated velocity magnitude map (Bottom middle), estimated velocity angle map (Bottom right).
Figure 19: Modification of Figure 3 and Figure 6: Yiu, B. Y. S. & Yu, A. C. H. (2017). Spiral Flow Phantom for Ultrasound Flow Imaging Experimentation. IEEE Transactions on Ultrasonics, Ferroelectrics, and Frequency Control, 64(12), 1840–1848.

This list of phantoms described in the literature for Doppler ultrasound is unlikely to be exhaustive. Belt phantoms, vibrating phantoms, string phantoms, moving plate phantoms have been also proposed in the literature (Browne et al 2014). Further information about Doppler ultrasound QA tests and flow ultrasound phantoms designs are provided by reviews of Hoskins (2008), Culjat et al (2010), Browne (2014) and Hoskins et al (2017, p. 231-253), therefore, is was not felt necessary to perform a systematic review.

1.6.4 Doppler Ultrasound flow phantoms available on the market

Unfortunately, the ultrasound flow phantom market does not offer many compelling choices.

The Institute of Physics and Engineering in Medicine (IPEM) provided, in 2010, the guidelines for Ultrasound QC through Report 102 - Quality Assurance of Ultrasound Imaging System. Report 102 opens “Chapter 3 – Doppler” stating that “The limited availability and high price of suitable portable, commercial test-objects designed for Doppler testing combined with a poor evidence base for the validity of such testing have made the prescribing of appropriate tests for Doppler difficult” (IPEM Report 102, Institute of Physics and Engineering in Medicine 2010, p. 19). The report was written in 2010, however, the ultrasound flow phantom market has not provided valuable alternatives even in 2018. There are not many flow phantoms available, they are usually expensive (>10000 GBP) and specifications and tolerances are unclear. When Manufacturers are asked to provide evidence about how to reproduce their tests (in order to match their tolerances) materials either lack information or provide values with no evidence of the measurement methods (Dudley and McKenna 2017). Report 102 recommends the use of a simple string test object (string phantom), consisting of a moving filament of O-ring rubber immersed in a fluid with speed of sound of 1540 ms^{-1}. A detailed description of a string phantom and instructions for conducting QC tests is provided by Chapter 3 of the IPEM Report 102 (IPEM Report 102, Institute of Physics and Engineering in Medicine 2010). However, Cournane et al (2014) reported errors exceeding +/- 20 %, +/- 50 % and +/- 40 %, on experimental mean velocity measurements carried out on a string phantom for linear, curvilinear and phased array probes, respectively. These errors are higher than the limit of +/- 10-20 % suggested by the BS EN 61685:2002-IEC 61685:2001 (BS EN 61685:2002, IEC 61685:2001). Doppler flow phantoms consisting of a straight cylindrical conduit embedded into an ultrasound TMM, are also commercially available and offer an alternative to the string phantom (BS EN 61685:2002, IEC 61685:2001). However, flow phantoms are expensive, tolerances are not well specified (Dudley and McKenna 2017), fluid dynamics properties are not described (laminar flow, transient flow, Reynolds number etc), the flow is simplified, and the phantom does not reproduce complex flow features that resemble physiological flows (i.e. complex flow patterns). TMMs often consist of a hydrogel and durability is limited because of desiccation. The acoustic properties are not consistent over time, not well specified, or when measured, deliver results that are different to that declared by Manufacturers (Browne et al 2003). Examples of commercially available string phantoms and flow phantoms are shown in Figure 1.13a and Figure 1.13b, respectively. Further limitations of these two phantom technologies are discussed in Chapter 4, Section 4.5.

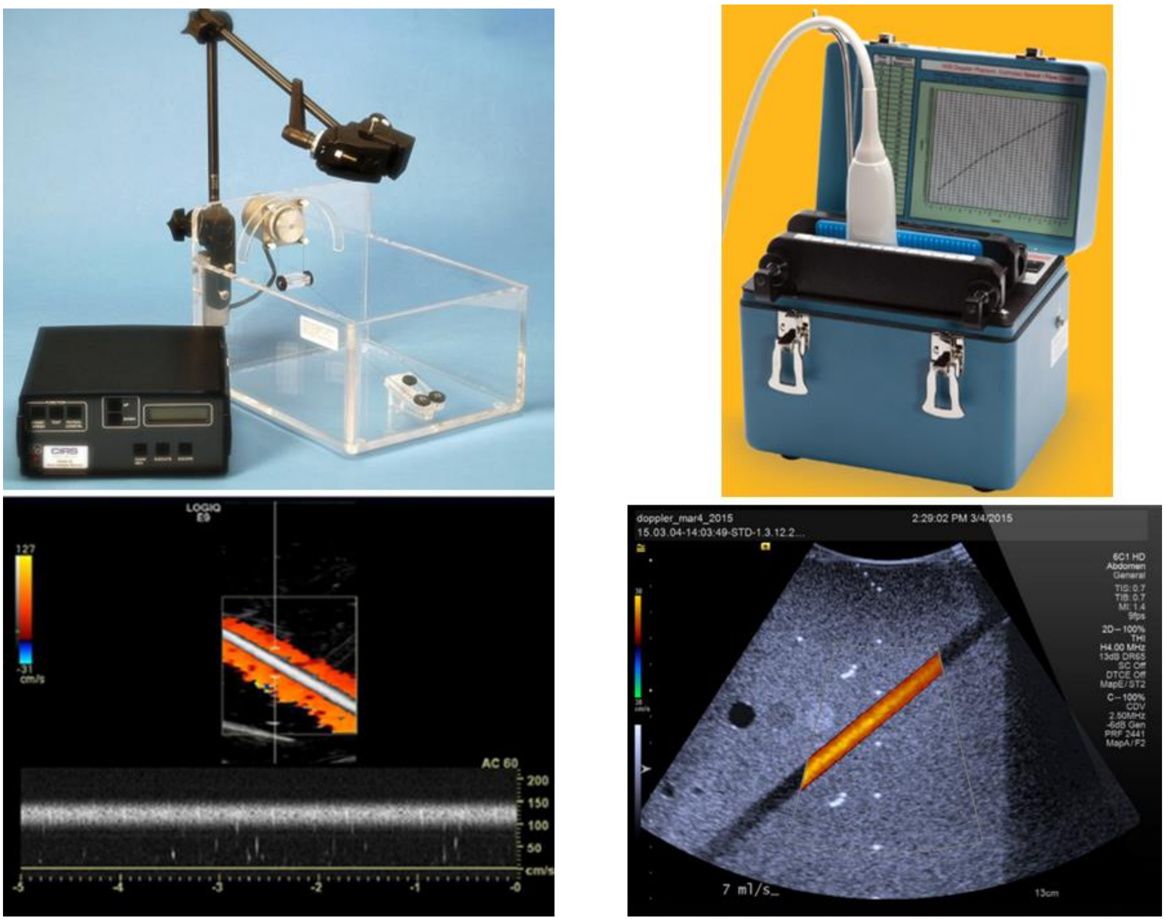

(a) (b)

Figure 1.13: String Phantom (a) manufactured by Cirs (Cirs Inc., Norfolk, VA, USA) and flow phantom (b) manufactured by Sun Nuclear (Sun Nuclear Corporation, Melbourne, FL, USA)
Figure 1.12a: CIRS (2018). *Doppler String Phantom*. Available at: http://www.cirsinc.com/products/all/69/doppler-string-phantom/
Figure 1.12b: Sun Nuclear (2018). *Doppler 403 Mini-Doppler 1430 Flow Phantoms*. Available at: http://www.cirsinc.com/products/all/69/doppler-string-phantom/

1.6.5 MRI flow phantoms

Similar to ultrasound, the construction of MRI flow phantoms is particularly challenging, especially the choice of tissue mimicking materials (TMMs). In MRI, TMMs should mimic tissues of interest in terms of T1 (longitudinal magnetic relaxation time), T2 (transverse relaxation time) and proton density (concentration of protons, usually hydrogen nuclei in tissues). However, if the study focuses, for example, on velocity measurements, the properties of the TMM are not of interest. A number of solid materials (i.e. silicone, polyester and acrylic) can be used. Commonly, these materials are chosen to be transparent, thus they are compatible with optical imaging modalities (i.e. Laser Particle Imaging Velocimetry) and comparative studies can be performed.
The main challenge is related to the potential interaction with the strong and homogeneous magnetic fields (commonly 1.5 T or 3 T) that are typically employed in MRI. Materials that are placed into the Magnetic Resonance environment must not be ferromagnetic and must not interfere with radiofrequency currents. This significantly limits the choice of pumps and motors, commonly used to drive flows in a controllable way. Although there are MRI compatible linear motion systems available on the market (i. e. http://www.simutec.com), the cost is high (over 10000 GBP in 2018). Ultrasonic motor designs have been also proposed in the literature (Tavallaei et al 2016) but are still undergoing validation stage. In addition, all of the mentioned systems are limited in maximum achievable speed and maximum range of motion. Hazards, regulation, material restrictions in Magnetic Resonance Units, and a cost-effective solution to develop an MRI compatible multimodal phantom design, are described in detail in Chapter 8.

1.6.6 Magnetic Resonance Compatible flow phantoms proposed in the literature

The first Magnetic Resonance flow phantom developed for research applications was proposed by Stahlberg et al (1986). The phantom consisted of a water-filled cylindrical acrylic chamber which comprised of two, four or eight tubes with diameters relevant to vessels of interest. A number of flow phantoms were then constructed to mimic vascular geometries in healthy and diseased conditions (Holdsworth et al 1991; Frayne et al 1993; Frayne et al 1995). An anthropomorphic carotid phantom, which incorporated different stenotic geometries, was developed by Smith et al (Smith et al 1999). A portable, silicone-based phantom containing parallel straight and stenosed flow channels in one layer and a U-bend in a second layer, has been proposed by Summers et al (2005). More recently, a phantom design able to produce complex flow patterns has been proposed and validated by Toger et al (2016). The phantom employed vortex rings to validate Four-Dimensional Flow MR velocities (4D-MRI). The system developed by Toger et al (2016) is innovative and was the first phantom to provide complex flow patterns. The phantom design involves a servo motor that powers a ball screw linear actuator, which in turn moves a piston-cylinder apparatus that pushes the flow through a flow rectifier and then into a water tank. However, the motor is not MRI compatible (the motor pump is kept outside the 2 mT safety line of the Magnetic Resonance Room), the apparatus is longer than a meter (excluding the pump) and the water tank has a volume over 20 litres. The system is probably over-engineered, indeed the declared manufacturing cost is 10000 EUR (excluding taxes and labour), and it is in-practical. Key aspects of our phantom design are portability and cost-effectiveness, in order to be market oriented. Ideal requirements for the development of the phantom are summarised in Figure 4.1 (Chapter 4). A detailed and recent review that describes quantitative MRI phantoms is provided by Keanan et al (2018). The review is written by members of the Standards for Quantitative Magnetic Resonance committee and highlights the needs for appropriate phantom designs to refine international standard protocols for quantitative Magnetic Resonance Imaging.

1.6.7 Magnetic Resonance Compatible flow phantoms available on the market

At the time of writing (2018), Gold Standard Phantoms (Gold Standard Phantoms, London, UK) and Shelley Medical Imaging Technologies (Shelley Medical Imaging Technologies, Ontario, Canada) are the only companies on the market that provide programmable flow phantoms for Magnetic Resonance Imaging. Gold Standard Phantoms (Gold Standard Phantoms, London, UK) designed QASPER (https://www.goldstandardphantoms.com), a flow phantom that mimics vessels geometries and flow velocities of the arteries. Shelley Medical Imaging Technologies (Shelley Medical Imaging Technologies, Ontario, Canada) offers a multimodal Perfusion Flow Phantom compatible with CT, MRI and PET, and two semi-anthropomorphic flow phantoms that mimic the left ventricle of the heart. The so-called DCE Perfusion Flow Phantom, the MRI Compatible Multimodality Motion Controller, the Dynamic Multimodality Heart Phantom and the Dynamic Left Ventricle Phantom, developed by Shelley Medical Imaging Technologies (Shelley Medical Imaging Technologies, Ontario, Canada), are shown in Figure 1.14a, Figure 1.14b, Figure 1.15a and Figure 1.15b, respectively. Formal quotes for these phantoms ranged from 30000 to 50000 USD at the time of writing (2018).

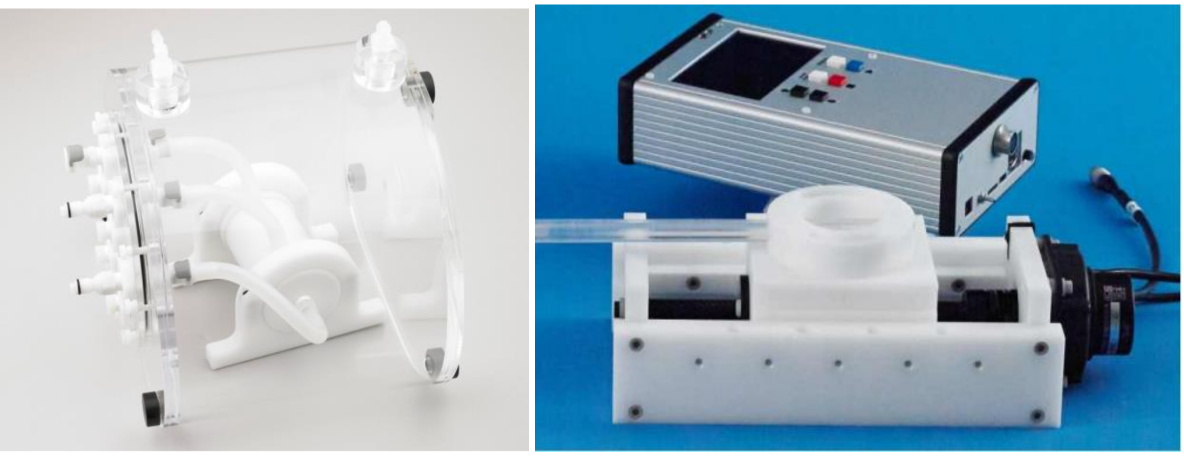

(a) (b)

Figure 1.14: DCE Perfusion Flow Phantom (a) and MRI Compatible Multimodality Motion Controller (b) developed by Shelley Medical Imaging Technologies (Shelley Medical Imaging Technologies, Ontario, Canada)
Figure: Adaptation of images from Shelley Medical Imaging Technologies (Shelley Medical Imaging Technologies, Ontario, Canada) website. Available at http://www.simutec.com/index.html

(a) (b)

Figure 1.15: Dynamic Multimodality Heart Phantom (a) and Dynamic Left Ventricle Phantom (b) developed by Shelley Medical Imaging Technologies (Shelley Medical Imaging Technologies, Ontario, Canada)
Figure: Adaptation of images from Shelley Medical Imaging Technologies (Shelley Medical Imaging Technologies, Ontario, Canada) website. Available at http://www.simutec.com/index.html

1.6.8 Summary

A literature review and a market analysis of flow phantom technologies has been presented both for Ultrasound and Magnetic Resonance flow imaging modalities. It is evident that there are few compelling choices on the market and there is a need for appropriate flow phantom designs to support Quality Control checks, calibration, validation of innovative techniques and to refine (or establish) international standard protocols. Fundamental challenges relate to the choice of materials compatible with the modality of interest. Since the development of a flow phantom design compatible with both advanced Doppler ultrasound and Magnetic Resonance would be challenging, the phantom described in this thesis is developed firstly for Ultrasound Vector Flow Imaging modalities and then adapted for use in a Magnetic Resonance environment.

1.7 Discussion

State of the art medical imaging for quantitative blood flow assessment includes advanced diagnostic techniques such as Ultrasound Vector Doppler Imaging (VFI) and Phase Contrast Magnetic Resonance Imaging (PC MRI). 4D flow Phase Contrast MRI has great potential for estimating complex flow fields typical of healthy and pathological conditions of the cardiovascular system. However, Magnetic Resonance devices are very expensive and the 4D flow MRI technique is not clinically accepted (yet) because of long scanning and post-processing times. The use of Doppler ultrasound techniques over Magnetic Resonance Imaging offers numerous advantages and disadvantages. Doppler ultrasound is non-invasive, cost-effective, portable, universally available and compatible with all types of patient. By the time an MRI scan is performed (usually 1 to 2 hours), up to 5 ultrasound scans can be completed. Moreover, a hospital commonly has a larger number of ultrasound machines than Magnetic Resonance rooms. The use of Doppler ultrasound can significantly reduce waiting lists with comparable diagnostic results to MRI. This allows in quicker diagnosis and improved outcomes. Conventional Doppler ultrasound techniques provide real-time qualitative and quantitative information about intravascular blood flow patterns with high accuracy. However, these techniques are strictly angle dependent. Advanced angle independent Ultrasound Vector Flow Imaging (VFI) techniques have been developed to overcome this limitation. Ultrasound Vector Flow Imaging has attracted great interest in recent years. VFI accuracy and clinical efficacy have been widely demonstrated. Several 2D VFI approaches have been validated and are already implemented on clinical and research ultrasound scanners. In 2013, VFI was FDA approved and recommended as the first choice for the assessment of cardiovascular flows and analysis of blood fluid dynamics. A major problem for medical physics departments involved in medical devices Quality Control is the lack of test objects technologies on the market able to challenge these innovative devices. Calibration of medical imaging devices is recommended as part of the Quality Management System stated by the ISO 9000-2015. Quality Control checks should be performed with periodic acquisition of images on specially designed test objects. Specific imaging quality parameters are quantified and if the values of interest differ from pre-defined threshold values, corrective actions must be undertaken. In order to challenge state of the art technologies, phantom designs must ideally develop alongside the medical imaging device market. The main advantages of using test objects over human (or animal) subjects and biological tissues are related to the reproducibility of results (it is possible to carry out comparative studies over time), high control (high precision in manufacturing) and absence of ethical issues (licencing, health and safety regulations, and ethics). For these reasons, phantoms play a fundamental role and find wide application for calibration, Quality Control, training, research and development of medical imaging devices, testing and validation of novel techniques at the research level. Flow phantoms are commonly used for the investigation of flow field velocities, the cross-validation of flow-field data obtained from independent measurement methods (i.e. medical imaging modalities and optical imaging systems) and for the investigation of a potential relationship between fluid dynamics and biological functions. A flow phantom can be designed as anthropomorphic, semi-anthropomorphic or non-anthropomorphic. It should invoke motion, mimic relevant physiological conditions and produce a known flow field within specified tolerances. From an analysis of the literature and of the market, there are few flow test objects available. Current flow phantom technologies are expensive, inappropriate, they fail to mimic relevant physiological conditions and often lack accuracy specifications. There are no cost-effective flow phantoms technologies able to reproduce complex flow patterns to challenge advanced medical imaging technologies clinically available, such as Ultrasound VFI and PC MRI. Consequently, calibration, testing and validation of medical imaging scanners for quantitative blood flow assessment and definition of standards for Quality Control checks is very challenging. Novel emerging Ultrasound and MRI methods would benefit from a routine standardisation and a calibration tool. A complex flow test object would allow the undertaking of measurements, collection of data, optimisation of scanning parameters for optimising procedures and training to the clinicians. A standard tool is essential to engage with scientific community, compare results across centres and widespread the use of these innovative medical imaging technologies. Appropriate flow phantom designs can create well-defined international standard guidelines (IPEM 2010; Browne 2014; Dudley and McKenna 2017; Keanan et al 2018) and validate new research techniques. This thesis consists to the design, development, testing and validation of a semi-anthropomorphic flow phantom that offers complex flow patterns comparable to relevant physiological conditions. The flow phantom must comply with all of the requirements (stability, controllability, predictability, reproducibility, reliability) recommended for test objects and manufactured from material compatible with multiple imaging technologies for flow measurements. However, the choice of materials compatible with both Ultrasound and Magnetic Resonance technologies is very challenging. The test object aims to deliver a flow benchmark for calibration of clinical scanners and for the validation of advanced velocity estimating algorithms at research level. The key element is the flow itself, rather attempting to mimic surrounding tissues or vessels. Therefore, the first objective is the identification and characterisation of a flow that can satisfy all the desirable requirements. The prototype is designed to operate in free-field (deionised water) and to be compatible with Doppler Ultrasound Vector Flow Imaging modalities, already clinically available since 2013. Optically transparent materials are preferred, in order to allow the undertaking of comparative experiments with optical imaging techniques, such as Laser-PIV and video cameras. After the design characterisation and validation, a cost-effective solution for the adaptation to a Magnetic Resonance environment is proposed in Chapter 8.

1.8 Conclusion

Medical imaging diagnostic modalities for quantitative assessment of the cardiovascular system and basic physical principles are discussed. Although PC MRI is recognised as a gold standard for flow measurements, Doppler Ultrasound Vector Flow Imaging is an attractive alternative because it does not involve ionising radiation, it is cost-effective, portable, fast and provides qualitative and quantitative information in real-time and with results comparable to MRI. Doppler Ultrasound Vector Flow Imaging is available on a number of clinical scanners since 2013, but there is a lack of test objects that can support calibration and Quality Control of these devices or that can offer a flow benchmark for comparative studies and validation of innovative techniques. This thesis aims to provide a complex flow phantom for medical imaging compatible with advanced Doppler ultrasound modalities and optical transparent imaging techniques for comparative studies. After prototype validation and characterisation of the main physical parameters, the design is adapted (Chapter 8) to operate in a Magnetic Resonance environment.

CHAPTER 2

Vortex rings in the cardiovascular system

2.1 Introduction

The desirable requirements for the development of a flow phantom for medical imaging were described in detail in Section 1.5 of the previous chapter (Chapter 1). The major challenges associated with the development of such technology, are the choice of suitable tissue mimicking materials and the identification of a flow with specific characteristics. With the intent to simplify the problem the phantom will be designed to operate in the free-field (deionised water) with the possibility of embedding tissue mimicking materials on demand. Consequently, the first target is the identification of a flow that resembles complex flow patterns relevant to physiological conditions, but also has to be stable, reproducible, predictable and controllable. A literature analysis is conducted within this chapter to identify a flow that fulfils part or all of these requirements.

A simple way to approximate the laws of fluid dynamics in the cardiovascular system would be to interpret flow into vessels as the equivalent of flow into a cylindrical pipe. Assuming a parabolic velocity profile, Poiseuille's law could be applied to find mathematical relations that link the main physical parameters (i.e. velocity, pressure, Reynolds number). Unfortunately, cardiovascular flows are pulsatile and not steady, therefore Poiseuille parabolic flow only becomes adequate as an approximation for time-averaged analysis or regions where the pulsatility is negligible (Kheradvar and Pedrizzetti 2012, p.14-15). In addition, the blood circulatory system exhibits complexities, turbulence, recirculation and vortices. In particular, cardiac blood ejection is characterised by the formation of vortices that lends extra momentum to the flow and directs the blood towards the aorta. Quantitative analysis of these complex flow patterns can provide significant support for the early diagnosis of cardiovascular pathologies (Pedrizzetti et al 2014).

Interestingly, analogies between intra-cardiac vortices and vortex rings have been demonstrated. Such fluid dynamics phenomena have been widely studied in vitro. After complete formation, vortex ring fluid dynamics are predictable. Analytical and mathematical models, which describe relationships between the main physical parameters, are available in the literature (Hill 1894; Lamb 1932; Kaplanski-Rudi 1999). It has been demonstrated that simple vortex ring physical parameters, such as the formation time, can be used as a quantitative index of cardiac health. Indeed, the literature indicates that vortex rings can be created in the laboratory, in a controlled environment, with encouraging reproducibility.

Important aspects of vortex formation within the left ventricle of the heart, analogies with vortex ring, analytical models and physiologically relevant parameters are described in this chapter. This includes experimental studies presented in the literature and basic fluid dynamics concepts.

2.2 Intracardiac Flow – Vortex Ring

In the proximity of valves, heart chambers and vessel bifurcations, the fluid dynamics of the cardiovascular system exhibit complex flow velocity fields (turbulence, recirculation, jets, vortices) both in healthy and pathophysiological conditions (Pedrizzetti et al 2014; Arvidsson et al 2016). Particularly, the blood circulation within the heart chambers is balanced by the formation of vortices. During diastole, the blood flows into the left ventricle through the mitral valve and generates a shear layer that "rolls up" into a vortex. This vortex is asymmetric, due to the unbalanced shape of the mitral valve (the anterior leaflet is larger than the posterior leaflet) (Kheradvar and Pedrizzetti 2012, p.47). The vortex forms from the boundary layers at the distal tip of the mitral valve leaflets, it then propagates rapidly into the ambient fluid of the left ventricle and becomes a stable structure. The process of vortex formation is shown in Figure 2.1. A numerical simulation and mathematical model of the left ventricle vortex formation and propagation is described in detail by Domenichini et al (2005).

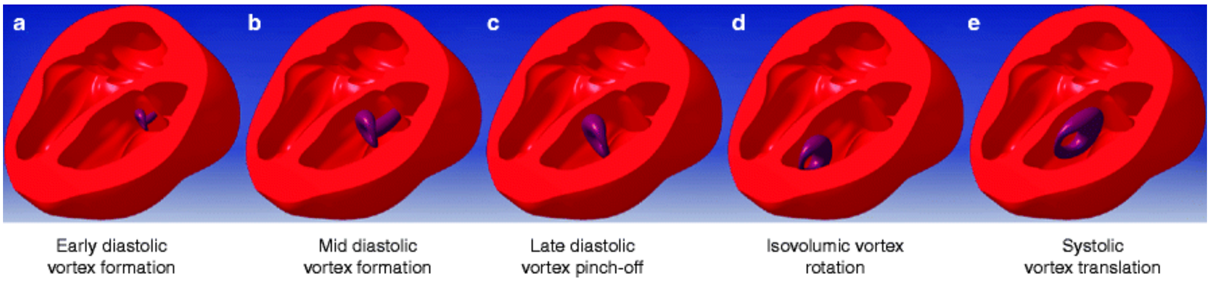

Figure 2.1: Vortex formation process in the left ventricle chamber
Figure 3.2: Kheradvar, A. and Pedrizzetti, G. (2012). Vortex Formation in the Cardiovascular System. London: *Springer-Verlag*.

At the end of diastole, the vortex provides extra momentum to the circulation of blood. The incoming fluid from the left atrium is decelerated, while the outflow towards the aorta is accelerated (Pedrizzetti et al 2014). This physical phenomenon balances the dynamic between the motion of the myocardial tissue and the circulation of the blood flow. It is a natural process that happens in healthy left ventricles and facilitates cardiac blood ejection. By way of example, two echocardiographic images of vortex formation in healthy subjects in late diastole and at the end of the diastole are shown in Figure 2.2a and Figure 2.2b, respectively. In the late diastolic phase (Figure 2.2a), the asymmetry of the vortex is visible.

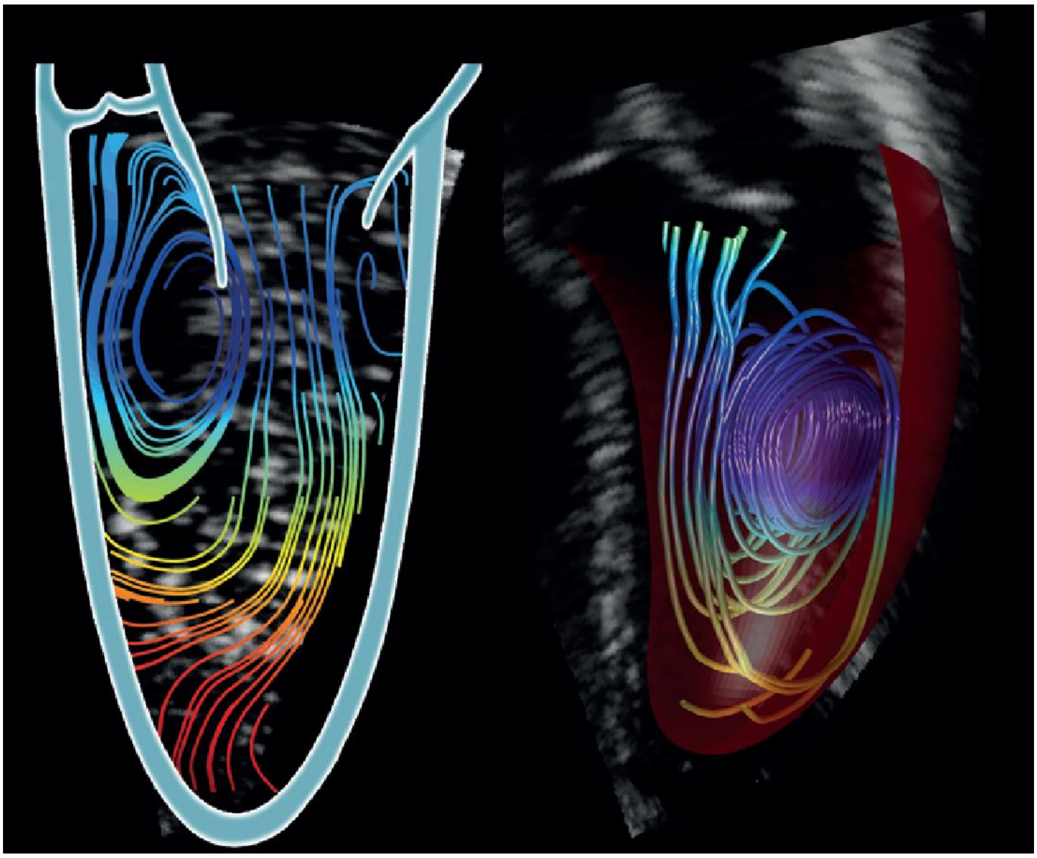

a) Late diastole b) End of diastole

Figure 2.2: Ultrasound echo-PIV imaging of vortex formation in healthy subjects in late diastole (a) and end of diastole (b) (onset systole). Streamlines, reconstructed from multiplane acquisitions, depict the flow spiralling out from the vortex and moving towards the aorta.
Figure 3: Pedrizzetti, G *et al* (2014). The vortex-an early predictor of cardiovascular outcome? *Nature Reviews Cardiology*, 11, 545-553.

The flow inside the right ventricle is expected to form a complex pattern, which involves vortex formation in a similar way. Unfortunately, the right ventricular function is difficult to evaluate due to its asymmetrical lunar shape and the difficulties of applying 2D echocardiography techniques. The flow inside the right ventricle is still unclear, due to the lack of technologies to map 3D spatial and temporal details of the fluid dynamics in that region of interest (Kheradvar and Pedrizzetti 2012, p.56). Although the correct functioning of all the four heart chambers is crucial, the dynamics of the left ventricle regulates the cardiac output. Malfunctions of this section of the heart affect the overall health of the cardiovascular system.

Quantitative analysis of vortex dynamics can be crucial for early diagnosis and has attracted the attention of several scientists during the last decades. In early 1995, Kim et al (1995) provided the first quantitative description of vortex motion inside the left ventricle using a 1.5-Tesla 15S Gyroscan HP Philips (Philips, Eindhoven, Netherlands). In 2006, Gharib et al (2006) noted similarities between vortices observed in vivo (within the left ventricle chamber) and a rotating fluid mass, the vortex ring, which had been broadly studied and fully characterised in vitro (Akhmetov and Kirasov 1969; Maxworthy 1977; Didden 1979; Gharib et al 1998; Akhmetov 2001; Dabiri and Gharib 2004; Krueger et al 2004; Akhmetov 2009). Using quantitative parameters and analytical equations already described for the vortex ring in vitro, Gharib et al (2006) demonstrated that major aspects of cardiac function are accompanied by vortex formation in blood flow during diastole. Gharib et al (2006) correlated physical parameters of vortex formation, obtained experimentally in-vitro, with existing quantitative indexes of cardiac health (i.e. the left ventricle ejection fraction).

Gharib's observations (Garib et al 2006) precipitated several studies. There is extensive evidence in the literature that the vortex ring formation (described in detail in following Section 2.4) can be related to:

- left ventricular filling and mitral valve efficiency (Pierrakos and Vlachos 2006);
- dimensions of the mitral valve annulus (Kheradvar et al 2007);
- ventricular pressure drop (Kheradvar and Gharib 2007);
- diastolic dysfunction (Kheradvar and Gharib 2009; Kheradvar 2011) and
- mitral valve leaflet length (Kheradvar 2010).

Correlating vortex ring formation with the dimensions of the mitral valve annulus, Kheradvar et al (2007) observed that the smaller annulus (corresponding to stenotic valves) and larger annulus (corresponding to dilated cardiomyopathy) were related to different vortex ring formation. In 2012, Segupta et al (2012) confirmed that relevant clinical information can be obtained if complex flow patterns are analysed and the full velocity vector field is available. Kheradvar and Pedrizzetti (2012) authored a book that describes the fluid dynamics aspects of vortex formation within the heart chambers. Dynamics of vortex evolution in viscous fluids, relations between vortex ring physical parameters and heart dysfunction, diagnostic techniques for vortex imaging analysis are also described (Kheradvar and Pedrizzetti 2012). More recently Pedrizzetti et al (2014) concluded that the vortex ring is a sensitive precursor of left ventricle malfunction and can support therapeutic strategies. Finally, Ardvisson et al (2016) demonstrated that the vortex ring provides an epigenetic blueprint for the human heart. Vortex ring formation and fluid dynamics analysis both provide unique physiological and mechanical information about cardiac function and have potential clinical utility as measures of cardiac health (Arvidsson et al 2016).

2.3 Vortex Ring: definition and analytical description

As deduced from the literature mentioned at the end of the previous section (Section 2.2), quantitative description of intra-cardiac vortices is valuable for assessment of the cardiovascular system. Vortex fluid dynamics provide relevant information on physiological and anatomical events, which are directly related to cardiac performance. A pivotal moment was when Gharib et al (2006) approximated the intraventricular vortex flow to a vortex ring based on fluid dynamics that were extensively studied in vitro (Akhmetov and Kisarov 1969; Maxworthy 1977; Didden 1979; Gharib et al 1998; Akhmetov 2001; Dabiri and Gharib 2004; Krueger et al 2004; Akhmetov 2009). Through Gharib's approximations (2006), existing mathematical models for vortex rings were applied to intraventricular blood flow and quantitative indexes of cardiac health defined. A vortex ring can be defined as a "toroidal volume of vortical fluid moving in a surrounding medium at an approximately constant translational speed perpendicular to the ring plane. The fluid motion is axisymmetric, and the vector of vorticity in the torus is directed along the circles concentric with the circular axis of the torus. A certain volume of the fluid which embraces the ring and looks like an ellipsoid flattened along the direction of motion is moving together with the toroidal vortex ring. This enclosed volume of fluid is called vortex atmosphere. Inside the vortex atmosphere, the fluid is circulating along the closed streamlines encompassing the toroidal core of the vortex. The motion of the fluid surrounding the vortex atmosphere resembles a pattern of flow without separation past a corresponding solid body" (Akhmetov 2009, p.5). Analytical solution of Navier-Stokes equations for describing the vortex ring behaviour have been attempted under simplified incompressibility assumptions with highly idealised and axisymmetric conditions (Tryggeson 2007). However, the preferred description is in terms of

stream function Ψ. Three particular idealisations, consistent with the Navier-Stokes equations, have been provided by Hill (1894), Lamb (1932), and Kaplanski-Rudi (1999) (Figure 2.3).
In 1894, Hill (1894) described the vortex ring as a sphere of radius *a* with uniform distribution of vorticity. Almost 40 years later, Lamb (1932) described vortex ring dynamics as a "thin ring" with constant vorticity inside the vortex core (where *a* is the core radius and *R* the ring radius, limit as a/*R*-> 0). Finally, Norbury (1973), Fraenkel (1972) and Kaplanski-Rudi (1999) assumed a Gaussian (linear) distribution of vorticity within a larger core radius to ring radius ratio (if *a* is the core radius and *R* the ring radius, Limit as *a/R*-> 2). Idealised models and stream functions Ψ are shown in Figure 2.3. The schematic stream function Ψ depicts the vortex ring rotating cores (of radius *a*), the vortex atmosphere (of radius *R*) and the streamlines.

Model (class)	**Spherical** (Hill, 1894)	**Thin** (Lamb, 1932)	**Thick** (Kaplanski-Rudi, 1999)	**Used Symbols**
Schematic Stream Function ψ	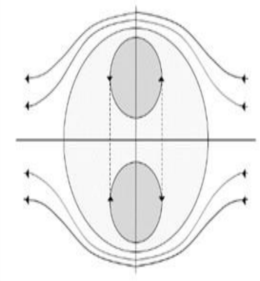	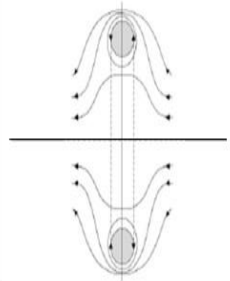	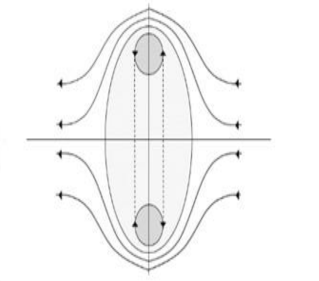	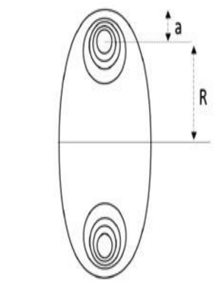
Circulation Γ	$\Gamma = 5aV$	Constant Γ	$\Gamma = \frac{I}{\pi R^2}[1-\exp\left(-\frac{\tau^2}{2}\right)]$	
Impulse I	$I = 2\rho\pi a^3 V$	$I = \rho\Gamma\pi R^2$	Const I	ρ = density of the fluid a = core radius R = ring radius τ = R/1, where 1 is the diffusivity of the ring's core I1 = first-order Bessel function 2F2 = generalized hypergeometric function
Energy E	$E = \left(\frac{10}{7}\right)\rho\pi a^3 V^2$	$E = \frac{1}{2}\rho\Gamma^2 R[\ln\frac{8R}{a} - \frac{7}{4}]$	$E = \frac{I^2}{2\pi^2}\frac{\tau}{R^3}[\frac{1}{12}\sqrt{\pi}\tau^2\,{}_2F_2\left(\left\{\frac{3}{2},\frac{3}{2}\right\},\left\{\frac{5}{2},3\right\},-\tau^2\right)]$	
Velocity	Constant V	$V = \frac{\Gamma}{4\pi R}(\ln\frac{8R}{a} - \frac{1}{4})$	$V = \frac{I}{4\pi^2}\frac{\tau}{R^3}\{3\sqrt{\pi}\exp\left(-\frac{\tau^2}{2}\right)I_1\left(\frac{\tau^2}{2}\right) + \frac{1}{12}\sqrt{\pi}\tau^2\,{}_2F_2\left(\left\{\frac{3}{2},\frac{3}{2}\right\},\left\{\frac{5}{2},3\right\},-\tau^2\right) - \frac{3}{5}\sqrt{\pi}\tau^2\,{}_2F_2\left(\left\{\frac{3}{2},\frac{5}{2}\right\},\left\{2,\frac{7}{2}\right\},-\tau^2\right)\}$	

Figure 2.3: Axisymmetric approximations and description of ring vortex through Navier-Stokes equations.
Symbols used: Stream function Ψ, circulation Γ, density of the fluid ρ, core radius a (dark grey), ring radius *R* (light grey), $\tau = R/1$ where 1 is the diffusivity of the ring's core, first-order Bessel function I_1, generalized hypergeometric function ${}_2F_2$.
Table 1: Adapted from Ferrari, S. *et al* (2017). The Ring Vortex: Concepts for a Novel Complex Flow Phantom for Medical Imaging. *Open Journal of Medical Imaging*, 7, 28-41.

2.4 Vortex Ring: Formation Time

Analytical descriptions (Figure 2.3) of vortex ring dynamics provide mathematical relationships between the main physical parameters. However, it is not straightforward to determine whether the produced vortex reflects the spherical approximation (Hill 1894), the thin approximation (Lamb 1932) or something in between (Norbury 1973; Fraenkel 1972; Kaplanski-Rudi 1999).

A great contribution to *in vitro* experimental work has been provided by Garib et al (1998). Gharib et al (1998) performed experiments with a water tank and a constant-head tank, computer-controlled by a flow monitoring valve. The flow from the constant-head tank moved a piston that pushed a column of fluid out of a cylindrical nozzle. A vortex ring formed at the nozzle output-end and propagated across the connected water-filled tank. The computer-controlled valve controlled the flow from the constant-head tank and thus the velocity profile. A flow meter was used to monitor the ejected volume. A schematic representation of the vortex ring generator proposed by Gharib et al (1998) is shown in Figure 2.4.

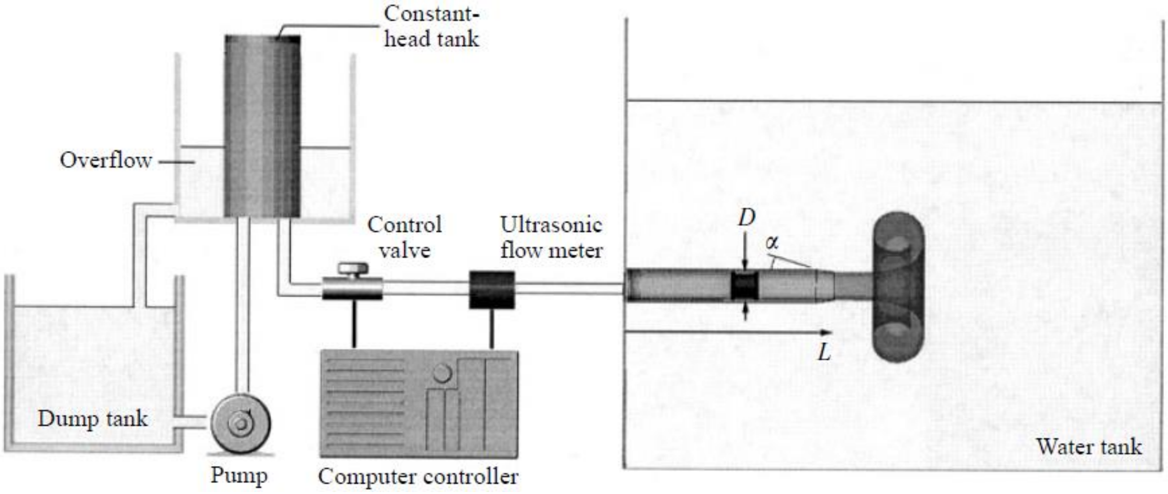

Figure 2.4: Vortex ring generator proposed by Gharib *et al* (1998).
Figure 1: Gharib, M. *et al* (1998). A universal time scale for vortex ring formation. *J Fluid Mech*, 360, 121-140.

Fluorescent particles were introduced into the system and Digital Particle Image Velocimetry was performed to analyse the flow. A range of vortex rings were generated by varying the volume ejected (*L*), the nozzle diameter *D*, and different non-impulsive velocity profiles *Up (t)*.

Gharib et al (1998) experimentally observed that (Figure 2.5):

- the flow fields produced by small values of *L/D* ratios showed a single vortex ring;
- the flow field produced by large *L/D* ratios showed a leading vortex ring followed by a trailing jet;
- the transition between these two phenomena occurred when the *L/D* ratio lay in between 3.6 and 4.5.

The non-dimensional value which corresponded to the transition between the two phenomena (*L/D* ~ 4) was named "formation number" or "formation time" (Gharib et al 1998). The "formation time" is equivalent to the ratio of length to the diameter of the ejected column of fluid (the stroke ratio), *L/D = Upt/D*, where *Up* is the average ejection (i.e. the piston, the column of fluid) velocity. The maximum circulation that the vortex ring can reach during its formation is reached at the “formation time (Gharib et al 1998).

Critical *L/D* ratio values for vortex ring formation observed in experimental and numerical studies are summarised in Table 2.1.

Digital Particle Image Velocimetry images of vortex rings generated for *L/D* = 2, *L/D* = 3.8 and *L/D* = 14.5 are shown in Figure 2.5 (Gharib et al 1998).

Formation Number	Vortex ring formation	Technical Notes
$L/D < 0.05$	No vortex ring formation	L / D too small, the vortex may move back into the generator
$0.05 < L/D < 0.1$	Vortical fluid rolls up into a spiral, entraining irrotational fluid, but no appreciable translational motion Is noticed	The maximum vortex ring diameter (2R, Figure 2.3) reached at the end of the stroke is not sufficient to form a stable vortex ring with appreciable translational motion (Didden et al 1979)
$0.1 < L/D < 1.5$	Formation of diffusive vortex rings with thick core	Low Reynolds number, diffusive vorticity distribution, tending to the Hill’s fat-limit case (Shariff & Krueger, 2018)
$1.5 < L/D < 3.6$ (i.e. $L/D = 2$, Figure 2.5)	Single stable vortex ring is generated and travels with self-induced velocity	No noticeable vorticity is observed in the trail jet behind it (Gharib et al 1998)
$3.6 < L/D < 4.5$ (i.e. $L/D = 3.8$, Figure 2.5)	There is a clear separation between the formed vortex ring and the trailing jet region behind it	all the discharged fluid is entrained into the vortex ring (Gharib et al 1998)
$L/D > 4.5$ (i.e. $L/D = 14.5$, Figure 2.5)	Vortex ring has the same size and leaves a trailing jet behind	Vortex ring is not able to absorb more of the fluid’s mass or vorticity, it does not grow in size (same diameter, 2R, Figure 2.3) and leaves a trailing jet behind it (Gharib et al 1998)

Table 2.1: Critical *L/D* ratio values for vortex ring formation observed in experimental and numerical studies

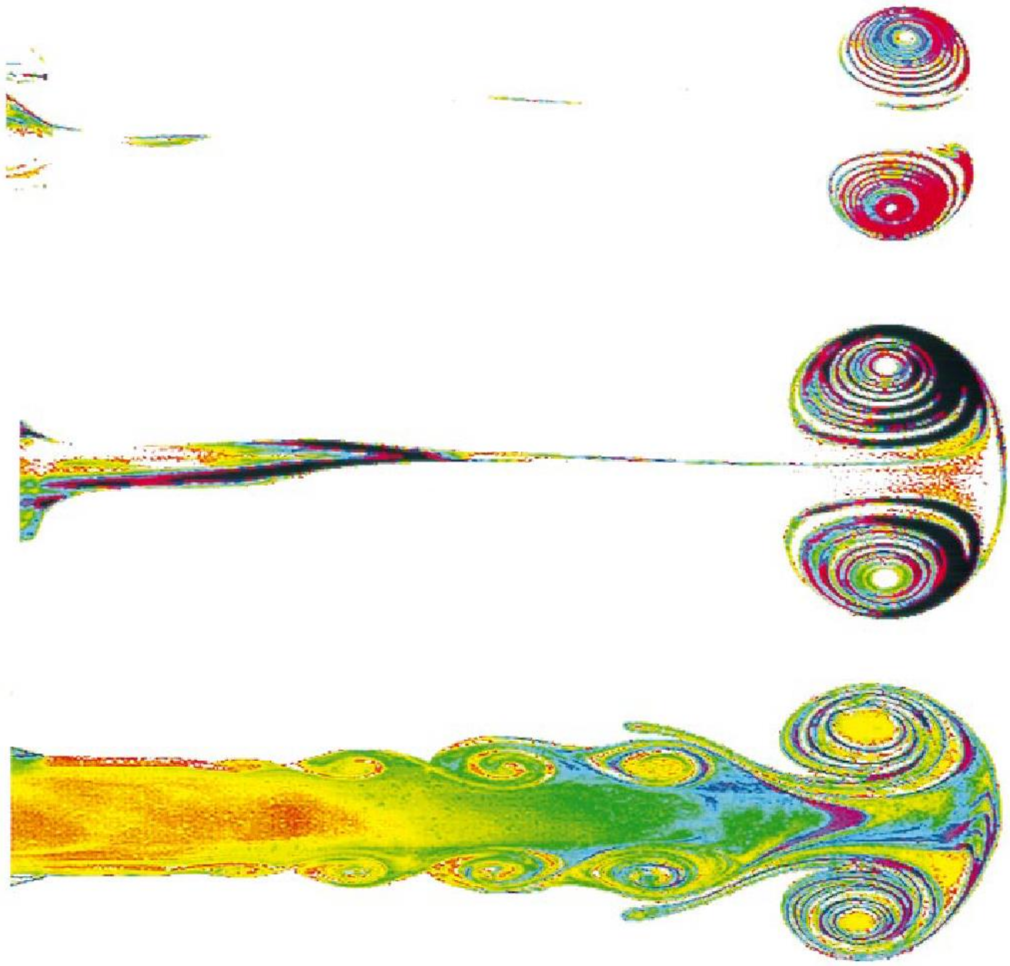

Figure 2.5: Vortex rings generated for L/D = 2 (Top), L/D = 3.8 (Middle), L/D = 14.5 (Bottom). Digital particle velocimetry imaging.
Figure 3: Gharib, M. *et al* (1998). A universal time scale for vortex ring formation. *J Fluid Mech*, 360, 121-140.

2.5 Formation Time as a quantitative index of cardiac health

As described in Section 2.2, the vortex ring is a fundamental phenomenon that transfers extra momentum from the left atrium to the left ventricle and regulates the efficiency of the cardiac output. Gharib et al (2006) demonstrated that the vortex ring formation number can be used as a measure of cardiac health.

Defining D, as the average mitral valve diameter (equivalent to the nozzle diameter in Gharib et al 1998), and $\bar{U}$, as the average velocity of the transmitral starting jet (Figure 2.1), the vortex formation time (VFT) through the mitral valve can be calculated as (2.1) (Gharib et al 2006):

$$VFT = \left(\frac{\bar{U}}{D}\right) t \qquad (2.1)$$

Gharib et al (2006) suggested carrying out vortex formation time (VFT) measurements in healthy patients and to use statistical analysis to establish a range of values as a baseline. Stenotic mitral valves, malfunction or change of a mitral leaflet's length, mitral annulus motion, deformation of the left ventricular wall, muscle contraction, and diastolic dysfunction are a few examples of pathological conditions that significantly affect the transmitral vortex formation time (Kheradvar and Pedrizzetti 2012). Having a baseline of healthy subjects, it would be possible to quantify the presence of a number of heart malfunctions or pathologies, based on the efficiency of the vortex formation time (Gharib et al 2006).

Vortex formation time (formation number) can also be related to existing equations of transmitral flow and ejection fraction (EF) as follows (2.2) (Gharib et al 2006):

$$VFT = \frac{4\,(1-\beta)}{\pi}\,\alpha^3 \times EF \qquad (2.2)$$

$$\text{where} \quad \beta = \frac{V_a}{EDV} = \frac{VTI_a \times \frac{\pi}{4} D_E^2}{EDV}; \quad \alpha = \sqrt[3]{\left(\frac{EDV}{D_E^3}\right)}; \quad D_E = \sqrt[2]{\frac{GOA}{\pi}}$$

where:

- VFT = transmitral vortex formation time;
- EF = left ventricle ejection fraction;
- β = fraction of stroke volume contributed from the atrial component to the left ventricle filling;
- V_a = blood volume into the left ventricle during the atrial contraction;
- EDV = left ventricular volume at the end of the diastole;
- VTI_a = velocity time integral of the atrial contraction (A-wave);
- DE = diameter of the mitral geometric orifice area (GOA);
- α^3 = non-dimensional volumetric parameter for the left ventricle.

Such analyses indicates that vortex formation is significantly affected by the presence of artificial valves and vortex formation time can be used to determine the positioning and design of mechanical and bioprosthetic heart valves or to monitor patients after surgical procedures (Kheradvar and Pedrizzetti 2012).

However, further studies need to be undertaken to provide a better understanding of these phenomena. This will ascertain if there is further evidence of clinical efficacy, sufficient to promote the method.

2.6 Vortex Ring: fluid dynamics in viscous fluids (in vitro experiments)

Section 2.4 has already shown that theoretical approximations of vortex ring generation phase and evolution (described in Section 2.3) do not adequately explain vortex dynamics for a broad range of initial conditions (Dabiri and Gharib 2004; Tinaikar et al 2018). Further experimental data is needed to obtain information about vortex formation, evolution, interaction and decay (Tinaikar et al 2018).

In the spirit of classification this section provides basic information on vortex ring evolution, Reynolds number dependence and velocity distribution profiles.

2.6.1 Vortex ring evolution

A vortex ring naturally forms when a bulk of fluid is forced through a smaller orifice into another expansive fluid environment. Under specific initial conditions, the fluid rolls up at the edge of the orifice (or nozzle) and propagates into the adjacent fluid environment. Within an initial period, the structure is unstable with continuous momentum addition and viscous effects strictly dependent on the main generating parameters (stroke length, nozzle diameter, Reynolds number and piston velocity profile). Subsequently, it stabilises and propagates with a self-induced velocity, exhibiting a smooth vorticity distribution and predictable dynamics. For a configuration consisting of a piston and a nozzle (Figure 2.4), the vortex becomes stable (for defined Reynolds numbers) after propagating over a distance 2-3 times greater than the nozzle diameter (Tinaikar et al 2018). Because of diffusion effects (finite viscosity) in real fluids, the propagating vortex ring exhibits time-dependent vorticity fields. For a fully developed vortex ring (beyond the initial unstable period), the vortex core (Figure 2.3) may be approximated as a rigid disc and the vorticity distribution can be approximated as a Gaussian profile (Saffman 1970; Maxworthy 1977; Saffman 1978; Weigandand and Gharib 1997; Akhmetov 2001; Tinaikar et al 2018). Typically, the core vorticity reduces due to viscous dissipation and the core radius (Figure 2.3) increases as the vortex propagates. The vortex entrains more fluid and the ring velocity decreases as a consequence of sharing the same momentum with more bulk mass of fluid (Reynolds 1876; Tinaikar et al 2018). Streamlines and vorticity flow fields captured with Digital Particle Image Velocimetry, Laser Induced Fluorescence and Particle Imaging Velocimetry in two relevant research studies are shown in Figure 2.6a, Figure 2.6b and Figure 2.6c, respectively.

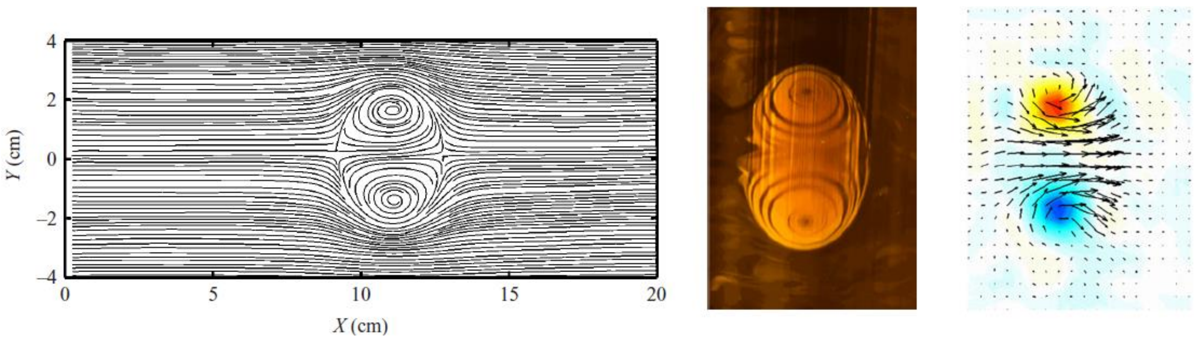

(a) (b) (c)

Figure 2.6: Streamlines and vorticity of propagating vortex ring with Digital Particle Image Velocimetry (a), Laser Induced Fluorescence (b) and Particle Image Velocimetry (c). Direction of propagation is from left to right.

Figure 2.6a. Modification of Figure 3: Dabiri, J.O. and Gharib, M. (2004). Fluid entrainment by isolated vortex rings. *J Fluid Mech,* 511, 311-331.

Figure 2.6b and 2.6c. Modification of Figure 5: Tinaikar, A. *et al* (2018). Understanding evolution of vortex rings in viscous fluids. *J Fluid Mech*, 836, 873-909.

2.6.2 Vortex ring evolution – Reynolds Number dependency

Vortex ring evolution depends on the generating condition which is strongly influenced by the Reynolds number (*Re*). The Reynolds number captures the ratio between inertial and viscous forces and defines the stability of the fluid motion. In a straight pipe, flow motion with low Reynolds numbers (*Re* < 2300) is defined as laminar and it is orderly, smooth, highly viscous and with high-pressure loss. As the Reynolds number increases (*Re* >2300) the flow exhibits more chaotic dissipation of kinetic energy and it is less smooth. Instabilities start to occur as *Re* further increases and the flow becomes fully turbulent for *Re* > 10000.

In vortex ring experimental studies, *Re* has been commonly estimated as the ratio of the core circulation to the kinematic viscosity (Weigand and Gharib 1997) or with regards to the generating condition (input flow velocity profile and orifice/nozzle diameter) (Rosenfeld et al 1998; Akhmetov et al 2001). For laminar vortex rings, the vorticity of the rotating core is smooth, the core size is narrow, and the ring keeps a circular shape as it travels. In turbulent vortex rings, the core rotates violently, intensely and can develop into unstable shapes. By way of example, vortex rings with laminar and unstable cores are shown in Figure 2.7(a) and Figure 2.7(b), respectively (Yan et al 2018).

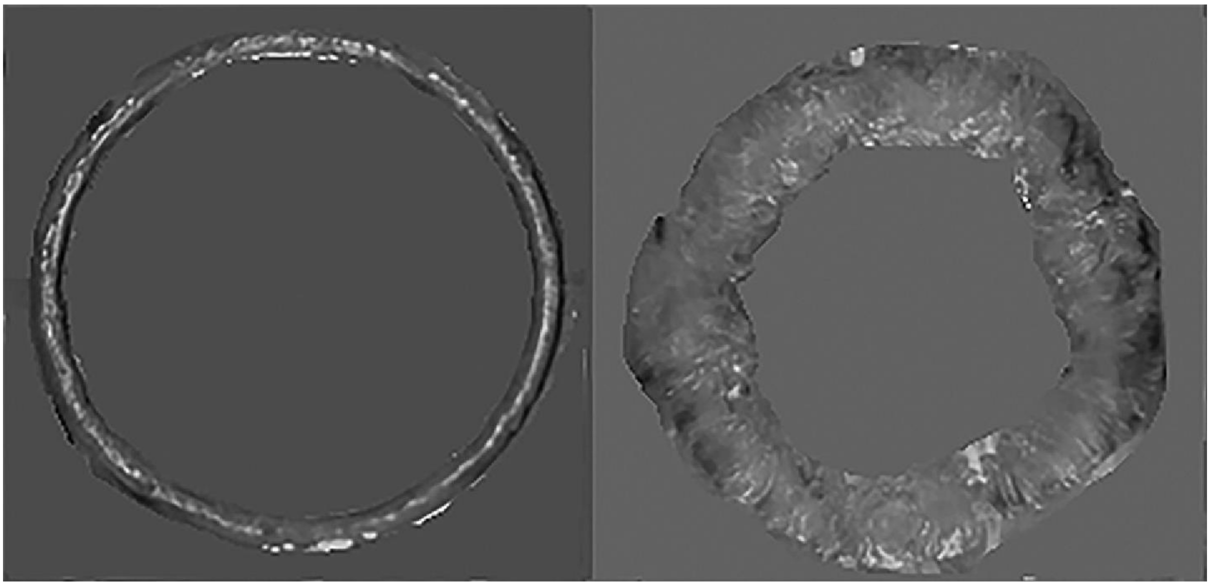

(a) (b)

Figure 2.7: Vortex ring core for laminar (a) and turbulent (b) conditions
Figure 5a: Yan, X. *et al* (2018). Laminar to Turbulent Buoyant Vortex Ring Regime in Terms of Reynolds Number, Bond Number, and Weber Number.

Different Reynolds numbers provide different evolutionary dynamics. A complete review, which includes mathematical models describing how the Reynolds number affects the vortex ring evolution in viscous fluids, is provided by Kaplanski et al (2012). Reynolds numbers in human blood vessels are normally below 1000 (in healthy subjects). In the ascending aorta and sometimes in the left ventricle it can reach the critical threshold (~2300) for short intervals. However, turbulence is weak and does not affect dynamics and vortex ring formation. Reynolds number might be transitional only in mid-diastole in the left ventricle and in mid-systole in the aorta, reaching a maximum value of ~7000 as the peak for short periods (Kheradvar and Pedrizzetti 2012, p. 14 and p. 43).
Experimental work on the evolution of laminar vortex rings with Reynolds numbers (defined by the ratio of the core circulation to the kinematic viscosity) in the range 830 < *Re* < 1650 has been conducted by Weigand and Gharib (1997). One year later, Rosenfeld et al (1998) determined the dependency the vortex ring circulation from formation time and Re (based on the maximal piston velocity and the orifice diameter) ranging from 1250 to 5000. Analogous experiments were conducted by Akhmetov (2001). With a fixed *L/D* value of ~ 5, Akhmetov (2001) observed that laminar vortex rings with a layered spiral structure, which doesn't change during the motion, can be generated for *Re* < 1-20000. Further experimental studies (with Reynolds number of 1400, calculated on the piston speed and cylinder exit diameter, and Reynolds numbers varying between 2000 < *Re* < 4000,

calculated on the ring circulation) have been conducted by Dabiri and Gharib (2004). A numerical simulation for vortex rings with Reynolds numbers ranging from 3000 to 10000 is provided by Archer et al (2008).

Finally, a more recent research study that includes a comparison with all the previously proposed models is provided by Tinaikar et al (2018). Tinaikar et al (2018) performed experiments with Reynolds numbers (in circulation) ranging from 100 to 1500. Results of peak vorticity, circulation, ring core size, the standard deviation of the Gaussian distribution and formation number results as a function of time are provided (Tinaikar et al 2018). Except for the standard deviation of the Gaussian distribution, all the variables in these experiments showed high repeatability with an error lower than +/- 10 %. Results provided by Maxworthy (1972), Weigand and Gharib (1997), Rosenfeld et al (1998), Dabiri and Gharib (2004), Archer et al (2008) and Tinaikar et al (2018) show good agreement in terms of dependence of vortex ring evolution from the Reynolds numbers (both with Reynolds number defined as the ratio of the core circulation to the kinematic viscosity and Reynolds number based on the maximal piston velocity and the orifice diameter).

2.6.3 Vortex ring core – Gaussian distribution profile

By arbitrarily assuming that the vortex ring size is $a = k1\sigma$, where $k1$ is a specific vortex core parameter described by Tinaikar et al (2018), σ is the standard deviation of a Gaussian distribution and that ω_{avg} is the average vorticity (considering the ring core as a rigid disc with linear ω variation), the vorticity distribution profile of the ring core can be suitably approximated by the Gaussian profiles shown in Figure 2.8(a) and 2.8(b). As the Reynolds number (test conducted for $100 < Re < 10000$) decreases, viscous effects become dominant, the core size increases, the distribution of vorticity is less concentrated, the standard deviation of the Gaussian profile is larger and increases with time and there is more diffusivity. As the Reynolds number decreases and approaches 100, the vorticity distribution can be aptly described by the Hill's spherical model (1894) (Tinaikar et al 2018; Akhmetov 2001). Increasing the Reynolds number (with respect to the laminar flow limit and to the values tested into the mentioned experiments), the core size becomes smaller and the circulation is more concentrated with higher velocity gradients. For higher Reynolds numbers, internal viscous interaction (dissipation) is negligible compared to the external dissipative effects, therefore the circulation of the core can be approximated as a solid disc.

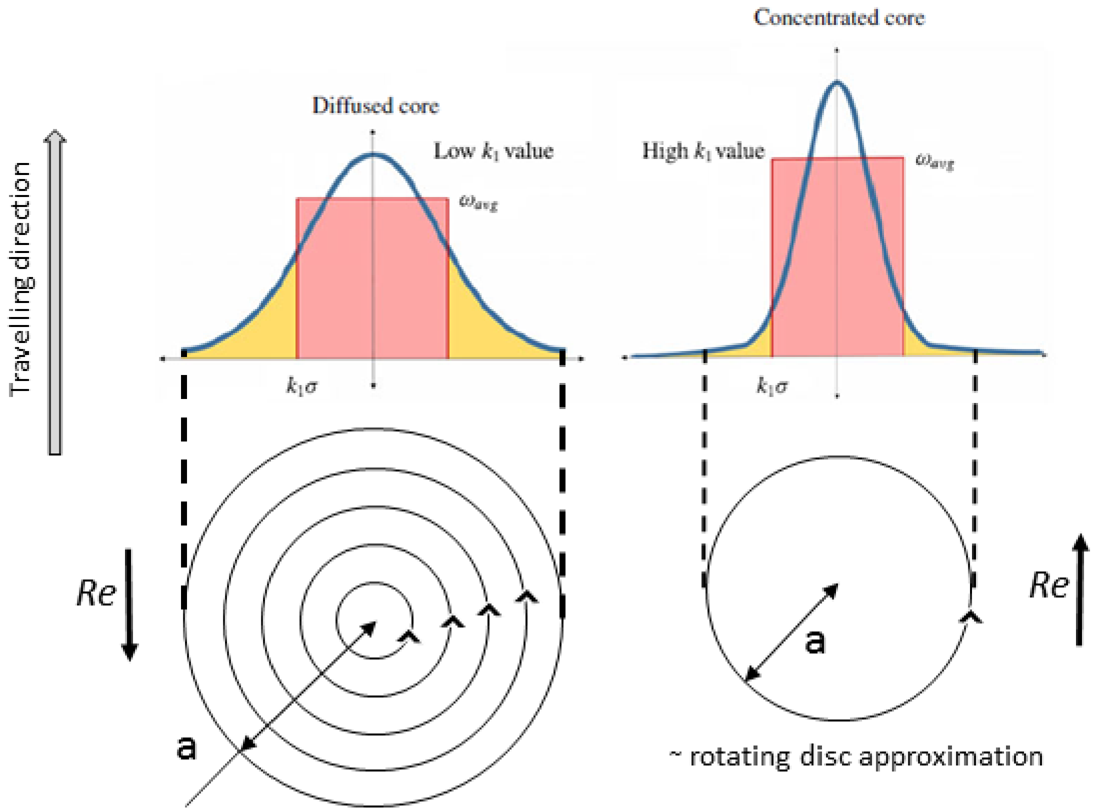

(a) (b)

Figure 2.8: vortex ring core vorticity distribution profile for low Reynolds numbers (a) and for high Reynolds numbers (b), considering an experimental range of 100 < *Re* < 4000.
Modification of Figure 5 from: Tinaikar, A. *et al* (2018). Understanding evolution of vortex rings in viscous fluids. *J Fluid Mech*, 836, 873-909.

2.7 Discussion

In summary, the first challenge associated with the development of a complex flow phantom that operates in a free field (deionised water) is the identification of an appropriate flow. The flow must be stable, predictable, reproducible and controllable. In addition, the flow should exhibit complex flow patterns that mimic relevant physiological conditions. This literature analysis identifies a flow that could be a potential candidate as a test object. Turbulence, recirculation, vortices and jets are characteristics of cardiovascular fluid dynamics both in healthy and pathological conditions. Particularly, the efficiency of cardiac output is regulated by the formation of vortices in the proximity of the mitral valve. Interestingly, analogies between vortices, intra-cardiac vortices, and vortex rings have been widely demonstrated. With simple physical parameters relevant to vortex ring formation being used as a quantitative index of cardiac health.
In addition to the physiological relevance, the main advantage of using the vortex ring as the test object is that it has been extensively studied in vitro and important parameters characterised. Idealised analytical and mathematical models and relationships between the main physical parameters are available in the literature (Hill 1894; Lamb 1932; Kaplanski-Rudi 1999). Vortex ring generation in a system consisting of a tube and an orifice depends on the stroke length (*L*), nozzle diameter (*D*), Reynolds number (*Re*) and piston velocity profile (*Up (t)*). After complete formation and under specific generating conditions (i.e. *L/D* ≈ 4), the vortex ring propagates in a free field (expansive

fluid) with self-induced velocity and predictable fluid dynamics. Vortex rings can be generated in a laboratory, in a controlled environment, with reproducibility of the main parameters typically better than +/- 10 %. All the evidence indicates that the vortex ring has the potential to constitute a flow benchmark for the development of complex flow test object. Arguably, it is physiologically relevant, stable, predictable and controllable, and it satisfies all the requirements discussed in Chapter 1. To assess this hypothesis, two vortex ring generators able to operate in air and in fluid were built. Experimental measurements and numerical simulations were performed, and results were compared. The systems, the experiments and the results are discussed in detail in the following chapter (Chapter 3).

2.8 Conclusion

This literature analysis identifies an appropriate flow for the development of a complex flow test object for medical imaging. The vortex ring, a fluid dynamical phenomenon extensively studied and characterised in vitro, is a potentially excellent candidate, especially since physical parameters studied in vitro can also be used as quantitative indices of cardiac health. These phenomena have relevance to many areas, from the wing tip vortices of aircraft, to the physiology of the human heart. Experimental studies have indicated that vortex rings can be generated in a lab in a controlled manner with encouraging reproducibility. All the evidence warrants its consideration as a candidate for a flow test object. To this end, two vortex ring generators are described and experiments conducted, as described in the next chapter.

CHAPTER 3

Vortex ring as flow reference for the development of a novel test object?

3.1 Introduction

Current design limitations described in Chapter 1 are part of the motivation for this PhD, which aims to build and validate a multimodal complex flow phantom for medical imaging. Literature analysis (Chapter 2) has also provided evidence that the vortex ring is a form of complex flow that can be found under physiological conditions. Main features of the ring vortex (i.e. translational speed, ring size) are predictable and controllable, described through mathematical equations (Figure 2.3, Chapter 2). Consequently, the vortex ring has been identified as potential candidate for the development of a complex flow test object.

To validate this hypothesis and to investigate credibility of the ring as a quantifiable flow for imaging, an Air-based Vortex Ring Generator (First Prototype) and an equivalent Liquid-based Vortex Ring Generator (Second Prototype) were built, as described in this chapter.

Experiments were undertaken, and comparative analysis was conducted on both prototypes evaluating:

- simple relationships described by theoretical models summarised in Figure 2.3 (Section 2.3, Chapter 2);
- measurements performed with video camera and software;
- computational Fluid Dynamics (CFD) simulations.

The work of this chapter is supported by the publication of a research paper (Ferrari et al 2017) and a conference research paper (Ferrari et al 2018).

3.2 First Prototype – Proof of Concept - Air-based Vortex Ring Generator

3.2.1 Introduction

An Air-Based Vortex ring generator was built to investigate reliability of the vortex ring in terms of stability, reproducibility and predictability. The system relied on the energy provided by a speaker (woofer) driving air through an orifice, controlled by a laptop. Stable vortex rings were generated and measurements were performed to assess reproducibility in terms of vortex ring size and translational position as a function of time. Computational Fluid Dynamics (CFD) simulations were also performed using appropriate generating conditions. A comparison between theoretical models, summarised in Figure 2.3 (Section 2.3, Chapter 2), CFD simulations and experimental measurements was performed. Although the system was simple and low cost, it demonstrated basic concepts and features of the vortex ring.

All the results obtained are reported in an open access scientific paper published by the Open Journal of Medical Imaging (OJMI – Scirp). As indicated in the paper, the first two authors Simone Ferrari and Simone Ambrogio contributed equally to the preparation of the manuscript.

3.2.2 Materials

Vortex ring generation requires a mechanism capable of propelling a slug of fluid through an orifice or a nozzle. Once ejected, the fluid swirls at the orifice interface and forms a stable toroidal structure that propagates along its axis (see Figures 2.4 and 2.5, Section 2.4, Chapter 2). The system should exhibit sufficient reproducibility to allow consistent measurements of flow features of interest. A cost-effective and simple way to build a system demonstrating our design concept, is by exploiting the energy provided by the membrane displacement of a speaker (woofer). The woofer was coupled to a chamber, for vortex ring development. A vaporised fluid was used for visualisation. An electrical signal was applied to the voice coil, moving it back and forth and generating a pressure wave (sound wave) in response to the electrical signal applied. A laptop was used to generate a single one-half cycle of sinusoidal oscillation signal at 10 Hz. The signal was amplified by connection with a 20 W stereo audio amplifier (Adafruit, MAX9744, USA), compatible with the speaker (woofer) power requirements. The output of the amplifier was used to drive the membrane of a Monacor SP-45/8 speaker (Monacor, SP-45/8, Germany). Plastic chambers, providing the orifice and essential for the vortex ring development, were 3D printed in cylindrical, funnel and conic shapes. The chambers were coupled to the speaker with elastic bands. Differences in vortex ring formation and circulation can be controlled by the 3D printed shapes, as reported by an experimental study conducted by Rosenfeld et al (2009). For further flexibility, an iris was used to modify the output diameter (and consequently the vortex ring diameter and vortex ring formation time) on demand. A transparent tunnel was manufactured from Poly (methyl methacrylate) (PMMA) and was used to minimise external atmospheric disturbances during the propagation of the vortex ring. A schematic block diagram of the system and pictures of the components are shown in Figure 3.1 and Figure 3.2, respectively.

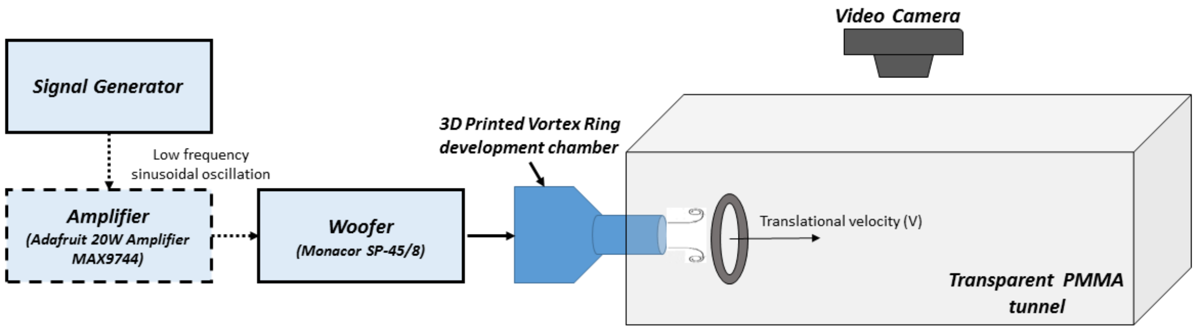

Figure 3.1: Block Scheme of the air-based vortex ring generator. Please note that this is a schematic representation and elements are not to scale.

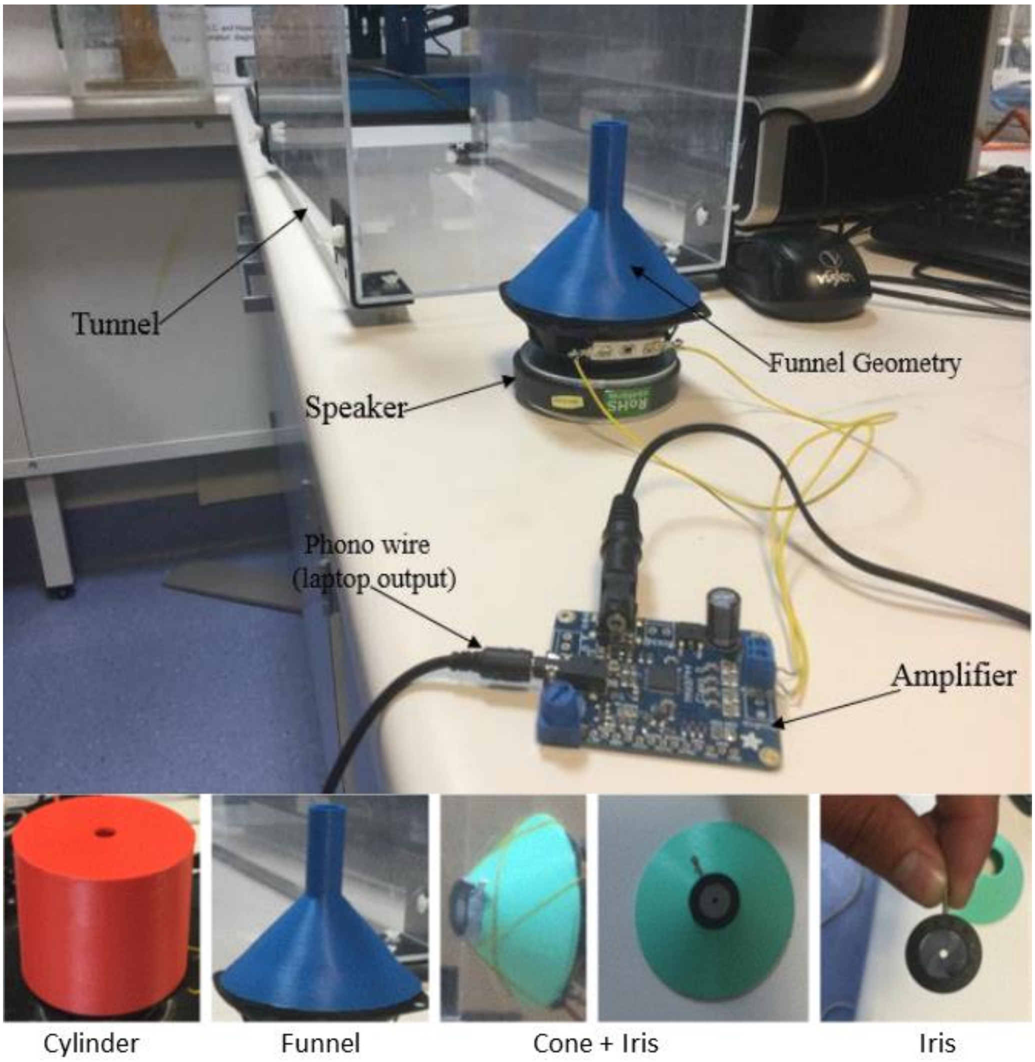

Figure 3.2: components of the air-based vortex ring generator.

In terms of operation, the selected 3D printed chamber was filled with a vaporised fluid by a smoke fog machine (Atmotech, VS400, United Kingdom) for visualising the ring vortex. The fog was generated by a mixture of water and glycerol (QTX Fog Smoke Machine Fluid, UK). The half cycle waveform generation was then activated, producing a controlled displacement of the woofer membrane. A smoke-filled vortex ring emerged from the orifice and travelled along the PMMA tunnel. The vortex ring movement was captured by a video camera, enabling measurements through post-processing and analysis. This involved measuring vortex ring position (pixel) and vortex ring size as a function of time from the captured frames of the video.

3.2.3 Method

Simple parameters, such as vortex ring size and vortex ring translational velocity as a function of time, were evaluated through the comparison of three different methods: simple relationships provided by analytical formulae found in literature, results obtained from optical/video acquisitions and Computational Fluid Dynamics (CFD) simulations.

The CFD study was conducted in partnership with a member of the VPH-CaSE consortium (http://www.vph-case.eu/), namely Simone Ferrari, hosted by the University of Sheffield.

Optical/video measurements were performed capturing the ring vortex at 30 frames per second (fps) with a video camera connected to a Laptop Dell Inspiron 13 (Inspiron 13, 5000 Series, Dell, USA). The same laptop was used for generating the signal (single one-half cycle of low-frequency sinusoidal oscillation, 10Hz) driving the coil (and the membrane) of the woofer. A program-script, written in MATLAB (MathWorks Inc., USA) allowed synchronisation of the generation of the vortex ring with the camera acquisitions. The frame rate of the camera and in-house-developed software (Figure 3.3) allowed measurements of salient features such as vortex ring size and vortex ring translational velocity as a function of time.

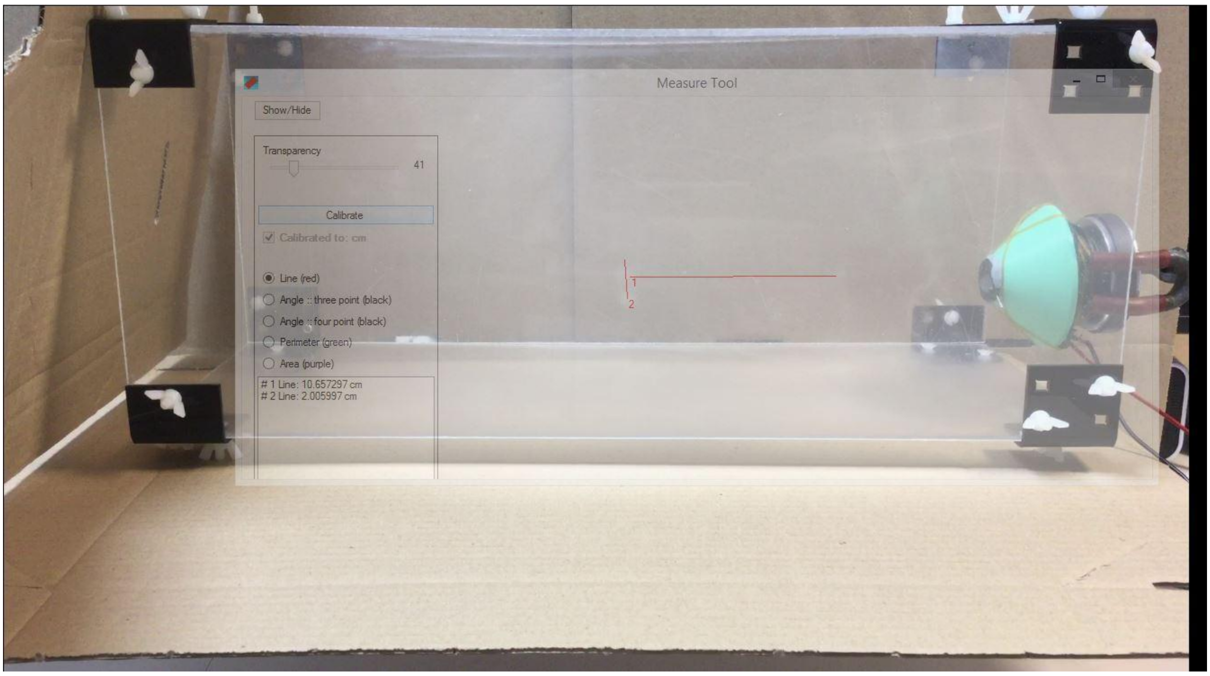

Figure 3.3: In-house developed software for vortex ring size and vortex ring translational velocity as function of the time calculations.

For proof of concept, data were collected with a conical shape chamber and iris-orifice diameter set at 10 mm +/- 0.5 mm. Simulated CFD Reynolds numbers (Re) at the throat of the orifice were *Re* = 500, *Re* = 1000 and *Re* = 2000. These parameters were selected because of physiological relevance. Bale-Glickman (2003) reported values of *Re* = 560 and *Re* = 1680, corresponding to peak systole in stenosed common carotid arteries (diameters from ~4.5 mm to ~8 mm), respectively. Experimental acquisitions were performed with an estimated Reynolds number of ~2000. This value was calculated with reference to the programmed average velocity of the membrane (woofer) displacement, the membrane (woofer) diameter and the orifice size. The vaporised fluid density and the dynamic viscosity were approximated as air under standard conditions (i.e. room temperature and pressure 1 atm). Equivalent generating conditions were used for both experimental optical/video measurements and CFD simulations. The CFD simulation data was provided by Simone Ferrari for comparison with the experimental results.

3.2.4 Results

Computational Fluid Dynamics results are reported for Reynolds numbers 500, 1000 and 2000, and experimental results have been plotted for Reynolds number 2000. Vortex ring position, size (2R + 2a, Figure 2.3, Section 2.3, Chapter 2) and translational velocity as a function of time are plotted in Figure 3.4, Figure 3.5 and Figure 3.6, respectively. Figure 3.7 shows a linearised plot of the vortex ring velocity as a function of distance travelled. The plots on the left depict experimental optical and video results whilst the right-hand plots show numerical simulation data. For completeness, correlation plot of vortex ring position estimated with optical/video and CFD simulations are shown in Figure 3.8.

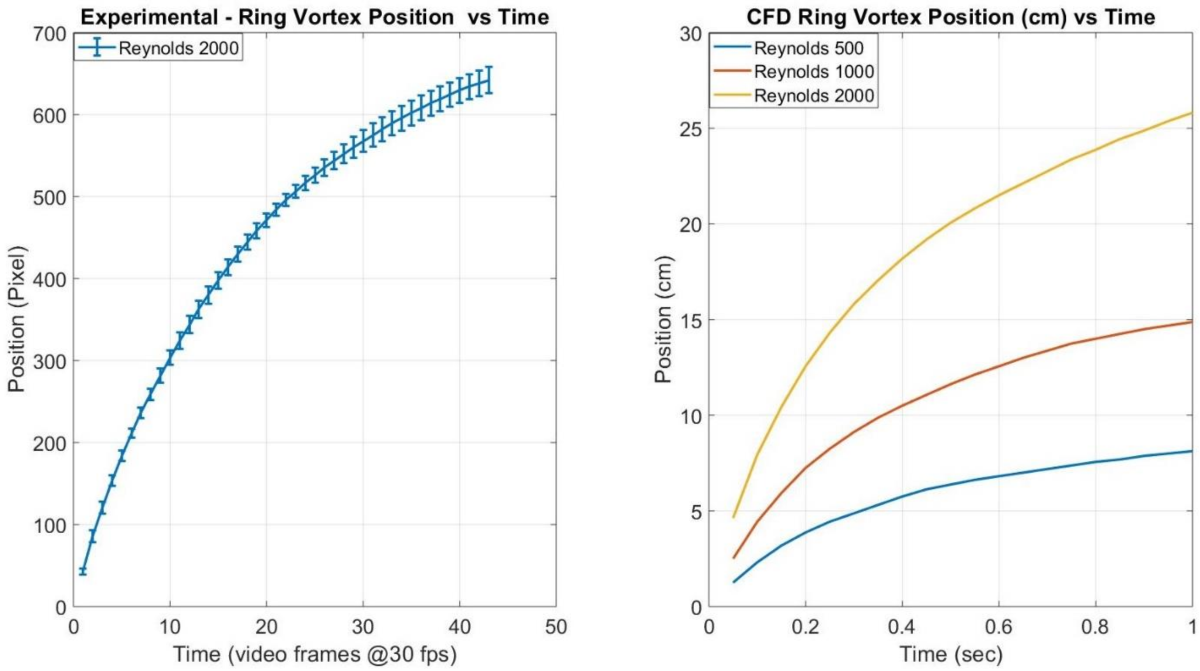

Figure 3.4: Vortex ring position as function of time. Experimental results (left) and CFD results (right)
Plot results from: Ferrari, S., Ambrogio, S., Walker, A., Verma, P., Narracott, A. J., Wilkinson, I. & Fenner, J. W. (2017). The Ring Vortex: Concepts for a Novel Complex Flow Phantom for Medical Imaging. *Open Journal of Medical Imaging*, 7(1), 28–41. Retrieved from
http://www.scirp.org/journal/doi.aspx?DOI=10.4236/ojmi.2017.71004

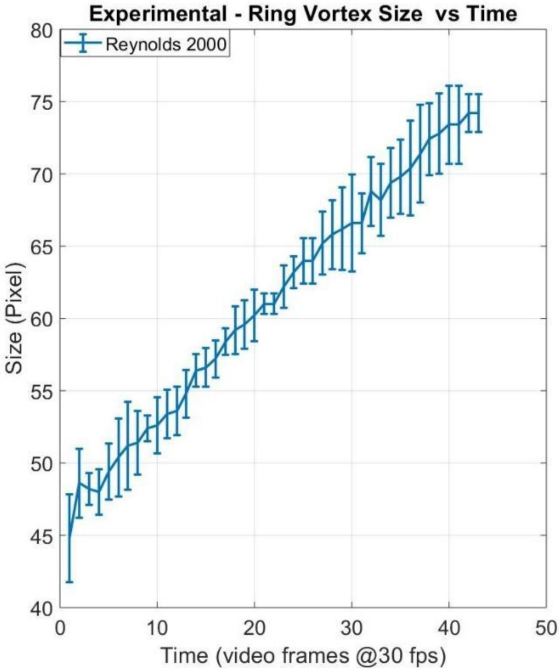

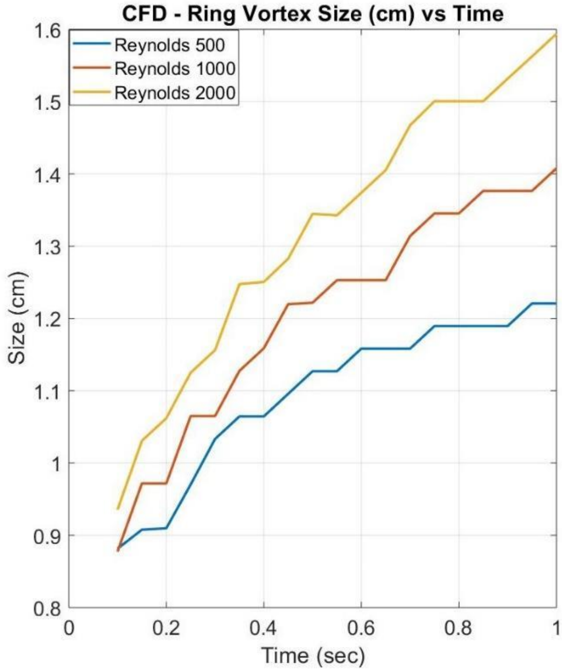

Figure 3.5: Vortex ring size as function of time. Experimental results (left) and CFD results (right). The CFD plots are not smooth due to spatial discretisation.
Plot results from: Ferrari, S., Ambrogio, S., Walker, A., Verma, P., Narracott, A. J., Wilkinson, I. & Fenner, J. W. (2017). The Ring Vortex: Concepts for a Novel Complex Flow Phantom for Medical Imaging. *Open Journal of Medical Imaging*, 7(1), 28–41.

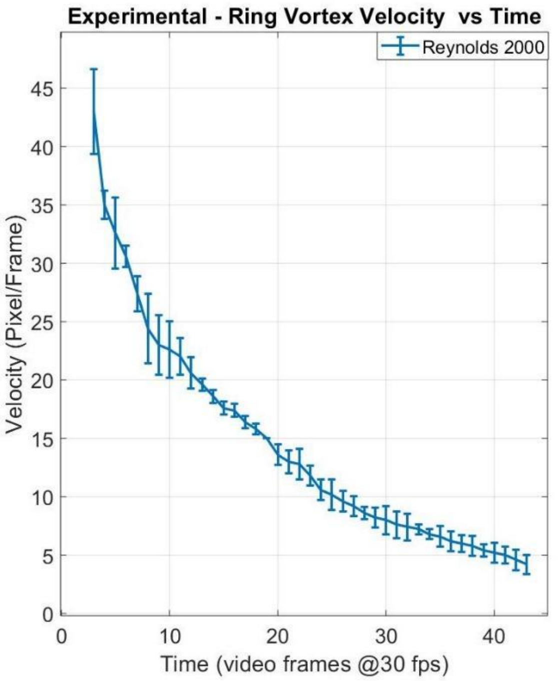

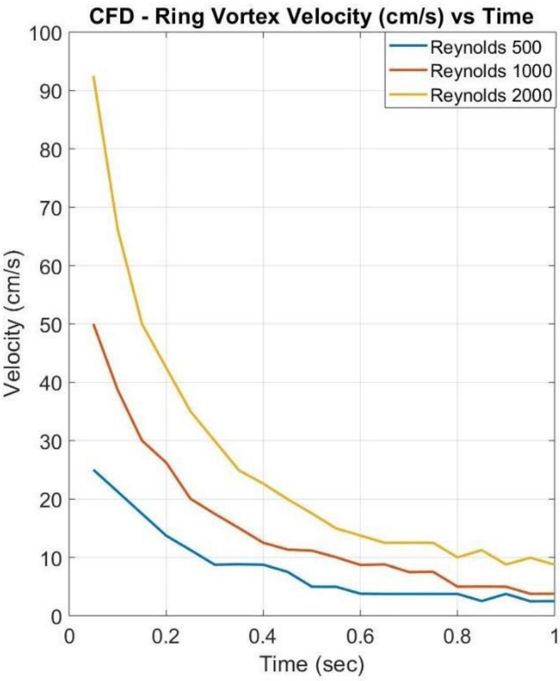

Figure 3.6: Vortex ring translational velocity as function of time. Experimental results (left) and CFD results (right). The CFD plots are not smooth due to spatial discretisation.
Plot results from: Ferrari, S., Ambrogio, S., Walker, A., Verma, P., Narracott, A. J., Wilkinson, I. & Fenner, J. W. (2017). The Ring Vortex: Concepts for a Novel Complex Flow Phantom for Medical Imaging. *Open Journal of Medical Imaging*, 7(1), 28–41.

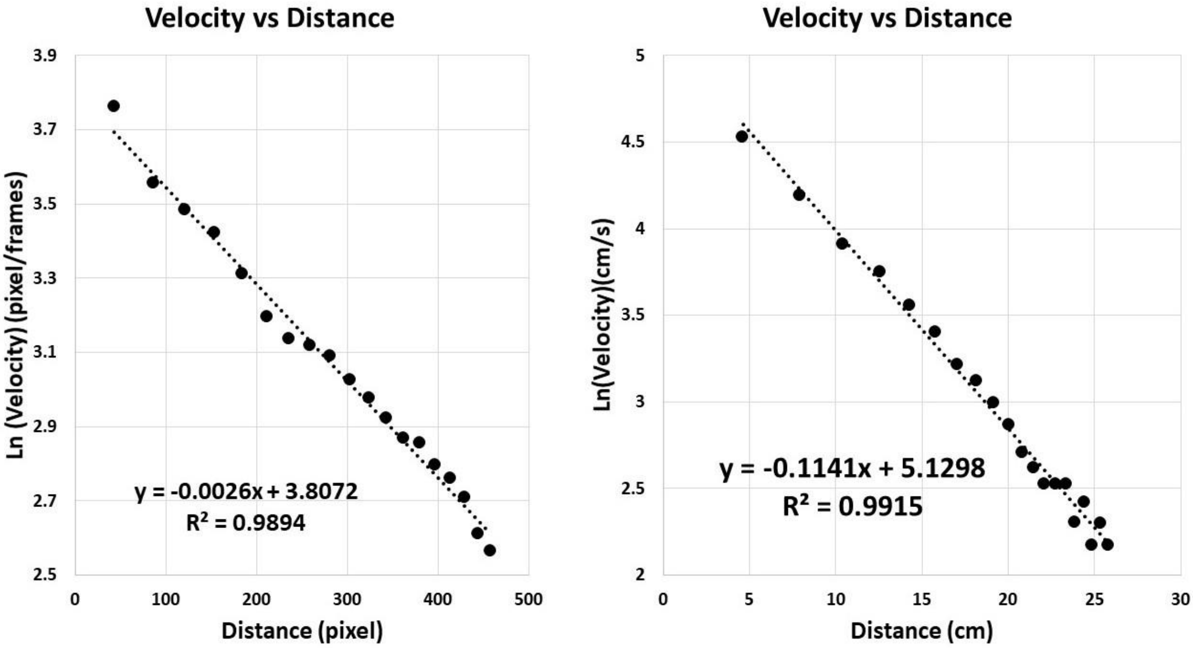

Figure 3.7: Natural logarithm of vortex ring translational velocity as function of distance travelled. Experimental results (left) and CFD results (right)
Plot results from: Ferrari, S., Ambrogio, S., Walker, A., Verma, P., Narracott, A. J., Wilkinson, I. & Fenner, J. W. (2017). The Ring Vortex: Concepts for a Novel Complex Flow Phantom for Medical Imaging. *Open Journal of Medical Imaging*, 7(1), 28–41.

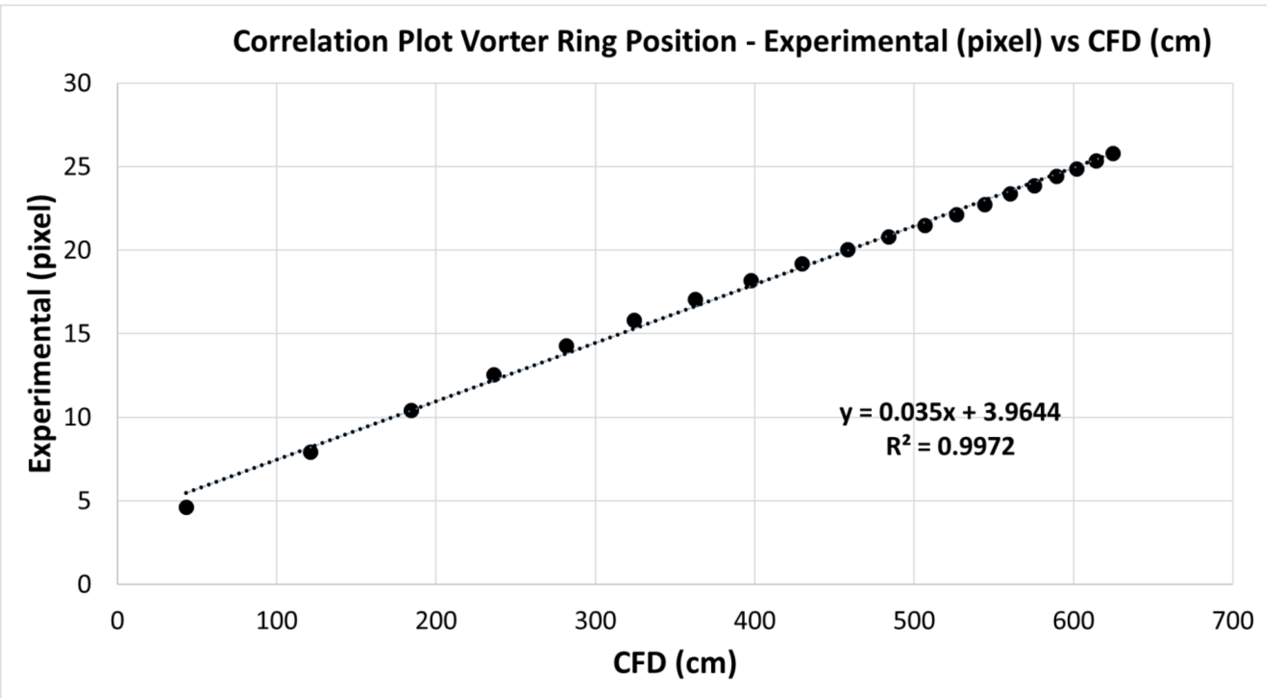

Figure 3.8: Correlation plot of vortex ring position for *Re* = 2000 – experimental data versus CFD simulations

Reproducibility and stability are crucial for the development of a flow test object. Measurements on the ring vortex size and translational velocity were performed experimentally (using optical/video methodology) on the acquisition of 5 different vortex rings. Results indicate reproducibility of better than +/- 10 %. Plots of the results are shown in Figure 3.9, Figure 3.10 and Figure 3.11 for the vortex ring position, size and translational velocity, respectively. The results refer to a programmed Reynolds number of 2000 with the fluid dynamics expected to exhibit greater instabilities compared to the lower Reynolds numbers simulated (500 and 1000). The first five frames for vortex ring translational velocity (Figure 3.10) have been excluded for better data visualisation (the vortex has not fully formed yet).

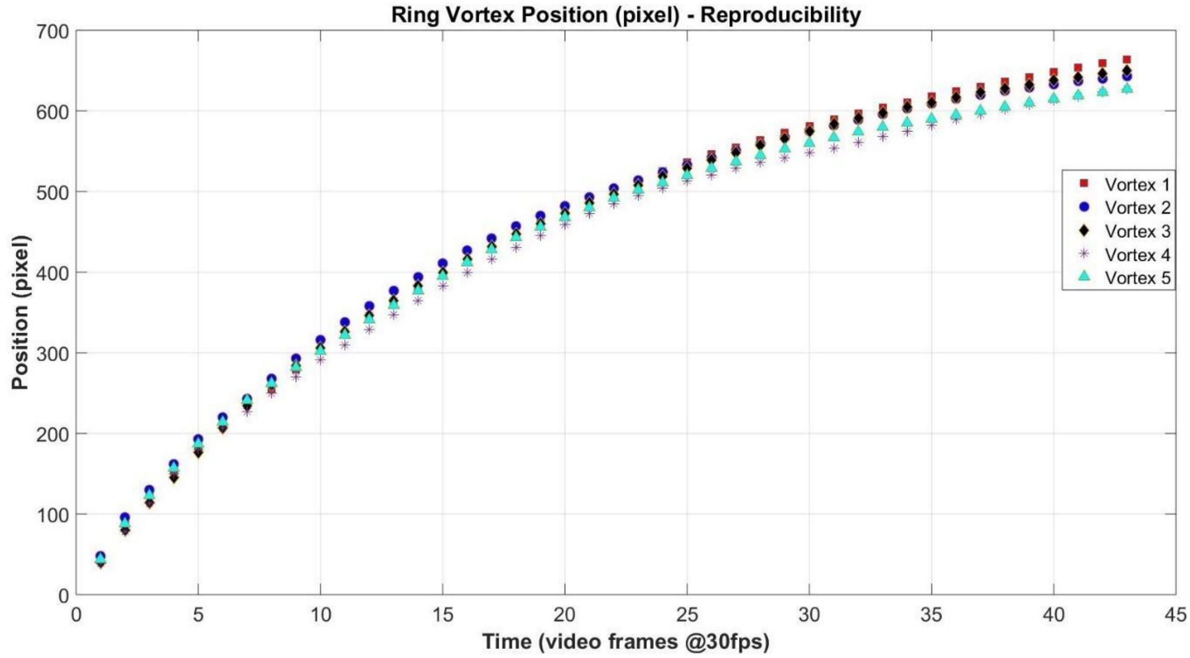

Figure 3.9: Reproducibility of the evolution of vortex ring position as function of time (all using the same generating conditions). Measurements refer to the acquisition of 5 vortex rings. Each acquisition is represented with a different marker shape.

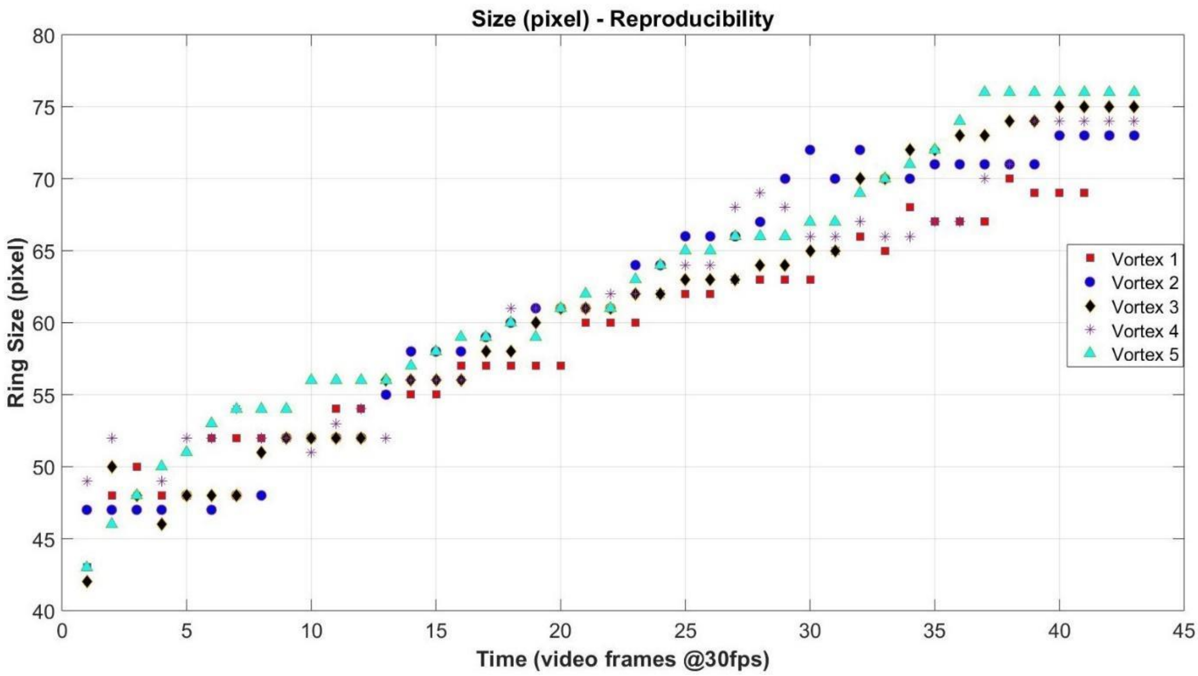

Figure 3.10: Reproducibility of the evolution of vortex ring size as function of time time (all using the same generating conditions). Measurements refer to the acquisition of 5 vortex rings. Each acquisition is represented with a different marker shape.

Plot results from:Ferrari, S., Ambrogio, S., Walker, A., Verma, P., Narracott, A. J., Wilkinson, I. & Fenner, J. W. (2017). The Ring Vortex: Concepts for a Novel Complex Flow Phantom for Medical Imaging. *Open Journal of Medical Imaging*, 7(1), 28–41.

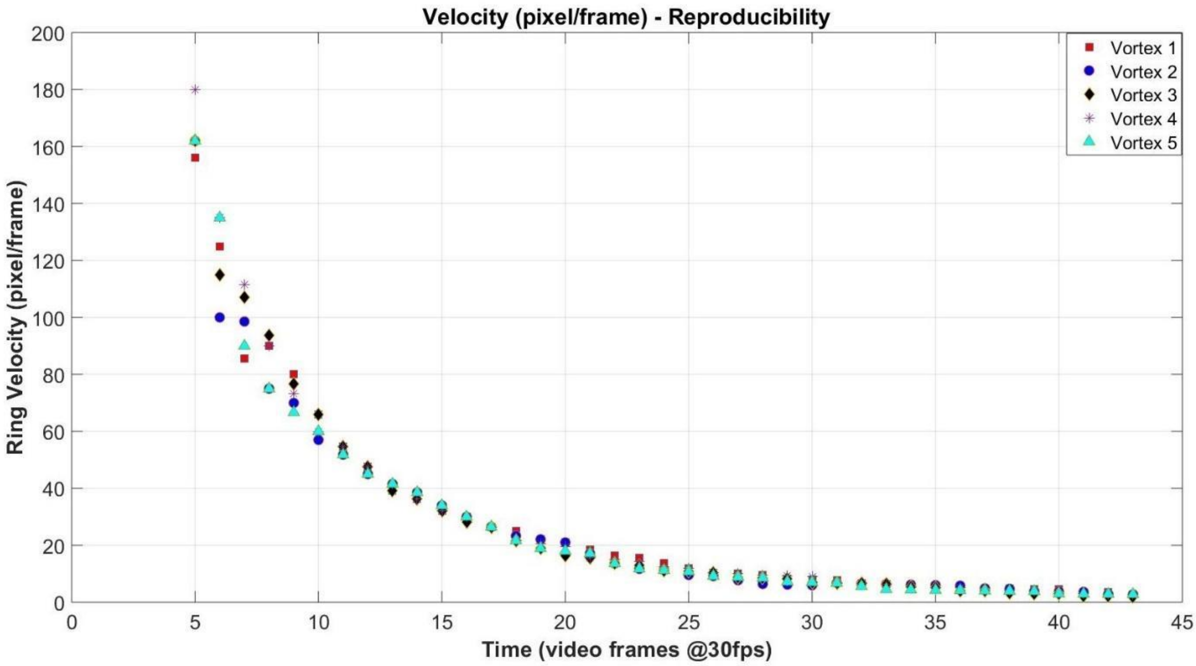

Figure 3.11: Reproducibility of the vortex ring translational velocity as function of time time (all using the same generating conditions). Measurements refer to the acquisition of 5 vortex rings. Each acquisition is represented with a different marker shape.
Plot results from: Ferrari, S., Ambrogio, S., Walker, A., Verma, P., Narracott, A. J., Wilkinson, I. & Fenner, J. W. (2017). The Ring Vortex: Concepts for a Novel Complex Flow Phantom for Medical Imaging. *Open Journal of Medical Imaging*, 7(1), 28–41.

3.2.5 Discussion

An Air-based Vortex Ring Generator was built in order to evaluate the basic features of the vortex rings that were generated experimentally. Measurements on vortex ring position and size as a function of time were performed with a video camera using in-house software developed by the University of Sheffield. Computational Fluid Dynamics (CFD) simulations were performed reproducing equivalent initial conditions. Experimental results are also worth comparing with the analytical models described in Chapter 2 (Figure 2.3, Section 2.3, Chapter 2) as well as the CFD simulations.

The theoretical approximations, described Section 2.6 and more in detail in Akhmetov (2009), reveal simple relationships between the vortex ring's translational velocity, its size, time and position. The vortex ring translational velocity decays exponentially with distance (Figure 3.7, R^2 ~ 0.99) and the vortex ring size grows approximately linearly with the propagation time. Numerical simulations suggest that the ring radius *R* grows steadily with piston displacement *L* and that the piston velocity determines the velocity of the ring (Ferrari et al 2017). The optical/video and numerical simulation plots show good (qualitative) agreement with theoretical concepts, both for the vortex ring's translational velocity and its size evolution over time, indicating that, if the generating conditions are known, the fluid behaviour of vortex ring (produced) can be mathematically predicted/approximated. As described in Section 2.6.1, the vortex embraces more fluid as it propagates. As a consequence of this, the core radius increases whilst the translational velocity decreases because the momentum is shared with the greater mass of the fluid (Reynolds 1876; Ferrari et al 2017; Tinaikar et al 2018). As described in Section 2.6.1 (Chapter 2), after an initial period (in which formation of the ring is incomplete) the vortex ring stabilises and propagates with a self-induced velocity and predictable dynamics (Tinaikar et al 2018). The vortex flow field depends on the following generating conditions: the velocity profile input, the orifice diameter and the Reynolds number. Due to the exploratory nature of this system, flow performance has not been characterised in detail but it has been extensively demonstrated by numerous experimental studies (Weigand and Gharib 1997; Gharib et al 1998; Rosenfeld et al 1998; Akhmetov 2001; Dabiri and Gharib, 2004; Krueger et al 2004; Akhmetov 2009). For proof of concept the Reynolds number of approximately 2000 has been experimentally reproduced and results reported. The fluid dynamics for Re = 2000 (transitional within the throat of the orifice) can be expected to exhibit greater instabilities than the lower Reynolds number selected for CFD simulations (1000 and 500). Furthermore, a Reynolds number of 2000 is the maximum value suggested by the EN 61685-IEC 61685:2001 (BS EN 61685:2002, IEC 61685:2001), International standard (stability date 2020) for the development of a Doppler Ultrasound flow phantom. Measurements on vortex ring position, size and translational velocity as a function of time, performed experimentally (optical/video method) on the acquisition of five consecutive vortex rings, demonstrated reproducibility within +/- 10 %. The natural logarithm of the vortex ring's translational velocity proved to be linear, plotted as a function of the distance travelled for both the experimental data and the CFD simulation for Reynolds 2000. Indeed, high correlation coefficients (R^2 = 0.989, for experimental, and R^2 = 0.991, for CFD) were found. Greater data dispersion is observed in the final stages of the CFD simulations because the vortex velocity decreased significantly enough that the spatial discretisation of the numerical simulation provided non-smooth curves.

3.2.6 Limitations

The analysis conducted on the Air-based Vortex Ring Generator was limited by the simplified experimental set-up. Experiments and numerical simulations were conducted varying the Reynolds number only, as one of the three main generating parameters that determine the fluid dynamics. Since measurements of the woofer membrane displacement proved to be challenging, an assumption that the displacement profile was equivalent to the signal provided was made. Under this assumption, a membrane average velocity has been used for Reynolds number calculation in the experimental set-up. Notably, software measurement calibration was not performed at the time of the experiment, consequently, the results are not directly comparable since the experimental data are reported in pixels and frames while the CFD data are reported in meters and seconds. Nonetheless the strong correlation illustrated in the plot of Figure 3.8 implies good comparability.

3.2.7 Conclusion

Experiments were performed on a simplified Air-based Vortex Ring Generator to evaluate broad characteristics of the flow. Analytical, experimental and computational behaviour of the ring vortex are reported. The system suffered from several limitations, however, these experiments provided the first evidence that the vortex ring may be a good candidate for the development of a flow test object because it demonstrates predictability, reproducibility, stability and controllability. Preliminary results obtained with the study were encouraging and provided motivation for the development of a more advanced Liquid-based Vortex Ring Generator system. A liquid environment is crucial for Ultrasound imaging compatibility. In addition, a more controlled environment is expected to improve the reproducibility of the flow features of interest.

3.3 Second Prototype - Liquid-based Vortex Ring Generator

3.3.1 Introduction

The preliminary analysis conducted on the simplified Air-based Vortex Ring Generator design has provided an indication that the ring vortex is suitable candidate for a reference complex flow. In addition, the flow resembles complex patterns typical of physiological in vivo condition (Section 2.2, Chapter 2). Such characteristics are invaluable for the development of a flow test object (phantom) for medical imaging. Since a water environment (or alternatively a tissue mimicking fluid or material) is fundamental for Ultrasound and Magnetic Resonance Imaging compatibility, working principles need to be demonstrated with respect to a liquid-based system. Consequently, a low-cost Liquid-based Vortex Ring Generator was developed, and comparable experiments were performed. The Liquid-based system relied on a water tank and a 200 ml syringe driven by a stepper motor. Piston displacement and piston velocity were controlled by a square wave signal delivered by a laptop computer. The work described below was presented at the "European Congress on Computational Methods in Applied Sciences and Engineering" (VipIMAGE 2017, Porto, Portugal) and published in "Lecture Notes in Computational Vision and Biomechanics – Springer International Publishing AG". Once again, the first two authors Simone Ferrari and Simone Ambrogio contributed equally to the manuscript writing.

3.3.2 Materials

The Liquid-based Vortex Ring Generator system relied on a NEMA 23 External Linear Stepper Motor (OMC Corporation – Stepper Online, China) coupled with a 200 ml commercially available syringe and a water tank. The OMC Nema 23 is 36 V, 3 A, and it is able to provide a linear travel/step of 0.04 mm and accuracy of +/- 5 % (datasheet: https://www.omc-stepperonline.com/download/23LS22-3004E-150G.pdf). At the time that the experiment was performed (late 2017), it was one of the most powerful (~100 W) and cost-effective stepper motors on the market. The stepper motor was controlled by a DM542 fully digital stepper driver (OMC Corporation – Stepper Online, China) which was connected to a compatible power supply (S-150-36, OMC Corporation – Stepper Online, China). The microcontroller ATmega328P (Atmel Corporation, USA) of an Arduino[1] Uno Board was used to generate a 25 pulses square-wave signal of amplitude 5-Volt, width ~1 millisecond and duty cycle 50 %. The signal was delivered to the stepper driver and, consequently, to the coils that drive the rotor of the stepper motor. Interacting with the phases of the bipolar stepper motor, the square wave signal provided a displacement of 0.5 mm at 0.01 m/s (assuming steady displacement and average velocity). Further details about Arduino Uno Board programming and stepper motor working principles are provided in sections 4.4.4 and 4.4.5 (Chapter 4). The syringe/piston surface area was 1643.05 mm^2 and the orifice diameter 10.40 mm. These generating conditions produced a flow of Reynolds number ~2000 at the orifice interface (as for the Air-based Vortex Ring Generator experiment). The syringe was prefilled with a mixture of water and coloured dye to produce a visible vortex ring propagating through the tank. The leak proof tank, whose dimensions were 18 cm (L) x 9 cm (W) x 9 cm (H), was filled with water. Dimensions were chosen to be large enough for walls that would not influence the vortex ring behaviour. The main components (motor, syringe and waterproof tank) were fixed together on a wood base, using hinges and screws (Figure 3.13). A 25 fps video camera was used to capture images and in-house software to measure vortex ring size and translational velocity. A

[1] Arduino was developed by a student in Ivrea (Italy) but there are still legal ownership disputes.

schematic diagram of the liquid-based system is shown in Figure 3.12 while the assembled system is shown in Figure 3.13.

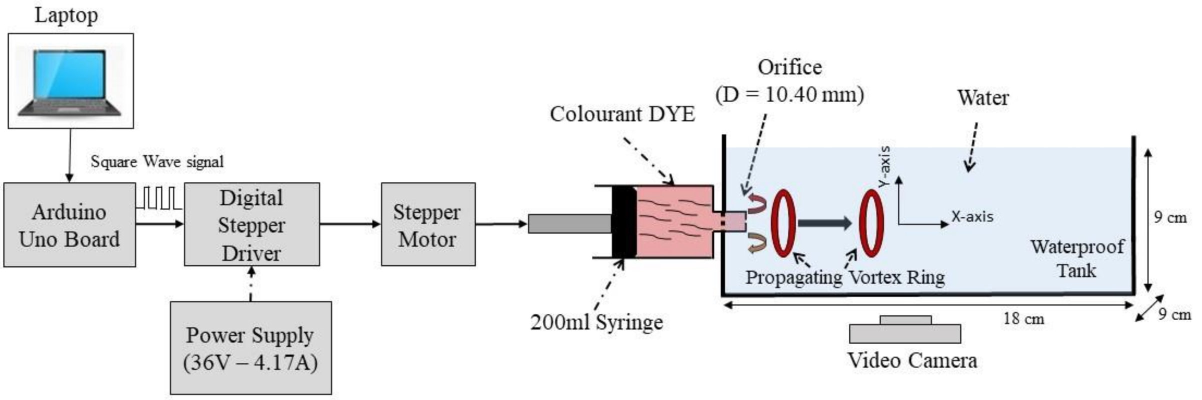

Figure 3.12: Schematic block diagram of the Liquid-based vortex ring generator used in Ferrari et al (2018) experiment. Please note that this is a schematic representation and elements are not to scale.

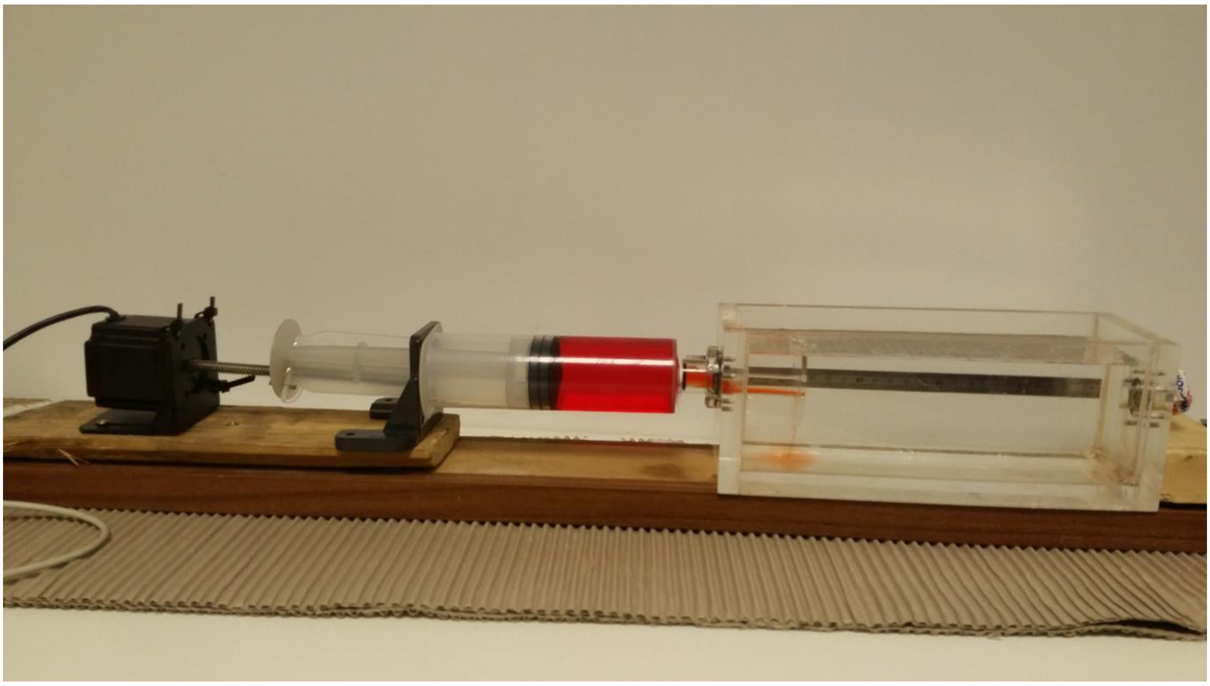

Figure 3.13: Liquid-based vortex ring generator assembled.
Figure 26: Modification of Figure 2: Ferrari, S., Ambrogio, S., Walker, A., Narracott, A. J. & Fenner, J. W. (2018). The Ring Vortex: A Candidate for a Liquid-Based Complex Flow Phantom for Medical Imaging. *Lecture Notes in Computational Vision and Biomechanics*, 27, 893–902.

3.3.3 Method

The methods (described in detail in Section 3.2.1) used to carry out measurements were similar for both air-based and liquid-based systems. The only difference was that the Laptop Dell Inspiron 13 (Inspiron 13, 5000 Series, Dell, USA) could not be used for controlling both the Arduino Uno Board (which drives the piston) and acquiring images in MATLAB. At the time of writing (late 2017), the MATLAB support packages for simultaneous camera communications with Arduino boards were missing or defective. Consequently, a 25 fps video camera was used to continuously capture images and in-house software used to measure vortex ring size and translational velocity. The system (syringe plus water tank) was filled with water and then coloured food dye was introduced into the syringe to provide contrast between the generated vortex ring and the surrounding water. Experiments were conducted with Reynolds number ~2000 and a video camera operating at 25 fps. The Reynolds number was calculated based on the piston speed, the water viscosity and the output orifice diameter. The stepper motor offered valuable flexibility and controllability of the system. The piston displacement and the piston velocity were controlled by varying the frequency and the number of pulses of the square wave signal with 50 % duty cycle.

Vortex rings were generated, both in experimental measurements and CFD simulations, under the following generating conditions:
- Reynolds number ~ 2000;
- Stroke ratio ~ 1;
- the assumption of Constant (steady) piston velocity.

The ring vortex size and the ring vortex position (along the x-axis), as a function of time, were calculated following the method described in Section 3.2.3. A ruler was attached to the water tank face to support the measurements and to allow software calibration (pixel to cm conversion) (Figure 3.13). Figure 3.14 shows the vortex ring vorticity flow field generated in numerical simulations and the experimental vortex ring generated with the Liquid-based Vortex Ring Generator (a blue dye colour was used in this experiment). The vortex atmosphere, as well as the inner and outer ring cores, can be recognised in the images.

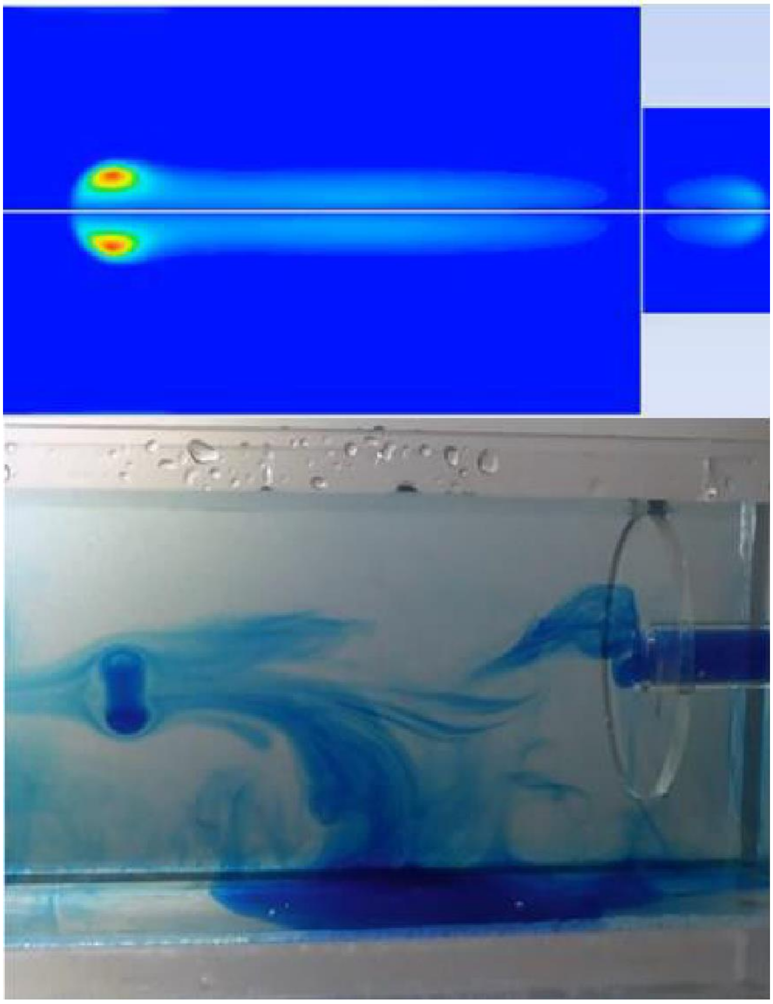

Figure 3.14: vorticity field of ring vortex generated with numerical simulation (top) and with blue coloured dye in a Liquid-based vortex ring generator.
Figure 4: Ferrari, S., Ambrogio, S., Walker, A., Narracott, A. J. & Fenner, J. W. (2018). The Ring Vortex: A Candidate for a Liquid-Based Complex Flow Phantom for Medical Imaging. *Lecture Notes in Computational Vision and Biomechanics*, 27, 893–902.

3.3.4 Results

Plots of vortex ring position, size and translational velocity, calculated from optical/video acquisitions (as for the Air-based Vortex Ring Generator system), are depicted in Figures 3.15, 3.16 and 3.17, respectively. The results refer to average and standard deviation (error bars, +/- 1 SD) values calculated from the acquisition of five consecutive vortex rings. In agreement with the air-based system and the theoretical models, the vortex ring size grows (Figure 3.16) as a function of time and the vortex ring velocity varies with the reciprocal of time. A schematic diagram for clarifying what is being measured is depicted in Figure 3.18.

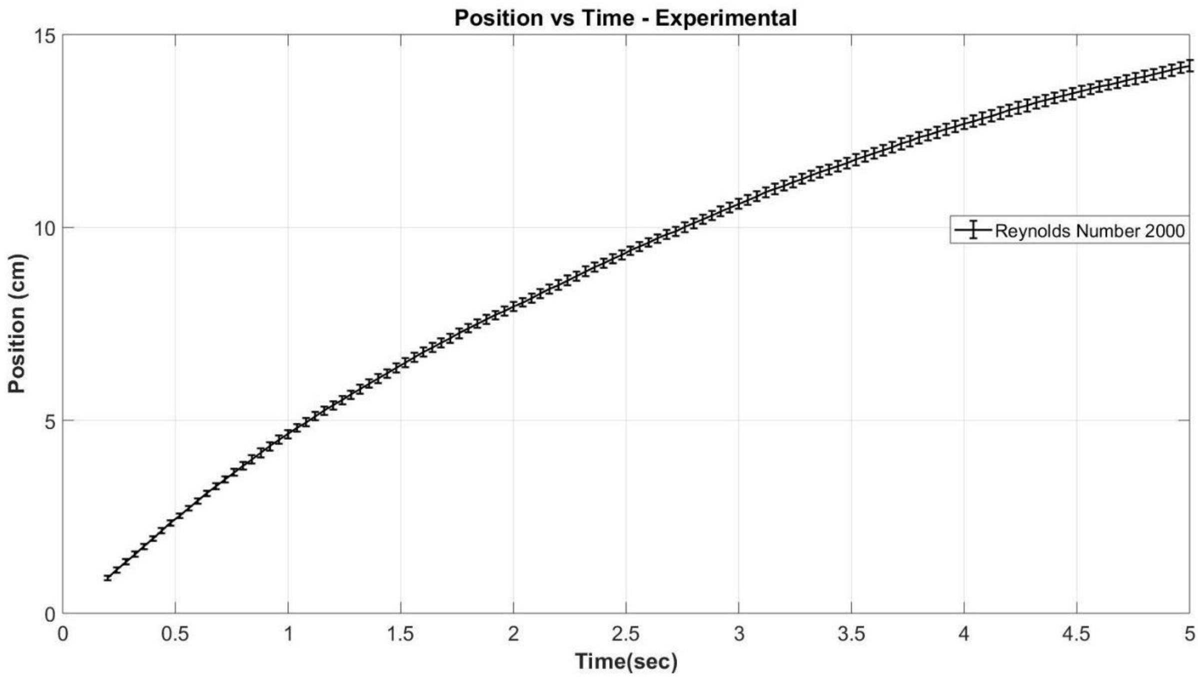

Figure 3.15: Vortex ring position as a function of time. Plot refers to average value and error bar to standard deviation, both calculated on the acquisition of 5 vortex rings under equivalent generating condition. Figure 5c: Ferrari, S., Ambrogio, S., Walker, A., Narracott, A. J. & Fenner, J. W. (2018). The Ring Vortex: A Candidate for a Liquid-Based Complex Flow Phantom for Medical Imaging. *Lecture Notes in Computational Vision and Biomechanics*, 27, 893–902.

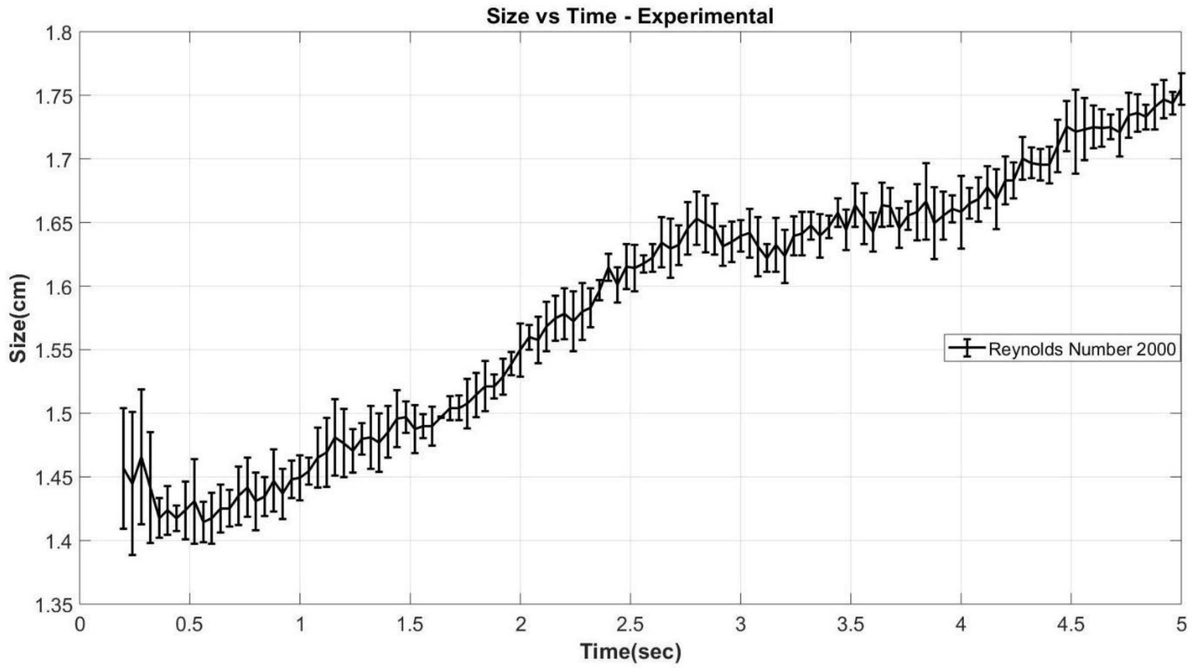

Figure 3.16: Vortex ring size as a function of time. Plot refers to average value and error bar to standard deviation, both calculated on the acquisition of 5 vortex rings under equivalent generating condition. Figure 5d: Ferrari, S., Ambrogio, S., Walker, A., Narracott, A. J. & Fenner, J. W. (2018). The Ring Vortex: A Candidate for a Liquid-Based Complex Flow Phantom for Medical Imaging. *Lecture Notes in Computational Vision and Biomechanics*, 27, 893–902.

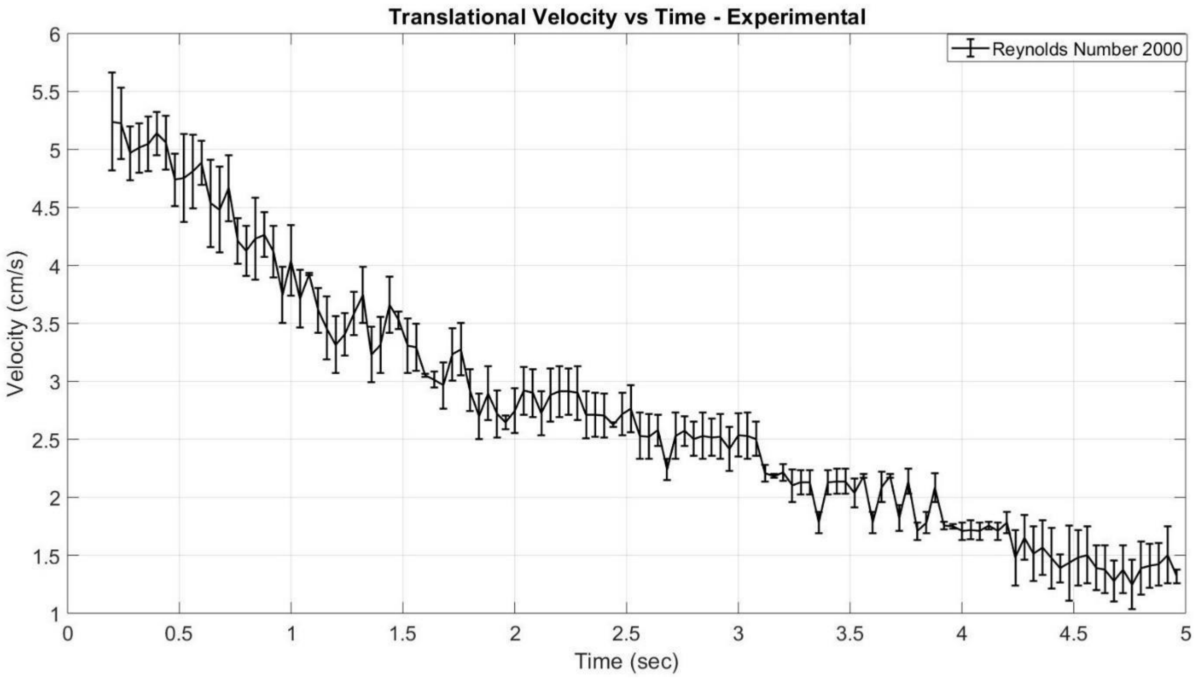

Figure 3.17: Vortex ring translational velocity as a function of time. Experimental data refers to average and standard deviation calculated on the acquisition of 5 vortex rings. CFD plot are not smooth due to spatial discretisation.

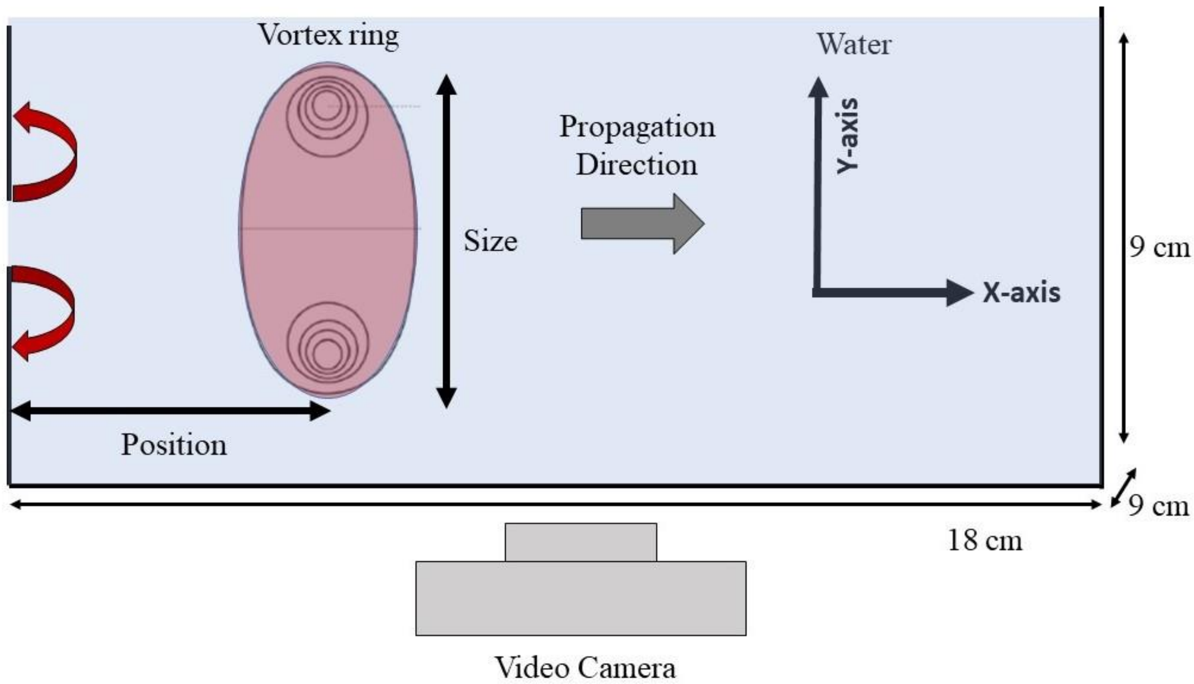

Figure 3.18: Schematic block of propagating vortex ring and quantity measured (vortex ring position, vortex ring size and vortex ring translational velocity as a function of time). Please note that this is a schematic representation and elements are not to scale.

Figure 3.19 and Figure 3.20 show plots of the quantified correlation between measurements on the vortex ring position and the vortex ring size obtained with experimental measurements (average) and numerical simulation. There was a very high correlation in both cases with coefficients of R^2 = 0.999 and R^2 = 0.949 for the vortex ring position and size, respectively. However, the offset and gradients of the best fit line do show some discrepancies (line of perfect agreement between the two modalities is plotted in blue in Figure 3.19, in order to illustrate the bias). A significant dispersion of the data around the best fit line is also observed in vortex ring size measurements.

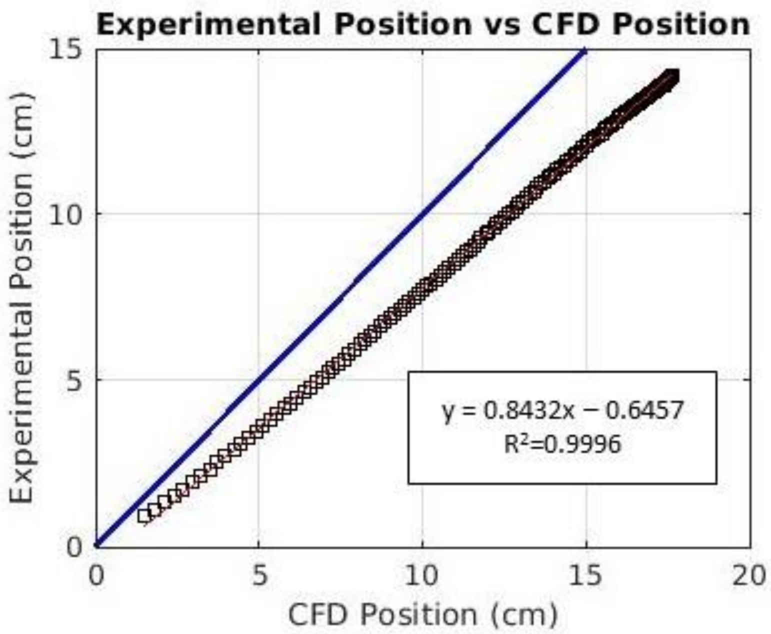

Figure 3.19: Correlation between experimental and CFD simulation results on vortex ring position measurements. Line of perfect agreement is shown in blue color to highlight the bias offset.
Figure 5a: Ferrari, S., Ambrogio, S., Walker, A., Narracott, A. J. & Fenner, J. W. (2018). The Ring Vortex: A Candidate for a Liquid-Based Complex Flow Phantom for Medical Imaging. *Lecture Notes in Computational Vision and Biomechanics*, 27, 893–902.

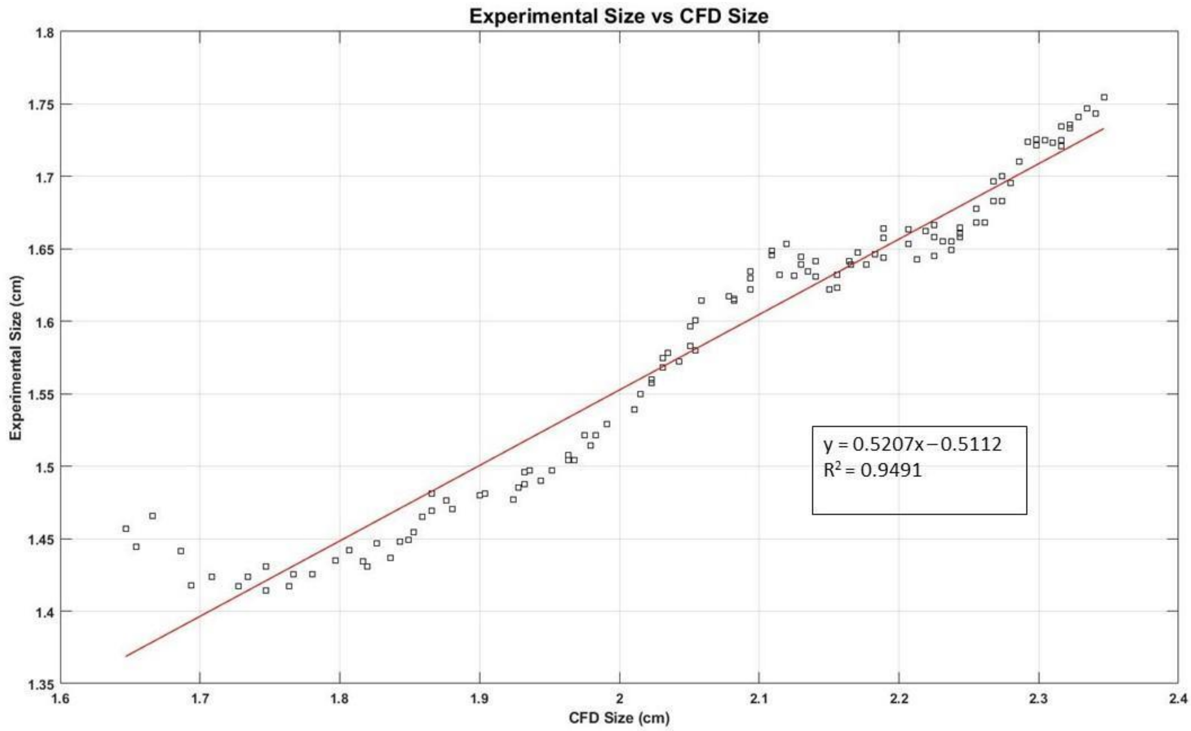

Figure 3.20: Correlation between experimental and CFD simulation results on vortex ring size evolution measurements.
Figure 5a: Ferrari, S., Ambrogio, S., Walker, A., Narracott, A. J. & Fenner, J. W. (2018). The Ring Vortex: A Candidate for a Liquid-Based Complex Flow Phantom for Medical Imaging. *Lecture Notes in Computational Vision and Biomechanics*, 27, 893–902.

Similar to the air-based system, reproducibility was evaluated on the acquisition of five consecutive vortex rings that were generated under the same experimental conditions. The vortex ring position, vortex ring size and vortex ring velocity as a function of time are plotted in Figures 3.21, 3.22 and 3.23, respectively. Dispersion is greater in the early stages, both for the vortex ring position and the vortex ring size measurements. The error becomes smaller as the vortex ring propagates. An error of approx. +/- 7 % is present for the vortex ring position initially. The error (variability between multiple measurements) drops to values lower than +/- 2 % as the ring vortex propagates. Equivalent results are also seen for the vortex ring size evolution. In the early stage, errors up to +/- 4 % were estimated whilst the values drop lower than +/- 2 % when the vortex ring was fully developed. Finally, errors lower than +/- 8 % were estimated in the translational velocity measurements. In all these cases, error is characterised as standard deviation calculated from the five vortex rings generated.

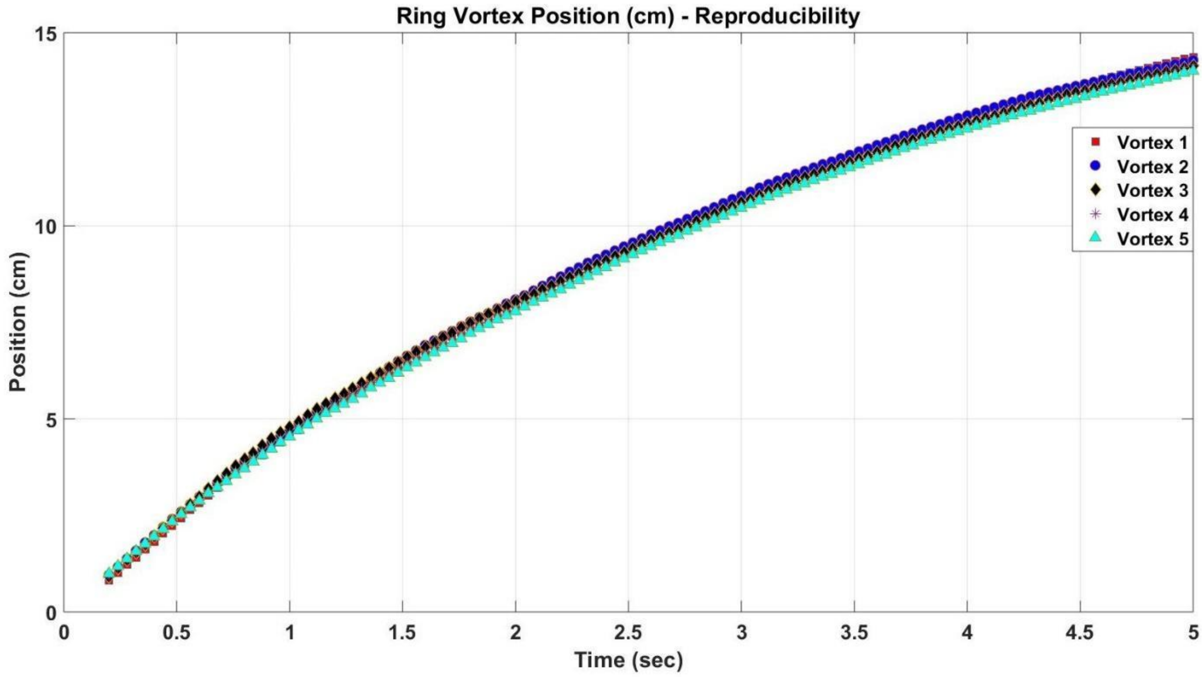

Figure 3.21: Vortex ring position as function of the time - reproducibility. Measurements refer to the acquisition of 5 vortex rings. Each acquisition is represented by a different marker shape.
Figure 6a: Ferrari, S., Ambrogio, S., Walker, A., Narracott, A. J. & Fenner, J. W. (2018). The Ring Vortex: A Candidate for a Liquid-Based Complex Flow Phantom for Medical Imaging. *Lecture Notes in Computational Vision and Biomechanics*, 27, 893–902.

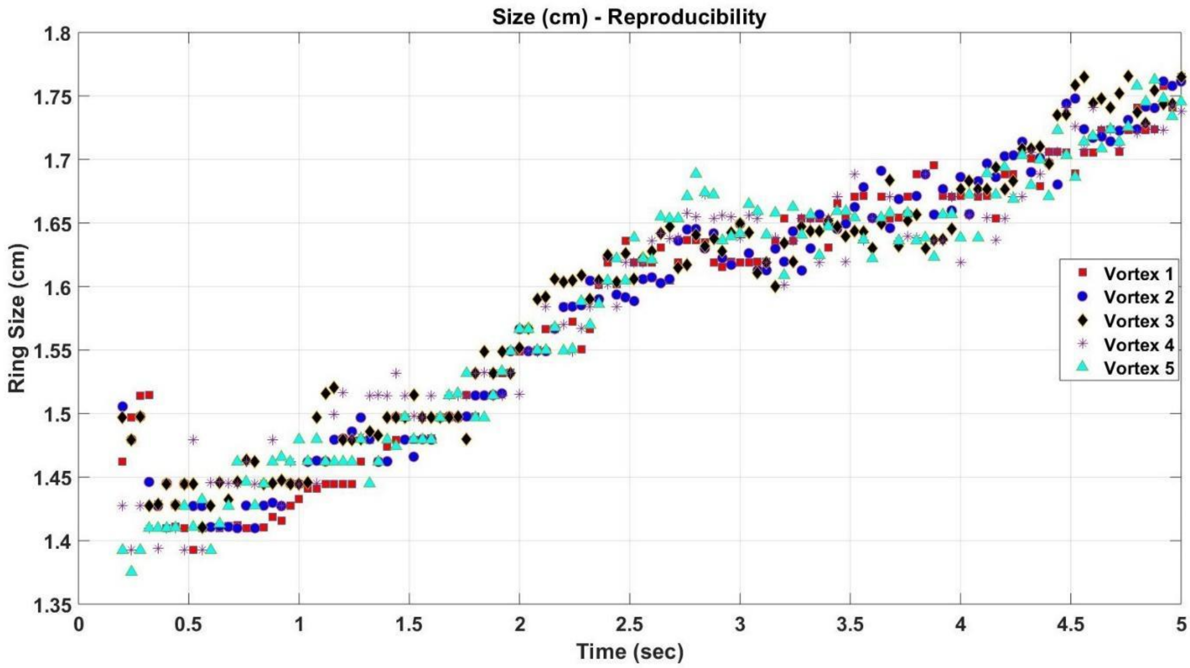

Figure 3.22: Vortex ring size as function of the time - reproducibility. Measurements refer to the acquisition of 5 vortex rings. Each acquisition is represented by a different marker shape.
Figure 6b: Ferrari, S., Ambrogio, S., Walker, A., Narracott, A. J. & Fenner, J. W. (2018). The Ring Vortex: A Candidate for a Liquid-Based Complex Flow Phantom for Medical Imaging. *Lecture Notes in Computational Vision and Biomechanics*, 27, 893–902.

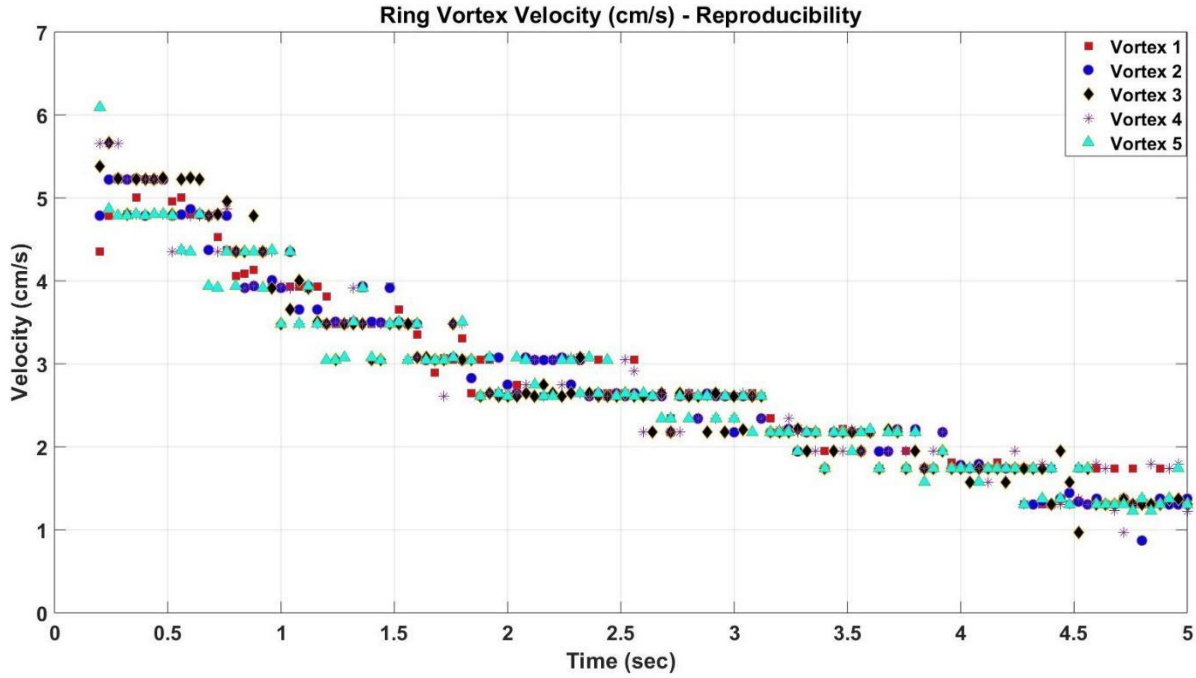

Figure 3.23: Vortex ring velocity as function of the time - reproducibility. Measurements refer to the acquisition of 5 vortex rings. Each acquisition is represented by a different marker shape.

3.3.5 Discussion

The Liquid-based Vortex Ring Generator has overcome many of the limitations exhibited by the first prototype (Air-based Vortex Ring Generator). Relying on a piston-cylinder system driven by a stepper motor and a water tank for the vortex ring propagation. The stepper motor offered controllability, reproducibility and flexibility for the generating conditions and the tank offered a more stable environment than in air. Following the methods used with the Air-Based system, optical/video camera acquisitions and CFD simulations were performed under equivalent generating conditions. For the optical/video measurements, coloured food dye was used to mark the propagating ring and to make it visible to the camera. Measurements were performed on the vortex ring position, size and translational velocity as a function of time for both methods. The results confirmed that the water offers a more stable environment and the reproducibility was improved compared to the previous system. Interestingly, larger variability was observed in the early stages when the vortex was not fully developed, characterised by continuous momentum addition. Later, the vortex stabilised, propagating with self-induced velocity and improved reproducibility. This is consistent with the vortex ring fluid dynamics, described in detail in Section 2.6 (Chapter 2). The vortex rings were produced experimentally with errors, typically better than +/- 7 %, +/- 4 % and +/- 8 %, estimated for position, size and translational velocity, respectively. Optical video measurements on vortex ring position and size (average values) plotted against the equivalent CFD data to quantify the correlation. The offset and gradients of the best fit line for the vortex ring position (Figure 3.18) both show some discrepancies between the experimental and numerical results although the two variables are strongly linearly correlated. The slope and intercept of the linear equation suggest that higher position (or velocity) values are estimated by the CFD simulations. After 5 seconds, the ring travelled 14 cm as estimated with the optical video measurements whilst a distance of 17.65 cm was obtained from the CFD simulations. Difficulties were also found in the comparison of the vortex ring size data estimated and simulated by the two techniques. Significant dispersion of the data around the best fit line was observed despite the correlation value being very high (R^2 = 0.94). Experimentally, it is challenging to precisely define the boundaries of the vortex core and this undoubtedly adds to the dispersion. Overall, the CFD simulations exceeded vortex ring size values (up to 28 %) in comparison with experimental measurements.

The reason for the discrepancy between the two methods (experimental plus CFD) is not clear and further studies should be conducted to assess contribution of the two approaches. However, experimental measurements showed promising reproducibility and provide the motivation for the construction of a more advanced liquid-based prototype, although measurement methods need to be considered to validate the system. Adequate functionality in water, which is crucial for the compatibility with medical imaging technologies of interest (i.e. Doppler ultrasound and MRI), has been successfully demonstrated.

3.3.6 Conclusion

A Liquid-based Vortex Ring Generator was developed to undertake measurements analogous to those performed on the simplified air-based prototype. The system showed encouraging reproducibility for vortex ring position, size and velocity as a function of time. However, significant discrepancies were found between results provided by the optical/video camera measurements and the Computational Fluid Dynamic simulations although a high correlation coefficient was estimated. Higher dispersion of the data was found in the early stages (i.e. post formation) when the vortex was not fully developed. It is possible that instabilities in the generating process might be the reason for the discrepancies in the results of the two approaches (experimental vs CFD). Uncertainties can be reduced with new measurement techniques to validate the flow. Nonetheless functionality in water, crucial for the compatibility with medical imaging technologies of interest (i.e. Doppler Ultrasound and MRI), was successfully demonstrated. Overall, the system has exhibited improved reproducibility compared to the air-based prototype.

3.4 Discussion

The physiological relevance of vortex rings has already been discussed. In addition, fundamental requirements for the development of a flow test object are the stability, predictability, reproducibility and controllability of the flow. The two simple prototypes described here have enabled comparative studies to be undertaken (Section 3.2 and Section 3.3).

The first prototype, named Air-based Vortex Ring Generator, consisted of a 20 W woofer coupled with a 3D printed plastic chamber for the vortex ring development. The system was simple and showed several limitations, however, it enabled comparative studies and demonstrated vortex ring stability and controllability. Optical/video measurements and CFD simulations showed good agreement with theoretical concepts (Section 2.6, Chapter 2) and provided the motivation for the development of a second liquid-based prototype. Functionality in water needed to be demonstrated for the compatibility with medical imaging technologies of interest (US and MRI). The second prototype, named Liquid-based Vortex Ring generator, relied on a ~100 W stepper motor and a 200 ml syringe, coupled with a water tank for the vortex ring propagation. Experimental measurements for simulated Reynolds number of ~2000 demonstrated high stability and controllability of the flow. Vortex rings were generated with reproducible sizes and translational velocity typically less than +/-8 %. However, significant discrepancies were found when comparing experimental results with CFD simulations. CFD simulations approximate well the theoretical predictions but provide absolute values that differ by up to 28 % from the experimental results. The propagating characteristics of the ring are dominated by the generating phase that is captured by numerical methods. The vortex ring generation phase is a phenomenon that has not been fully characterised and numerical simulations may struggle to approximate generating conditions. Consequently, experimental results cannot be directly compared with CFD simulation results and new measurement methods must be performed to validate the design through cross-validation of the results. Laser-PIV measurements are selected as an alternative to CFD to characterise both macro and microflow conditions.

3.5 Conclusion

Two prototypes have been developed in order to generate vortex rings in the lab and to carry out comparative studies. The first prototype was a simplified air-based system. Encouraging results provided by the air-based system provided the motivation for the development of a second liquid-based system. As expected, reproducibility and stability of the flow improved in the liquid-based system compared to the air-based generator. Discrepancies were found in comparison of experimental results and numerical simulations. CFD simulations demonstrated important characteristics of the flow but were insufficiently accurate to predict details under equivalent generating conditions even though the flow was highly reproducible. Consequently, different measurement methods, such as Laser-PIV, will be considered to validate the flow. Overall, the experiments conducted on the two prototypes, which are complemented by the publication of two scientific articles, have provided evidence that the vortex ring has characteristics that are sufficiently predictable, reproducible, stable and controllable to warrant consideration as a flow benchmark for the development of a flow test object for medical imaging.

CHAPTER 4

Vortex Ring based Complex Flow Phantom for Doppler Ultrasound – Design Specifications

4.1 Introduction

The physiological relevance of vortex rings was discussed in Chapter 2 with Chapter 3 providing the motivation for the development of an advanced Vortex Ring based Complex Flow Phantom prototype. Reproducibility, stability, controllability and predictability of vortex rings have been demonstrated through preliminary experiments on two simplified phantom prototypes. These characteristics, fundamental for a test object, have been demonstrated in air and in water with optical/video measurements and Computational Fluid Dynamics (CFD) simulations supporting simple relationships described by theory. However, discrepancies between absolute values provided by the optical/video method and the CFD simulations were evident. The generation phase is challenging for computational simulations and affects the ring propagation behaviour. Laser-PIV offers an alternative to CFD simulations to characterise the flow at both macro and micro levels. Nevertheless, Chapter 3 provides evidence that the vortex ring has features that are key to the development of a complex flow phantom for medical imaging. This chapter extends this work and provides details and technical specifications for the construction of a credible flow test object. As discussed in Chapter 1, the prototype is designed to operate in a free-field and to be compatible with advanced Doppler Ultrasound modalities. After extensive design characterisation and validation, a Magnetic Resonance compatible version is proposed in Chapter 8. Regulations for MRI unit regulations and hazards are also described in detail within that chapter.

This chapter is supported by the publication of a journal article (Ambrogio et al 2019). The phantom design was also presented at "The Annual Meeting of the European Society of Radiology 2019" (ESR 2019, Vienna, Austria, February 27 – March 3) within the "Invest in the Youth" support program and was demonstrated at the Leeds Test Objects Ltd exhibition booth. Leeds Test Objects Ltd (Leeds Test Objects Ltd, Boroughbridge, United Kingdom) is beneficiary partner of the VPH-CaSE (Marie Skłodowska-Curie grant agreement No 642612).

4.2 Main challenges associated with the development of a credible flow test object - Summary

The main challenges associated with the design of the test object are the identification of an appropriate complex flow, dimensions and materials. Fundamental requirements for the development of the phantom are summarised in Figure 4.1.

Design Requirements

- ✓ Innovative
- ✓ Compact
- ✓ Portable
- ✓ User-friendly
- ✓ Easy and fast to set up
- ✓ Compatible with Hospital environment
- ✓ Affordable

Materials Requirements

- ✓ Cost-effective
- ✓ Robust
- ✓ Optically transparent
- ✓ Compatible with multiple imaging modalities
- ✓ Compatible with a range of fluids
- ✓ Good quality
- ✓ Non-hazardous

Flow Requirements

- ✓ Provide complex flow patterns
- ✓ Stable
- ✓ Controllable
- ✓ Predictable
- ✓ Mimic Human Physiological Conditions
- ✓ Reproducible

Figure 4.1: Challenges associated with the development of a credible flow test object.

The test object aims to provide a reference flow for:

- clarifying the capacity of new clinical technologies to quantify physiological flows;
- allowing testing and validation of improved quantitative flow algorithms in both clinical and research facilities;
- allowing comparative studies between different flow related imaging techniques (i.e. optical and Ultrasound);
- supporting Quality Control checks in the clinical environment and training.

The design should be compact and portable, to allow easy transportation and delivery. It should be user–friendly and easy (fast) to set-up in hospital environment. Typically, clinical scientists (or technicians, medical physicists, biomedical engineers etc.) perform multiple measurements on several devices in a single day. They would not consider or promote a device that requires excessive time to set up and use. Materials should be affordable, robust, compatible with different medical imaging modalities (such as Ultrasound and MR) and optically transparent to allow complementary measurements with optical methods (such as Laser Particle Imaging Velocimetry). A good balance between cost and quality of materials must be maintained. They must be non-hazardous and compatible with the typical health and safety regulations of the hospital environment. The flow should mimic relevant *in vivo* conditions where possible, providing complex flow patterns. Nonetheless, it should be stable, reproducible (within well-defined tolerances), controllable and predictable. Ideally, the fluid dynamical behaviour of the flow should be known to specified tolerances.

4.3 Vortex Ring based Complex Flow Phantom – why did the Ultrasound prototype come first?

Ultrasound was chosen over Magnetic Resonance Imaging because it is clinically available and currently the first choice as a diagnostic modality for the assessment of several cardiovascular pathologies (Hansen et al 2017). As described in Section 1.4 (Chapter 1), state of the art Ultrasound techniques include 2D and 3D real-time angle independent Doppler imaging, based on Vector Flow Imaging (VFI), particle velocimetry tracking (Speckle Tracking) and volume quantification in post-processing (Hoskins et al 2010; Garcia et al 2010; Westerdale et al 2011; Kokkalis et al 2015; Jensen et al 2016; Badescu et al 2017-a; Badescu et al 2017-b; Hansen et al 2017). Transverse Oscillation (TO) is an advanced and specific Ultrasound Vector Flow imaging technique that has been FDA (US Food and Drug Administration) approved (2013) and it is currently implemented on clinical scanners manufactured by BK Ultrasound (BK Ultrasound, Nova Scotia, Canada) and Carestream (Carestream Health, Ontario, Canada). Transverse Oscillation is the recommended technique for real time quantitative analysis of complex flow within valves, bifurcations and heart chambers (Jensen et al

2013; Jensen et al 2016). Ultrasound scanners manufactured by Hitachi (Hitachi Ltd, Tokyo, Japan), GE Healthcare (Ge Healthcare, Illinois, USA) and Mindray (Mindray Medical International Limited, Shenzen, China) implement Colour Doppler Based VFI technique (Jensen et al 2016). The GE Healthcare Vivid E95™ (GE Healthcare, Illinois, USA) includes also a speckle tracking technique named Blood Speckle Imaging. None of these technologies was available for demonstration purposes at the latest conference of The British Medical Ultrasound Society (The 50th Annual Scientific Meeting of the British Medical Ultrasound Society, Manchester, 4-6 of December 2018), but when Manufacturers like Hitachi and GE Healthcare were asked about these technologies, they affirmed that market demand is currently so high that they cannot cover both market and exhibition requests. A consistent number of ultrasound scanners with advanced flow mapping techniques will be soon available and there are no effective phantom technologies on the market for supporting Quality Control checks of these innovative devices.

4.4 Vortex Ring based Complex Flow Phantom Design – Technical Specification

4.4.1 Introduction

As described in Chapter 2 (Sections 2.3 and 2.4), a vortex ring is a natural fluid dynamic phenomenon that forms when a bulk of fluid is pushed through an orifice (or a nozzle) into an expansive fluid environment. Under specific generating conditions (Reynolds number, velocity stroke ejection profile, orifice diameter), the fluid "rolls up" at the orifice output surface and propagates with self-induced velocity along its central axis. Examples of vortex rings in ordinary life are the underwater rings generated by dolphins or smoke rings generated using cigarette smoke. The initial stage of vortex ring generation occupies a distance estimated as 2-3 times the orifice diameter (Tinaikar et al 2018) and is characterised by instabilities characteristic of vortex ring formation (as described in Section 2.6, Chapter 2, and demonstrated in Section 3.3.2 and Section 3.3.3, Chapter 3). Beyond the initial stage, the vortex ring stabilises, assuming a toroidal shape that travels with self-induced velocity and predictable dynamics across the volume beyond the orifice.

The Vortex Ring based Complex Flow Phantom necessarily accommodates such features and the design relies on the assembly of three main components: a piston/cylinder system and interchangeable orifices for vortex ring generation, a water-tight imaging tank for the vortex ring propagation and a computer-controlled actuator system. The piston, linked to a programmable external linear stepper motor, drives a known volume of fluid towards an orifice that connects to the water-tight tank. As described in Section 2.4 (Chapter 2), the characteristics of the generated vortex ring depend on the stroke length (piston displacement), on the piston velocity profile, on the Reynolds number and on the nozzle diameter. Piston displacement and piston velocity profiles are modified on demand through dedicated software. Four different interchangeable orifice diameters are provided with the prototype. Reynolds number is derived from a combination of these parameters (i.e. flow velocity, flow density, orifice diameter). Consequently, a wide range of vortex rings with different characteristics can be produced on demand.

The phantom is almost entirely manufactured from PMMA (Perspex) – a material that is durable, waterproof, easy to manufacture (i.e. cut, engrave), available in different colour or as clear (transparent) (particularly useful for Optical measurements techniques). Moreover, PMMA has X-ray attenuation properties comparable with soft tissues at relevant diagnostic energies (Boone et al 2012; ICRU Report 87, 2012). Therefore, no significant modifications need to be applied to the design for potential compatibility with X-ray imaging modalities (such as CT). In contrast, Magnetic Resonance

Imaging (MRI) imposes several restrictions. Particularly, ferromagnetic materials and electric circuits must be excluded from the design to avoid projectile hazards and electromagnetic interference. These aspects are ignored in this design but given specific consideration in Chapter 8.

Technical CAD drawings of the phantom components, design, materials and methods are described below.

4.4.2 Design – Imaging tank

The water-tight imaging tank constitutes a semi-closed environment in which the vortex ring forms and propagates. The tank is entirely manufactured from clear PMMA (Perspex). It rests on four small screw-able nylon pegs that slot into a transparent PMMA base. The PMMA base, designated the "imaging tank base", has six threaded holes for additional screw-able feet. The feet on the base can be useful for phantom alignment on soft surfaces, such as beds for medical examination. The CAD drawing of the PMMA base that supports the imaging tank ("Imaging Tank Base") is shown in Figure 4.2.

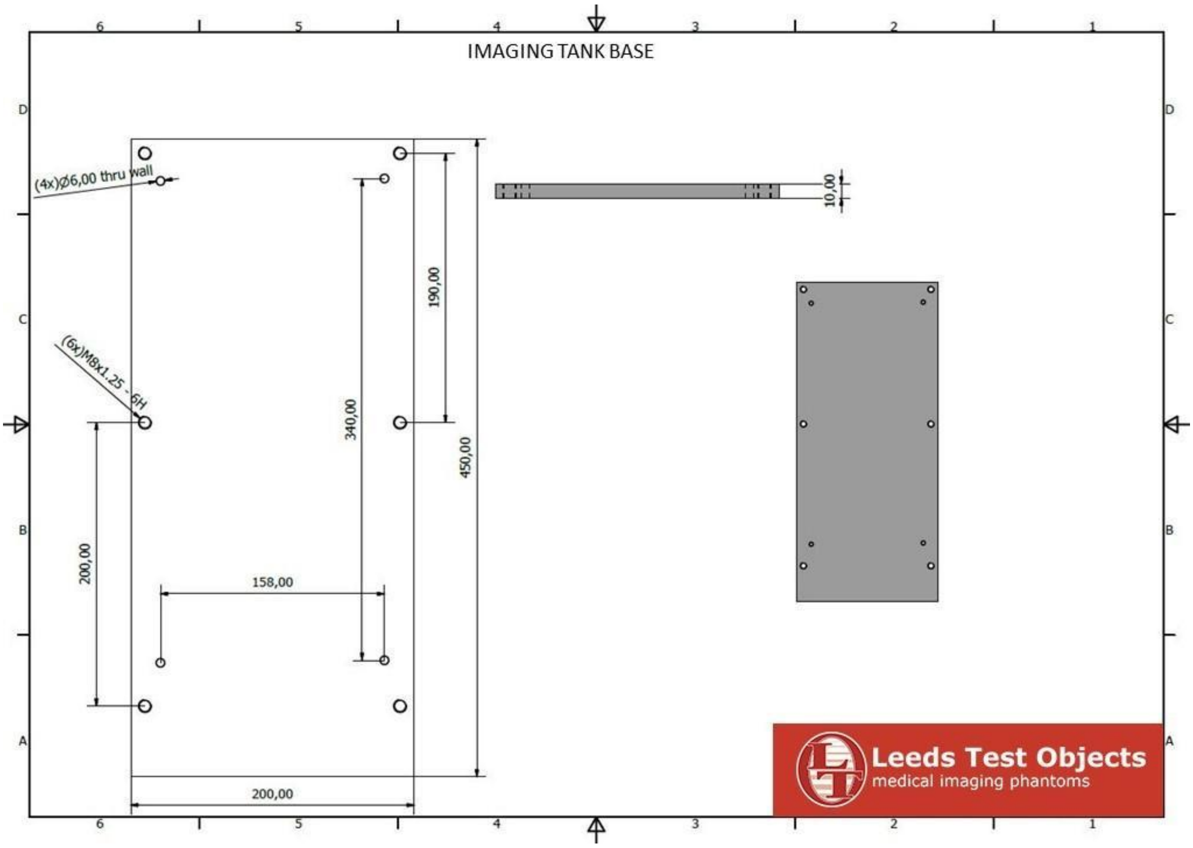

Figure 4.2: CAD drawing - Vortex Ring based Complex Flow Phantom – Imaging Tank Base.

The use of transparent materials is recommended to allow direct visualisation of flow and measurements with optical techniques, such as cameras or Laser Particle Imaging Velocimetry (Laser PIV) (Hoskins et al 2017).
The top surface of the water-tight tank is open. Diagnostic ultrasound scans cannot be performed through PMMA walls due to the acoustic properties of the material. The open surface of the tank allows the ultrasonic probes to be placed directly into the fluid where the vortex ring is propagating. As mentioned in the introduction section (Section 4.4.1), PMMA was chosen because it is water-tight,

durable, and it provides transparency and offers attenuation to X-ray comparable to human soft tissues at diagnostic energy range. A couple of spirit levels are placed on top of two opposite walls of the tank for accurate levelling. Screw-able nylon pegs and spirit levels allow the levelling of the system. The water-tight imaging tank has internal dimensions of 15 cm (width) x 35 cm (length) x 16.5 cm (height). The choice of tank dimension is critical, and as frequently occurs in design engineering, it relies on numerous compromises. Tank internal height and width should be large enough that the walls do not provide large reflections in ultrasound imaging. In addition, the proximity of the walls should not influence on vortex ring generation and propagation. On the other hand, large dimensions have negative impact in terms of portability and practicality of the device. Filling and emptying a device with volumes higher than seven litres in a hospital environment might be impractical. Since blood mimicking fluids (BMF) typically used in Ultrasound imaging have a commercial price of *~500 GBP per litre*, a large volume has implication in terms of costs of the experiments. Clearly, a compact design is easier to transport, pack, deliver, etc.

In order to support reproducible positioning in comparative studies between different techniques, several reference position markers and a ruler have been engraved into the tank surfaces. A threaded hole for a compatible drain cap has been cut to facilitate emptying. The CAD drawing of the water-proof tank ("Imaging Tank") is shown in Figure 4.3. Dimensions, indicated in Figure 4.2 and Figure 4.3, have tolerances of +/- 0.25 mm. Wall thicknesses are 10 mm with production tolerance of +/- 10 % plus additional 0.4 mm, in agreement with the ISO 7823-1:2003 (ISO 7823-1:2003).

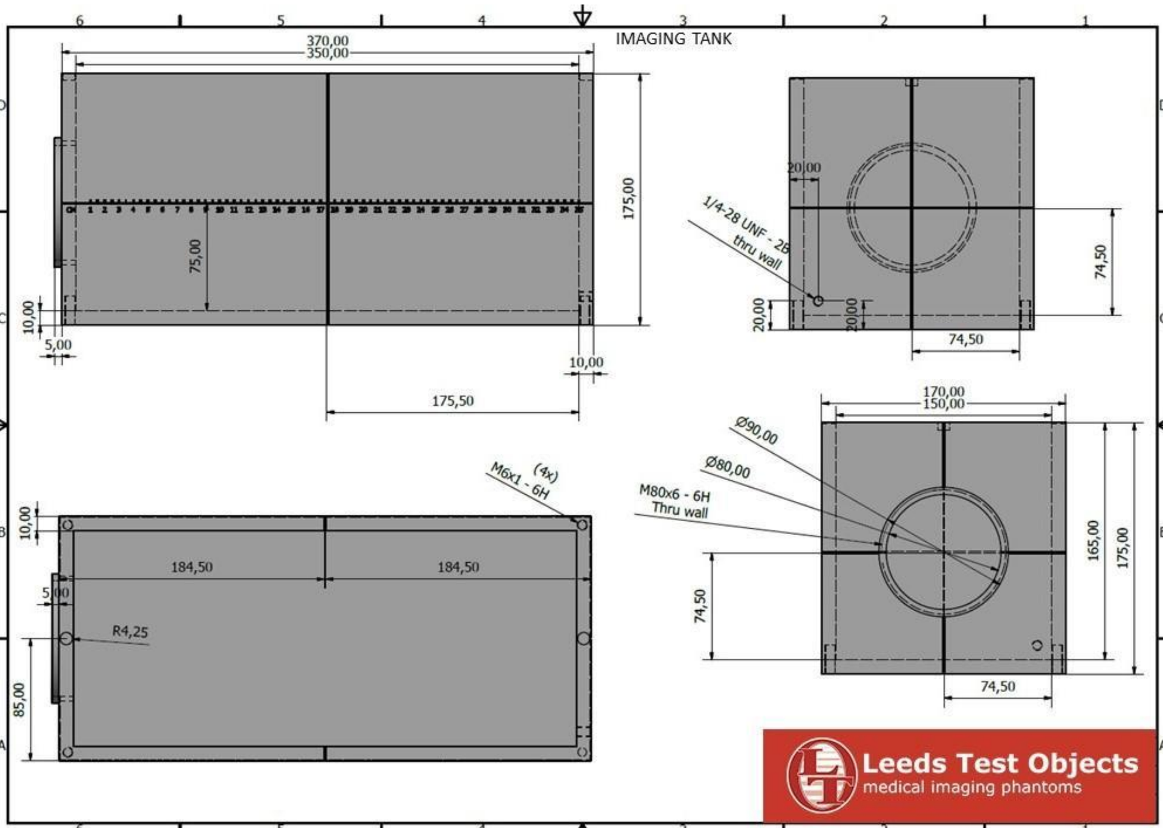

Figure 4.3: CAD drawing - Vortex Ring based Complex Flow Phantom – Water-tight Imaging Tank.
Figure 1: Ambrogio, S., Walker, A., Narracott, A., Ferrari, S., Verma, P. and Fenner, J. (2019). A complex flow phantom for medical imaging: ring vortex phantom design and technical specification. Jorunal of Medical Engineering and Technology, 43(3):190-201.

4.4.3 Design – Piston/Cylinder System

The generation of vortex rings requires a system able to thrust a volume of fluid through an orifice or a nozzle. A simple mechanism is a piston/cylinder assembly with a smaller orifice at the output face. The cylindrical channel was manufactured from frosted PMMA (Perspex). The "Cylinder", as named in Figure 4.4, has an internal diameter of 70 +/- 0.25 mm and 10 mm wall thickness (production tolerance of +/- 10 % plus additional 0.4 mm; ISO 7823-1:2003). One open-end of the cylindrical chamber is threaded and it supports a water-proof screw coupling to accommodate interchangeable orifices and the water-tight imaging tank. The other side is also threaded and is coupled with a compatible threaded cap. A square hole is cut in the threaded cap with dimensions compatible with the piston stem. The square shape acts as a guide for the piston. It impedes undesired movements during the dynamic piston action. The threaded cap, named "Piston Guide", is shown in Figure 4.4. Four interchangeable screw-in orifices are provided with the prototype. Orifice diameter dimensions, which range from 10 +/- 0.25 mm to 25 +/- 0.25 mm, have been selected to generate vortex rings with dimensions comparable to physiological conditions (Figure 4.5). Different diameters or shapes can be manufactured on request. The plunger has been manufactured from white PMMA and contains a hollow stem that travels along the rotating lead screw of an external linear stepper motor. Piston stem and stepper motor screw are coupled through a threaded nut. The nut transforms the rotating action of the motor to linear piston displacement. The plunger cap (front-end largest part) includes a groove that accepts a nitrile rubber O-ring. The O-ring provides a piston/cylinder water-tight seal. However, nitrile rubber is not ideal in terms of the coefficient of friction when it is in contact with PMMA (Perspex). Petroleum jelly (Vaseline) is typically used as a lubricant to reduce frictional forces. Different materials and piston designs have been investigated and are described in the following thesis sections (Sections 6.3.1, 6.3.2 and 6.3.3, Chapter 6). The CAD drawings of the piston cylinder system, which refers to "Cylinder, "Piston Guide" and "Plunger", are provided in Figure 4.4. CAD drawings of the orifices provided with the prototype, named "Interchangeable Output Orifices", are shown in Figure 4.5.

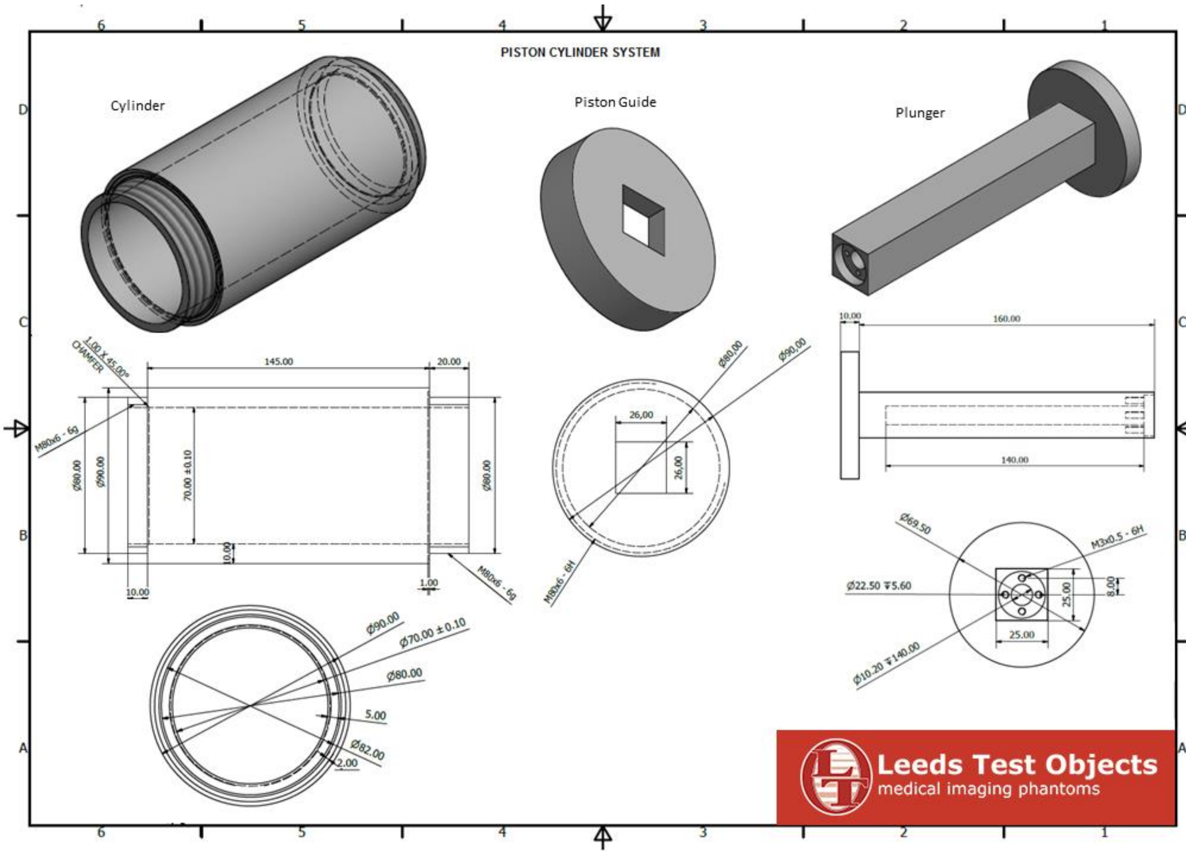

Figure 4.4: CAD drawing - Vortex Ring based Complex Flow Phantom – Piston cylinder system.
Figure 2: Ambrogio, S., Walker, A., Narracott, A., Ferrari, S., Verma, P. and Fenner, J. (2019). A complex flow phantom for medical imaging: ring vortex phantom design and technical specification. Jorunal of Medical Engineering and Technology, 43(3):190-201.

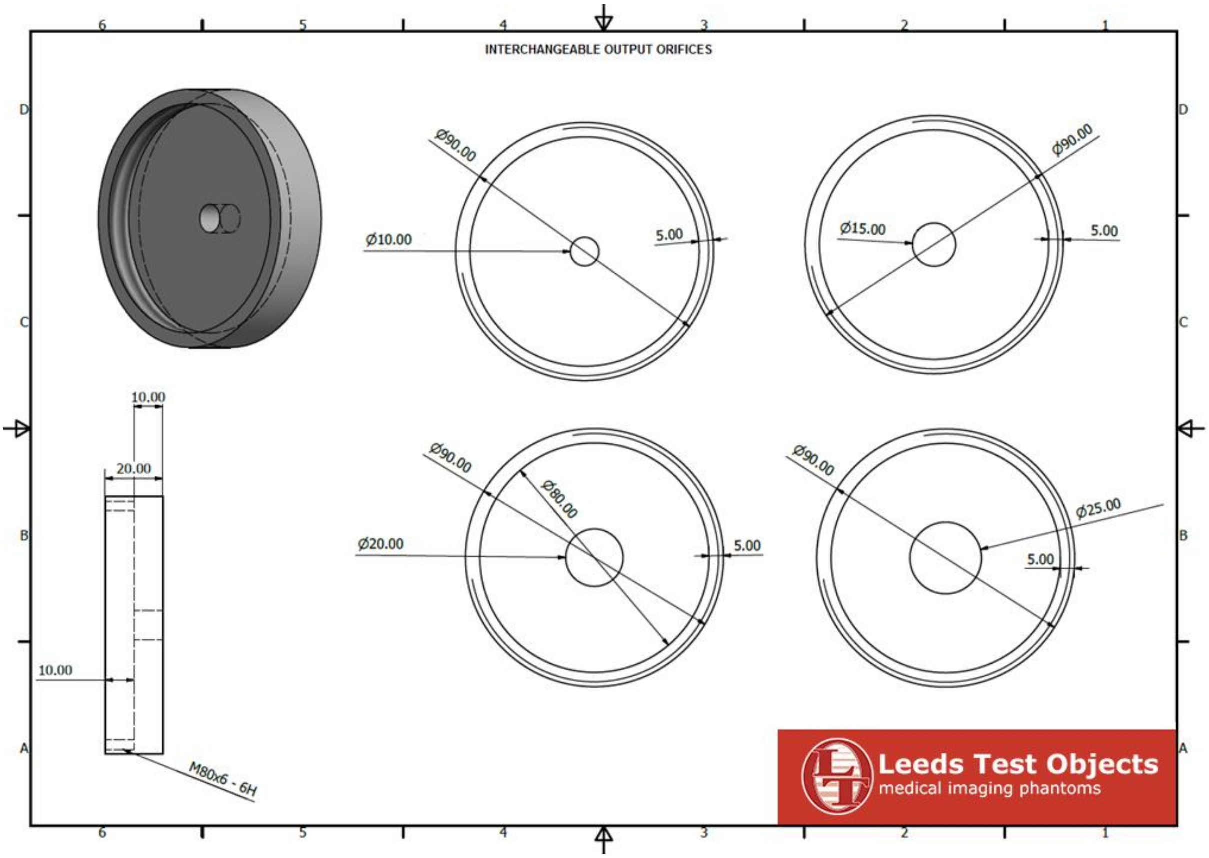

Figure 4.5: CAD drawing - Vortex Ring based Complex Flow Phantom – Interchangeable Output Orifices. Figure 3: Ambrogio, S., Walker, A., Narracott, A., Ferrari, S., Verma, P. and Fenner, J. (2019). A complex flow phantom for medical imaging: ring vortex phantom design and technical specification. Jorunal of Medical Engineering and Technology, 43(3):190-201.

4.4.4 Design – Programmable Actuator System

The piston and the external linear stepper motor actuator are coupled with a nut/lead screw arrangement that transforms rotation into linear motion. This assembly is driven by the programmable actuator system of the phantom. The external linear stepper motor is a Nema 23, 1.8 degrees, 36 V, 3 A (Nema 23 external linear actuator, OMC Corporation Limited, Nanjing, China). The Nema 23 drives the piston over a threaded screw of 150 mm in length. The stepper motor is fixed on a compatible mounting bracket that screws into a PMMA (Perspex) block. The PMMA block is glued into the PMMA base and guarantees alignment between the motor and the piston cylinder system. The piston/cylinder alignment is crucial for smooth effort. Free movement is essential to accurately and reproducibly translates motor rotation to linear piston movement (to warrant comparable piston displacements independently from the piston position). The CAD drawing of the PMMA base, named "Stepper Motor Base", is shown in Figure 4.6. The "Stepper Motor Base" is coupled with the "Imaging Tank Base" through a PMMA hinge. The hinge guarantees a rigid connection when the phantom is in operation and also allows folding of the system for easier transportation. The PMMA hinge is consistent with future adaptation of the design for Magnetic Resonance Imaging. Like the "Imaging Tank Base", the "Stepper Motor Base" has four threaded holes for additional screw-able feet.

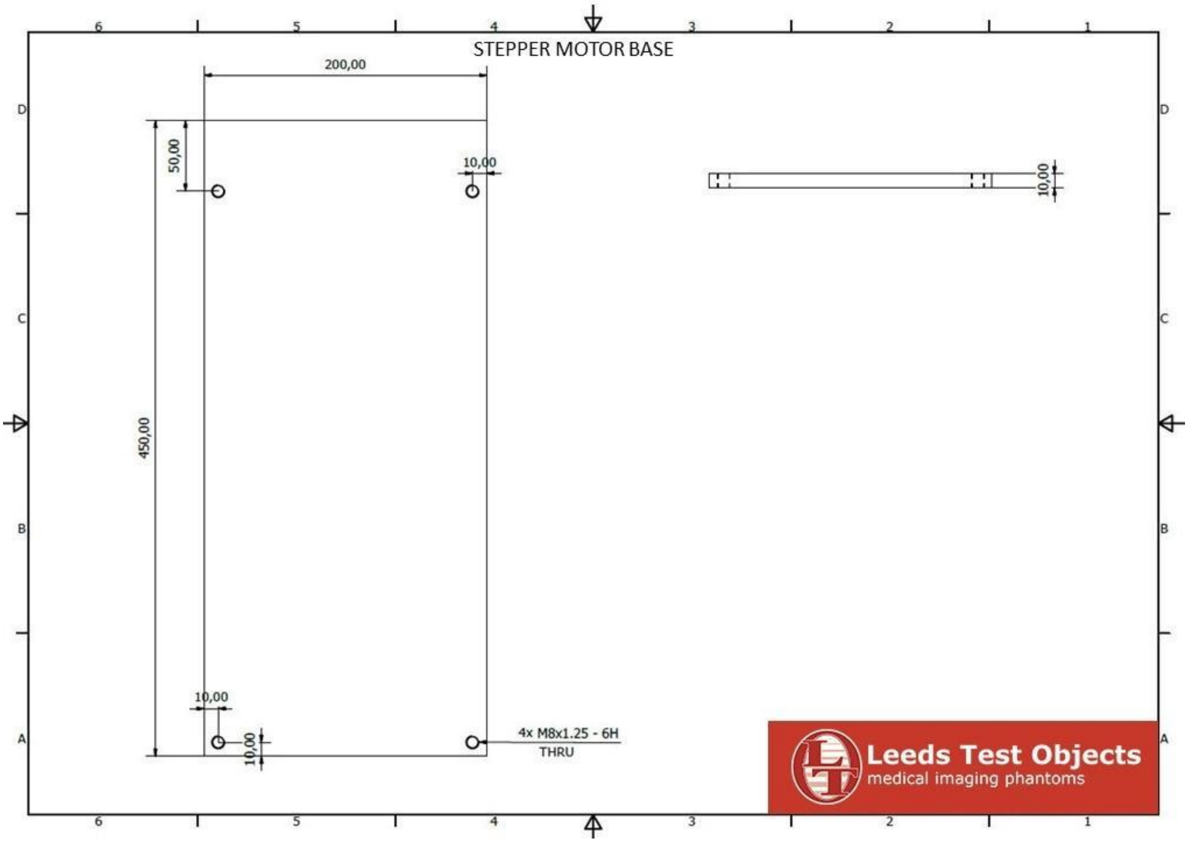

Figure 4.6: CAD drawing - Vortex Ring based Complex Flow Phantom – Interchangeable Output Orifices.

The stepper motor is bipolar, relying on two leads for each set of phase coils, neither of which is connected to ground. Typically, a cylindrical permanent magnet is attached to a rotor. The rotor is surrounded by toothed electromagnets that constitute the stationary magnetic field (stator). The electromagnets are divided into groups (phases) and these usually follow an alternating arrangement (i.e. A-, B-, A+, B+). The phase coils (A+, A-, B+, B-) are connected to a digital stepper driver DM542 (Leadshine, DM542, OMC Corporation Limited, Nanjing, China). The internal components of the stepper motor are illustrated in Figure 4.7.

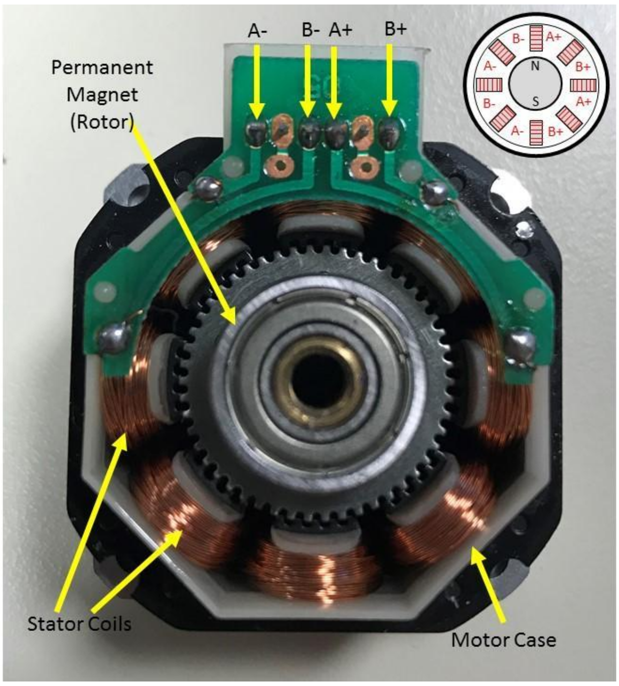

Figure 4.7: Internal components of a stepper motor.

The DM542 is connected to a compatible switching power supply 150 W, 36 V, 4.17 A (OMC Corporation Limited, Nanjing, China) (High Voltage Pins – V (+) and GND, Figure 4.8) and to the I/O digital pins of an Arduino Uno board (Arduino, still unclear who is the Owner). Three different digital pins D9, D10 and D11, are used as outputs to set the motor steps, to set the rotating direction and to enable the motor, respectively. Digital pin D7 is connected to a push button which is used to activate/run the motor/piston displacement program. The DM542 limits the current supplied to the motor to 2.69 A (RMS current) to avoid overheating. The Arduino Uno board logic is based on the Atmega328P (Atmel Corporation, San Jose, California, USA) microcontroller. The Atmega328P is a low-power, high performance AVR® 8-bit microcontroller. The unit is programmable through simple USB connection to a computer and dedicated open source Arduino Software (IDE). Typically, a stepper motor is programmed through a square wave signal that alternates the polarities of the phase coils (A+, A-, B+, B-) between (+) and (-). The central permanent magnet of the motor (rotor) moves in discrete steps, as commanded by the digital signal, and generates torque (Figure 4.7). The total cost of all the components forming the programmable actuator system was less than one hundred Euros at the time of writing (2018). A diagram illustrating Arduino Uno, push button, driver DM542, stepper motor and power supply connections is shown in Figure 4.8.

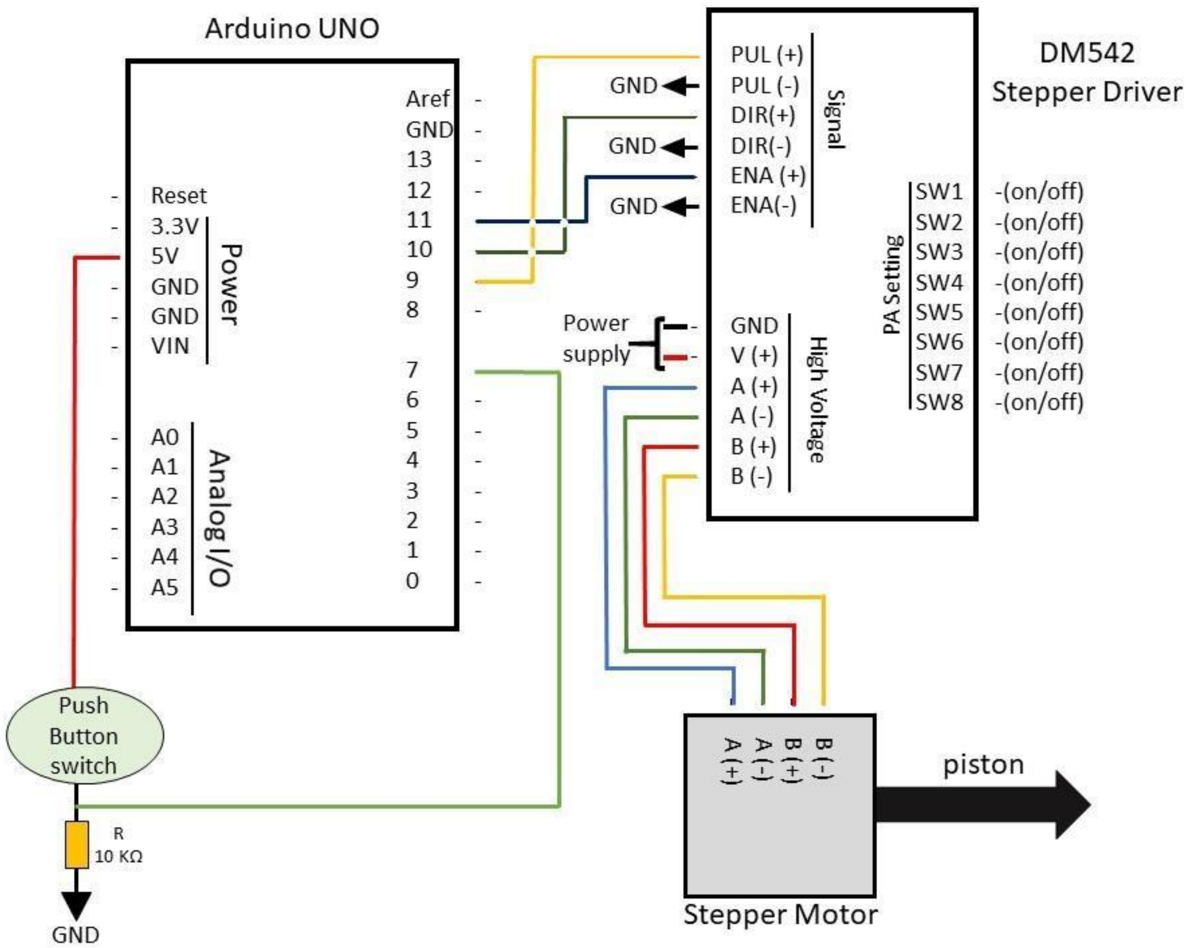

Figure 4.8: Arduino Uno board, push button switch, stepper driver DM542, stepper motor and power supply connections.

4.4.5 Design – Stepper Motor Programming

One of the simplest ways to drive a stepper motor is by providing a digital square wave signal. The Atmega328P microcontroller embedded into the Arduino Uno board is programmed to generate a digital square wave signal with 50 % duty cycle in CMOS logic 0-5 V. The number of pulses of the square wave signal determines the number of motor steps, thus the piston displacement. The frequency of the square wave signal determines at what rate the polarities of the face coils are alternated, thus it controls piston speed. By simply changing the number of pulses and the pulse width of a square wave signal it is possible to control the rotation of the actuator and, consequently, the piston displacement/velocity profiles. A square wave signal can be easily created with a *for* loop on the dedicated Arduino Software (IDE). A flow chart of the Arduino code for programming the motor is depicted in Figure 4.9 and a snapshot of the main part of the code is shown in Figure 4.10 (the whole code is reported in Appendix 1).

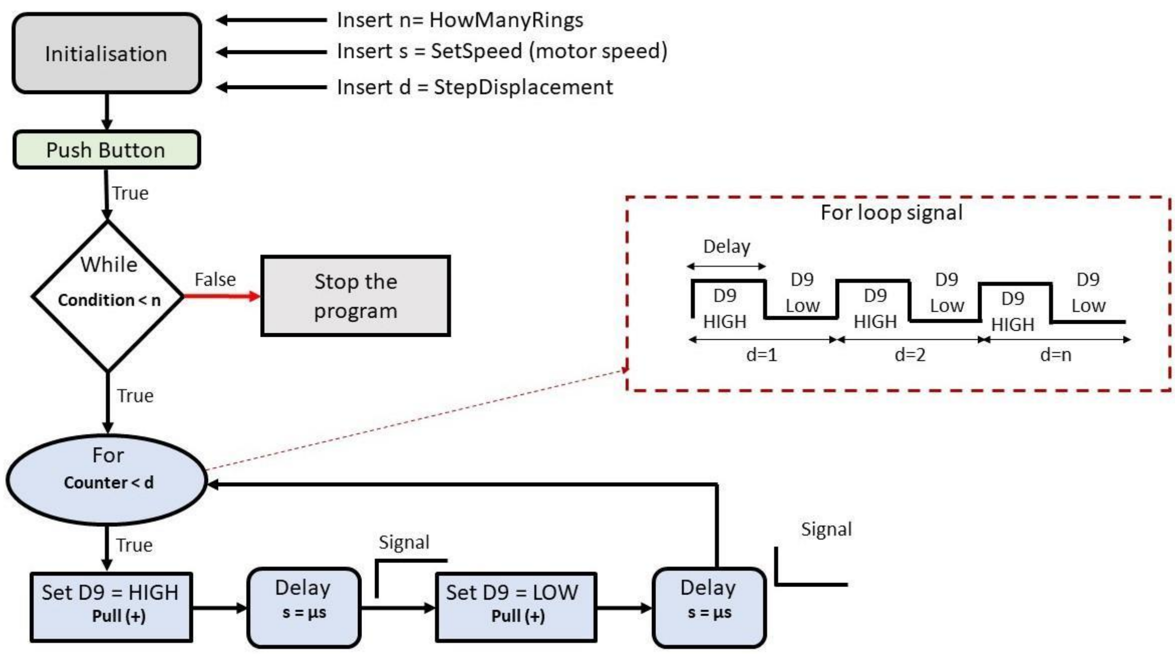

Figure 4.9: flow chart of the generating code for stepper motor programming.

```
void loop() {
     buttonState = digitalRead(buttonPin);
     if (buttonState == HIGH){
          delay(5000);
         while (revolution < HowManyRings) {
    for (int i = 0; i <=  StepDisplacement; i++) {
      digitalWrite(pulPin, HIGH);
      delayMicroseconds (SetSpeed);
      digitalWrite(pulPin, LOW);
      delayMicroseconds(SetSpeed);
    }
// in case of overheating, disable and enable the motor
  digitalWrite(enblPin, HIGH);
  delay (8000);
  digitalWrite(enblPin, LOW);
  delayMicroseconds(6);
    digitalWrite(dirPin, HIGH); // High --> piston forward =, LOW--> piston backward
  delayMicroseconds(6);
  digitalWrite(pulPin, LOW);
  delay (2000);
     //   delay(10000);
    revolution++;
  }
     }
```

Figure 4.10: Vortex Ring based Complex Flow Phantom – Snapshot of the Arduino code that generates a ring.

The first part of the programme is dedicated to initialisation of the variables. A push button is used to run the program and to trigger the piston displacement. The digital I/O pin D5 is set to provide a digital *trigger* signal (“*triggerpin”*) for potential synchronisation with external measurement methods. A *while* loop is used to program “how many consecutive vortex rings” the user wants to generate. A *for* loop is used to generate the square wave signal that controls the piston velocity/displacement profile (Figure 4.9). Digital pins *enblPin*, *dirPin* and *pulPin* control the enabling/disabling of the motor, the motor direction and motor input signal, respectively. These signals must be controlled in a predefined order and with predefined delays, as indicated from the DM542 datasheet. The current flows through the winding coils of the motor both when the rotor is enabled and when it is stationary. The motor holds the load in place, which is particularly useful for vertical or leaning applications. Since the piston is in horizontal position during the phantom applications, there is no need to hold the load. Keeping the motor enabled during inactivity increases the chance of overheating. Therefore, the enabling signal is switched on/off between each vortex ring generation. In the example in Figure 4.10, a 20 seconds delay (*delay(18000)*, in milliseconds, plus a *delay(2000),* in milliseconds, between motor activation and vortex ring production) has been chosen between each vortex ring generation. A limit of 15 seconds delay is effective for prolonged experiments with the phantom. Design improvements and an instrumentation pack, for evaluating design performances, are described in Chapter 6. Particularly, the instrumentation pack clarifies if the motor can be used at reduced power without affecting the vortex ring generation. This may be extremely advantageous for preventing the motor from overheating during prolonged application. Experimental studies with the instrumentation pack are described in detail in Chapter 7.

4.4.6 Design – Assembled System

A block diagram of the Vortex Ring based Complex Flow Phantom is depicted in Figure 4.11.

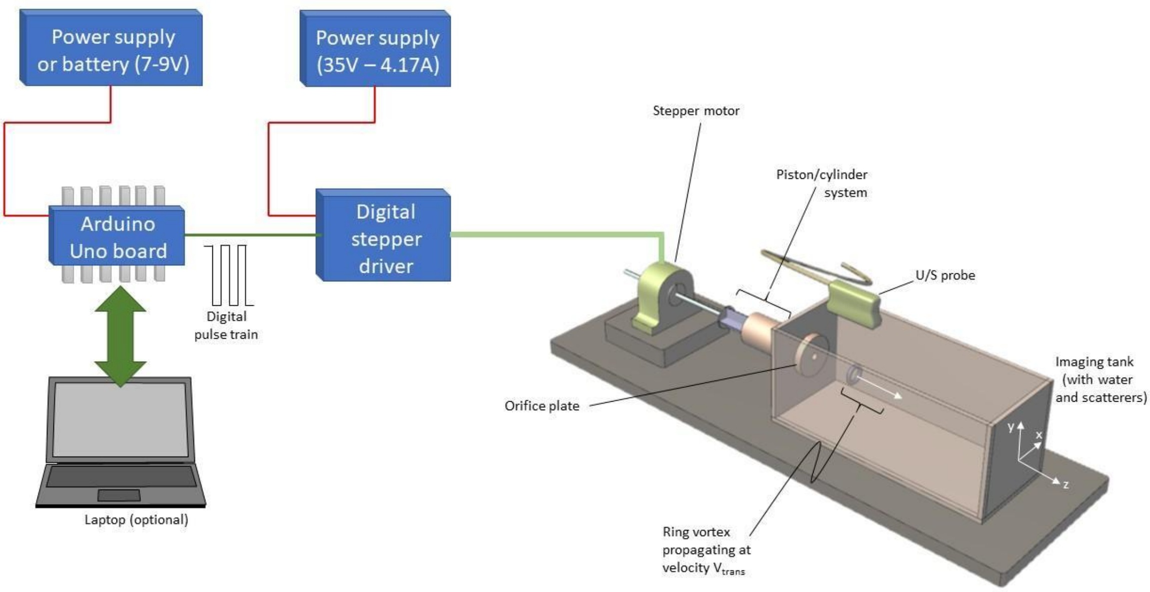

Figure 4.11: Vortex Ring based Complex Flow Phantom – Schematic block diagram of the system. Please note that this is a schematic representation and elements are not to scale.
Figure 4a: Ambrogio, S., Walker, A., Narracott, A., Ferrari, S., Verma, P. and Fenner, J. (2019). A complex flow phantom for medical imaging: ring vortex phantom design and technical specification. Jorunal of Medical Engineering and Technology, 43(3):190-201.

Assembling all the components described from sections 4.4.2 to 4.4.4 provides the system illustrated in Figure 4.12

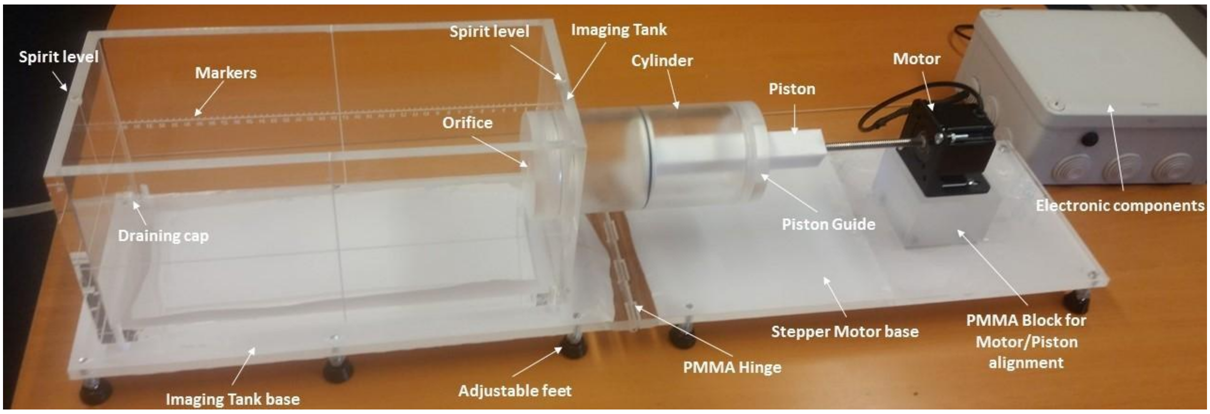

Figure 4.12: Vortex Ring based Complex Flow Phantom – Assembled System.
Figure 4b: Ambrogio, S., Walker, A., Narracott, A., Ferrari, S., Verma, P. and Fenner, J. (2019). A complex flow phantom for medical imaging: ring vortex phantom design and technical specification. Jorunal of Medical Engineering and Technology, 43(3):190-201.

The electronic components illustrated in Figure 4.8 are placed and secured into a water and impact proof junction box manufactured by Schneider Electric (RS Components Ltd, Corby, UK, Stock No. 151-791). The power supply, also positioned within the electric safety box, is connected to the main socket (230V, 50 Hz) through a standard UK three-pin type G plug and a residual-current device (RCD) socket. The RCD socket is a life-saving device that quickly breaks the electrical circuit if there any leakage current is present. Since the system operates in water proximity, it is strongly suggested that connection of the phantom to the mains plug (230V, 50 Hz) occurs through RCD socket for extra safety. If the device is meant to be commercialised, it is recommended (but not compulsory) that it complies with the Low Voltage Directive (LVD - 2014/35/EU) and that it undergoes electromagnetic compatibility (EMC) and electromagnetic interference (EMI) testing. The LVD ensures high level of protections for electrical equipment between 50 and 1000 V while the electromagnetic compatibility assures that the system does not introduce intolerable electromagnetic disturbances to anything in the environment. All the single electric components (stepper motor, Arduino Uno, Stepper Driver, power supply) are RoHS, CE and FCC marked, therefore they have already undergone electrical safety testing. However, the interconnection of the components create a new electrical system, which may not comply with LVD or EMC testing.

As described in detail in sections 4.4.4 and 4.4.5, the stepper motor is connected to the piston and is programmed through the Arduino Board to deliver a pre-configured piston displacement/velocity profile. The piston moves within the cylinder chamber and propels a known volume of fluid through the orifice (i.e. 3 cm^3 in 50 ms). The outcome is the generation of a controlled, propagating vortex ring, that travels with self-induced velocity (velocities up to 1 ms^{-1}) along the whole length of the tank (Figure 4.13). A blue food dye colourant was used for vortex calibration and a ratchet strap was used to minimise vibration errors during the piston action in reproducibility studies (Figure 4.13). By changing orifice diameter or piston displacement/velocity profile, the *L/D* ratio of Gharib's formula ("formation time", Section 2.4, Chapter 2) can be modified on demand, producing vortex rings with different characteristics. Travelling vortex rings can be imaged, for instance, with an Ultrasound transducer placed at the free water interface (Figure 4.11). As mentioned before, the system is fully transparent to aid measurements. Ring vortex features can be captured with different imaging methods such as Laser Particle Imaging Velocimetry (Laser PIV) or optical/video cameras.

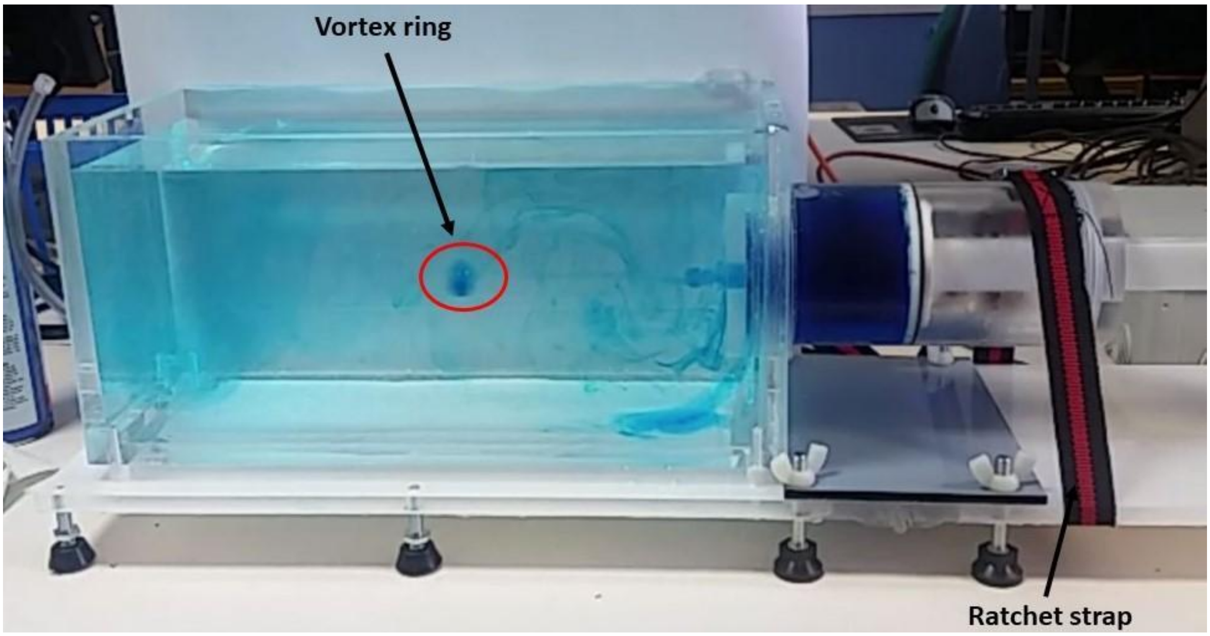

Figure 4.13: Vortex Ring based Complex Flow Phantom – Assembled System with blue dye to visualise the ring.

4.5 Discussion

The vortex ring characteristics (physiological relevance, stability, controllability, predictability and reproducibility) make our proposed design of phantom a good candidate for the development of a complex flow phantom for medical imaging (described in Chapter 2 and Chapter 3). A Vortex Ring Based Complex Flow Phantom prototype has been built and technical drawings are provided. The system relies on the action of a ~100 W stepper motor connected to a piston cylinder system and a water tank for vortex ring formation and propagation. As described in Sections 2.4 (Chapter 2), vortex ring generation depends mainly on a non-dimensional parameter described as "formation time" or "formation number" (Garib et al 1998). For a defined orifice-output geometry, the formation time can be described as $T^* = (\bar{U}/D)T_p$ where $\bar{U}$ is the average velocity of the piston, D is the orifice-output diameter and T_p is the duration of the piston impulse. Assuming to work always in water (or equivalent fluid vastly composed by water), the piston velocity profile (piston velocity and piston displacement in unit of time) and the orifice-output diameter also determine the Reynolds number. The prototype is provided with pre-programmed modes but the Arduino Board is essentially open-source. Any software code can be uploaded with a computer through the USB connection (Type A male to Type B male) and Arduino Software (IDE), to produce different flows. Alternatively, the pre-set parameters, described in the script in Figure 4.10, can be modified to change the piston velocity profile. The device offers great flexibility and allows the user to vary independently each element of Gharib's formula for experimental studies. By simply altering the frequency of the square wave signal (stepper motor speed, $\bar{U}$ in Gharib's formula), the number of pulses of the square wave signal (stepper motor displacement extent, T_p in Gharib's formula) or the orifice-output diameter size, vortex rings with different Reynolds numbers, different diameters, velocities, volumes and different core thicknesses can be generated on demand.

The prototype has been described in detail and needs to be validated through experimental measurements to prove its credibility. Considering the inconsistencies between experimental and CFD simulation (described in Chapter 3), two different methods, namely optical/video and Laser PIV technique, are considered for quantifying the vortex ring behaviour under a number of generating conditions. Ultrasound compatibility will also be demonstrated. Experimental measurements are described in the next chapter. Technical drawing and software source code were also provided, consequently, phantom and experiments can be replicated in any laboratory. The test object design is novel, simple and cost-effective, and requires less than thirty minutes for set-up. Flow phantoms offer parabolic flow and a limited range of vessel diameters. In order to make these test objects portable, vessel inlet length is often reduced, which limits the range of velocities in which the flow is laminar (Appendix 2). Cavitation in the pump head in many systems produces air bubbles even at low velocities (~60-70 cm/s), distorting the Doppler spectrum. When not in use, blood mimicking fluid scatterer particles tend to settle in the reservoir. Bubbles cannot be easily removed and scattering particles are difficult to mix in a closed commercial system, where there is no access to the reservoir. Finally, previously developed ultrasound flow phantoms are typically not transparent, which makes it difficult to cross validate results or verify performance using other measurement methods. No tolerances on flow velocities are usually specified, and the pump is expected to behave in the same way for the whole phantom life (typically, warranty is 10+ years). The string phantom, which is commercially produced only by CIRS (CIRS Inc., Norfolk, USA), relies on the movement of a silk filament to produce the backscatter signal. However, the silk filament entraps air bubbles and the motor vibration at certain velocities affects the Doppler measurement accuracy (Browne, 2014). The vortex ring phantom overcomes commercial phantom limitations: it offers a range of translational velocities between 7 and 90 cm/s; interchangeable orifices with any diameter can be produced on demand; scatterer particles can be mixed and air bubbles can be manually removed. Similar to the string phantom, it operates in free field (water or blood mimicking fluid) and do not provide acoustic attenuation comparable to soft tissues. However, tissue mimicking materials with different geometries can be embedded into the water tank. Differently from existing commercial systems, the complex flow phantom is open source and offers flexibility for both clinical measurements and research studies.

4.6 Conclusion

Technical drawings and specifications have been provided for the construction of a novel, cost-effective, portable, robust and multimodal (in flow features) Vortex Ring based Complex Flow Phantom. The system is designed with pre-programmed user-friendly modes but it is essentially fully programmable, allowing great flexibility. Chosen materials are non-hazardous, of good quality and optically transparent to allow comparative studies with optical techniques for testing. Electric safety regulations have been discussed and precautions have been taken for secure use of the device. The system is tested through optical/video, Laser PIV and ultrasound techniques. Details are provided in the next chapter.

CHAPTER 5

Vortex Ring based Complex Flow Phantom for Doppler Ultrasound –Testing and Validation

5.1 Introduction

A vortex ring based complex flow phantom design with technical specifications was provided in Chapter 4. Credibility of the system needs to be assessed through experimental studies. Three identical phantom prototypes were manufactured by Leeds Test Objects Ltd (Leeds Test Objects Ltd, Boroughbridge, United Kingdom), as a beneficiary partner of the VPH-CaSE consortium (http://www.vph-case.eu/) within the European Union's Horizon 2020 research and innovation programme (Marie Skłodowska-Curie grant agreement No 642612). Optical/video camera, Laser PIV measurements were undertaken on the different systems, in two different premises, on two different days, and results were compared. Conventional ultrasound techniques (B-Mode, Colour Doppler, PW Spectral Doppler) were also performed on a phantom prototype. The third prototype was provided to the CREATIS consortium (CNRS UMR 5220 - INSERM U1206 – Universite' de Lyon 1 – INSA Lyon – Universite' Jean Monnet Saint-Etienne) for the application of high frame rate ultrasound Vector Flow Imaging techniques. CREATIS consortium is also a beneficiary partner of the VPH-CaSE training network programme.

All the measurement techniques were performed independently and results were cross checked to confirm the rigour of the methods. A flow chart depicting manufactured prototypes and different measurement approaches performed is depicted in Figure 5.1.

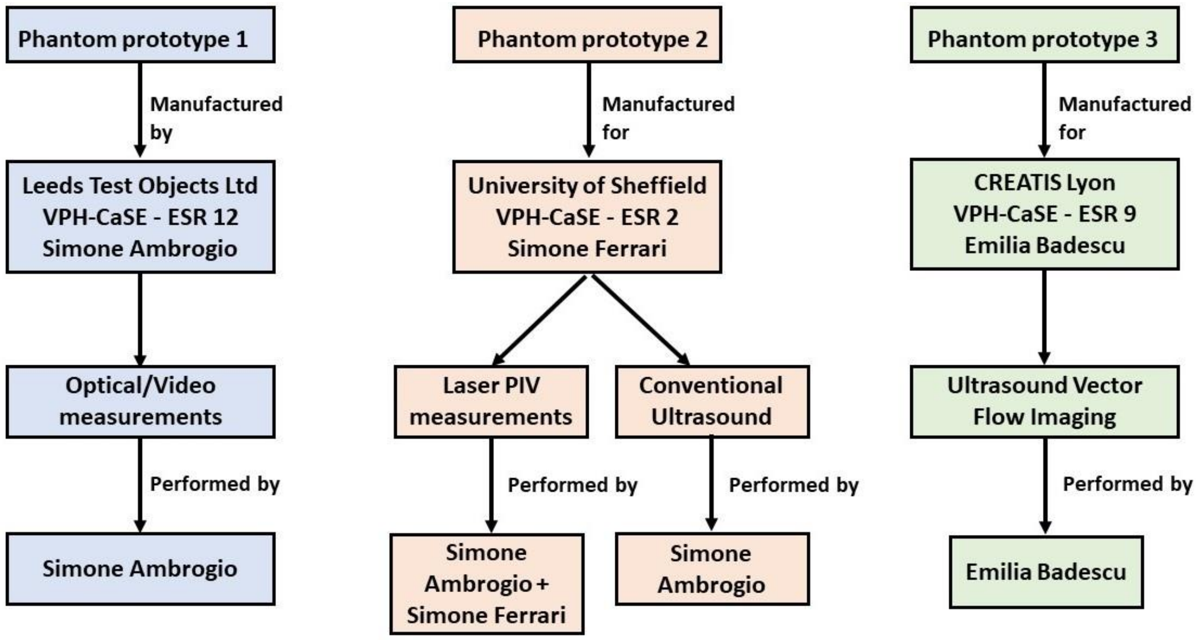

Figure 5.1: Phantom prototypes manufactured by Leeds Test Objects Ltd and measurement method performed.

Optical/video and Laser PIV methods and results of this chapter are supported by the publication of a journal article (Ambrogio et al 2019). Ultrasound results have also been presented with a poster at "The 50th Annual Scientific Meeting of the British Medical Ultrasound Society" (BMUS, Manchester, United Kingdom, 4-6 of December 2018) (Appendix 3). The poster was awarded the "Best Scientific Poster Prize 2018". Ultrasound Vector Flow Imaging results have been published by Badescu et al (2018).

5.2 Optical/Video vs Laser PIV acquisitions

5.2.1 Introduction

Optical/video and Laser PIV measurements have the aim of demonstrating the reproducibility, stability and reliability of the system. These measurements were performed under a combination of motor configurations and orifice sizes, to demonstrate the phantoms functionality. All the configurations tested are listed in Table 5.1. As depicted in Figure 5.1, optical/video measurements were performed at Leeds Test Object Ltd (Leeds Test Objects Ltd, Boroughbridge, United Kingdom) following the methods described in sections 3.2.3 and 3.3.3 (Chapter 3). Independently, Laser PIV measurements were carried out with a calibrated LaVision PIV system (LaVision GmbH, Gottigen, Germany) at the "Department of Cardiovascular Science" of the University of Sheffield (Royal Hallamshire Hospital, Sheffield, United Kingdom). Laser PIV has become an established technique for quantitative assessment of complex flow velocity fields (Grant 1997; Westerweel et al 2013). Health and safety regulations and experimental set-up to perform accurate Laser PIV measurements require domain expertise. Therefore, Laser PIV measurements were performed under the supervision of a LaVisionUK Ltd (LaVisionUK Ltd, Bicester, United Kingdom) application consultant. Two cameras, calibrated following the method described by Wieneke (2005), were used to obtain stereoscopic view. Optical/video and Laser PIV measurements were carried out for all the orifice diameter sizes manufactured for the phantom prototypes (Figure 4.5). For both optical/video and Laser PIV methods, the system (imaging tank and piston/cylinder system) was filled with water. A main piston displacement of 0.8 +/- 0.04 mm and two main piston speeds, 2 +/- 0.1 cm/s and 1.33 +/- 0.06 cm/s, were programmed for these experiments. The piston displacement of 0.8 +/- 0.04 mm was selected because this produced particularly stable vortex rings. However, a further piston displacement of 0.6 +/- 0.03 mm was tested to prove extended operation. The piston speed of 2 cm/s was of interest because it pushes the motor close to its maximum obtainable speed. Piston speed of 1.33 +/- 0.06 cm/s and a further speed of 1 cm/s were also tested. Finally, Configuration 3 (Table 5.1) was tested at the beginning (morning) and at the end of an arduous experimental session. Results were compared to verify the consistency of the phantom and of the measurement method over prolonged experimental periods. Reynolds number and formation time (*L/D*) calculations are based on the cylinder chamber diameter, orifice diameter and average piston velocity.

Configuration	*Orifice Diameter (mm)*	*Piston Speed (cm/s)*	*Piston Displacement (mm)*	*Reynolds number*	*L / D ratio*	*Number of Runs*
1	10	2	0.8	9800	3.92	10
2	10	1.33	0.8	6517	3.92	10
3	15	2	0.8	6534	1.16	10
4	15	2	0.6	6534	0.87	10
5	15	1.33	0.8	4345	1.16	10
6	15	1	0.8	3267	1.16	10
7	20	2	0.8	4900	0.49	10
8	20	1.33	0.8	3258	0.49	10
9	25	2	0.8	3920	0.25	10
10	25	1.33	0.8	2606	0.25	10

Table 5.1: summary of the experimental configuration tested.

5.2.2 Method – Optical/Video Acquisitions

Optical/video acquisitions required visible contrast between the vortex ring and the fluid of the imaging tank. The system was entirely filled with water, an interchangeable orifice was selected and screwed into the cylinder. A few drops of food dye colouring were mixed with the volume of water in the cylinder chamber to produce visible vortex rings. A video camera Sony HDR-PJ220E (Sony Corporation, Tokyo, Japan) was fixed on a tripod and placed at a distance of 3.8 m from the imaging tank. The camera telephoto lens was selected at 32x extended zoom, to ensure a focused view of the travelling vortex rings. The camera was placed at the maximum achievable distance that permitted a clear view of the vortex ring propagation in a selected region of interest for the measurements. This camera configuration (maximum distance and maximum extended zoom) minimises perspective errors in measurements. The camera records video images at 25 frames per seconds. The field of view was focused around a region of 10 cm near the orifice. Vortex rings travelling from the 5th ("Imaging Tank" reference markers, Figure 4.3, Chapter 4) to the 15th centimetre mark were distinctly imaged. This region of interest was chosen for both optical/video and Laser PIV measurement methods. In order to support the measurements with visible timing data, a 1/100 seconds universal digital counter-timer (Stock No 612-445, RS Components Ltd, Northants, United Kingdom) was placed within the field of view of the camera. In addition to the engraved reference markers ("Imaging Tank" reference markers, Figure 4.3, Chapter 4, Chapter 4), further reference markers were painted in red colour on the opposite wall of the imaging tank. These reference markers supported pixel digital measurements and provided information on vortex ring translational displacement. Video camera framerate and the timer counter provided timing data. Combining the information, vortex ring translational velocities were estimated measuring the displacement along the X-axis (Figure 5.2 and Figure 5.3) in consecutive frames. Average translational velocities and standard deviation values (represented as error bars, +/- 1SD) were calculated as a function of vortex ring position in the tank ("Imaging Tank" reference markers, Figure 4.3, Chapter 4) from the acquisition of ten consecutive vortex rings, generated for each configuration listed in Table 5.1. A block diagram of the experimental set up is shown in Figure 5.2. For improved clarification, a schematic diagram depicting the layers of circulating flow constituting vortex ring toroidal core and translational velocity (V_{trans}) is shown in Figure 5.3.

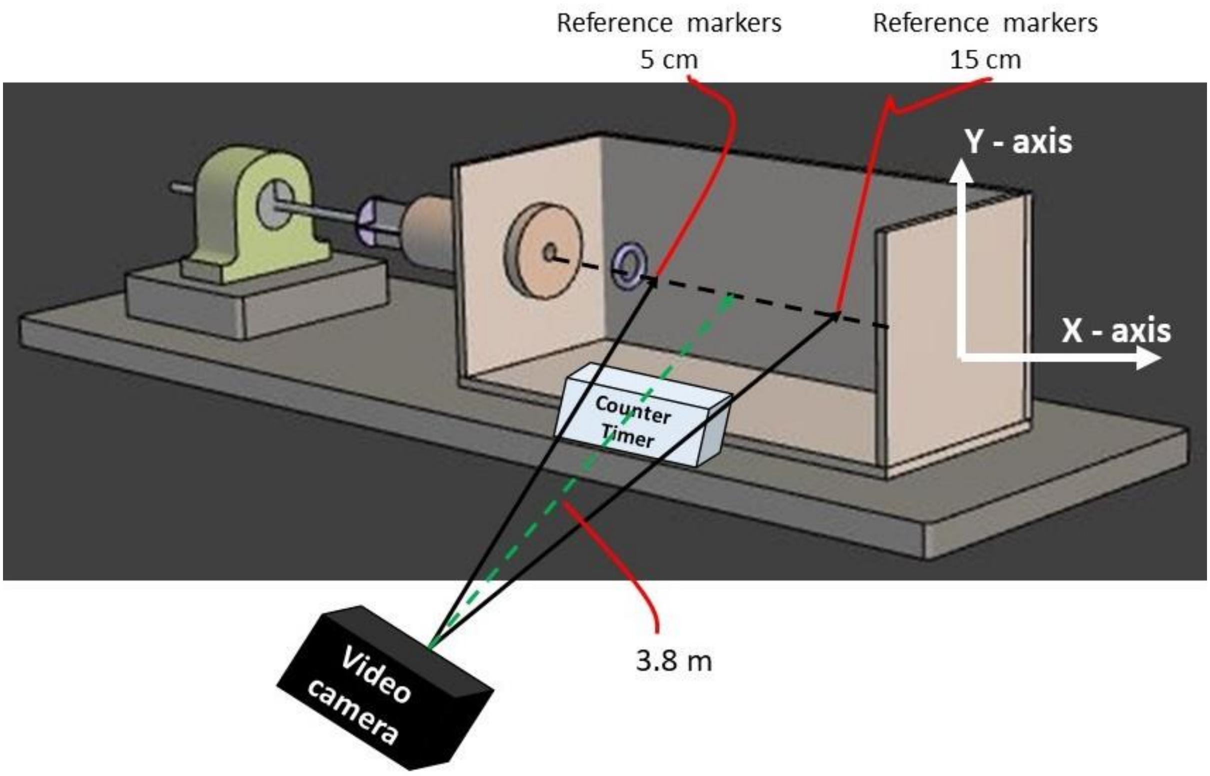

Figure 5.2: Optical/video measurements – schematic diagram of the experimental set up. Please note that this is a schematic representation and elements are not to scale.

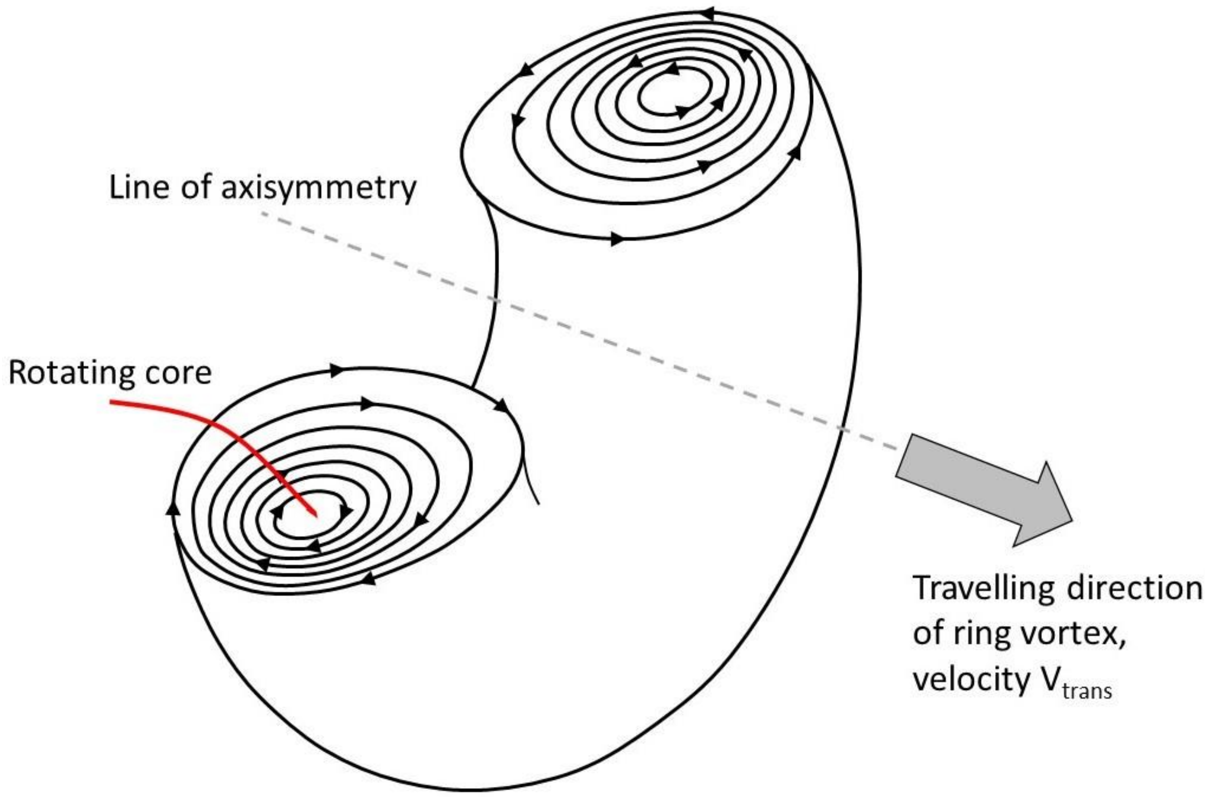

Figure 5.3: Layers of concentric circulating flow constituting the toroidal core, propel the ring vortex forward along its axis of symmetry at velocity V_{trans}.
Figure 4: Ambrogio, S., Walker, A., Narracott, A., Ferrari, S., Verma, P. and Fenner, J. (2019). A complex flow phantom for medical imaging: ring vortex phantom design and technical specification. Jorunal of Medical Engineering and Technology, 43(3):190-201.

5.2.3 Method – Laser PIV Acquisitions

Laser Particle Imaging Velocimetry (Laser PIV) is an experimental flow visualisation technique that involves capturing sequential camera exposures of Laser illuminated particles in a region of interest. The Laser PIV experimental set-up requires neutrally buoyant light scattering particles mixed with a volume of water in the tank-cylinder system. Typically, the particle concentration, the particle density and the particle size are chosen to not affect the fluid dynamics. Ideally, the particle motion should not affect the ambient fluid flow. Consequently, a small concentration (~ 10 g) of nylon particles of size 10-20 micron were mixed within the volume of water (~8 L). The imaging tank was placed on a table and a double pulse Nd:YAG Laser (LaVisionUK Ltd, Bicester, United Kingdom) was placed below. The Laser sheet cut the travelling vortex ring through its centre in a vertical plane. Two camera projections (stereoscopic view) were used to record the particle displacement in sequential frames within a region of interest. Digital image correlation algorithms allowed the reconstruction of the flow field (Wieneke 2005) with a spatial resolution of 0.4 mm at 14 Hz (time interval between adjacent samples 0.071 s). Accuracy of the reconstructed flow field velocities as declared by LaVisionUK Ltd was better than +/- 0.1 %. A schematic diagram and a photograph of the Laser PIV experimental set up are shown in Figure 5.4 and Figure 5.5, respectively.

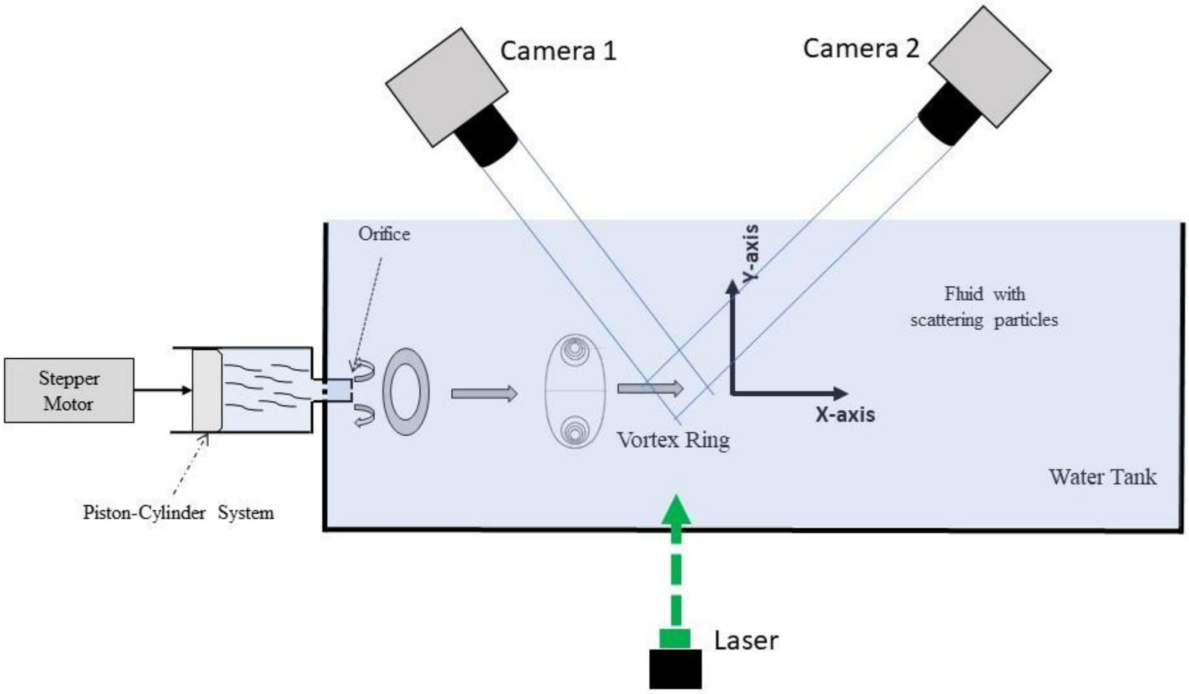

Figure 5.4: Laser PIV measurements – schematic diagram of the experimental set up. Please note that this is a schematic representation and elements are not to scale.

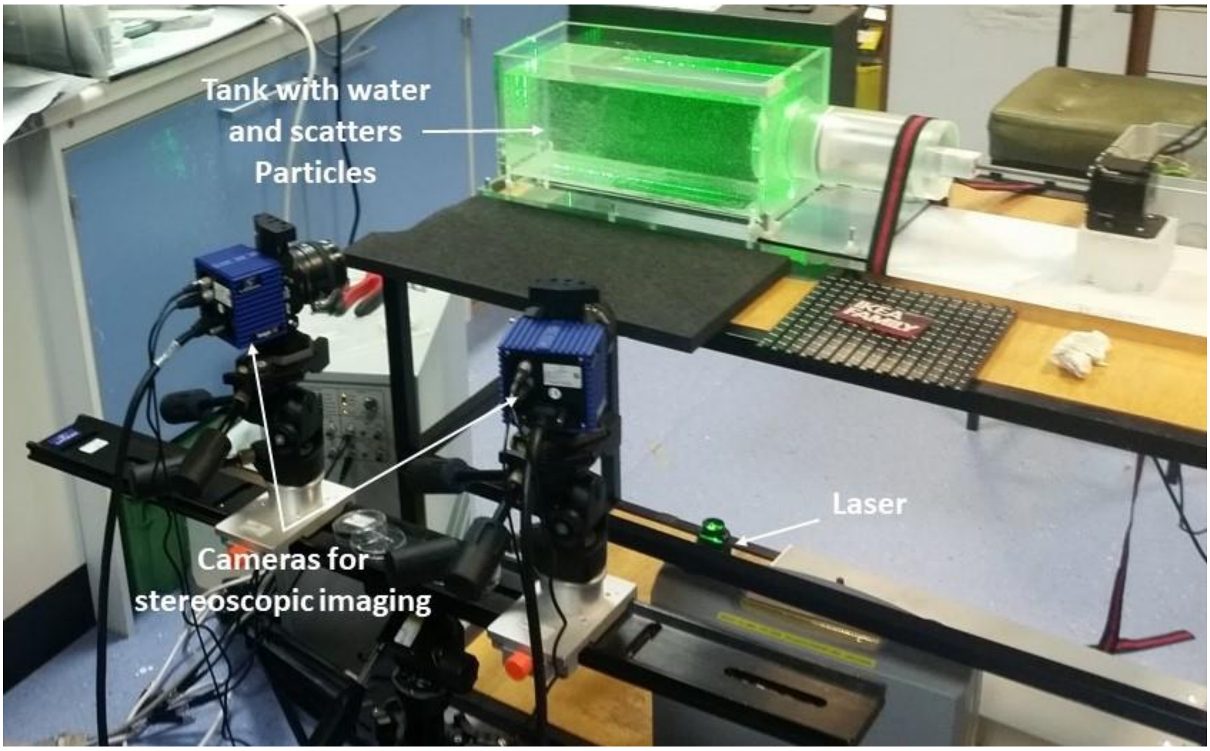

Figure 5.5: Photograph of Laser PIV experimental set up.

Knowing the frame rate (14 frames per seconds), translational velocities of the travelling vortex rings were calculated as well as mapping the flow field of the Vx components (along the X-axis in Figure 5.4) at each frame. Average and standard deviation values of vortex ring translational velocities as a function of the vortex ring position in the tank ("Imaging Tank" reference markers, Figure 4.3, Chapter 4) were calculated from ten consecutive vortex ring acquisitions, generated for each configuration listed in Table 5.1.

5.2.4 Results – Optical/Video

Average vortex ring translational velocity (V_{trans}, Figure 5.3) and standard deviation values (illustrated as error bars) were plotted as a function of vortex ring position in the imaging tank ("Imaging Tank" reference markers, Figure 4.3, Chapter 4). All the tested configurations refer to Table 5.1. For improved clarity of results, configurations (Table 5.1) that produced vortex rings with faster translational velocities (15-80 cm/s) are shown in Figure 5.6 while slower translational velocities (0-15 cm/s) are shown in Figure 5.7. As mentioned previously, the experimental work with the two measurement techniques were undertaken on two different days, in two different premises on two identically manufactured but different Vortex Ring based Complex Flow Phantom prototypes. Each configuration of Table 5.1 corresponds to a specific marker-shape combination and colour, in order to directly compare data obtained with optical/video and Laser PIV measurement methods. Optical/video data are depicted with bold lines and filled markers while Laser PIV results are illustrated with dashed lines and open markers. Variability, which is cited as coefficient of variation (%) within the text, was estimated on the basis of ten consecutive vortex rings (for each configuration of Table 5.1) and is expressed as +/- 1 SD on the plots. Variability estimated with the optical/video measurement method were always lower than +/- 10%.

5.2.5 Results – Laser PIV

Average vortex ring translational velocity (V_{trans}, Figure 5.3) and standard deviation values were also calculated from ten vortex ring consecutive acquisitions with the Laser PIV method, for consistency of results. Results are plotted as a function of the vortex ring position ("Imaging Tank" reference markers, Figure 4.3, Chapter 4) for each configuration listed in Table 5.1 (as for the optical/video method). Similar to the optical/video results, configurations generating vortex rings with faster translational velocities (15-80 cm/s) are depicted in Figure 5.6 while slower translational velocities (0-15 cm/s) are shown in Figure 5.7. Laser PIV results have been plotted with dash lines and open markers of the same shape as the optical/video data. The same colours have been used for Laser PIV and optical/video results, separating each configuration of Table 5.1. Coefficient of variation (+/- %) of the data were calculated as for the optical/video measurements. Laser PIV results show similar behaviour to the optical/video measurements, nothing that the measurements were carried out in two identically manufactured but different prototypes. However, variability progressively increases for vortex ring configurations with translational velocities lower than 8 cm/s (Configuration 8, Configuration 9 and Configuration 10, Table 5.1). Configuration 7 (Table 5.1), which corresponds to vortex rings with translational velocities of ~10 cm/s, demonstrated a percentage of variability (error) lower than +/- 10 %. Finally, the percentage of variability is always lower than +/- 8 % for all the other configurations (Configuration 1 to 6, Table 5.1) and reached the lowest value of +/- 3 % for an orifice diameter of 10 mm, piston speed of 1.33 cm/s and piston displacement of 0.8 mm (Configuration 2, Table 5.1).

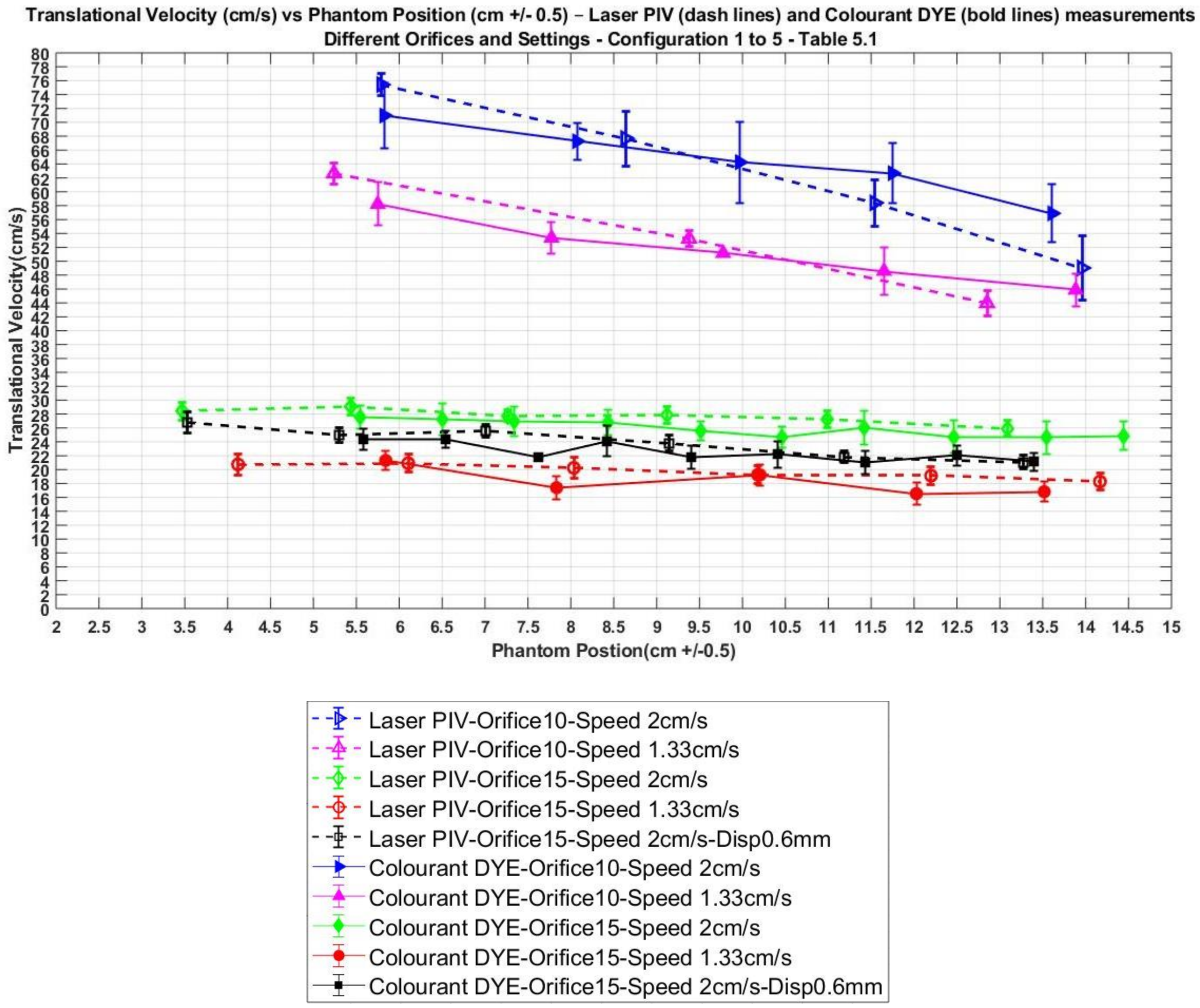

Figure 5.6: Results - optical/video and Laser PIV vortex ring translational velocity measurements relevant to configuration 1 to 5 listed in Table 5.1. Each configuration corresponds to a combination of marker/shape and colour. Optical/video results are depicted with solid markers and bold lines while Laser PIV data are illustrated with dash lines and open markers.

Figure 6: Ambrogio, S., Walker, A., Narracott, A., Ferrari, S., Verma, P. and Fenner, J. (2019). A complex flow phantom for medical imaging: ring vortex phantom design and technical specification. Jorunal of Medical Engineering and Technology, 43(3):190-201.

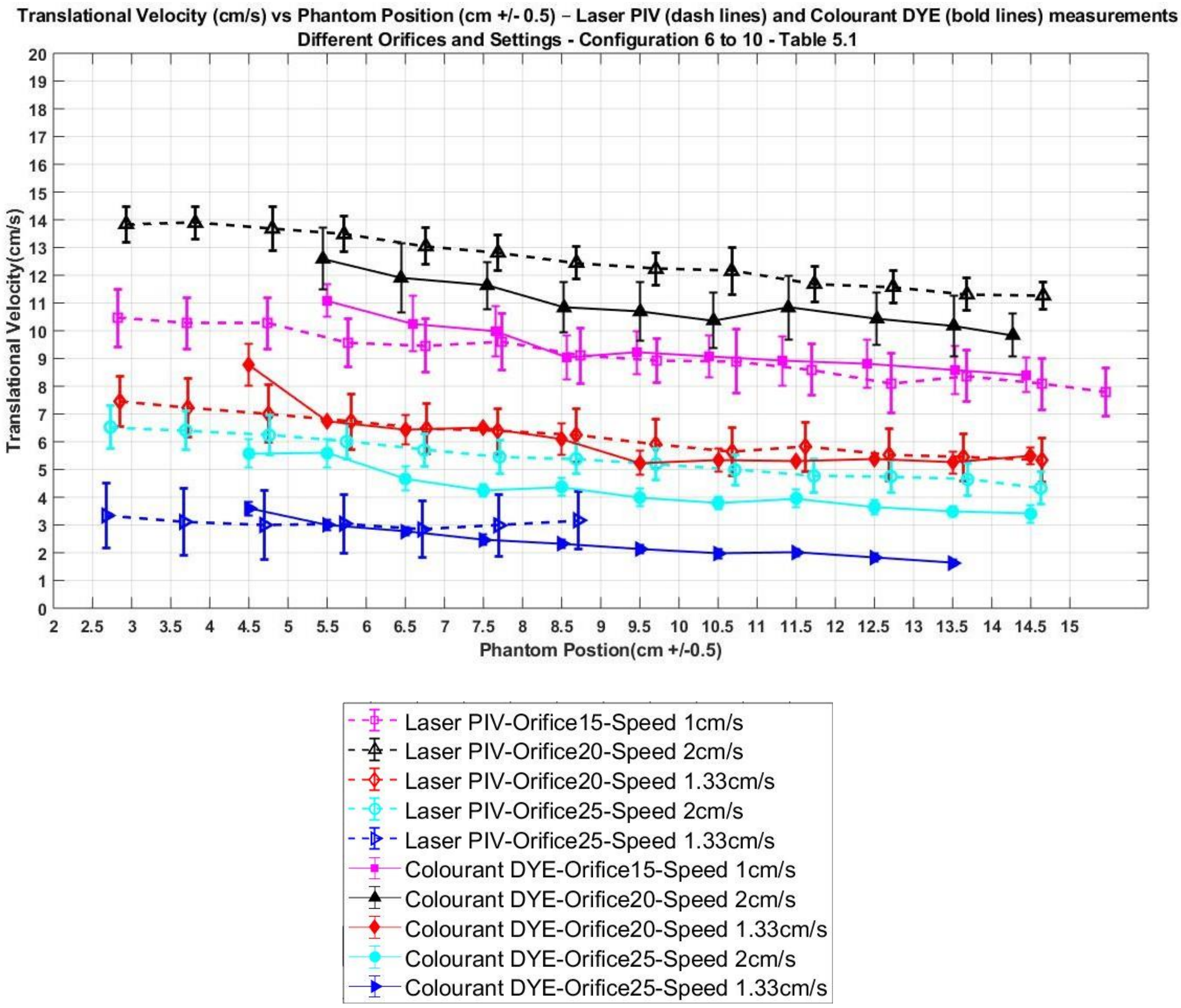

Figure 5.7: Results - optical/video and Laser PIV vortex ring translational velocity measurements relevant to configuration 6 to 10 listed in Table 5.1. Each configuration corresponds to a combination of marker/shape and colour. Optical/video results are depicted with solid markers and bold lines while Laser PIV data are illustrated with dash lines and open markers.

Figure 7: Ambrogio, S., Walker, A., Narracott, A., Ferrari, S., Verma, P. and Fenner, J. (2019). A complex flow phantom for medical imaging: ring vortex phantom design and technical specification. Jorunal of Medical Engineering and Technology, 43(3):190-201.

5.2.6 Additional Results – Laser PIV

For completeness, additional Laser PIV results are shown in figures 5.8 and 5.9. Figure 5.8 depicts Laser PIV acquisition results obtained at the beginning (first experiment) and at the end (last experiment) of an arduous experimental session (more than 8 hours session and more than 100 runs). A maximum percentage difference (difference between the values divided by the average of the two values) of 5 % is apparent between the two curves. Vortex ring position as a function of time for five selected configurations (Table 5.1) is plotted in Figure 5.9. Variability is always better than +/- 10 % with the exception of configuration 10 where it grows up to +/- 40 %.

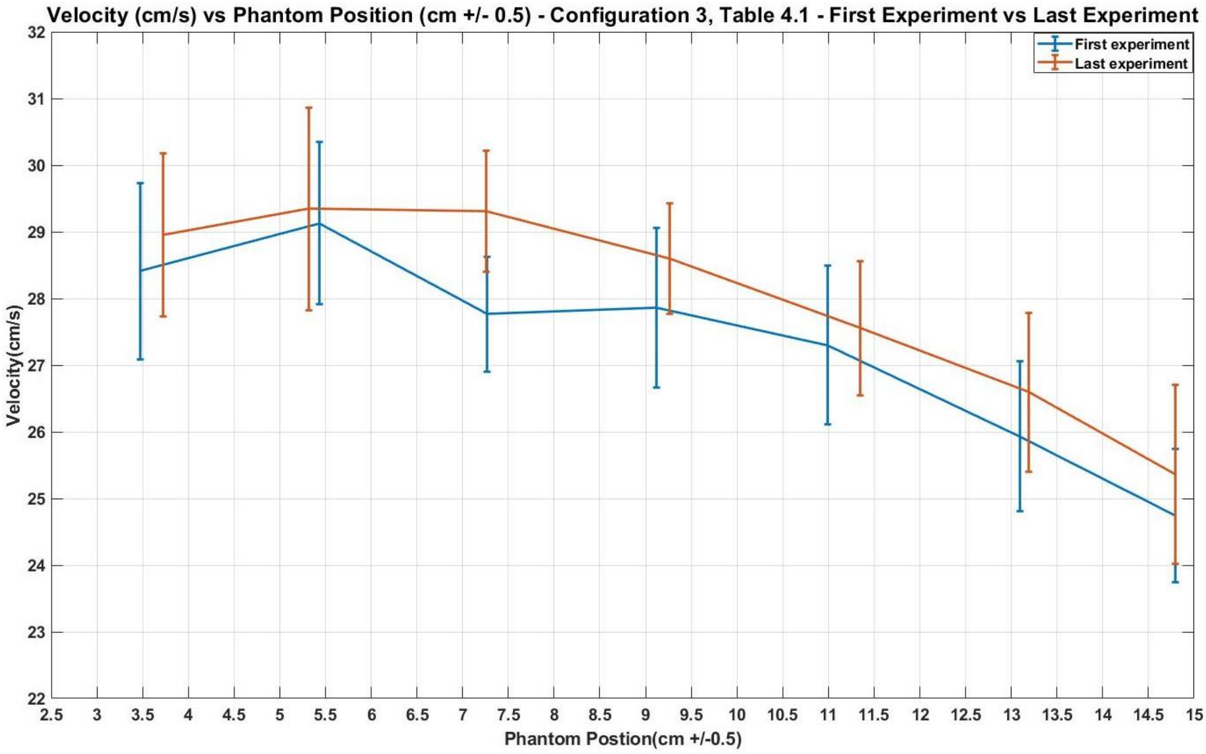

Figure 5.8: Results – Laser PIV measurements performed for Configuration 3, Table 5.1, at the beginning (First experiment) and at the end (Last experiment) of an 8-hour experimental session.

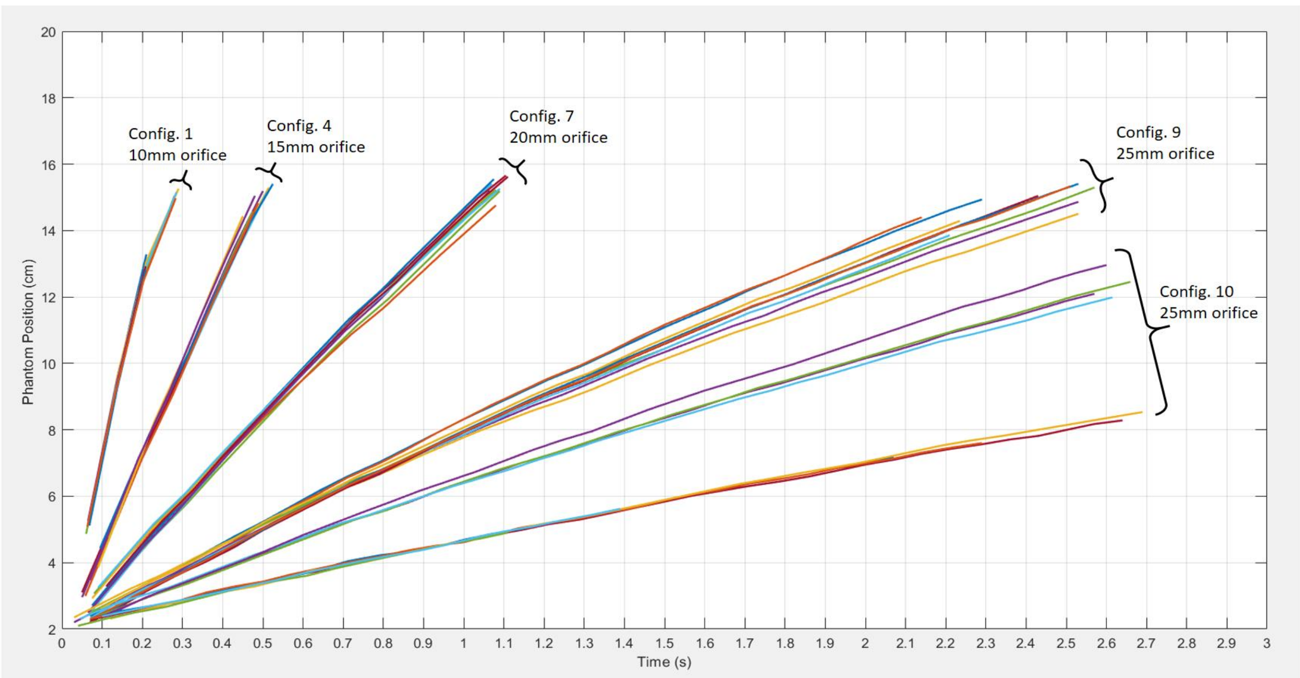

Figure 5.9: Vortex ring position data as function of time for configurations 1, 4, 7, 9, 10 (Table 5.1). Variability increases for vortex rings generated with lower velocities.

Figure 8: Ambrogio, S., Walker, A., Narracott, A., Ferrari, S., Verma, P. and Fenner, J. (2019). A complex flow phantom for medical imaging: ring vortex phantom design and technical specification. Jorunal of Medical Engineering and Technology, 43(3):190-201.

5.2.7 Discussion

The flow performance of the Vortex Ring based Complex Flow Phantom have been assessed using two different measurement methods, two weeks apart, in two different premises (Sheffield Hallamshire Hospital, Sheffield, United Kingdom and Leeds Test Objects Ltd, Boroughbridge, United Kingdom), on two identically manufactured but different prototypes. Optical/video measurements and Laser PIV visualisation has enabled performance to be quantitatively compared. Average translational velocities and error values, estimated from ten consecutive vortex ring acquisitions for ten different configurations, demonstrated variability lower than +/- 10 %, although this was worse for the three slowest configurations (Configuration 8, Configuration 9 and Configuration 10, Table 5.1). This behaviour can be expected because slow configurations generate very diffusive cores due to a combination of low Reynolds number and low stroke length ratio (Table 2.1, Section 2.4, Chapter 2). The Laser PIV visualisation technique, widely considered a gold standard for complex flow field analysis, indicated that there are velocities where the vortex ring has high stability. Variability lower than +/- 3 % was estimated for the specific case of orifice 10 mm, piston speed of 1.33 cm/s and piston displacement of 0.8 mm (Configuration 2, Table 5.1). Laser PIV also indicates that vortex ring generated with high translational velocities, such as 60-80 cm/s (Configuration 1 and Configuration 2, Table 5.1), are more dissipative in their early stage than vortex rings generated with velocities lower than 30 cm/s (i.e. Configuration 4, Configuration 5, Table 5.1). Configuration 1 and Configuration 2 results demonstrated an initial velocity decay while the other configurations illustrate that vortex rings travel almost steadily, with little change in velocity or ring size across the whole length of the phantom imaging tank. Finally, a maximum difference of 5 % was found between Laser PIV acquisitions performed on Configuration 3 (Table 5.1) at the beginning and at the end of the experimental session. The error is an indication of system tolerances and demonstrates the stability of the phantom over prolonged experiments. Overall results are promising and highlight the potential of the technology as a novel complex flow test object. It is worth noting that this analysis focused on the macro-flow characteristics, but micro-flow information can be expected to provide further quantitative description of the flow. Ultrasound compatibility also needs to be assessed and is discussed in the following section.

5.2.8 Conclusion

Optical/video and Laser PIV acquisitions were performed on two identically manufactured Vortex Ring based Complex Flow Phantom prototypes in order to test the reliability of the design. Results were compared and in both cases a reproducibility in translational velocity typically better than +/- 10 % was assessed for most of the tested generating conditions. Overall results are encouraging and provide evidence of the stability and reliability of the system.

5.3 Ultrasound Compatibility

5.3.1 Introduction

The above optical/video and Laser PIV measurements demonstrated encouraging stability of the flow and have provided quantitative information on vortex ring behaviour. Results were referred to each other to verify the rigour of the methods and constitute reference values for future experimental approaches under equivalent generating conditions. Ultrasound compatibility needs to be demonstrated to establish the phantom's potential as a complex flow test object for Doppler ultrasound modalities. B-Mode, Colour Doppler and Pulsed Wave (PW) Spectral Doppler ultrasound acquisitions were performed using the facilities of the "Department of Medical Physics and Clinical Engineering" of the "Sheffield Teaching Hospitals NHS Foundation Trust" (Royal Hallamshire Hospital, Sheffield, United Kingdom). Ultrasound acquisitions in the Hospital often require experiments to be performed outside the normal clinical timetable and within a certain amount of (short) time. Since it was not possible to test all the configurations listed in Table 5.1, B-Mode and both Doppler ultrasound techniques were performed using Configuration 3 (Table 5.1) and with two different probe positions (Figure 5.10). Velocity flow fields estimated with Laser PIV visualisation technique were directly compared with PW Spectral Doppler ultrasound acquisitions (Table 5.4). Both measurements refer to a combination of the translational velocity (Vtrans, Figure 5.10) component and rotational velocity component (tangential velocity, $V_r = r\omega$, Figure 5.10).

In addition, high frame rate Doppler Ultrasound Vector Flow Imaging acquisitions were performed by Badescu et al (2018) on the phantom prototype manufactured for the CREATIS laboratory within the VPH-CaSE network (Figure 5.1). Detailed methods are not described within these sections because work was not performed by this author.

5.3.2 Method - Ultrasound Acquisitions

Ultrasound acquisitions were performed under the supervision of a Clinical Scientist and Ultrasound specialist of the "Sheffield Teaching Hospitals NHS Foundation Trust" (Royal Hallamshire Hospital, Sheffield, United Kingdom). Similar to Laser PIV, ultrasound imaging requires a signal from scattering particles to provide images. The system was filled with water and Orgasol™ (Orgasol™, Atochem, Paris, France) particles of 10 micron size were introduced with a syringe into the piston cylinder volume. Orgasol™ particles of 10 micron and 5 micron are commonly used for the development of blood mimicking fluids (BMF) (Ramnarine et al 1998; BS EN 61685:2002, IEC 61685:2001). Orgasol™ is non-toxic and FDA approved (FDA 177-1500 and FDA 175-300), however, being an ultrafine spheroidal powder of polyamide, precautions for breathing must be taken as reported by the Health and Safety datasheet (https://www.orgasolpowders.com). Vortex ring generating conditions of Configuration 3, Table 5.1, were tested in B-Mode, Colour Doppler and PW Spectral Doppler ultrasound for two different probe positions. Ultrasound acquisitions were obtained with a Siemens Sonoline Antares scanner (Siemens Healthineers, Erlangen, Germany) and a linear array transducer V13-5. The linear array probe has a length of ~4.7 cm and was fixed to a clamp. For B-Mode and Colour Doppler ultrasound imaging, the probe was positioned along the vertical Y-axis (Position 2, Figure 5.10) between centimetre 10 and centimetre 15 into the imaging tank ("Imaging Tank" reference markers, Figure 4.3, Chapter 4). It is well known that the attenuation of water is small at diagnostic ultrasonic frequencies (0.055 dB cm^{-1} at 5 MHz and 20°C, 0.25 dB cm^{-1} at 11 MHz and 20°C, Zeqiri et al 2010). Therefore, an anechoic ultrasonic absorber Aptflex F28 (Precision Acoustic Ltd, Dorchester, UK) was positioned at the bottom of the phantom to minimise acoustic echoes and strong reflections from the PMMA (Perspex) walls. No steering was applied to the colour box in Colour Doppler modality, therefore, velocity components parallel to the ultrasonic beam were detected. A schematic diagram of the ultrasound experimental set up is depicted in Figure 5.10. Velocity flow fields within the travelling vortex ring atmosphere (translational velocity component, V_{trans}, and rotational velocity component, V_r) and ultrasound probe positioning during the acquisitions are also shown.

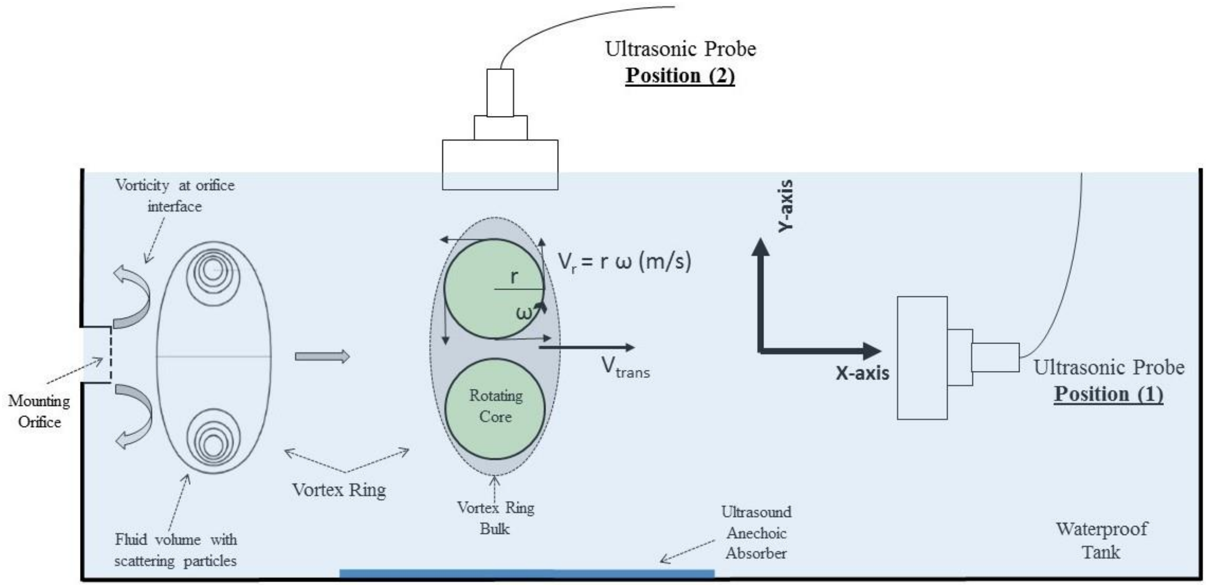

Figure 5.10: Vortex ring velocity components. Vtrans (m/s), translational velocity component of the travelling vortex ring. Vr, rotational velocity (m/s) component of the travelling vortex ring. B-Mode acquisitions were performed with the probe positioned along the Y-axis (Position 2) and an anechoic absorber was used to avoid strong wall reflections. PW Spectral Doppler acquisitions were performed with the probe placed along the X-axis (Position 1). Please note that this is a schematic representation and elements are not to scale.

Pulsed Wave Spectral Doppler acquisitions were performed with the probe placed in the water along the horizontal X-axis (Position 1, Figure 5.10). In this position, the probe is facing the travelling vortex ring and detects a spectrum of velocities directly comparable to the flow field reconstructed by the Laser PIV technique. The linear array transducer (V13-5) was held in the water with two clamps and was positioned at the 13.5 +/- 0.5 cm mark ("Imaging Tank" reference markers, Figure 4.3, Chapter 4). With reference to the longest side of the transducer, acquisitions were performed with the probe in horizontal position (right-left) and in vertical position (up-down). Measurements were performed with Doppler Sample Volume (Doppler gate) set to 1 mm size (smallest selectable size) and 12.5 mm size (largest size). Selected PW Doppler frequencies were 6.2 MHz and 5.3 MHz, Pulsed Repetition Frequency (PRF) 9.7 KHz. The PRF determines the Doppler sampling frequency of the transducer. In agreement with the Nyquist limit, the maximum rate at which the transducer can sample (or measure) the Doppler shift without aliasing is PRF/2. Doppler settings are summarised in Table 5.3. Scanner settings were varied to assess if there was any appreciable difference (parameter dependent) on the measurements. The focus and Doppler Gate were always positioned 3 cm from the transducer, in order to acquire measurements at the 10.5 +/- 0.5 cm mark in the imaging tank ("Imaging Tank" reference markers, Figure 4.3, Chapter 4). For clarity, a block diagram describing PW Spectral Doppler acquisitions with probe placed in Position 1 (Figure 5.10) is shown in Figure 5.11.

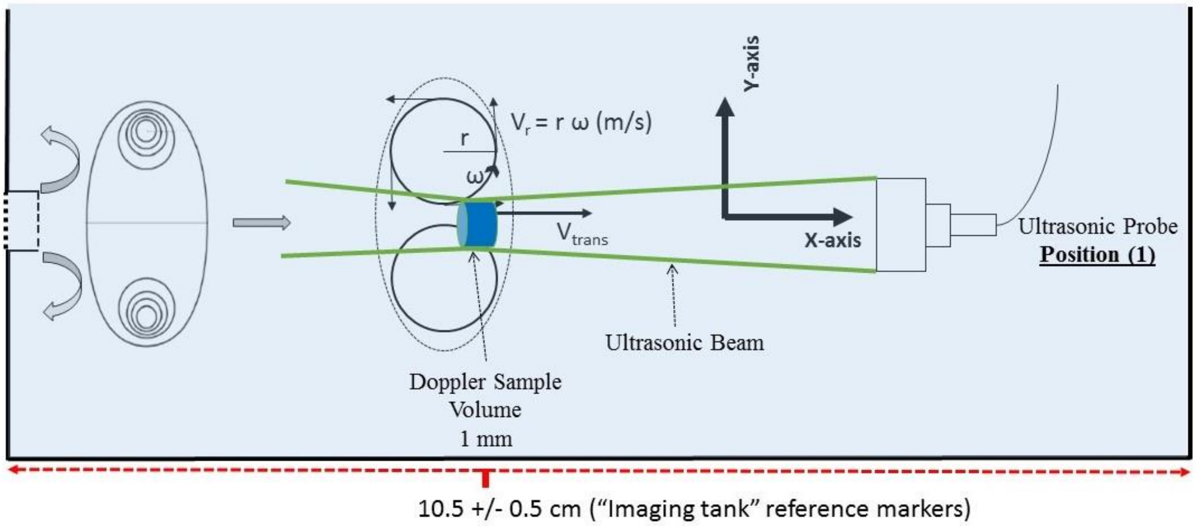

Figure 5.11: Block diagram of PW Spectral Doppler ultrasound acquisitions with probe in Position 1 (Figure 5.10). Sample volumes of 1 mm and 12.5 mm were selected and angle correction was set to 0 degrees. Consequently, velocities that correspond to the translational velocity component V_{trans} plus or minus the rotational velocity component were estimated. Please note that this is a schematic representation and elements are not to scale.

Since the best condition for Doppler estimation is when the ultrasonic beam is parallel to the direction of the flow ($cos\vartheta_D = 1$ and there will be the maximum Doppler shift signal, Section 1.4.2), PW Spectral Doppler measurements were performed with the probe placed along the X-axis (Position 1, Figure 5.10 and Figure 5.11) and angle correction on the scanner set to zero degrees. Under these conditions (0^o angle correction and probe in Position 1), the ultrasound scanner estimates a spectrum of velocities that correspond to the translational velocity component (V_{trans}, Figure 5.10 and Figure 5.11) plus or minus the rotational velocity component (tangential velocity component, Vr = r ω, Figure 5.10 and Figure 5.11) of the scatterers embraced within the rotating cores. Consequently, peak velocities estimated with the probe in Position 1 in PW Spectral Doppler ultrasound modality are directly comparable with the velocity flow fields reconstructed with Laser PIV technique. By way of example, a photograph of a B-Mode ultrasound acquisition with the probe positioned in Position 2 (Figure 5.10) is shown in Figure 5.12. The vortex ring encloses the Orgasol™ particles which generate contrast for the camera acquisition and scattering signal for the ultrasound scanner. As result, the vortex ring is visible both on camera and on the ultrasound screens.

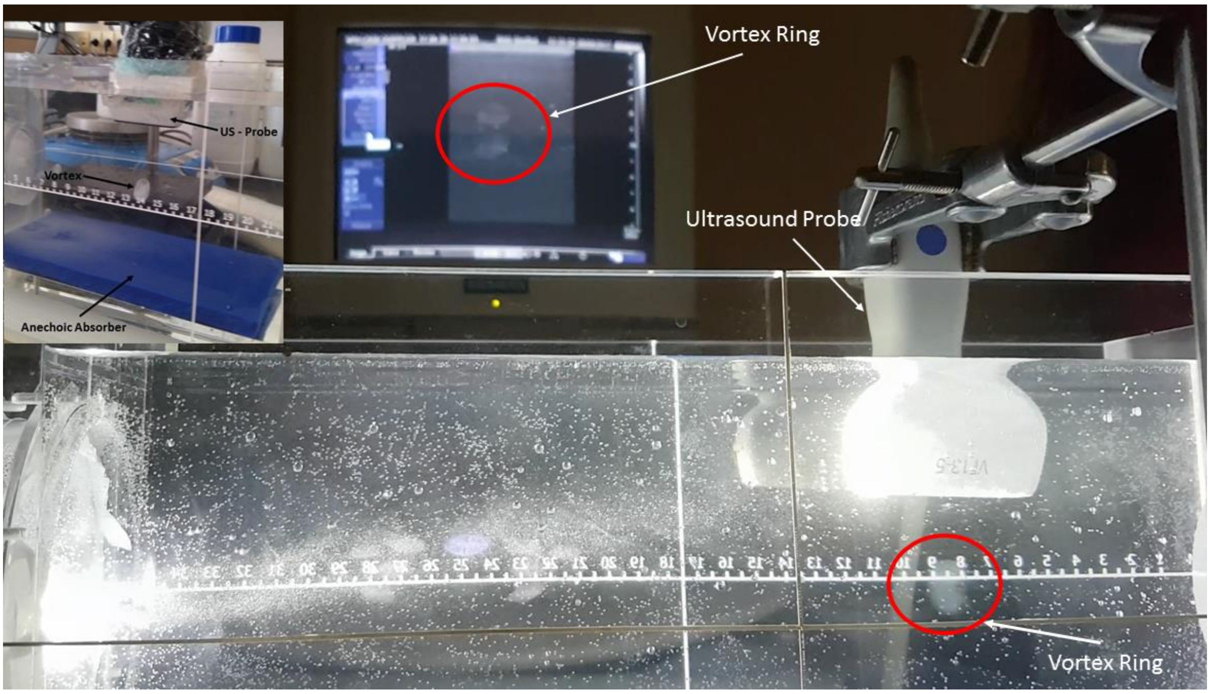

Figure 5.12: B-Mode ultrasound experimental set up. The vortex ring is marked by the Orgasol™ particles that make it visible both on camera and on the ultrasound scanner simultaneously. On the top left corner an image illustrating the set-up from a different point of view and showing the Aptflex F28 (Precision Acoustic Ltd, Dorchester, UK) anechoic absorber to avoid strong reflections.

5.3.3 Results – B-Mode Ultrasound

Conventional B-Mode ultrasound imaging modality is not commonly used for flow imaging. State of the art techniques, which rely on block-matching algorithms for speckle tracking within frames (echo-PIV and Blood Speckle Tracking, Section 1.4.4, Chapter 1), are used in post processing to estimate velocity vectors. However, these advanced techniques were not available at the University of Sheffield at the time of writing (2018). Potentially, vortex ring translational velocities might be estimated by manually tracking the vortex displacement, knowing the acquisition frame rate and the probe dimensions. Systematic errors in frame rate and displacement estimation might significantly affect the measurement, and more appropriate techniques, such as PW Spectral Doppler, were used to quantify velocities. However, B-Mode ultrasound imaging has value in obtaining information about vortex ring shape and dimensions. A travelling vortex ring captured with a Siemens Sonoline Antares scanner (Siemens Healthineers, Erlangen, Germany) with the probe in Position 2 (Figures 5.10) is shown in Figure 5.13. The vortex is travelling from left to right in the image. Two distinct rotating cores, characteristic of the vortex ring fluid dynamics (i.e. see previous *in vitro* experiments, Figure 2.3, Figure 2.5 and Figure 2.6, Chapter 2), are clearly visible in the image. As mentioned in Section 5.3.1, B-Mode ultrasound acquisitions were performed on vortex rings generated according to Configuration 3, Table 5.1.

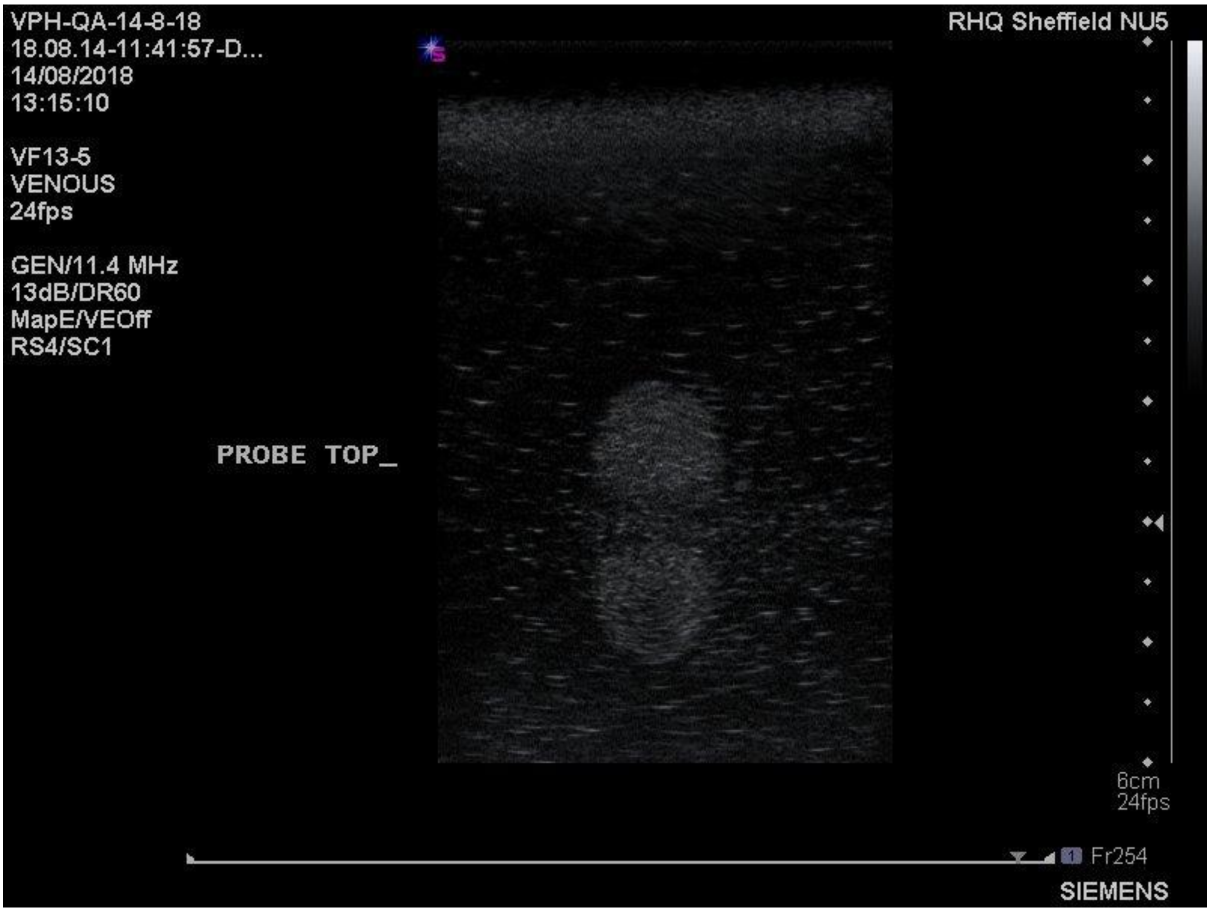

Figure 5.13: B-Mode ultrasound imaging of a travelling vortex ring. The two distinct cores that contained within the vortex ring atmosphere are clearly visible.

5.3.4 Results – Colour Doppler Ultrasound

By way of an example, images were acquired, keeping the probe in Position 2 (Figures 5.10) and setting the scanner in Colour Doppler mode. With the probe in Position 2 (Figure 5.10), the ultrasonic transducer detects velocity components parallel to the ultrasonic beam. In other words, the Colour Doppler image, shown in Figure 5.14a, provides qualitative and semi-quantitative information about flow direction and rotational speed components along the Y-axis (V_r, Figure 5.10) of the travelling vortex ring. Two cores, rotating in opposite direction each other, are clearly visible from Colour Doppler ultrasound imaging (Figure 5.14a). For comparison, vortex ring flow fields reconstructed with Laser PIV techniques are shown in Figure 5.14b.

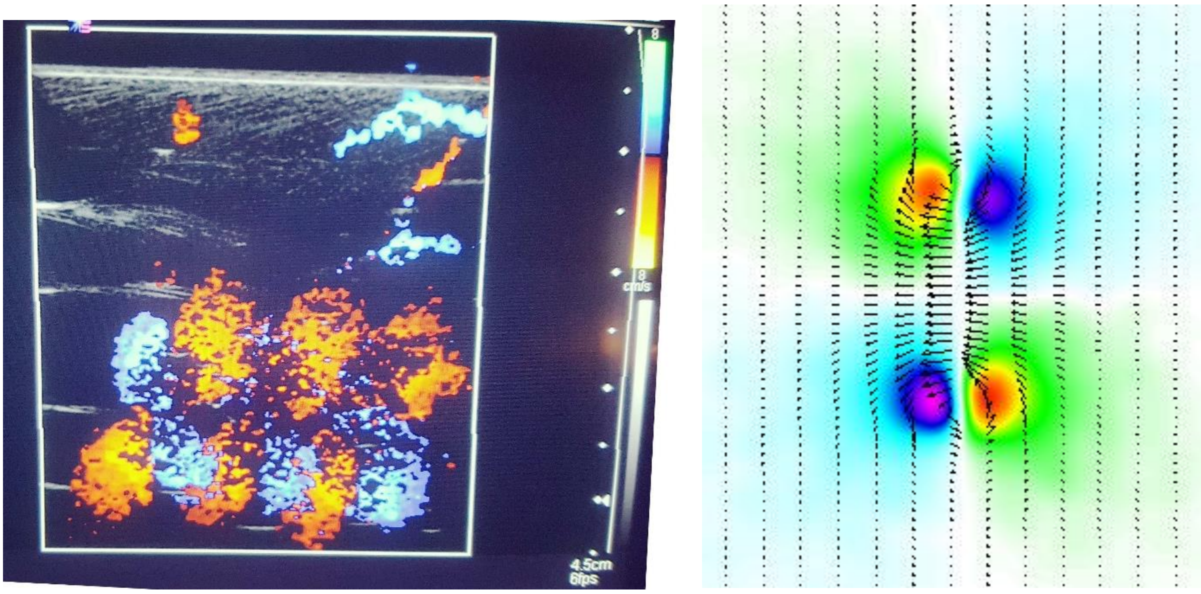

(a) (b)

Figure 5.14: Colour Doppler imaging (a) and flow fields reconstructed with Laser PIV techniques (b) of a travelling vortex ring. Both techniques image two rotating cores rotating in opposite direction. The probe is placed in Position 2, Figure 5.10.
Figure 9a: Ambrogio, S., Walker, A., Narracott, A., Ferrari, S., Verma, P. and Fenner, J. (2019). A complex flow phantom for medical imaging: ring vortex phantom design and technical specification. Jorunal of Medical Engineering and Technology, 43(3):190-201.

5.3.5 Results – PW Spectral Doppler Ultrasound

The Pulsed Wave Spectral Doppler ultrasound technique graphically displays velocity profiles over time. Diagnostic information can be obtained from qualitative and quantitative analysis of the curves. Velocity spectra of ten consecutive vortex rings were detected in PW Spectral Doppler mode with scanner settings listed in Table 5.3. By way of example, the velocity profiles of PW Spectral Doppler ultrasound acquisitions performed with Doppler Gate 1 mm and Doppler Gate 12.5 mm are shown in Figure 5.15a and Figure 5.15b, respectively. The probe was placed in Position 1 (Figure 5.10 and Figure 5.11) and zero degrees angle correction was set on the scanner. The spectrum corresponds to the translational velocity component (Vtrans, Figure 5.10 and Figure 5.11) plus or minus the rotational velocity component (Vr, Figure 5.10 and Figure 5.11) of the travelling vortex ring. The Doppler Sample Volume defines the position and the size of the region of interest from which velocity information is obtained. Only the flow going through the Doppler sample volume contributes to the Doppler measurements. As expected, the acquisition performed with a small Doppler sample volume (1 mm) shows a narrow distribution of velocities (Figure 5.15a) while the acquisition with a large gate shows a broad range of velocities in the Doppler spectrum (Figure 5.15b). If a large gate is selected, the range of measured velocities is much greater and the spectrum also includes low velocity components and, in the case of the vortex ring, reverse flow (Figure 5.15b).

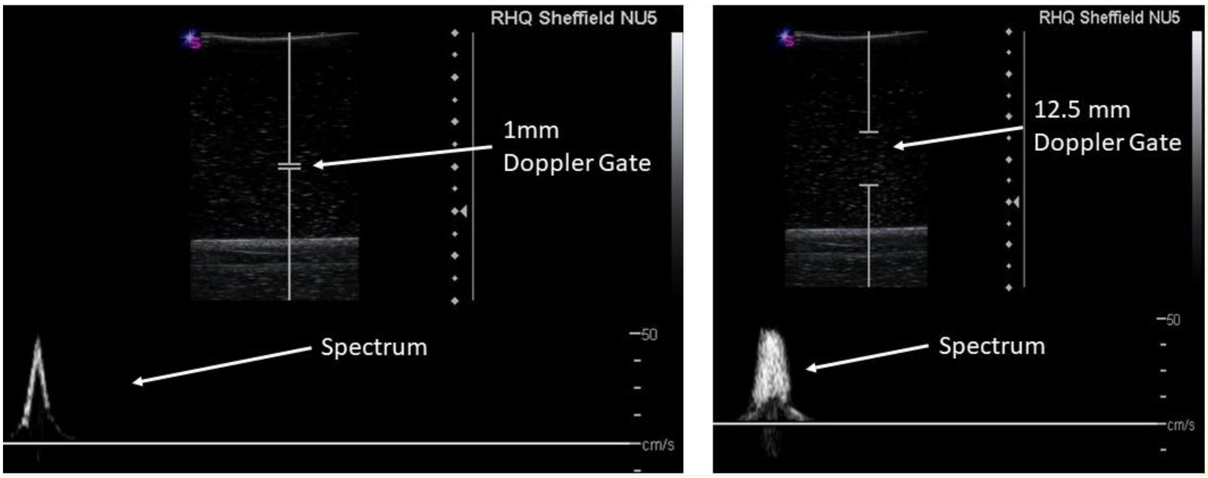

(a) (b)

Figure 5.15: Results – Pulsed Wave Spectral Doppler ultrasound imaging of a travelling vortex ring. Gate size 1 mm, Pulsed Wave Doppler frequency 5.3 MHz, angle correction 0 degrees. The probe is placed in Position 1, Figure 5.10.

Peak flow field velocities were recorded from raw Laser PIV data, acquired on ten vortex rings produced under the generating conditions of Configuration 3 (Table 5.1), at the frame when it had travelled 10.5 +/ 0.5 cm into the imaging tank ("Imaging Tank" reference markers, Figure 4.3, Chapter 4). The region of interest for the measurements is the same for PW Spectral Doppler acquisitions and Laser PIV, enabling comparison of the results. Laser PIV peak velocity results are reported in Table 5.2.

Laser PIV - Configuration 3, Table 5.1	
Acquisition	**Peak Velocity (cm/s)**
1	42.3
2	42.3
3	45.2
4	39.7
5	39.4
6	41.7
7	40.2
8	44.4
9	46.2
10	41.1

Table 5.2: Peak Velocity (cm/s) measurements estimated from Laser PIV raw data on the acquisition of ten consecutive vortex rings produced under generating conditions of Configuration 3, Table 5.1.

Unfortunately, raw data were not available for PW Spectral Doppler ultrasound measurements and therefore peak velocities were estimated from the images. For this reason, a tolerance of +/- 2.5 cm/s is implicit to the reported peak velocities. Ultrasound scanner settings and peak velocities results are listed in Table 5.3. Settings were varied to asses if the velocity measurement was dependent on any setting parameter.

Ultrasound Acquisitions - Siemens Sonoline Antares - Configuration 3, Table 5.1						
Acquisition	**Probe Position 2**	**PRF**	**Gate**	**Angle**	**PW**	**Velocity (cm/s)**
1	Vertical (up/down)	9766	12.5mm	0	6.2MHz	37.5 +/- 2.5
2	Vertical (up/down)	9766	12.5mm	0	6.2MHz	42.5 +/- 2.5
3	Vertical (up/down)	9766	12.5 mm	0	6.2MHz	47.5 +/- 2.5
4	Vertical (up/down)	9766	12.5 mm	0	6.2MHz	42.5 +/- 2.5
5	Vertical (up/down)	9766	1mm	0	6.2MHz	37.5 +/- 2.5
6	Vertical (up/down)	9766	1mm	0	5.3MHz	47.5 +/- 2.5
7	Vertical (up/down)	9766	1mm	0	5.3MHz	42.5 +/- 2.5
8	Vertical (up/down)	9766	1mm	0	5.3MHz	37.5 +/- 2.5
9	Horizontal (right to left)	9766	1mm	0	5.3MHz	42.5 +/- 2.5
10	Horizontal (right to left)	9766	1mm	0	5.3MHz	37.5 +/- 2.5

Table 5.3: PW Spectral Doppler measurements performed with a clinical Siemens Sonoline Antares scanner at the University of Sheffield. A +/- 2.5 cm/s tolerance is implicit to peak velocity estimation from the image data.

Finally, average and standard deviation values were calculated from the ten acquisitions performed with both methods (Laser PIV and PW Doppler ultrasound). Results, obtained on the same phantom prototype with experiments undertaken in two different days, show good agreement (Table 5.4). Intra-observer errors on peak velocity estimations were +/- 11 % and +/- 5% for PW Spectral Doppler ultrasound and Laser PIV technique, respectively.

Modality	Number of acquisitions	Region of Interest ("Imaging Tank" reference markers, Figure 4.3, Chapter 4)	Average Peak velocity +/- 1SD
PW Spectral Doppler	10	10.5 +/- 0.5 cm	41.5 +/- 4.61 cm/s
Laser PIV	10	10.5 +/- 0.5 cm	42.3 +/- 2.35 cm/s

Table 5.4: Average and standard deviation values calculated from peak velocity estimation with PW Spectral Doppler ultrasound and Laser PIV technique.

5.3.6 Additional Results – Vector Doppler Imaging

Ultrasound 2D and 3D acquisitions were performed in Lyon (France) in a collaborative project between VPH-CaSE (http://www.vph-case.eu/) within the European Union's Horizon 2020 research and innovation programme (Marie Skłodowska-Curie grant agreement No 642612) and LABEX PRIMES (ANR-11-LABX-0063, Universite' de Lyon, Lyon, France) within the "Investissements d'Avenir" (ANR-11-IDEX-0007) program. 2D acquisitions were performed with a Verasonics Vantage 256 research scanner (Verasonics Inc, WA, USA) and a 5 MHz linear transducer ATL L7-4 with 128 elements. The probe was placed 10 cm (+/- 0.5 cm) away from the orifice and insonified the test object by using a series of 0 degrees plane waves. Velocity flow fields were estimated using echo-PIV, by tracking the real envelope speckle patterns using phase correlation, and Vector Doppler, by using a receive dual beam approach (Jensen et al 2016). For Vector Doppler, the signals were beamformed at two receive angles (plus and minus 15 degrees Experimental set-up and acquisition planes are shown in Figure

5.16. Velocity flow fields estimated with echo-PIV and Vector Doppler are shown in Figure 5.17a and Figure 5.17b, respectively.

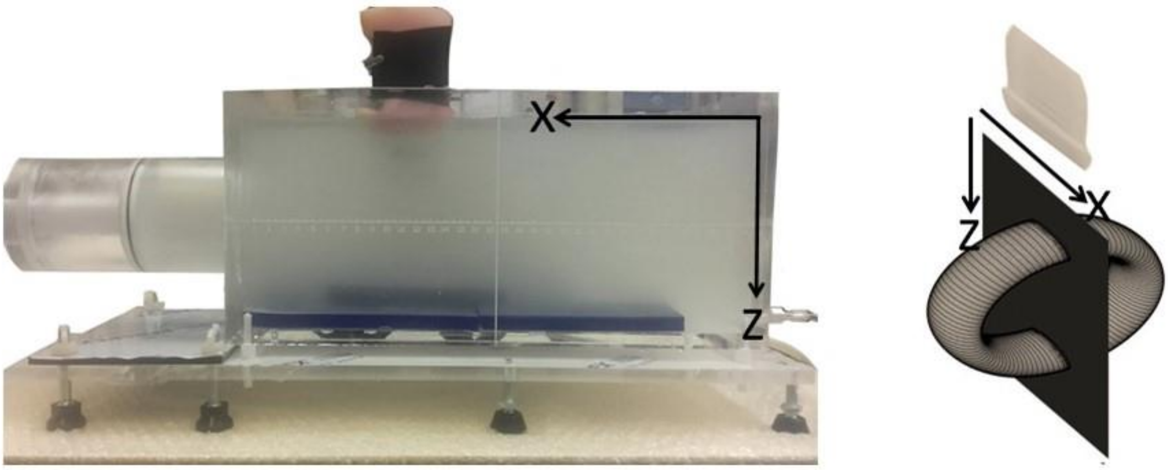

Figure 5.16: Experimental set up – Vortex ring acquisitions with a Verasonics Vantage 256 research scanner (Verasonics Inc, WA, USA) and a 5 MHz linear transducer ATL L7-4 with 128 elements.
Figure 2: Badescu, E., Ambrogio, S., Fenner, J., Liebgott, H., Friboulet, D. & Garcia, D. (2018). Vortex Ring Phantom for Invetigation of Ultrasound Vector Flow Imaging, in: IEEE International Ultrasonic Symposium, IUS.

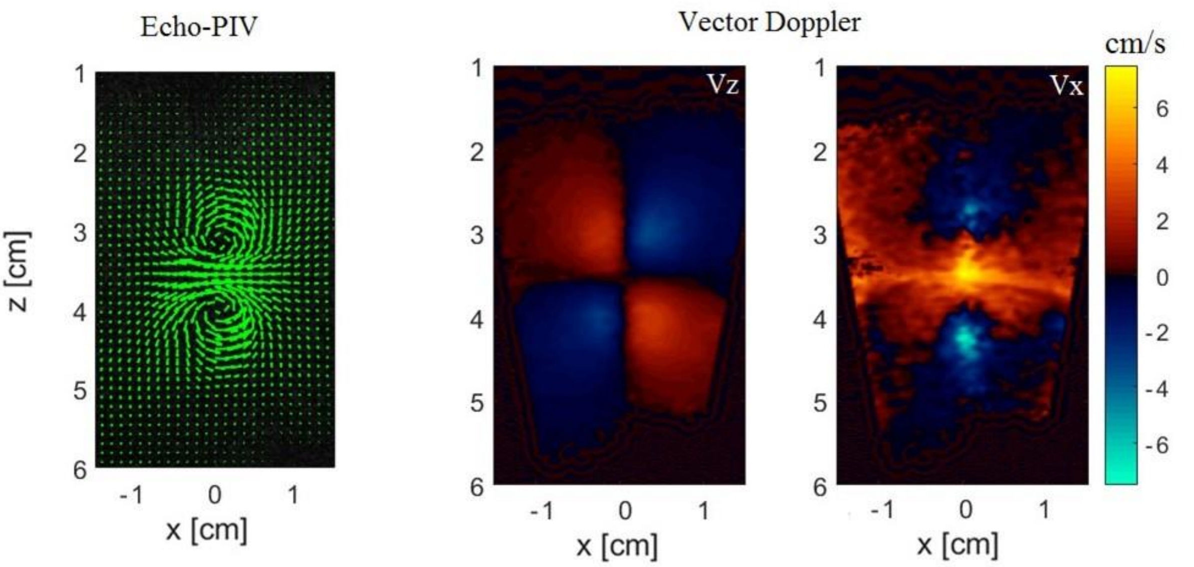

Figure 5.17: Vortex ring velocity flow fields reconstructed with echo-PIV (a) and Vector Doppler (b).
Figure 3: Badescu, E., Ambrogio, S., Fenner, J., Liebgott, H., Friboulet, D. and Garcia, D. (2018). Vortex Ring Phantom for Invetigation of Ultrasound Vector Flow Imaging, in: IEEE International Ultrasonic Symposium, IUS.

Since Laser PIV date were not available at the time of the experiments, multiple acquisitions have been performed for investigating the link between the velocity components along the Z-axis and the X-axis. Results for orifice output diameters of 20 and 25 mm are shown in Figure 5.18. Linear relationship and high correlation (R^2= 0.95) was found between the two velocity components.

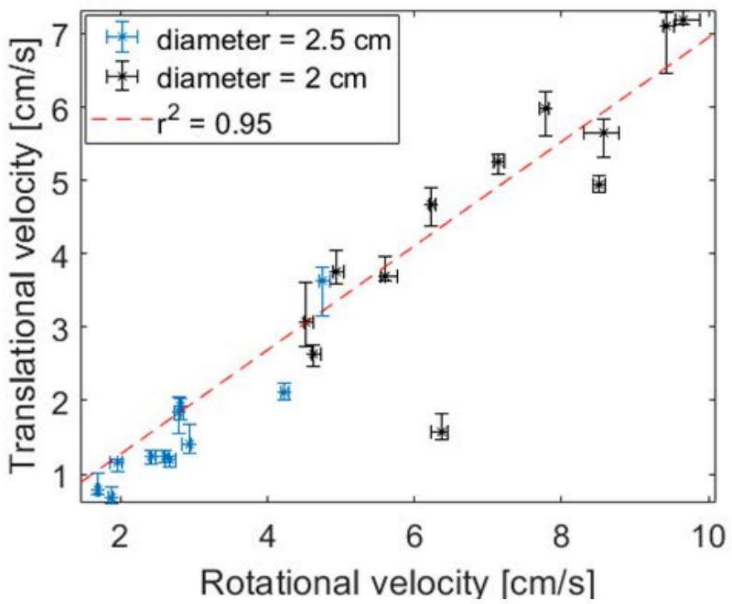

Figure 5.18: Correlation plot of vortex ring rotational and translational velocity components.
Figure 4: Badescu, E., Ambrogio, S., Fenner, J., Liebgott, H., Friboulet, D. & Garcia, D. (2018). Vortex Ring Phantom for Invetigation of Ultrasound Vector Flow Imaging, in: IEEE International Ultrasonic Symposium, IUS.

3D acquisitions were performed synchronising four Verasonics Vantage 256 (Verasonics Inc., WA, USA) research scanners for driving a customised 1024 element transducer. The Verasonics Vantage 256 scanners were provided by the FEDER program, Saint-EtienneMetropole (SME) and Conseil General de la Loire (CG42). Doppler velocity flow fields were estimated using a 2D autocorrelator applied on the IQ data. Details of acquisition and experimental set up have been described by Petrusca et al (2018). Experimental set up and 1D Doppler velocity components for the *x-z* and the *y-z* planes are shown in Figure 5.19 and Figure 5.20, respectively. Ultrasonic acoustic absorbers Aptflex F28 (Precision Acoustic Ltd, Dorchester, UK) were used for minimising reflections from the bottom of the phantom and Orgasol™ (Orgasol™, Atochem, Paris, France) particles of 10 micron size were introduced for providing backscattering signal for ultrasound imaging.

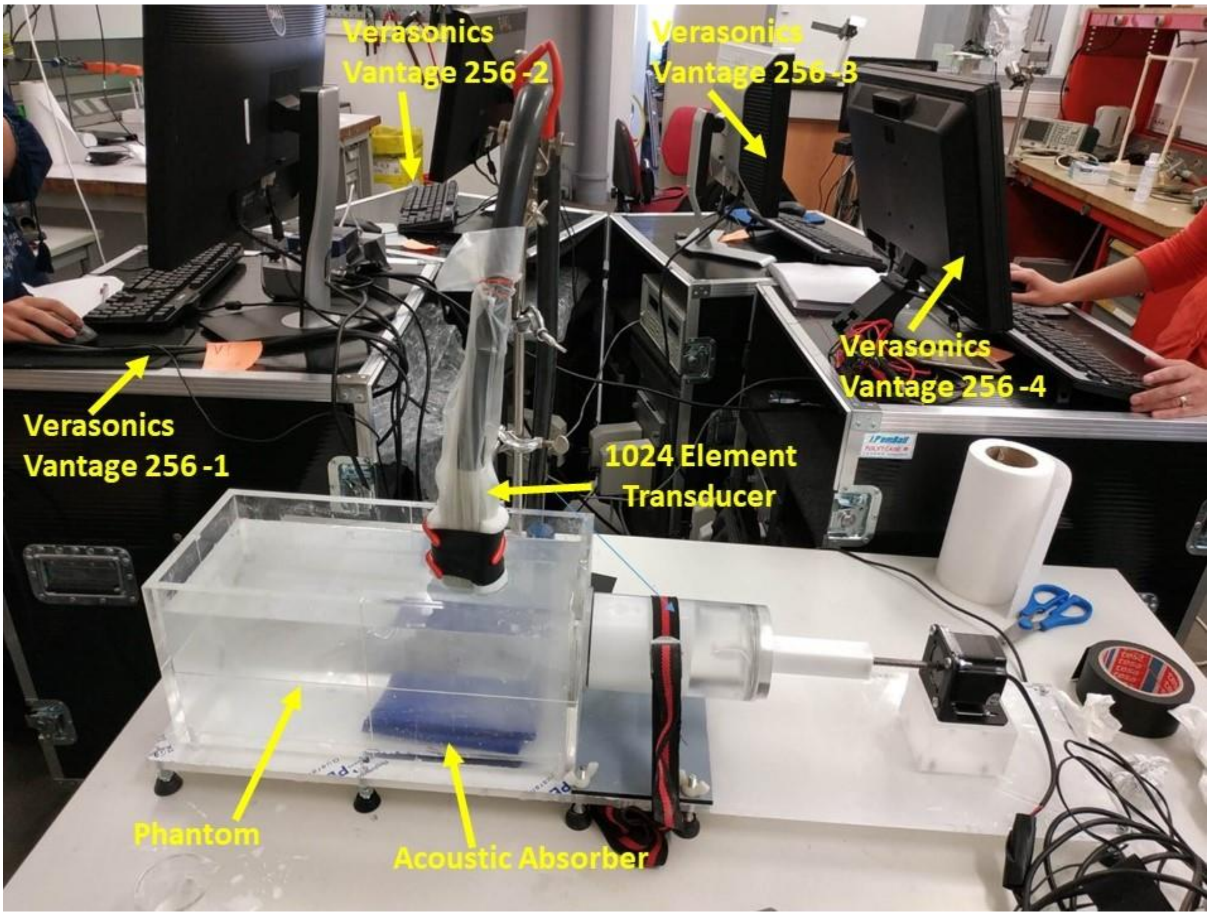

Figure 5.19: Four Verasonics Vantage 256 research scanner were synchronised for driving a customised 1024 elements transducer. Acoustic absorbers and Orgasol^{TM} particles were used for minimising reflections and providing a backscatter signal for ultrasound imaging.

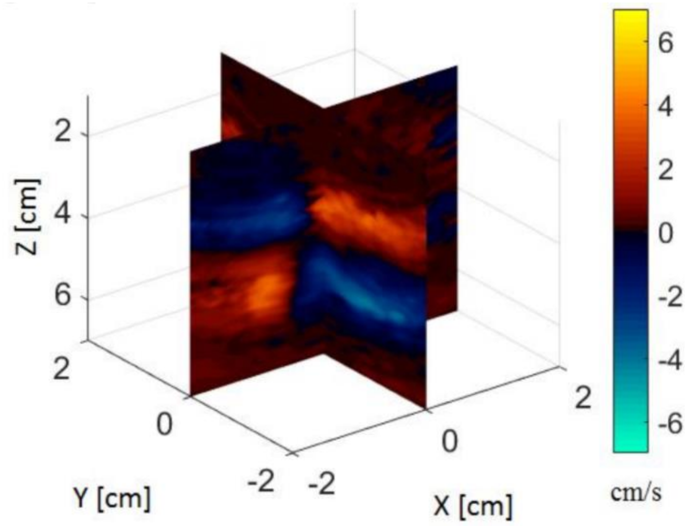

(a) (b)

Figure 5.20: 3D acquisitions –1D Doppler velocity components along the *x-z* and planes.
Figure 5: Badescu, E., Ambrogio, S., Fenner, J., Liebgott, H., Friboulet, D. & Garcia, D. (2018). Vortex Ring Phantom for Invetigation of Ultrasound Vector Flow Imaging, in: IEEE International Ultrasonic Symposium, IUS.

5.3.7 Additional Results – Colour Doppler

Figure 5.14 is an indication of mis-registrations and delays, observed during Colour Doppler imaging. Colour Doppler acquisition algorithms vary from one machine to another. But, most of the modern systems use array transducers with a large number of piezo-elements capable of independently transmitting and receiving pulses with different delays. A complete description is beyond the scope of this work and details can be found in a review of Evans et al (2011). Generally, the transducer output goes through a beamformer, it is amplified (to compensate for attenuation of echoes from deep within the body) and quadrature modulated to generate two components (in-phase and quadrature) of the Doppler signal. The demodulated signals are stored in a colour vector memory, filtered, processed (i.e. to extract power, mean frequency) and combined with pulse-echo images to generate a display with anatomical and velocity information (i.e. Figure 5.21). Images acquired with the Siemens Sonoline Antares scanner and the linear array used in previous experiments showed a mis-registration between the colour coded map and the pulse-echo. By way of example, four frames are shown in Figure 5.21. The B-Mode is delayed when compared with the Colour Doppler image.

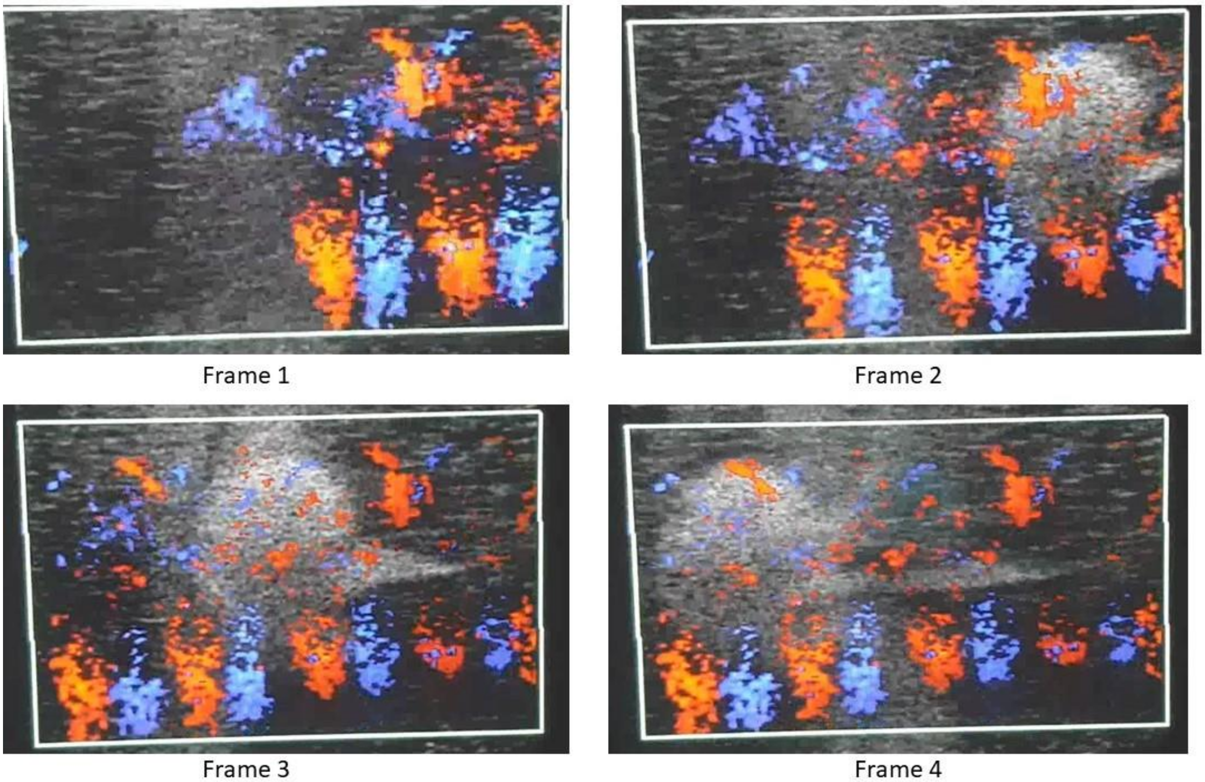

Figure 5.21: Four Colour Doppler frame images acquired with a Siemens Sonoline Antares scanner at the "Sheffield Teaching Hospitals NHS Foundation Trust". The images show a clear mis-registration between colour coded map and B-Mode.

The Siemens Sonoline Antares scanner was in use at the Sheffield Teaching Hospitals NHS Foundation Trust (Royal Hallamshire Hospital, Sheffield, United Kingdom) and it has regularly passed all the quality control checks that are routinely performed. This is a reliable scanner. Measured peak velocities in PW Spectral Doppler mode were very close to Laser PIV estimations. However, the phantom was also scanned with a Sonix scanner (BK Medical System, Naerum, Denmark) at CREATIS consortium (CNRS UMR 5220 - INSERM U1206 – Universite' de Lyon 1 – INSA Lyon – Universite' Jean Monnet Saint-Etienne) to verify if the mis-registration phenomenon was related to that particular device. Interestingly, equivalent results were obtained, whether beam steering was applied or not. By way of example, four frames of the acquisition are illustrated in Figure 5.22.

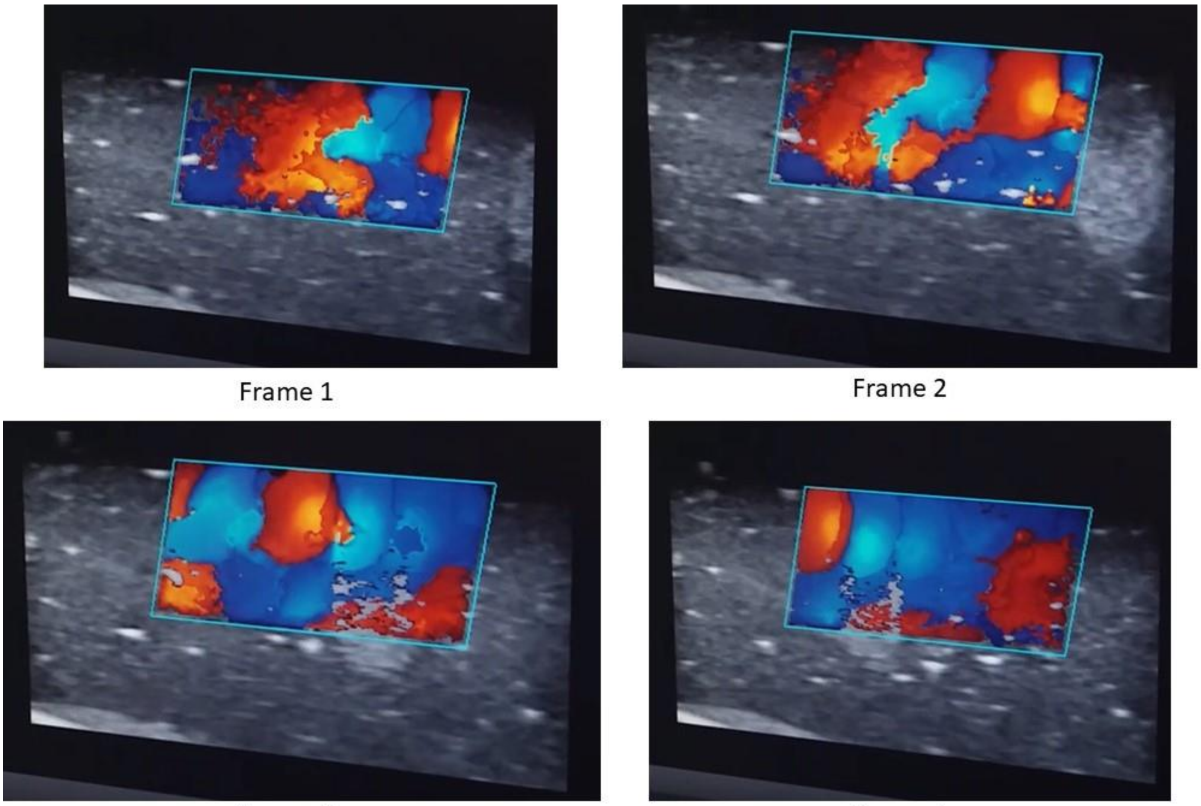

Figure 5.22: Four Colour Doppler frame images acquired with a Sonix scanner at CREATIS consortium (CNRS UMR 5220 - INSERM U1206 – Universite' de Lyon 1 – INSA Lyon – Universite' Jean Monnet Saint-Etienne). The images, with steering beam applied, show a clear mis-registration between the colour coded map and B-Mode.

5.3.8 Discussion

Ultrasound acquisitions performed on the Vortex Ring based Complex Flow phantom prototype point to its potential as an ultrasound QA flow phantom. B-mode, Colour Doppler and Pulsed Wave (PW) Spectral Doppler imaging were performed under the supervision of a Sheffield Teaching Hospitals NHS Foundation Trust ultrasound specialist. Travelling vortex rings, generated under initial conditions specified in Configuration 3 (Table 5.1), were imaged holding the probe at the top water surface (horizontal view, Position 2, Figure 5.10) and holding the probe into the water (frontal view, Position 1, Figure 5.11). Particularly, B-Mode and Colour Doppler imaging were performed with the probe in the horizontal position while PW Spectral Doppler was performed facing the probe to the travelling vortex ring direction. For all the acquisitions the phantom was filled with water and Orgasol^{TM} scattering particles (5 and 10 micron) were introduced into the piston/cylinder volume (Figure 4.4). B-Mode imaging is not commonly used for blood flow velocity estimation, but, it provided qualitative information about the vortex ring shape and has the potential to be used for measuring vortex ring dimensions. Colour Doppler ultrasound imaging provided qualitative and semi-quantitative information related to the velocity components parallel to the beam axis. B-Mode ultrasound, Colour Doppler ultrasound and Laser PIV techniques imaged the travelling vortex ring as two cores that rotate in opposite direction to each other as the ring propagates across the field of view. PW Spectral Doppler ultrasound acquisitions were performed, varying the probe orientation, Doppler Gate size and probe frequency. Angle correction was set to zero, so that detected velocities corresponded to the vortex ring translational velocity component plus (or minus) the rotational velocity component (Figure 5.10) and results were directly comparable with Laser PIV acquisitions. Encouraging agreement was found between peak velocities estimated with the two techniques (Laser PIV and PW Spectral Doppler ultrasound) on the same phantom prototype in two different experimental sessions. High frame rate Doppler ultrasound Vector Flow imaging was also performed on the prototype and highlighted the design potential for validating advanced vector flow estimation algorithms. Mis-registration between colour coded map and pulse-echo images was observed with two different scanners, operating (and calibrated) in two different countries (France and UK), with and without beam steering applied. The phantom has highlighted limitations of the correlation algorithms used in conventional Colour Doppler imaging, visible for the first time in the two machines. Other phantoms, such as rotating phantoms, flow phantoms and string phantoms (Section 1.6.2 and Section 1.6.3, Chapter 1) are too simple and have not been able to challenge the scanner at this level.

5.3.9 Conclusion

A Vortex Ring based Complex Flow Phantom prototype was scanned with conventional ultrasound imaging techniques (B-Mode, Colour Doppler and PW Spectral Doppler) in a clinical environment. Qualitative and quantitative information extracted from the images showed good agreement with Laser PIV measurements. Advanced Doppler ultrasound Vector Flow imaging algorithms were also exercised using research scanners. The vortex ring phantom prototype offers complex three-dimensional flow patterns in a controllable and reproducible environment. This is valuable in the context of QC, calibration and validation of Doppler ultrasound imaging techniques. Limitations of conventional Colour Doppler imaging algorithms were highlighted for the first time.

5.4 Discussion

Three Vortex Ring based Complex Flow phantom prototypes were built following technical specifications described in Chapter 4 with experiments performed on the prototypes to independently validate the design. The success of optical visualisation techniques (namely optical/video and Laser PIV) performed on two prototypes, two weeks apart, in two different premises is a tribute to the stability of the design. Vortex rings produced under a number of generating conditions were quantified. Vortex rings with translational velocities higher than 7 cm/s showed high stability and exhibited variability always lower than +/ 10 %. Furthermore, vortex ring generated with translational velocities between 50 cm/s and 80 cm/s were more dissipative in their early stages, exhibiting a noticeable decay of velocity as a function of distance travelled. In contrast, vortex rings produced with translational velocities between 10 cm/s and 30 cm/s showed almost steady translational velocities with little change in velocity across the phantom imaging tank. Velocities lower than 7 cm/s were more critical; generated vortex rings were diffusive, with a thick core and vorticity distribution tending to the Hill's fat limit (Section 2.3, Chapter 2). This corresponded with a combination of lower Reynolds number (compared to previous settings) and very low stroke length ratios (*L/D*) as generating conditions. The best generating conditions were a Reynolds number of ~6517 and *L/D* of ~3.92, which produced very stable vortex rings with translational velocity variability lower than +/- 5 %. The prototypes proved to be stable and reproducible over prolonged experiments. The robustness of the design was evident in the similarity of results acquired at the beginning and at the end of an arduous (more than 8 hours) experimental session.
After having independently established stability, controllability and reproducibility of the design with two measurement methods, two phantom prototypes were scanned with a clinical and a research

ultrasound scanner. Ultrasound B-Mode and Colour Doppler imaging, performed by placing the transducer orthogonal to the vortex ring propagation axis (Position 2, Figure 5.10), provided qualitative and semi-quantitative information on vortex ring shape and velocity flow field directions. In agreement with the Laser PIV visualisation technique, B-Mode and Colour Doppler showed two rotating cores propagating across the field of view. Pulsed Wave Spectral Doppler was performed with the probe facing the vortex ring propagation axis (Position 1, Figure 5.10) in order to have results directly comparable with Laser PIV technique. Spectral Doppler raw data were not available and peak velocity values were estimated from the ultrasound images. In addition, measurements were performed in water, which has a speed of sound of ~1482 m/s (Lubbers and Graaff 1998) at 20 °C. Ultrasound scanners assume a speed of sound of 1540 m/s in the medium and this mismatch provokes overestimation of dimensions and velocities. If a correction factor is applied, velocities listed in Table 5.3 are 3.8 % lower and average PW Spectral Doppler peak velocity (Table 5.4) is 39.94 cm/s. Although raw data was not available, peak velocities estimated from PW Spectral Doppler ultrasound and Laser PIV were in good agreement. A percentage difference of 5.7 % (value calculated considering the speed of sound correction factor for PW Spectral Doppler) was found between average values calculated from the acquisition of ten vortex rings. The phantom prototype was manufactured for CREATIS laboratory (CNRS, Lyon, France) within the VPH-CaSE network and high frame rate ultrasound Vector Doppler Flow Imaging was successfully applied by Badescu et al (2018). The unique phantom design highlighted interesting limitations of conventional Colour Doppler imaging reconstruction algorithms. Mis-registration between colour coded map and pulse-echo imaging was observed for the first time on two different ultrasound scanners calibrated in two different countries (France and UK). To the best of our knowledge, this is the first phantom technology able to challenge the ultrasound scanners at a complex and controlled level. Mis-registrations on the two scanners were observed for the first time by the operators, although the machines had been in use several years. This is despite the fact that calibration and quality control checks have been performed on the two scanners routinely, using commercial phantoms (i.e. flow and string phantoms).

Further improvements of the design are discussed in the following Chapter 6. Particularly, a linear encoder and a Laser diode system coupled with a photodiode receiving circuit were designed to create a reliable instrumentation package. The instrumentation pack provides a considerable amount of data that can be used for micro-flow characterisation, phantom self-calibration, energetic analysis etc. Micro-flow analysis may important for providing complete characterisation of the flow and to encourage the use of vortex ring as complex flow benchmark for advanced flow velocity estimation techniques (i.e. Vector Flow Imaging and 4D flow MRI).

5.5 Conclusion

The vortex ring offers three-dimensional flow patterns that resemble intra-cardiac vortices. Vortex Ring based Complex Flow Phantom prototypes were built to generate a flexible range of flows in a controlled environment. Stability and reproducibility of the flow, crucial for Quality Control purposes, were assessed with multiple measurement methods on two identically manufactured prototypes. Ultrasound compatibility was demonstrated through acquiring data from two prototypes with a clinical and a research scanner. Early results highlight the potential of the technology as an ultrasound complex flow test object for testing scanners operating both in conventional Doppler modes and advanced flow mapping modes. This is particularly valuable in a context in which available flow test objects in the market are inadequate and suffer from significant limitations (Sections 1.5.1 and 1.5.2, Chapter 1).

CHAPTER 6

Design improvements and instrumentation pack

6.1 Introduction

The specifications of the ring vortex phantom was presented in Chapter 4. Three prototypes were manufactured and multiple experiments independently demonstrated the credibility of the design. Ultrasound compatibility was proven through B-Mode, Colour Doppler, Pulsed Wave Spectral Doppler and high frame rate Vector Doppler.

However, limitations were apparent in the phantom design during the experiments. The piston/cylinder arrangement constitutes a critical component for phantom operation and any issues here can influence the system performance. Particularly, the piston incorporates a nitrile rubber O-ring that provides a seal between piston and cylinder. This has demonstrated significant stiction that may affect the reproducibility of the phantom during applications. Consequently, alternative piston/cylinder arrangements were investigated and a valid design is proposed below for improved confidence.

Experiments described in Chapter 5 provided valuable information at a macro-flow level about vortex ring fluid dynamics. However, micro-flow analysis may provide useful additional information on the vortex ring behaviour. This is helped by an instrumentation pack, consisting of a linear incremental magnetic encoder and an optical system and designed to further characterise system performance. Taking advantage of the piston design modifications, a groove compatible with the magnetic strip of a linear magnetic encoder was cut within the new modified piston stem. This complements an optical system, consisting of six Laser diodes and an array of six photodiodes, allowing collection of vortex ring translational velocities in real time. The instrumentation pack offers a cost-effective and reliable solution for phantom deployment that enables:

- self-calibration of the phantom without resorting to expensive and time-consuming techniques, such as Laser PIV;
- reproducibility checks on piston velocity profiles and vortex ring translational velocities;
- determination of main flow reference values;
- assessment of the impact of the piston velocity profile on vortex ring generation;
- assessment of motor input power needed for the generation of stable vortex rings;
- energetic analysis on vortex ring generation.

The new piston design, the encoder, the optical system and early experiments to prove the functionality of the instrumentation pack are described in detail in this chapter.

6.2 New piston design

6.2.1 Introduction

The original piston design incorporates a nitrile rubber O-ring to provide a sealed coupling with the cylinder. Nitrile rubber was used for the prototype described in Chapter 4. However, this material is particularly sticky when in contact with the internal Perspex (PMMA) walls of the cylinder. This implies a significant coefficient of friction during dynamic applications that may affect the reproducibility of the phantom. Experiments described in Chapter 5 were performed with the addition of petroleum jelly (Vaseline) as lubricant. This was crucial for obtaining uniform and reproducible piston displacements.

However, the phantom is specifically designed to be compatible with Ultrasound modalities. Accurate calibration or validation of Doppler Ultrasound technologies requires measurements to be performed with compatible blood mimicking fluids (BMF) rather than water. The water constitutes negligible Ultrasound attenuation (Zeqiri et al 2010) and lower speed of sound (typically assumed as ~1480 m/s at 20°C, Zeqiri et al 2010) compared to those of soft tissues (typically ~1540 m/s at 20°C, Zeqiri et al 2010). The BMF is designed to match blood properties in terms of (T = 22°C) speed of sound (1548 m/s, BS EN 61685:2002, IEC 61685:2001), density (1037 kg m^{-3}, BS EN 61685:2002, IEC 61685:2001), acoustic impedance (1.61 x 10^6 kg m^{-2} s^{-1}, BS EN 61685:2002, IEC 61685:2001), viscosity (4 x 10^{-3} Pa s, BS EN 61685:2002, IEC 61685:2001), attenuation (< 0.1 x 10^{-4} x f dB m^{-1} Hz^{-1}, BS EN 61685:2002, IEC 61685:2001) and backscatter coefficient ((1 to 10) x 10^{-31} x f^{4} m^{-1} Hz^{-4} sr^{-1}, BS EN 61685:2002, IEC 61685:2001). BMF recipes typically include synperonic N detergent surfactant (BS EN 61685:2002, IEC 61685:2001). Surfactants are compounds that naturally lower surface tension between two components, such as water and oil, and facilitate mixing. Consequently, lubricants cannot be used in the presence of BMFs because they will be ineffective within the phantom environment.

For this reason, alternative piston designs that do not require the addition of lubricants are needed for phantom Ultrasound compatibility.

6.2.2 Method

O-rings are generally an efficient and cost-effective sealing mechanism used in a wide range of static and dynamic applications. Several materials and coatings are commercially available, and a wide range of piston design approaches have been proposed in literature (i.e. Al-Ghathian et al 2005). The friction is influenced by the seal diameter, the amount of compression and types of materials involved. A balance should be chosen between these three parameters. A low O-ring compression results in leakage. On the other hand, friction increases significantly if the compression exceeds recommended limits (Al-Ghathian et al 2005). Different O-ring materials were evaluated in an attempt to find the optimal friction/sealing balance. Polytetrafluoroethylene (PTFE) O-rings and Fluorinated Ethylene Propylene (FEP) were recommended by several Manufacturers because of their low frictional coefficients. Test were run with both materials: PTFE exhibited a very low friction coefficient but insufficient elasticity and the piston leaked; FEP-Silicone (silicone core + FEP jacket) and FEP-Viton (viton core + FEP jacket) showed comparable or higher friction when compared to nitrile rubber. Consequently, a piston design that does not involve O-rings was considered.

Computer numerical control (CNC) machine tools allow the manufacture of plastic components from PMMA (Perspex) with very fine tolerances (sufficient to avoid the use of an O-ring). A piston distal-end-cap was machined from a block of PMMA with a CNC lathe tool. The (distal-end) cap was manufactured to match the internal dimensions of the cylinder component ("Cylinder", Figure 4.4, Chapter 4) with a tolerance of +/- 0.10 mm. The piston cap was glued into the compatible piston stem. The piston stem is hollow, in order to match the stepper motor screw ("Plunger", Figure 4.4, Chapter 4), and included a groove to match the dimensions of a magnetic strip of a linear encoder. CAD drawing of the piston design is shown in Figure 6.1.

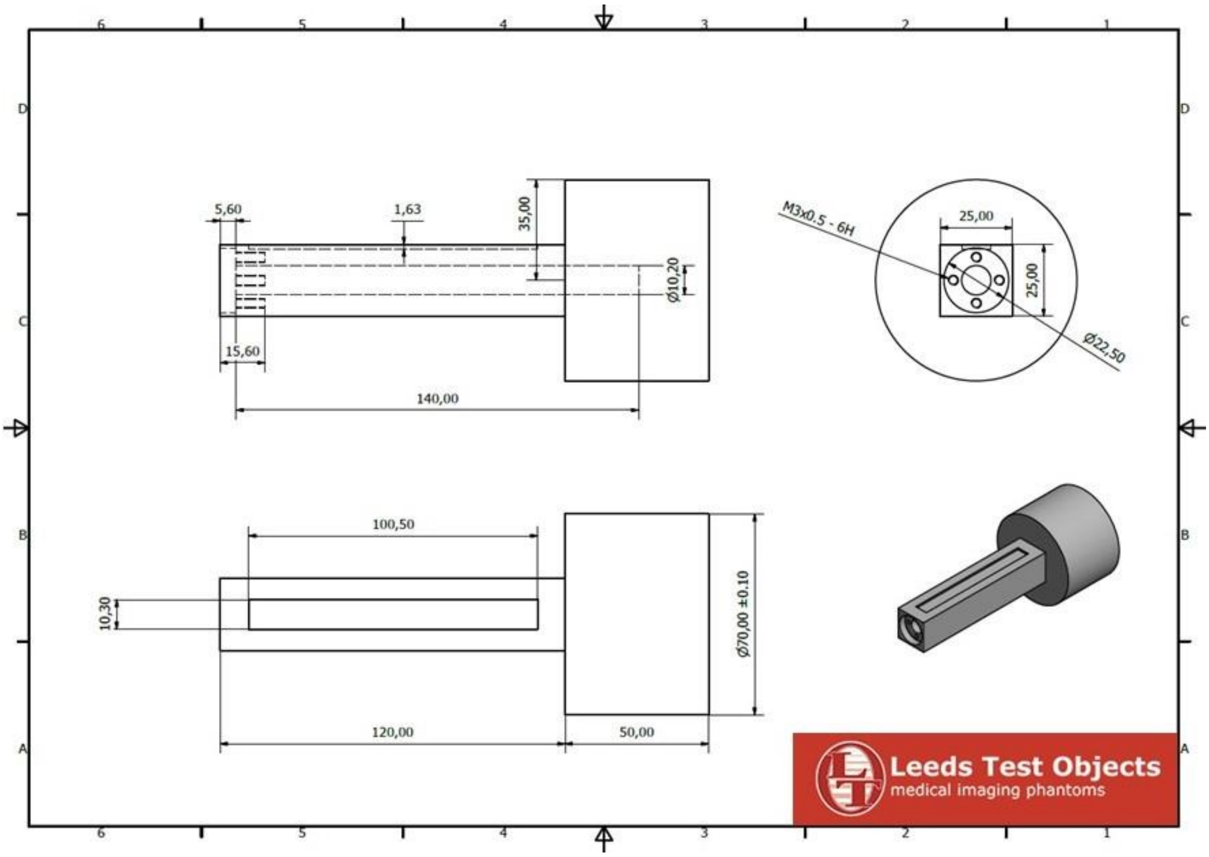

Figure 6.1: CAD drawing – Fine tolerance CNC machined Perspex Piston.

6.2.3 Assembled System

Assembly of the components depicted in the CAD drawing of Figure 6.1 produces the piston illustrated in Figure 6.2. The +/- 0.10 mm tolerance practically eliminates leakage while the smooth coupling PMMA/PMMA (piston cap/cylinder wall) delivers uniform piston displacements during dynamic applications. The engraved groove (10 mm W x 100 mm L x 1.63 mm H) on the piston stem is compatible with the magnetic strip of a Renishaw LM10 linear incremental magnetic encoder (Renishaw plc, Wotton-under-Edge, United Kingdom). Details about the encoder are provided in Section 6.3.2.

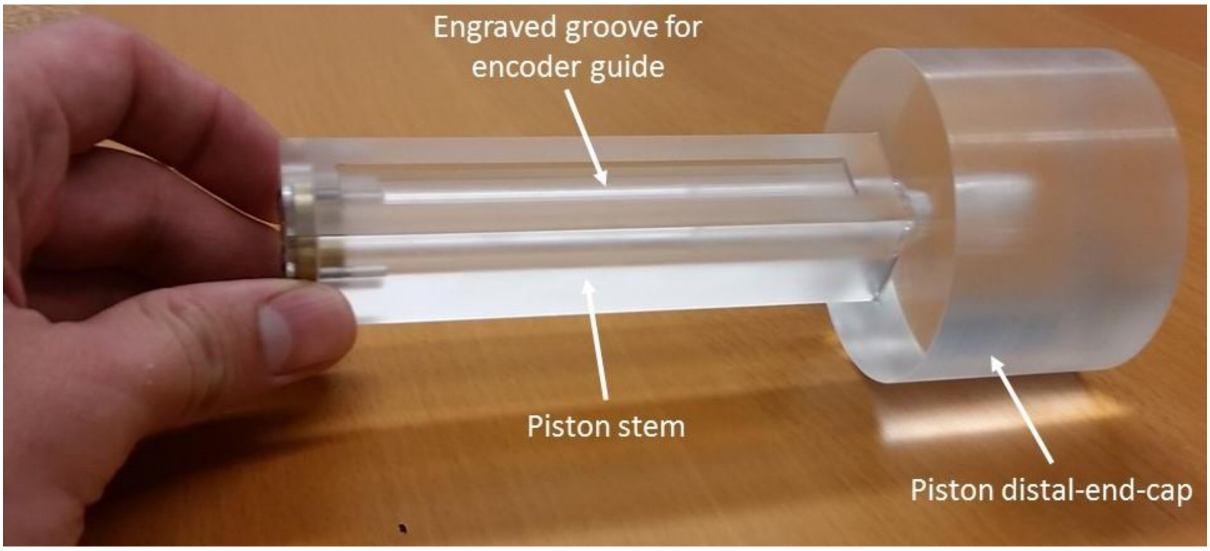

Figure 6.2: CNC machined Perspex piston.

6.2.4 Discussion

Doppler Ultrasound requires the use of compatible blood mimicking fluids (BMF) which contain surfactants. Surfactants naturally release the tensions between water and lubricants, facilitating the mixing. This adversely affects O-ring performance within the phantom. Consequently, a piston cap with +/- 0.10 mm tolerance was manufactured from PMMA (Perspex) to match the internal cylinder dimensions. PMMA/PMMA (piston/cylinder) surface and fine tolerances delivered minimal leakage and smooth coupling during dynamic applications. A groove compatible with the magnetic strip of a commercial linear incremental magnetic encoder was also cut within the piston stem. Description of magnetic encoder installation is provided in Section 6.3.2.

6.2.5 Conclusion

Limitations were found with the piston/cylinder arrangement during Ultrasound applications of the Vortex Ring based Complex Flow Phantom prototype (described in Chapter 4). The design promises smooth coupling with optimal sealing properties.

6.3 Instrumentation pack - Design

6.3.1 Introduction

An instrumentation pack was created to complement the new design and further support procedures such as phantom self-calibration, reproducibility testing, determination of main flow reference values under different generating conditions and collection of micro-flow level information. Although Laser PIV is effective and is considered the gold standard for fluid dynamics analysis, it is time-consuming, expensive and requires specialist expertise. This instrumentation pack obtains much of the confidence in the flow provided by the Laser PIV without the expense.

The proposed instrumentation pack consists of a high resolution linear magnetic encoder, affixed to the piston, and an optical system, attached to the imaging tank (“Imaging Tank”, Figure 4.3, Chapter 4). Since the vortex ring generation depends mainly on the piston velocity profile, the encoder provides crucial information about generating conditions, such as Reynolds number and stroke ratio. In addition, the optical system provides real time data about vortex ring translational velocities. By combining the information, it is possible for example to correlate each piston velocity profile with the generation of different vortex rings. A block diagram illustrating the instrumentation pack is depicted in Figure 6.3.

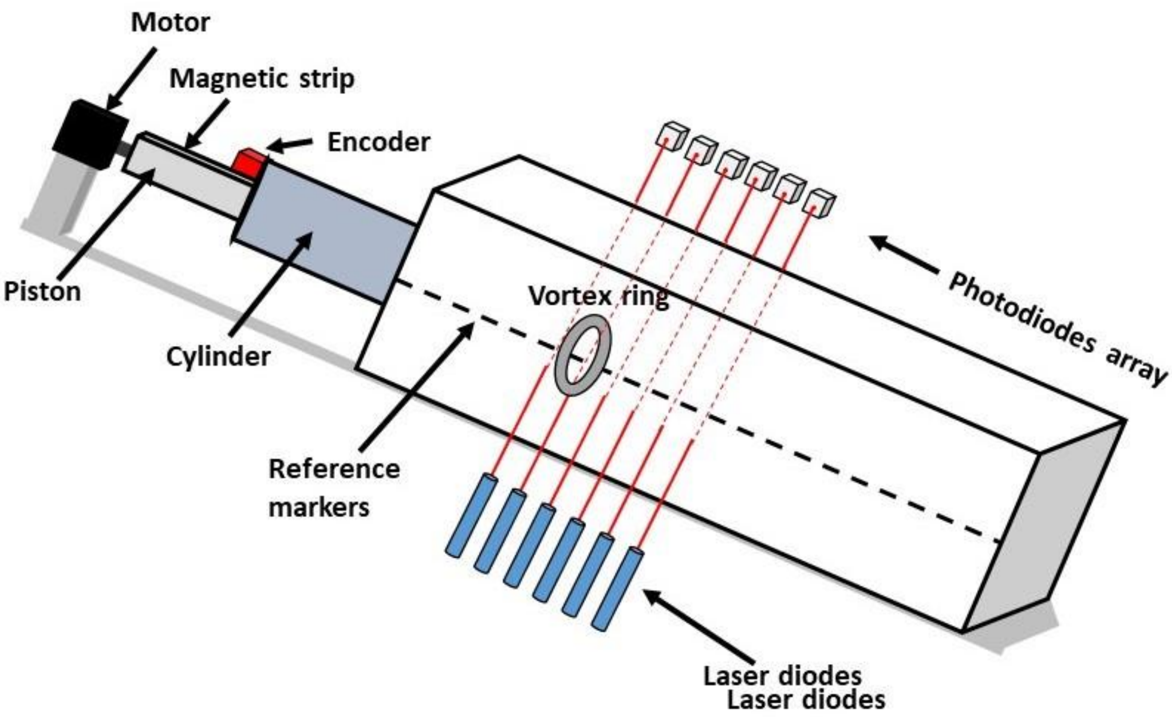

Figure 6.3: Block diagram of the instrumentation pack consisting of linear encoder, Laser diodes and photodiodes array. Please note that this is a schematic representation and elements are not to scale.

Several experiments were conducted with the instrumentation pack applied to the Vortex Ring Complex Flow Phantom prototype to demonstrate its utility. For improved clarity, details of the design and of the experiments are provided separately in Section 6.3 and in Chapter 7, respectively.

6.3.2 Materials - Linear Encoder

A magnetic scale strip was glued into the compatible groove cut into on the piston stem (Figure 6.2 and Figure 6.3). The piston guide (“Piston Guide”, Figure 4.4, Chapter 4) required slight modifications. A further Perspex part was machined (“Encoder Adaptor”, Figure 6.4) to match the dimensions of a Renishaw LM10 linear incremental magnetic encoder (Renishaw plc, Wotton-under-Edge, United Kingdom) and it was glued into the “Piston Guide” component (“Piston Guide”, Figure 4.4, Chapter 4). The LM10 is contactless, high-speed, with selectable resolutions from 0.244 µm to 250 µm and sampling frequencies from 0.05 MHz to 15 MHz. For the Vortex Ring based Complex Flow Phantom prototype, a LM10 with resolution of 1 µm and sampling frequency of 1 MHz was selected.

The encoder was fixed with three nylon screws to the compatible mounting part. As specified in the datasheet (https://www.klinger.fi/wp-content/uploads/migrated/attachment/RLS_LM10_inkrementti_datasheet.pdf), the LM10 is placed at a distance (ride height) of 0.1-1 mm from the magnetic strip with roll tolerance of +/- 3 %, pitch tolerance of +/- 3 % and yaw tolerance of +/- 1 %. The encoder incorporates an LED, which signals with a green light when the system is assembled within the specified tolerances. The LM10 provides selectable digital or analogue outputs. It is water-proof and resistant to shock, vibration and pressure (within a wide range limit). For this application, a LM10 with RS422 digital output was selected. The LM10 interfaces with a single channel encoder interface, E201 (Renishaw plc, Wotton-under-Edge, United Kingdom). The E201 has RS422 input, to receive the data from the encoder, and USB output to easily interface with any PC. The USB cable also provides power to the encoder, which uses a two-status LED to signal its activity. For improved clarity, all the components and the connections are illustrated in Figure 6.4.

Figure 6.4: Block diagram illustrating the encoder components, connections and installations.

A demo software application, which provides real-time reading of the encoder position, is provided by the Manufacturer. However, the demo software does not allow storing of the data for post-processing analysis. The Manufacturer also provides a MATLAB® (MathWorks, MA, USA) script with the main functions already implemented for encoder/Laptop interfacing. Exploiting the main functions provided by the Manufacturer, MATLAB® scripts can be easily written to collect encoder data. Typically, the encoder provides two outputs which refer to position and time. The two outputs can be easily stored in two arrays within a MATLAB® script loop. The velocity profile of the piston as a function of time can be calculated and plotted with the selected spatial and temporal resolution. However, the MATLAB® script reduces significantly the temporal resolution of the acquisition due to computational performance issues. Although the encoder transmits signals at 1 MHz, measurements performed with a Laptop Dell Inspiron 13–5000 Series (Inspiron 13, 5000 Series, Dell, USA) with 8th Generation Intel®Core™ i7-8565U Processor and 16 GB of RAM limited the temporal resolution of the acquisition to ~0.018 s. To the best of our knowledge, at the time of writing of the manuscripts (2018) no other software was available to store the encoder data and the MATLAB® environment was the only available option.

6.3.3 Materials - Laser diodes and photodiodes array system

A Laser diode array system and a receiving circuit (consisting of photodiodes) was built for the real time detection of vortex ring translational velocities. Six *mini* Laser diodes were connected in parallel to the 5 V output pin of an Arduino Mega board (Arduino, still unclear who the Owner is). The Laser diodes emitted wavelength of 650 nm (red light) with a power of 5 mW (Everything PI, Manchester, United Kingdom) and were compatible with Arduino and Raspberry Pi (Raspberry Pi Foundation, Cambridge, United Kingdom) boards. A base support was laser cut in order to keep the Laser diodes aligned at specific distances. Six arm-joints were 3D printed with specific dimensions for each Laser. Screws and nuts were used to keep the Laser diodes at the right height and to mechanically provide three degrees of freedom for alignment (Figure 6.6).

A 3D printed case hosts the Arduino Mega board and receiving circuit. The 3D printed case can be easily positioned on the opposite side of the Laser diodes assembly with a 3D printed hook, compatible with the dimensions of the phantom (Figure 6.6). Two screws on the sides of the 3D printed case provided positioning of the system to the desired level (height). The Arduino Mega Board controls the receiving circuit, it provides power for the Laser diodes circuit and receives signals from the Arduino Uno (Arduino, still unclear who the Owner is) that drives the phantom. All the components of the receiving circuit are soldered on a compatible Arduino Mega proto-shield 19.5 cm x 6.5 cm (SparkFun Electronics, Colorado, USA). The Laser diodes are powered through a mono jack plug connection 3.5 mm (RS Stock No 662-6239, RS Components Ltd, Corby, United Kingdom). The Arduino Mega board communicates with the phantom Arduino Uno board through a 4 pin din connector (Switch Electronics Ltd, Hull, United Kingdom), with the Arduino Uno sending a digital signal to the Arduino Mega few microseconds before activating the phantom (*triggerpin* digital pin described in Section 4.4.5, Chapter 4). This signal is used to automatically synchronise the two systems. A block diagram illustrating the Arduino Mega, Laser diodes and photodiodes connections is shown in in Figure 6.5. A photograph of Laser diode/arm joints assembly and the 3D printed case, which hosts the Arduino Mega and the photodiode receiving circuit, is shown in Figure 6.6.

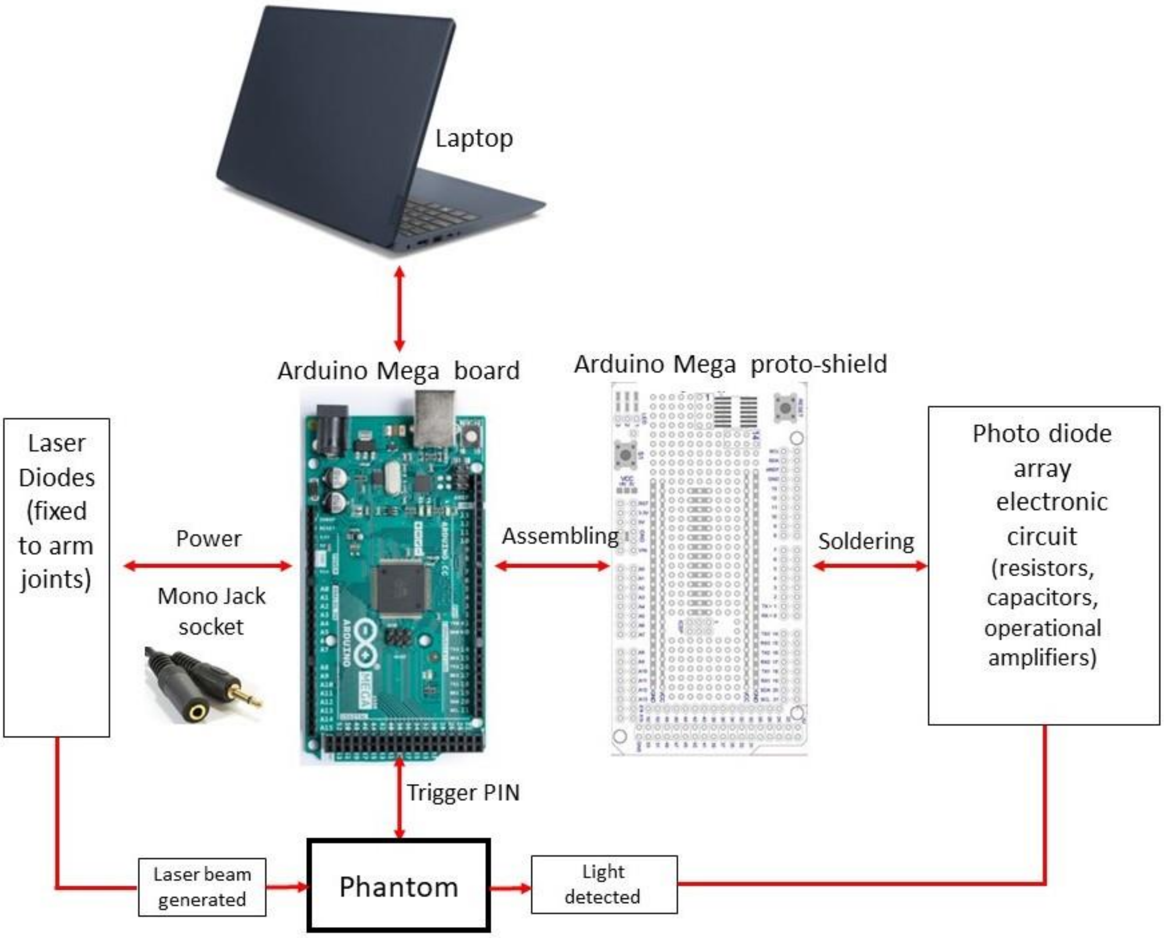

Figure 6.5: Block diagram illustrating Laser diodes and photodiode connections with the Arduino Mega board.

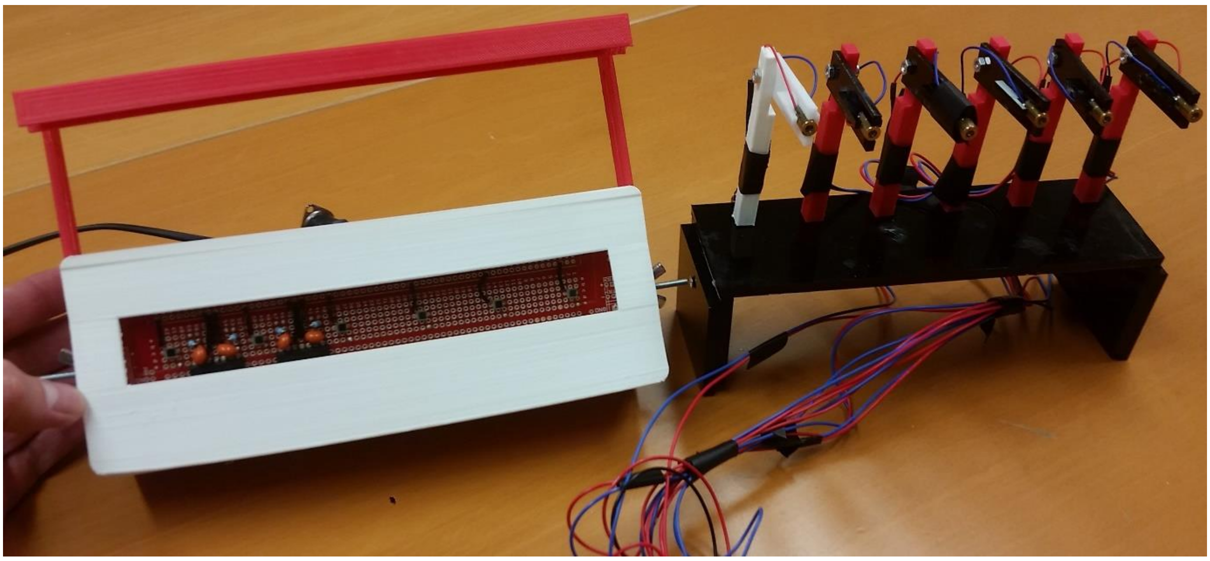

Figure 6.6: 3D printed case, with Arduino Mega Board and Receiving circuit soldered on a proto-shield (left), and Laser diodes assemblage (right).

6.3.4 Materials – Photodiodes receiving circuit

The receiving circuit consists of a system of six silicon-pin photodiodes BPW34 (Vishay Intertechnology Inc, Pennsylvania, USA) connected to two four-channel operational amplifiers LM2902KN (Texas Instruments Inc, Texas, USA). The BPW34 is a PIN photodiode with high speed and high radiant sensitivity to visible and near-infrared radiation. The sensitivity area of 7.5 mm^2 is almost square in shape. The LM2902KN is a 14 pins chip containing four independent, high gain, operational amplifiers designed to work with a single power supply 3-26 V. It has a typical gain bandwidth product of 1.2 MHz and typical slew rate of 0.5 V/µs.

The BPW34 photodiodes were connected in photovoltaic mode: the anodes (+) were connected to ground (GND) while the cathodes (-) were connected to the negative input of the LM2902KN operational amplifiers. The positive inputs of the LM2902KNs were connected to GND. In this configuration, the photodiode bias current is kept virtually at zero volts. This condition minimises dark current, noise and increases linearity and sensitivity (detectivity). The outputs of the operational amplifiers included negative feedback formed by a 5 MΩ resistor (RS Stock No 851-490, RS Components Ltd, Corby, United Kingdom) and a 1 pF ceramic single layer capacitor resistor (RS Stock No 831-2910, RS Components Ltd, Corby, United Kingdom). The resistance value was chosen to provide enough sensitivity but avoiding the saturation of the operational amplifier during signal acquisition. The central pins of the LM2902KN, Pin 4 and Pin 11, were connected to the ground line (GND) and to the power line (V_{CC} = 5 V) of the circuit, respectively.

The circuit configuration, shown in Figure 6.7, illustrates the use of transimpedance amplifiers (TIA). The TIA is a current voltage converter used in a wide range of applications with sensors.

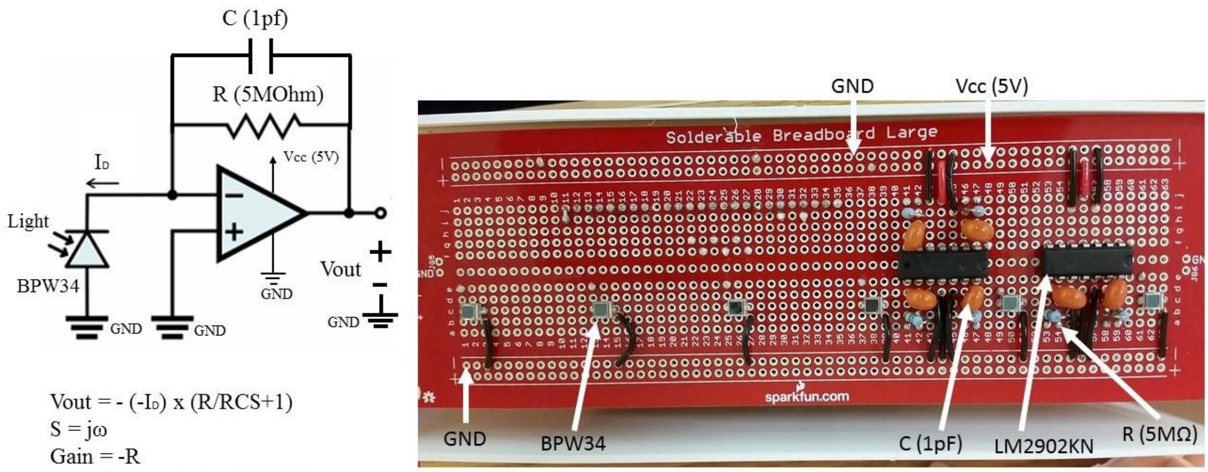

Vout = - (-I_D) x (R/RCS+1)
S = jω
Gain = -R
Cut off frequency = 1/ 2πRC
At low frequencies => Vout = -(-I_D) x R

Figure 6.7: Transimpedance receiving circuit consisting of BPW34 photodiodes, 5 MOhm resistance and 1pF Capacitor. When illuminated by the light, the circuit provides a voltage approximately proportional to the amount of radiation.

When illuminated by light, the photodiode generates a current approximately proportional to the power of radiation that strikes the active area. The current (*I_D*) flows from the cathode to the anode (in opposite direction of the arrow in the common diode representation, Figure 5.5). Ideally, all the output voltages of the LM2902KN generate a current through the feedback resistor (*R = 5 MΩ*) that compensates the photocurrent generated from the diode. A small capacitor (*C = 1 pF*) is connected in parallel to the feedback resistor to suppress unwanted signal oscillations and to ensure loop stability.

6.3.5 Method - Data Collection – Laser Diodes/Photodiodes - Arduino Software (IDE)

The Laser diodes/photodiodes data are collected by the analogic inputs of an Arduino Mega board. A basic script has been written in Arduino Software (IDE) to collect and store the data. A flow chart of the code is illustrated in Figure 6.8.

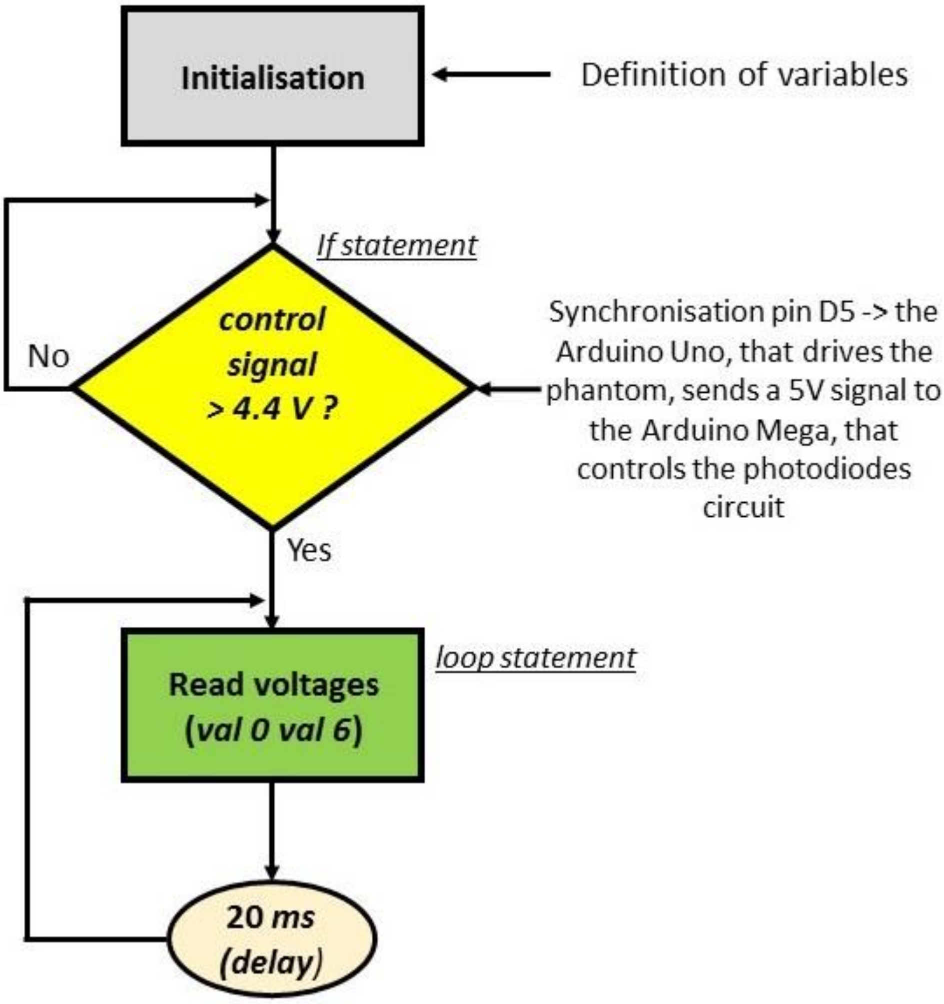

Figure 6.8: Flow chart of the Arduino Software code (IDE) for LM2902KNs voltage reading during vortex ring propagation. The instruction *delay(20)* correspond to a sample rate of 50 Hz (a sample each 20 milliseconds).

A *loop* is used to store the six output voltage values (*val0* to *val6*) in real time of the operational amplifiers (LM2902KNs). A delay of 20 milliseconds was introduced into the loop, in order to set a reading sample rate of 50 Hz (a sample each 20 milliseconds). The *loop* starts recording the analogue values (*analogRead*) when (*if*) the digital pin D5 (*triggerpin*, Section 4.4.5, Chapter 4) of the Arduino Uno Board that control the phantom sends a signal higher than 4.4 V (digital value, *HIGH*). This signal corresponds to the actuating pulse that generates a vortex ring. The sample rate, which is crucial for calculating the vortex ring translational velocity, has been tested in order to confirm the reliability of the reading circuit. For this, a LED was connected to a dedicated circuit and was programmed with an Arduino Uno board to flash with three different frequencies: 2 Hz, 1 Hz and 0.5 Hz. The receiving circuit was programmed with a sample rate of 50 Hz (sampling period of 20 milliseconds) in order to replicate the experimental conditions. Data were collected for five minutes for each of the three LED flashing frequencies. An average delay of 1.43 milliseconds (experimental reading 21.43 +/- 0.56 milliseconds) was found between the programmed reading and the experimental reading. Consequently, the sampling time used for vortex ring translational velocity calculation was 21.43 milliseconds (sampling rate 46.66 MHz) while the error (+/- 2.5 %) was considered negligible.

A snapshot of the *loop* that controls the data collection written on the Arduino Software (IDE) is shown in Figure 6.9, the code is reported in Appendix 9.

```
void loop()
{
  control=analogRead(analogPin15);
 if (control > 900)
  {
  val0 = analogRead(analogPin0);
  val1 = analogRead(analogPin1);
  val2 = analogRead(analogPin2);
  val3 = analogRead(analogPin3);
  val4 = analogRead(analogPin4);
  val5 = analogRead(analogPin5);// read the input pin
  Serial.println(val0);
  Serial.println(val1);
  Serial.println(val2);
  Serial.println(val3);
  Serial.println(val4);
  Serial.println(val5);
  delay(20);}
  }
```

Figure 6.9: Arduino script for LM2902KNs voltage reading. The instruction *delay(20)* correspond to a sample rate of 50 Hz (a sample each 20 milliseconds).

6.3.6 Method - Data Collection – Encoder- MATLAB®

Encoder data can be collected real-time and stored in the MATLAB® (MathWorks, Massachussetts, USA) environment. The E201 interfaces with MATLAB® software and provides real time information about the encoder's positioning and timing. Pre-set functions to activate the communications between E201 and MATLAB® environment are provided by the encoder Manufacturer (Renishaw plc, Wotton-under-Edge, United Kingdom). These functions need to be *"called"* into the main script and later can be modified on demand to perform the desired experiments. A flow chart of the MATLAB® script is illustrated in the schematic blocks depicted in Figure 6.10.

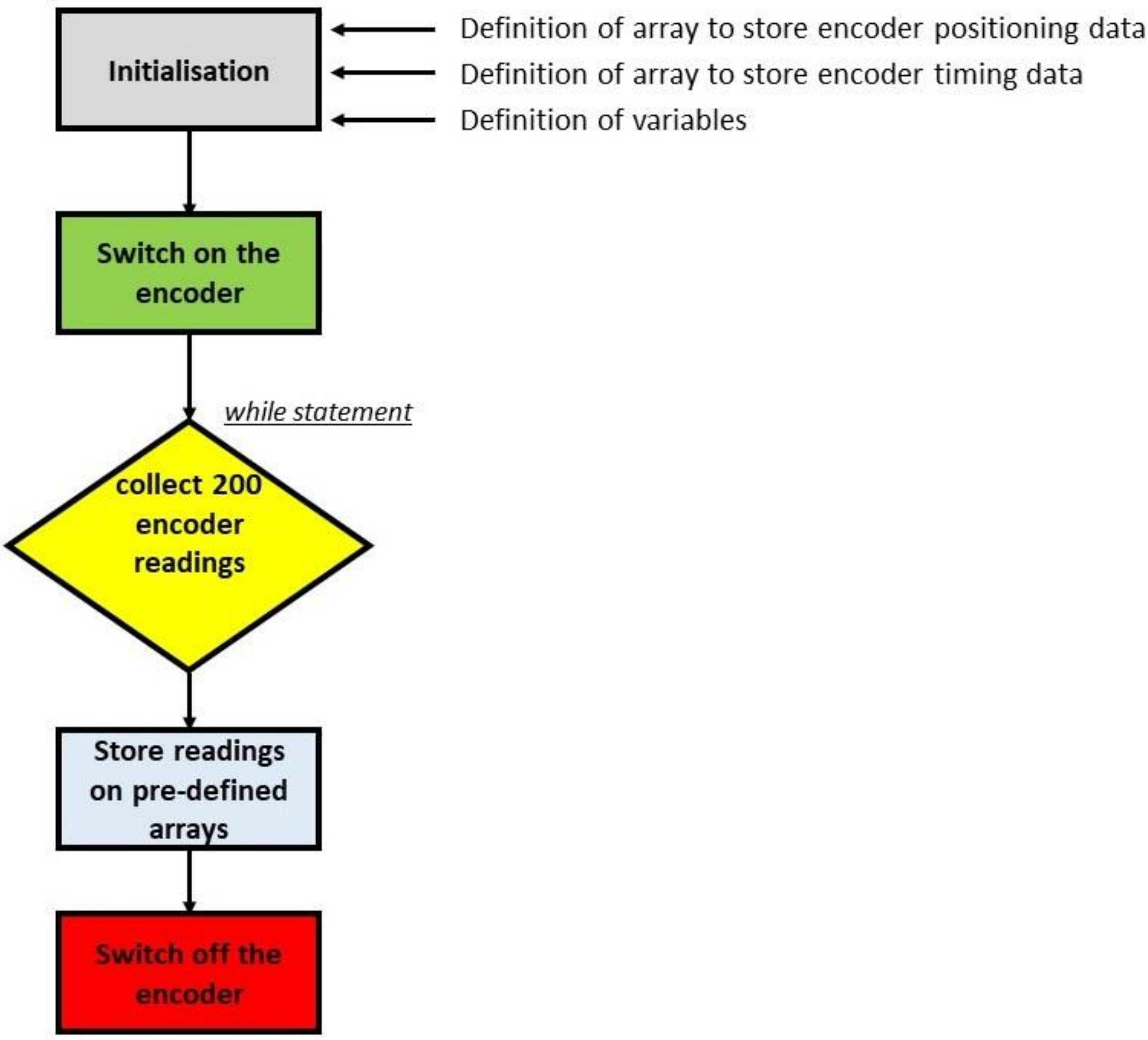

Figure 6.10: Flow chart of the MATLAB® script for encoder data collection during phantom piston action.

MATLAB® code requires the initialisation of variables and of two empty arrays for storing the encoder data (encoder positioning and encoder timing). A "*while*" loop was used to store 200 values in two different vectors. This guarantees continuous reading for about 3-4 seconds. Encoder position and time are stored in arrays called *Counter* and *Time*. Although the encoder transmits signals at 1 MHz, the temporal resolution of the MATLAB® *"while"* loop run with a Laptop Dell Inspiron 13 – 5000 Series (Inspiron 13, 5000 Series, Dell, USA) with 8th Generation Intel®Core™ i7-8565U Processor and 16 GB of RAM, was limited to ~ 0.018 s. This was tested with both encoder timing data and with the dedicated *"tic…toc"* stopwatch timer MATLAB® function, which is designed to measure elapsed time to perform required operations (http://matlab.izmiran.ru/help/techdoc/ref/tic.html). The *"while"* loop was run ten times and the sampling period was found to have a variability of +/- 0.02 %. This systematic error is negligible and was not considered in piston velocity profile calculations.

Similarly to the Arduino Software (IDE) implementation, a variable could be potentially used to synchronise the Arduino Uno that drives the phantom and the MATLAB® scripts that collect the encoder data. However, this proved to be challenging when working simultaneously with both encoder and Laser diodes/Photodiodes data collection systems, due to delays introduced into the communication (chain).

A snapshot of the MATLAB® script that illustrates the data collection (*while*) loop is shown in Figure 6.11, the code is reported in Appendix 10.

```
while i<200
    Enc_Count = E2019Q.GetEncCountDOUBLE(E2019Q_ID);
    Pos_Timestamp= E2019Q.GetTimestampDOUBLE(E2019Q_ID);
    Counter(i) = Enc_Count;
    Time (i) = Pos_Timestamp;
    %Velocity1(i) = Enc_Count/Pos_Timestamp;
    Enc_Reference=E2019Q.GetEncReferenceDOUBLE(E2019Q_ID);
    E2019Q.ClearReferenceFlag(E2019Q_ID);
    E2019Q.ResetCurrentCount(E2019Q_ID);
    E2019Q.ClearZeroOffset(E2019Q_ID);
    i= i+1;
end
```

Figure 6.11: MATLAB® script for LM10 linear encoder data collection. A *"while"* loop has been used to store position and timing data of the encoder

6.3.7 Results – Assembled System

Installing all the components described from sections 6.3.2 to 6.3.5 on a Vortex Ring based Complex Flow Phantom prototype provides the system illustrated in Figure 6.12. The magnetic strip is fixed to the piston stem and translates across the piston guide. The linear encoder is fixed through nylon screws to the piston guide adaptor, it communicates with the E201 encoder interface with the Laptop and provides information about piston displacement as a function of time. Laser diode and photodiode array circuits are connected to the Arduino Mega Board, which communicates with the Laptop and with the Arduino Uno board that drives the Vortex Ring based Complex Flow Phantom prototype. This allows synchronisation between piston action (vortex ring generation) and instrumentation pack data acquisitions.

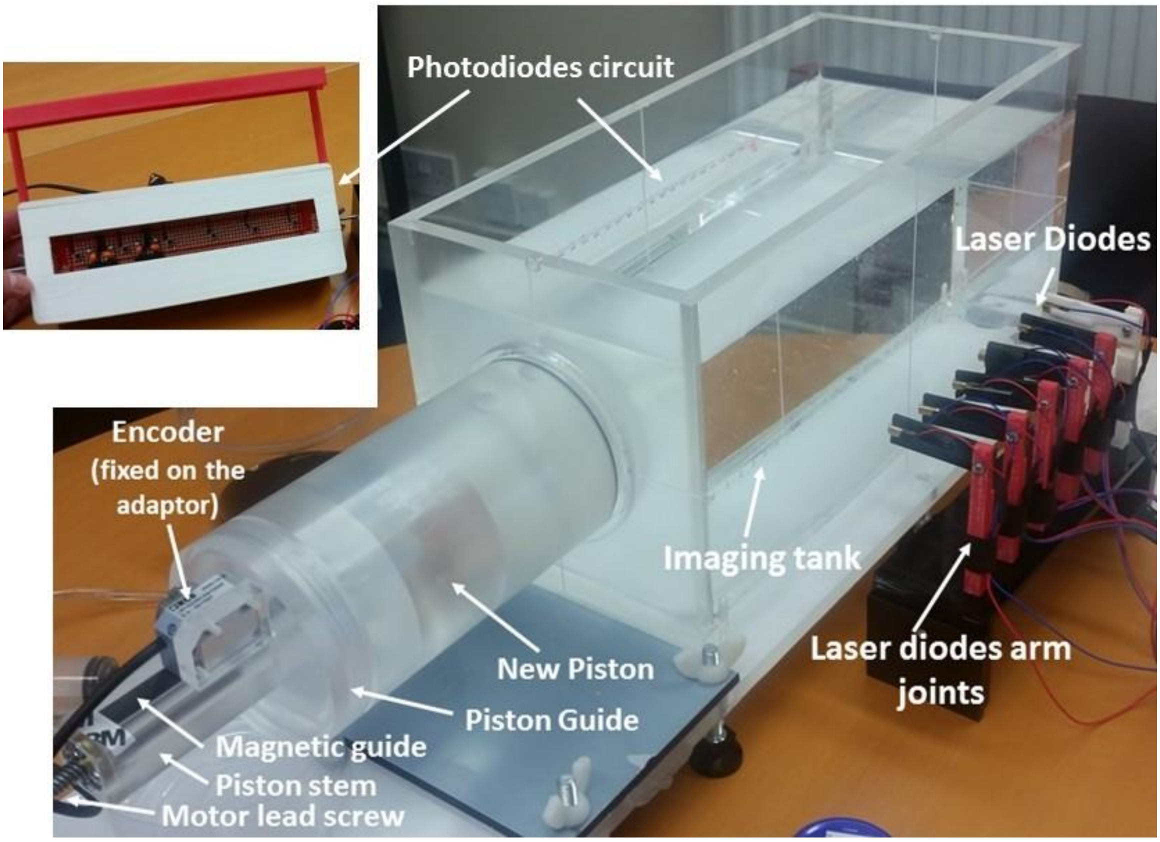

Figure 6.12: Instrumentation pack – Encoder, Laser Diode and photodiodes receiving circuit assembled on the Vortex Ring Based Complex Flow Phantom prototype.

6.3.8 Results - Demonstration and Application

Laser diodes and BPW34 photodiodes can be aligned using the engraved reference markers on the imaging tank ("Imaging Tank" reference markers, Figure 4.3, Chapter 4). Being positioned at the same known distance of 3 cm, each Laser diode points with a monochromatic (650 nm) straight beam to the corresponding BPW34 photodiode. The photodiodes were connected to the LM2902KNs which provides output voltage proportional to the intensity of light. Output voltages were read from the analogue input pins of the Arduino Mega board. Arduino Mega analogue pins A0 to A5 receive the output voltages from the LM2902KNs. The Arduino Mega analogue pin A15 receives a signal low (0 or ADC = 0) or high (5 V or ADC = 1023) from a digital pin (digital pin D5, *triggerpin*, Section 4.4.5, Chapter 4) of the Arduino Uno board that drives the phantom. The A15 signal is used for the synchronisation of the two systems. In normal conditions, the LM2902KNs are saturated (*Vout = 5 V +/- Amplifier Voltage Offset*) and the analogue inputs of the Arduino Mega receive a high signal of ~ 5 V (or ADC ~ 1023). When a vortex ring marked with dark food dye travels across the phantom, it creates shadowing of the Laser beams. Consequently, the output voltage of the corresponding operational amplifier drops. A thin layer of black paper was placed in front of the photodiodes to intensify the shadowing effect and to avoid disturbances from the external light of the room. Knowing the position of the Laser diodes, the position of the corresponding BPW34 photodiodes and the sample rate (50 Hz) of the reading signal, it is straightforward to calculate the translational speed of travelling vortex rings. The LM10 linear encoder is connected to the E201 and provides information on piston positioning and timing. These data are stored real-time in two empty arrays and post-processed to provide plots of piston velocity and displacement profiles as a function of time. Piston displacement (phantom action

– vortex ring generation), linear encoder LM10, Laser diodes and photodiodes receiving circuit are all controlled real-time by a single Laptop.

Figure 6.13, Figure 6.14 and Figure.15 show the experimental set-up with a vortex ring travelling across the system. The corresponding voltage-drop registered by the photodiodes and typical piston velocity and displacement profiles provided by the linear encoder, are also shown.

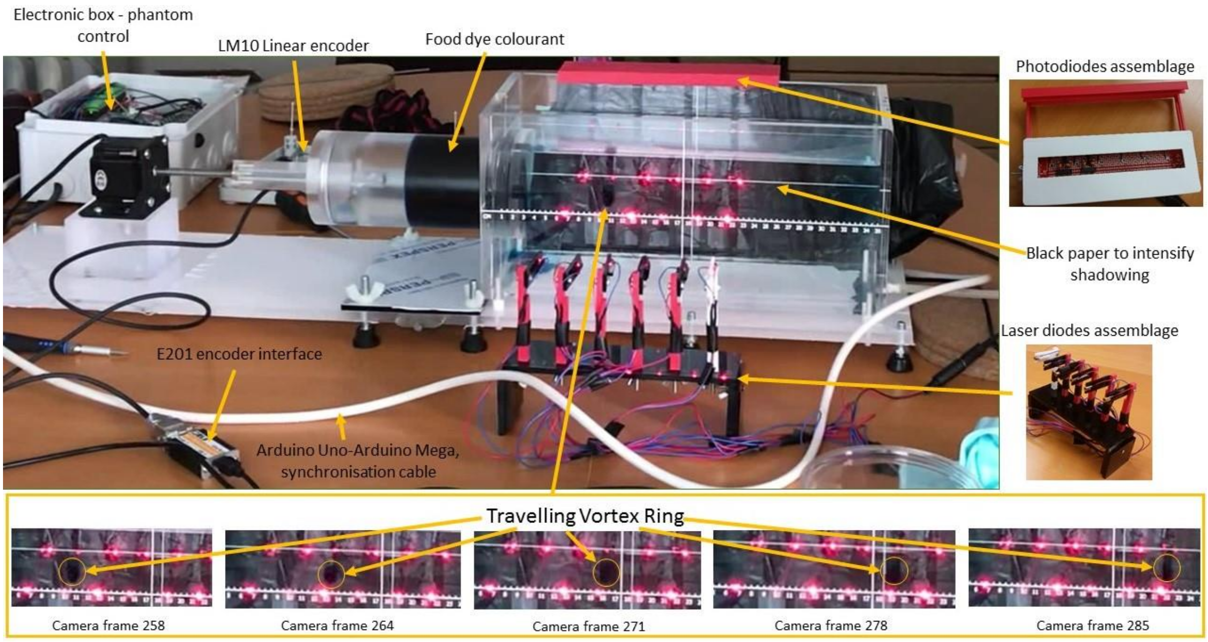

Figure 6.13: Experimental set-up for real time vortex ring translational velocity detection. The vortex, marked with dark food dye colourant, travels across the Laser beams, which creates shadowing that causes a drop in voltage reading in the photodiodes. As an example, five camera frame rates with the vortex travelling across the Laser beams are also shown. Encoder and E201 connections are also shown.

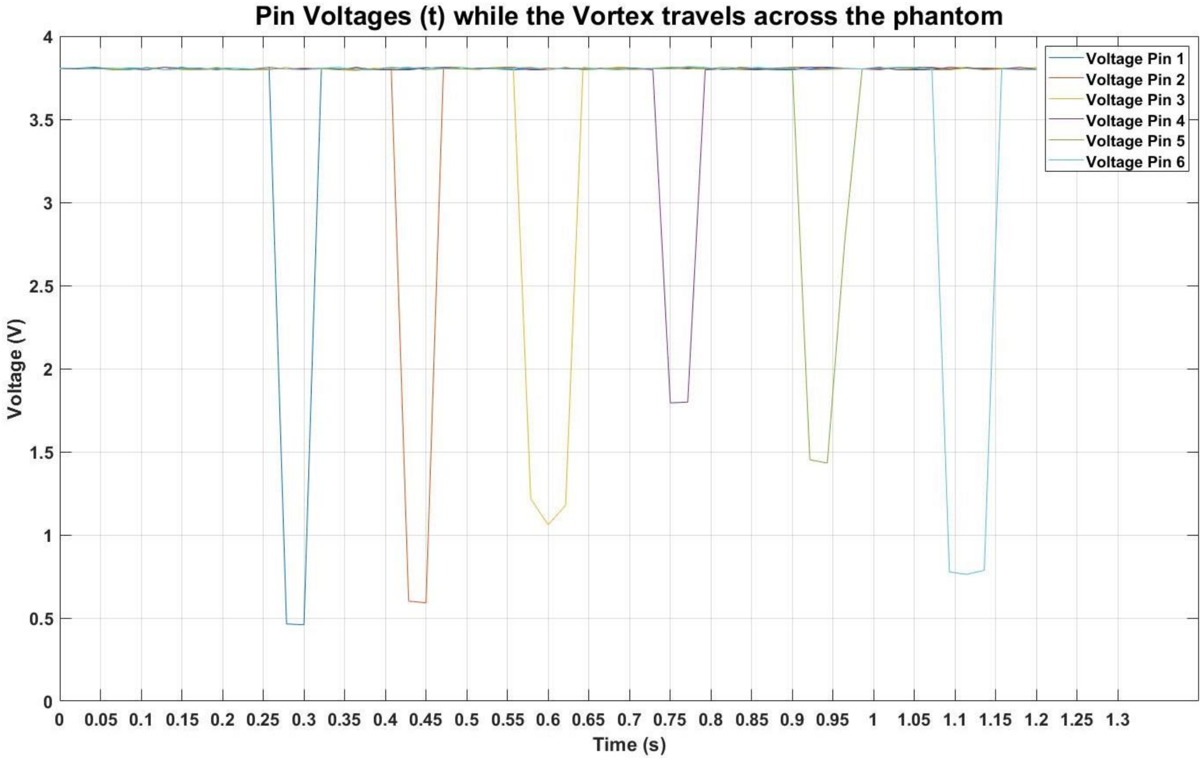

Figure 6.14: Receiving circuit data from the photodiodes – a voltage-drop is visible as the vortex ring travels across the laser beams.

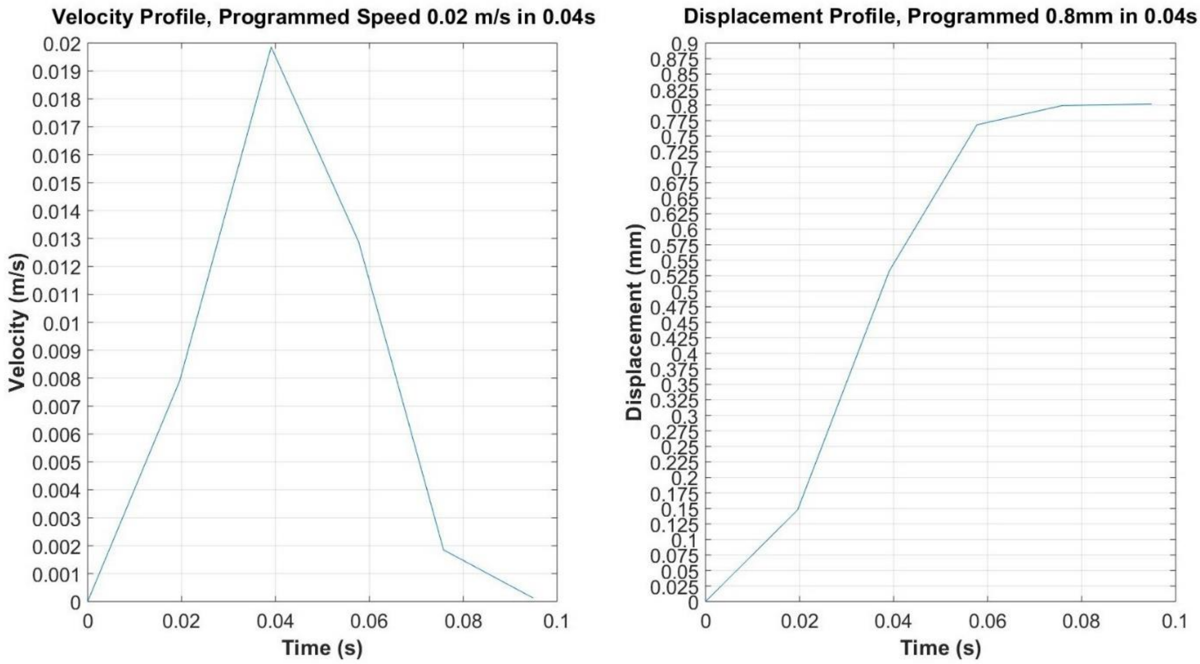

Figure 6.15: Encoder MATLAB® environment data – piston velocity profile and piston displacement profile during the generation of a vortex ring.

6.3.9 Discussion

An instrumentation pack tool has been built to provide relevant information and immediate feedback on the Vortex Ring based Complex Flow Phantom performance. The system is cost-effective and can be potentially used for several purposes such as:

- self-calibration of the phantom before performing an experiment;
- determination of reference values for different piston velocity profiles;
- assessment of the reproducibility of the phantom;
- assessment of the performance of the phantom.

The instrumentation pack consists of a magnetic linear encoder and a Laser diode/photodiode array system. The vortex ring generation depends mainly on the piston velocity profile and on the output orifice size. The orifice size is known and depends on which orifice is chosen (Figure 4.5, Chapter 4). The linear encoder, which is fixed on the piston stem, provides real time information about piston displacement as function of time. Consequently, the main vortex ring generating parameters (i.e. Reynolds number and stroke length ratio) can be determined with high accuracy and the Laser diode/photodiode array system provides real time information on vortex ring translational velocities. The phantom, the linear encoder and the Laser diodes/photodiodes system are all driven real-time by a single Laptop, so it is possible to collect data simultaneously and real-time from the three systems. A number of analysis might be conducted such as:

- correlating piston velocity profile with the generation of vortex ring with different translational velocities;
- calculating how much input power is needed for the piston to generate reproducible vortex rings (particularly valuable for reducing stepper motor overheating);
- performing a vortex ring energetic analysis.

Application of the instrumentation pack demonstrated functionality of the system. Data were simultaneously acquired from the encoder (in MATLAB® environment) and from the photodiode receiving circuit and result plots obtained. Sampling rate acquisition of the two systems, which are crucial for the piston displacement profile and vortex ring translational velocity calculations, have been assessed crossing the results versus independent and simple measurements methods. Sampling time systematic errors were found to be +/- 0.02 % and +/- 2.5 % for the photodiode receiving circuit and encoder reading, respectively. These values are negligible and are not considered in vortex ring translational velocity and piston velocity profile measurements. Encoder displacement data have a reproducibility better than +/- 1 µm, as declared by the Manufacturer datasheet. (https://www.rls.si/en/lm10-linear-magnetic-encoder-system). Laser diode/photodiode alignment is critical for the measurements and must be performed carefully to not introduce further noticeable systematic errors.

Attempts were made to automatically synchronise with a single MATLAB® script phantom operation, Laser diodes/photodiodes system and encoder reading. Unfortunately, all the attempts failed because of delays introduced by simultaneous communications between MATLAB®, Arduino boards and E201. Consequently, phantom and Laser diodes/photodiodes system were automatically synchronised, while the MATLAB® script was manually launched by the operator knowing the delay between each vortex ring generation. At the time of writing of the manuscript (2018), interactive communications between MATLAB® and Arduino Boards was improved compared to the 2017 designs (Chapter 3), but was still not optimal. Probably, improved MATLAB® packages will be released in future and a more powerful computer will allow the full synchronisation of the systems.

6.3.10 Conclusion

An instrumentation pack consisting of a linear encoder and an optical system has been built and installed on the Vortex Ring based Complex Flow Phantom prototype. The tool is simple to use, fast to set-up, cost-effective and requires connection through USB to a single Laptop. Crucial data on vortex ring fluid dynamics and phantom performances can be collected in real time without resorting to expensive and time-consuming measurement methods, such as Laser PIV. Functionality and reliability of the instrumentation pack was demonstrated and basic results are encouraging. Being confident that the tool provides reliable results, experiments were conducted on a Vortex Ring based Complex Flow Phantom prototype to further characterise the system. Experiments, methods and results are described in detail in following Chapter 7.

6.4 Discussion

Limitations were found during Doppler Ultrasound application with the original Vortex Ring based Complex Flow Phantom design. Particularly, the piston/cylinder arrangement involved a rubber O-ring which created stiction during dynamic applications. Consequently, lubricants were used to deliver smooth and uniform piston displacements. However, Doppler ultrasound requires working with blood mimicking fluids, which commonly contain surfactants which compromise lubricants, so a new piston was manufactured from PMMA (Perspex). Low tolerances (+/- 0.10 mm) and the PMMA/PMMA interface delivered smooth coupling with guaranteed minimal leaking. Taking advantage of the re-manufacturing of the piston, installation of a magnetic strip enabled use of an incremental encoder.

The combination of linear encoder and of a Laser Diode/Photodiode array system offers valuable instrumentation. The instrumentation pack provides real time information about the Vortex Ring based Complex Flow Phantom performance. With the encoder fixed on the piston stem, data is provided on piston displacement profile as function of time. The Laser Diodes/Photodiodes array system is placed on the imaging tank with dedicated 3D printed holders and provides information on vortex ring translational velocities. Self-calibration of the phantom, determination of vortex ring translational velocities reference values and phantom reproducibility checks are just some examples of operations that can be easily implemented. Details of the instrumentation pack design, methods for data collection and potential systematic errors have been discussed within the chapter. Application and demonstration of the functionality of the system were also described. A number of experiments, conducted in order to further characterise phantom and flow performance, are described in detail in the following chapter (Chapter 7).

6.5 Conclusion

A new piston was manufactured to overcome the limitations highlighted during Doppler Ultrasound acquisitions on Vortex Ring based Complex Flow Phantom prototypes. The new piston design also offered the possibility to install a linear encoder. A Laser Diode/Photodiode array system was designed and manufactured to measure real time vortex ring translational velocities. The linear encoder together with the Laser Diode/Photodiode array system constitute a powerful instrumentation pack that offers the possibility of clarifying performances of the phantom and of the flow without using expensive and time-consuming measurement methods. The system is simple, easy to set-up, reliable, cost-effective and only requires USB connection to a Laptop for data collection. Independent measurement methods were used to further test the reliability of the instrumentation pack.

CHAPTER 7

Instrumentation Pack – Experimental Analysis

7.1 Introduction – System reproducibility (Early Experiments)

An instrumentation pack adds value to the Vortex Ring based Complex Flow Phantom and details have been discussed in Chapter 6. Data collection methods involving a linear encoder and photodiode receiving circuit were also described in detail. Tolerances and reliability of the system were clarified and demonstrate that the tool is cost-effective. It proved to be reliable and was easily installed on a Vortex Ring based Complex Flow Phantom prototype. Core information about phantom performance and flow features can be easily extracted in real-time, and therefore a number of additional experiments have been conducted with the instrumentation pack in order to better characterise the phantom. These are described in detail within this chapter.

Experiments were progressive, therefore, they are described separately and discussion of critical sections are provided for each of them. Data of interest collected from earlier experiments was also used for later analysis.

Three main experimental sessions were conducted with the aim of:

- Confirming value of having an instrumentation pack;
- Reviewing piston velocity profile and displacement reproducibility;
- Comparing programmed versus experimental piston velocity and displacement profiles;
- Assessing the impact of piston action variability on the variability of vortex ring generation;
- Evaluating if lower input motor power can be used with comparable phantom performance to reduce overheating;
- Assessing dependencies of motor performance on different piston loads (different piston positions or different orifice sizes);
- Conducting an energetic analysis on vortex ring fluid dynamics.

Experimental methods and results are described below.

7.2 System reproducibility (Early Experiments)

7.2.1 Introduction

The first experimental session was performed to assess the reproducibility of piston velocity and piston displacement profiles, and to determine the impact of this variability on vortex ring generation. Data were collected simultaneously with the encoder and Laser diodes/photodiodes system in order to assess piston and vortex ring variability. The piston was placed at three different initial positions to estimate potential systematic errors (i.e. different motor performances with different piston loads or piston alignment errors). Methods and results are described in the following sections.

7.2.2 Method

Acquisitions were performed on ten vortex rings at different initial piston positions (Table 7.1 and Figure 7.1). Programmed piston displacement was 0.8 mm while programmed piston velocity was 2 cm/s (calculated as programmed displacement divided by programmed time). Motor input settings were 36 V and 2.69 A (rms current), which deliver a power of 96.84 W. Data were collected simultaneously from the LM10 linear encoder and Laser diodes/photodiodes system following the methods described in previous sections 6.3.5 and 6.3.6 (Chapter6). Post-processing was performed in MATLAB® and results were plotted, as illustrated in pervious section 6.3.8 (Chapter 6).

The test was conducted to:

- assess vortex ring translational velocities generated from different piston positions, which corresponds to different piston loads;
- assess vortex ring translational velocity reproducibility;
- assess total piston displacement and its reproducibility;
- assess average peak piston velocity and its reproducibility;
- assess average piston velocity and its reproducibility;
- assess the impact of piston variability on vortex ring generation;
- compare programmed total piston displacement with experimental total piston displacement;
- compare programmed average piston velocity with experimental average piston velocity.

Initial piston positions are listed in Table 7.1 and are illustrated in Figure 7.1. The piston was placed manually in position and the distance from the orifice was measured with a ruler. Consequently, a tolerance of +/- 2 mm is associated with the starting position as indicated in the table below.

Position	Ring vortex generated	Piston Position (+/- 2 mm)
1	Vortex 1, Vortex 2, Vortex 3	10 cm from the orifice, moving progressively forwards
2	Vortex 4, Vortex 5, Vortex 6, Vortex 7	7.5 cm from the orifice, moving progressively forwards
3	Vortex 8, Vortex 9, Vortex 10	5 cm from the orifice, moving progressively forwards

Table 7.1: System reproducibility - piston positions tested with instrumentation pack.

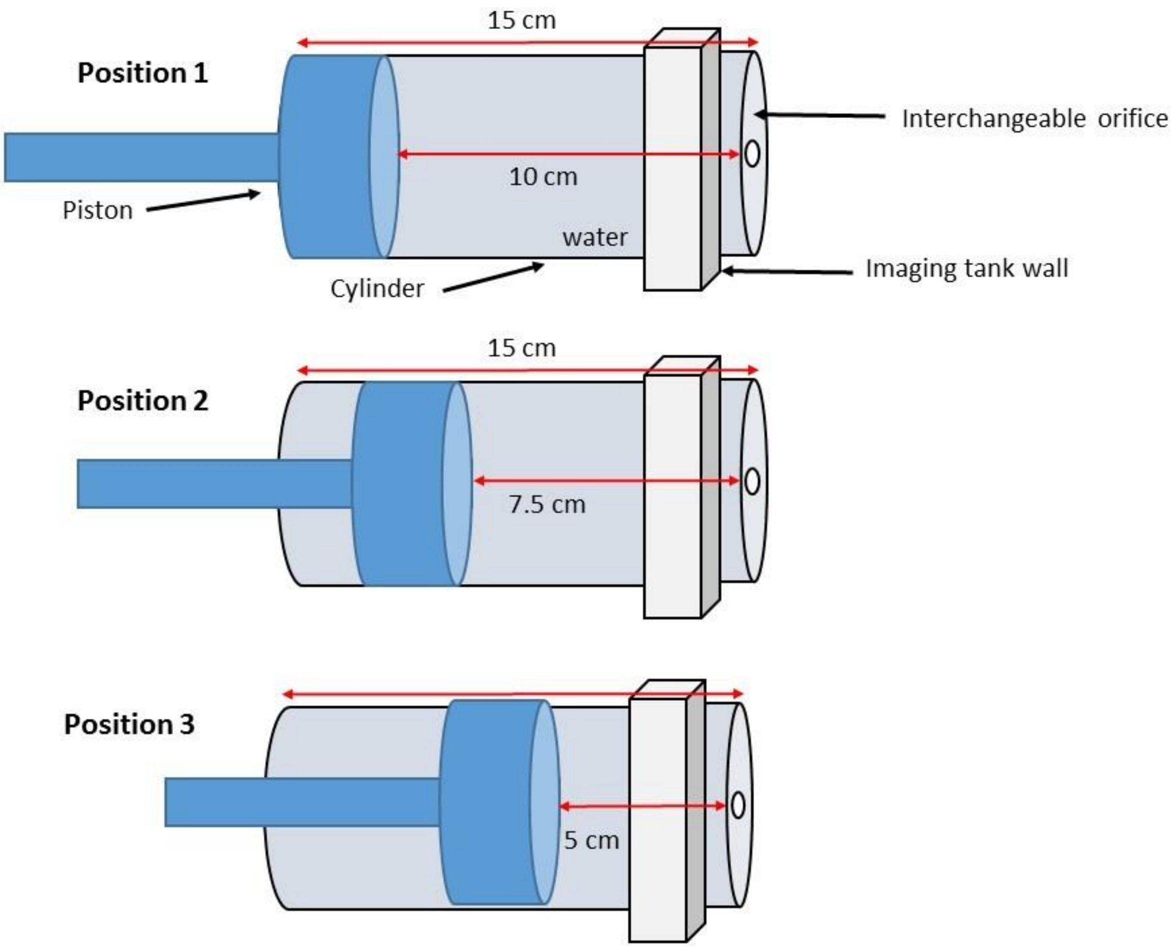

Figure 7.1: Schematic illustration of piston positioning listed in Table 7.1. Please note that this is a schematic representation and elements are not to scale.

7.2.3 Results

Piston velocity profiles (as a function of time), piston displacement profiles (as a function of time) and translational velocities (as a function of tank position) of the corresponding vortex ring generated are plotted in Figure 7.2a, Figure 7.2b and Figure 7.2c, respectively. Data were acquired with the piston initial positions listed in Table 7.1 and illustrated in Figure 7.1.

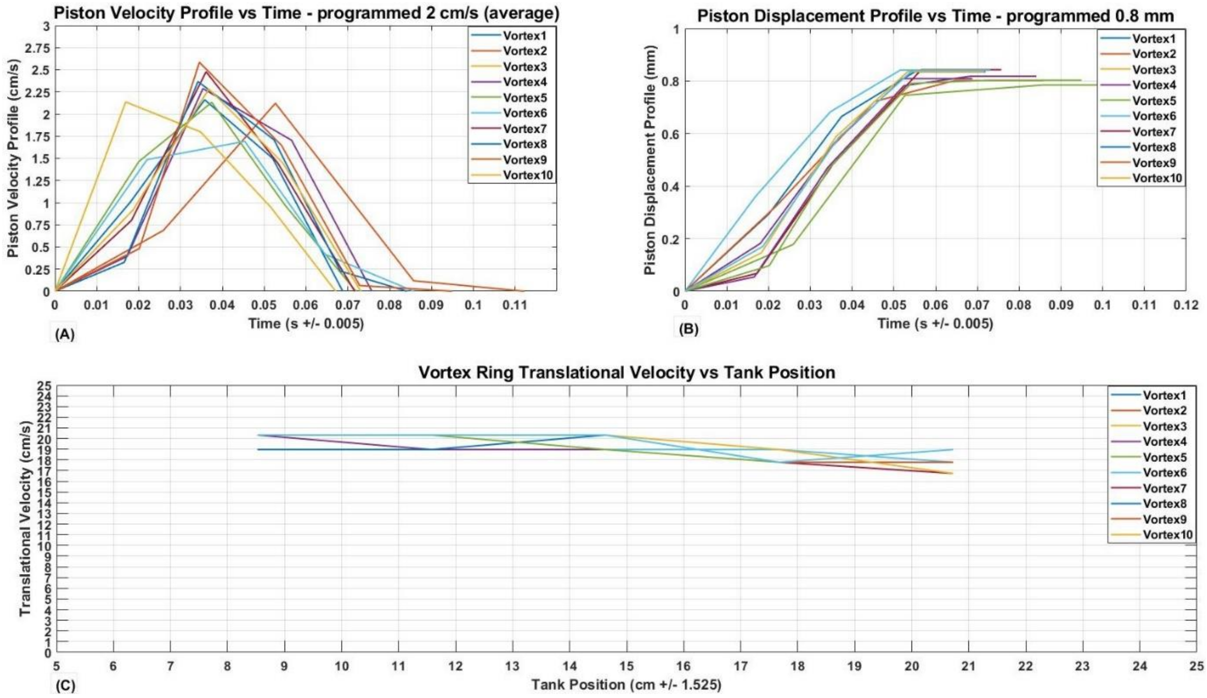

Figure 7.2: Plots of the piston velocity profile (top left), piston displacement profile (top right) and translational velocity of 10 vortex ring generated.

Average piston velocity profile (as a function of time), average piston displacement profile (as a function of time) and average vortex ring translational velocity (as a function of tank position) were calculated from the acquisition of ten consecutive vortex rings and are plotted in Figure 7.3 plot (A), (B) and (C), respectively. Error bars refer to standard deviation values (+/- 1 SD) also calculated on the acquisition of ten consecutive vortex rings. Percent errors (standard deviations divided by average values in percent) in vortex ring translational velocities were always within +/- 6 %. On a programmed total piston displacement profile of 0.8 mm, an experimental value for the piston of 0.8166 +/- 0.02533 mm (variability +/- 3.1 %) has been estimated. Finally, peak velocities of 2.19 +/- 0.28 cm/s (variability +/- 12.78 %) and average velocity of 1.44 +/- 0.2 cm/s (variability +/- 13.88 %) have been estimated on a programmed average piston velocity of 0.02 cm/s. All the errors (+/- %) have been calculated as the standard deviation divided by the average value in percent.

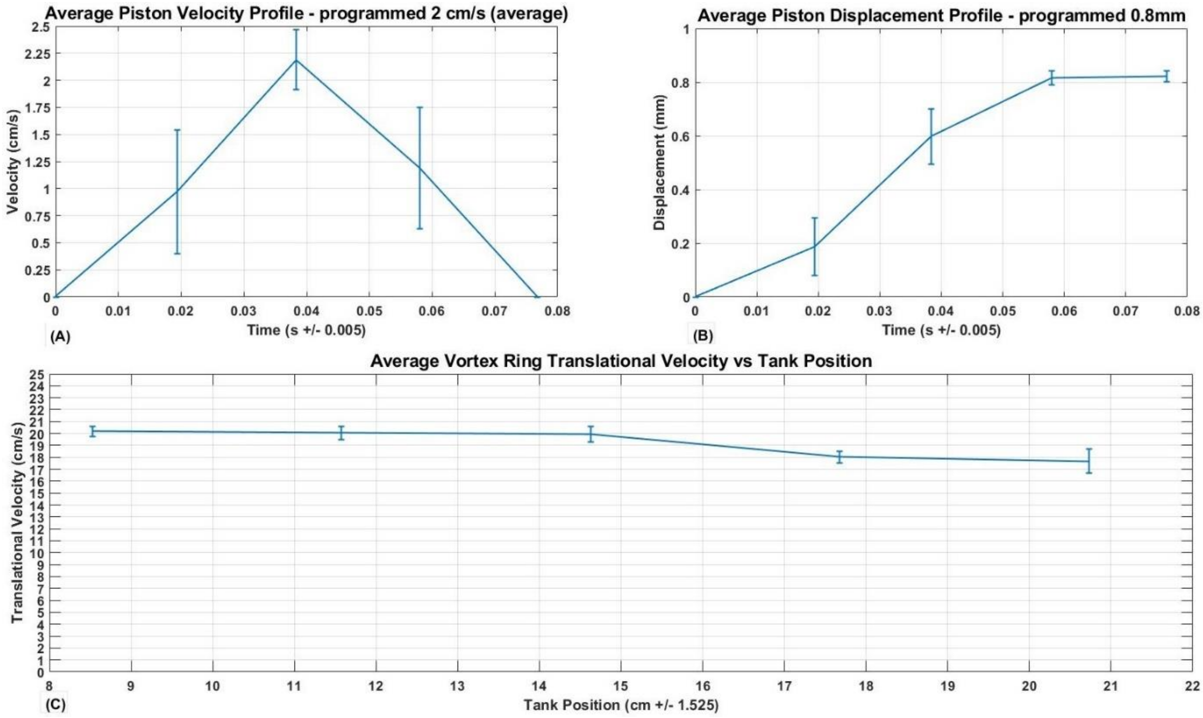

Figure 7.3: Plots of the average piston velocity profile (top left), average piston displacement profile (top right) and average vortex ring translational velocity. Average values calculated on the acquisition of ten vortex rings. Error bars refer to standard deviation on the acquisition of ten vortex rings.

Piston peak velocity values were calculated and were plotted against vortex ring peak translational velocity values (Figure 7.4a). Typical reproducibility error of +/-10 % in vortex ring velocity is represented as an error bar. Average piston velocity values were calculated for each vortex ring dividing the final displacement by the time spent to reach it. Values were plotted versus translational velocity values (Figure 7.4b). Although variability in piston peak and average velocities was notable (+/- 12.78 % and +/-13.88 %, respectively), this seems to not significantly affect the vortex ring generation.

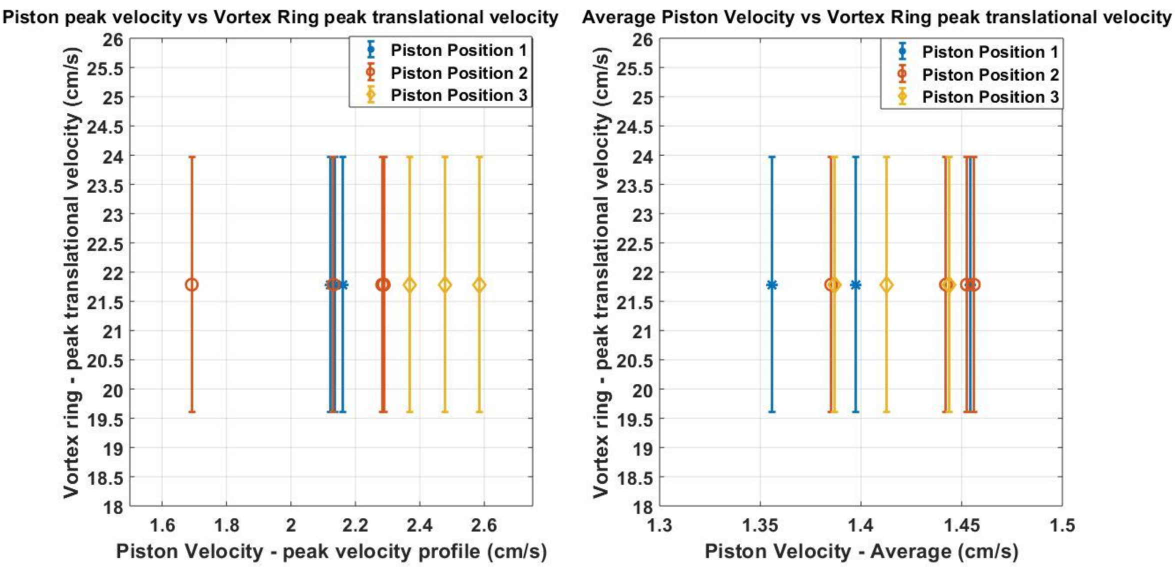

(a) (b)

Figure 7.4: Correlation plots – vortex ring peak translational velocity vs piston peak velocity (a) and vortex ring peak translational velocity vs piston average velocity calculated from final displacement and timing data (b). Peak velocity and average values measured do not significantly influence the vortex ring generation.

7.2.4 Discussion

These early experiments evaluate performance of the motor and the reproducibility of the vortex ring translational velocity. The acquisitions test if the initial piston position (which corresponds to different piston loads) influences the translational velocity of the vortex ring produced. No significant differences were found between translational velocities of vortex rings generated with the piston in position 10 cm (Position 1, Table 7.1 and Figure 7.1), 7.5 cm (Position 2, Table 7.1 and Figure 7.1) and 5 cm (Position 3, Table 7.1 and Figure 7.1) from the orifice. This effect is discussed more in detail in Section 7.3, however, Figure 7.4 clearly demonstrates that for an input power of 96.84 W the translational velocity of the vortex ring generated is not influenced by the piston load. Because the vortex ring generation was independent of the initial piston for 96.84 W motor input power, average values and standard deviations for the whole cohort were calculated. Vortex rings were generated with translational velocity errors lower than +/- 6 %. Peak velocity, average velocity and total displacement of the piston demonstrated variability lower than +/- 13 %, +/- 14% and +/- 3 %, respectively. Although variability was found for piston peak and average velocity estimation, this seems to not significantly affect the generation of vortex rings.

7.2.5 Conclusion

Early experiments performed on the Vortex Ring based Complex Flow phantom prototype have demonstrated the usefulness of the instrumentation pack. A considerable amount of information about the phantom performance can be obtained in real-time. For a set motor input power of 96.84 W, the vortex ring generation is not influenced by the initial piston position (piston load). Further experiments are conducted to assess the effects of different motor power at different piston positions (piston load) and to clarify the energetics involved in the vortex ring generation.

7.3 Different combination Piston/Loads – Motor inputs Power – Linear Encoder Acquisition

7.3.1 Introduction

An important limitation of the system concerns the overheating of the motor during prolonged experiments. All experiments have been performed with a motor current of 2.69 A (rms) and imposing a minimum delay of 20 seconds between the generation of consecutive vortex rings to minimise the overheating. This is true for all Laser PIV, optical/video and Ultrasound acquisitions, described in Chapter 5, and instrumentation pack acquisitions described in previous section. The 20 second restriction is effective in limiting the overheating of the motor during prolonged applications. The current (2.69 A, RMS) was selected to be the closest to the maximum motor requirements (3 A), supplying maximum power to achieve precision delivery of a fluid impulse to generate the ring. To reduce motor overheating, the enabling signal temporarily switches off the current between vortex ring generations.

However, the stepper driver DM542 (Section 4.3.4, Chapter 4) has a DIP switch that controls eight pins (SW1 to SW8). Pins SW1, SW2 and SW3 ("PA setting" in Figure 7.5, Table 7.2) can be manually set in ON/OFF positions to select the dynamic current delivered to the motor, thus regulating the motor input power. The experiments, described in Section 7.1, demonstrated that the vortex ring generation is not influenced by the piston load (piston position) for a selected power of 96.84 W (36 V, 2.69 A), but manipulation of the DIP switches provides opportunity to evaluate performance at lower powers.

Figure 7.5: DM542 (Leadshine, DM542, OMC Corporation Limited, Nanjing, China) digital stepper driver

All the possible pin combinations (SW1, SW2, SW3) for current control are engraved on the device (Leadshine, DM542, OMC Corporation Limited, Nanjing, China) and are summarised in Table 7.2.

Peak Current	RMS Current	SW1	SW2	SW3
1.00A	0.71A	ON	ON	ON
1.46A	1.04A	OFF	ON	ON
1.91A	1.36A	ON	OFF	ON
2.37A	1.69A	OFF	OFF	ON
2.84A	2.03A	ON	ON	OFF
3.31A	2.36A	OFF	ON	OFF
3.76A	2.69A	ON	OFF	OFF
4.20A	3.00A	OFF	OFF	OFF

Table 7.2: Pin combination to select the current delivered to the motor – DM542 stepper driver.

7.3.2 Method

Higher driver currents increase the motor power. Consequently, more torque is generated as output. Torque is transformed to force which controls acceleration of the piston. At the same time, higher power causes more heating of the motor and at the driver. The following experiment investigated how ring vortex generation is influenced by driver power.

Experiments were undertaken based on three different dynamic currents, two different piston loads (piston positions) and two different orifice diameters (which, again, implies different piston loads). Piston displacement was always 0.8 mm while the programmed piston velocity was 2 cm/s and 1.33 cm/s. These piston settings were programmed for a dynamic current of 2.36 A (OFF, ON, OFF – Table 7.2), 1.36 A (ON,OFF,ON – Table 7.2) and 0.71 A (ON, ON, ON – Table 7.2). The piston was placed at two different initial positions (different piston loads): 10 cm and 5 cm from the orifice (Position 1 and Position 3, Figure 7.1). The test was conducted to assess if there is a significative difference in piston velocity profiles during applications with different loads (related to how much water is in the cylinder and how small the output orifice is) and different input motor power settings. The orifice diameters of 10 mm and 15 mm were selected because these are the smallest provided with the phantom (Figure 4.5, Chapter 4). Clearly, configurations with the piston at 10 cm from the orifice, dynamic current of 0.71 A and orifice 10 mm (Configuration 10 and Configuration 16, Table 7.3) constitutes the theoretical worst case (lower input power and maximum piston load).

Early experiments (Section 7.1) were conducted with 2.69 A selected dynamic current. Being a 36 V motor, electrical power was 96.84 W, which is referred to in the test as 100 % selectable motor power. Equivalent experiments were performed decreasing the motor power to 87 % (2.36 A), 50 % (1.36 A) and 26 % (0.71 A). Data previously collected with 100% power (Section 7.1) was also used for the analysis. The experiments were performed both with the Vortex Ring based Complex Flow Phantom prototype empty (no water, no load) and in standard working conditions (filled with water). Ten acquisitions were performed with data aquired by the linear encoder for all the tested configurations, with the phantom empty (Configuration 1 to 6, Table 7.3) and five with the phantom with water (Configuration 7 to 30, Table 7.3).

A summary of the experimental conditions tested with the linear encoder is listed in Table 7.3.

Experimental Configuration – Encoder Data	Number of acquisitions	Orifice	Piston Velocity	Piston distance from the orifice	RMS Current	Power
1	10	NO LOAD, phantom empty	2cm/s	x	0.71A	25.56W (26%)
2	10	NO LOAD, phantom empty	2cm/s	X	1.36A	48.96W (50%)
3	10	NO LOAD, phantom empty	2cm/s	X	2.36A	84.69W (87%)
4	10	NO LOAD, phantom empty	1.33cm/s	x	0.71A	25.56W (26%)
5	10	NO LOAD, phantom empty	1.33cm/s	X	1.36A	48.96W (50%)

6	10	NO LOAD, phantom empty	1.33cm/s	X	2.36A	84.69W (87%)
7	5	10mm	2cm/s	5cm	0.71A	25.56W (26%)
8	5	10mm	2cm/s	5cm	1.36A	48.96W (50%)
9	5	10mm	2cm/s	5cm	2.36A	84.69W (87%)
10	5	10mm	2cm/s	10cm	0.71A	25.56W (26%)
11	5	10mm	2cm/s	10cm	1.36A	48.96W (50%)
12	5	10mm	2cm/s	10cm	2.36A	84.69W (87%)
13	5	10mm	1.33cm/s	5cm	0.71A	25.56W (26%)
14	5	10mm	1.33cm/s	5cm	1.36A	48.96W (50%)
15	5	10mm	1.33cm/s	5cm	2.36A	84.69W (87%)
16	5	10mm	1.33cm/s	10cm	0.71A	25.56W (26%)
17	5	10mm	1.33cm/s	10cm	1.36A	48.96W (50%)
18	5	10mm	1.33cm/s	10cm	2.36A	84.69W (87%)
19	5	15mm	2cm/s	5cm	0.71A	25.56W (26%)
20	5	15mm	2cm/s	5cm	1.36A	48.96W (50%)
21	5	15mm	2cm/s	5cm	2.36A	84.69W (87%)
22	5	15mm	2cm/s	10cm	0.71A	25.56W (26%)
23	5	15mm	2cm/s	10cm	1.36A	48.96W (50%)
24	5	15mm	2cm/s	10cm	2.36A	84.69W (87%)
25	5	15mm	1.33cm/s	5cm	0.71A	25.56W (26%)
26	5	15mm	1.33cm/s	5cm	1.36A	48.96W (50%)
27	5	15mm	1.33cm/s	5cm	2.36A	84.69W (87%)
28	5	15mm	1.33cm/s	10cm	0.71A	25.56W (26%)
29	5	15mm	1.33cm/s	10cm	1.36A	48.96W (50%)
30	5	15mm	1.33cm/s	10cm	2.36A	84.69W (87%)

Table 7.3: Experimental configurations – Encoder data – Different input motor powers and different piston loads (two orifice diameters, two piston positions) - For orifice diameters refer to Figure 4.5, Chapter 4 - For piston positioning, refer to Figure 6.16.

7.3.3 Results – Piston velocity and displacement profile reproducibility

Encoder acquisition results for each configuration listed in Table 7.3 are shown in Figure 7.6 (Configuration 1 to 3), Figure 7.7 (Configuration 4 to 6), Figure 7.8 (Configuration 7 to 12), Figure 7.9 (Configuration 13 to 18), Figure 7.10 (Configuration 19 to 24) and Figure 7.11 (Configuration 25 to 30). Graphs on the left side (A) represent the piston velocity (c*m/s*) as a function of time (*s*). Graphs on the right side (B) depict the piston displacement (*mm*) as a function of time (*s*). Average and error bar (+/- 1SD) values were calculated from the number of the acquisitions performed (Table 7.3).

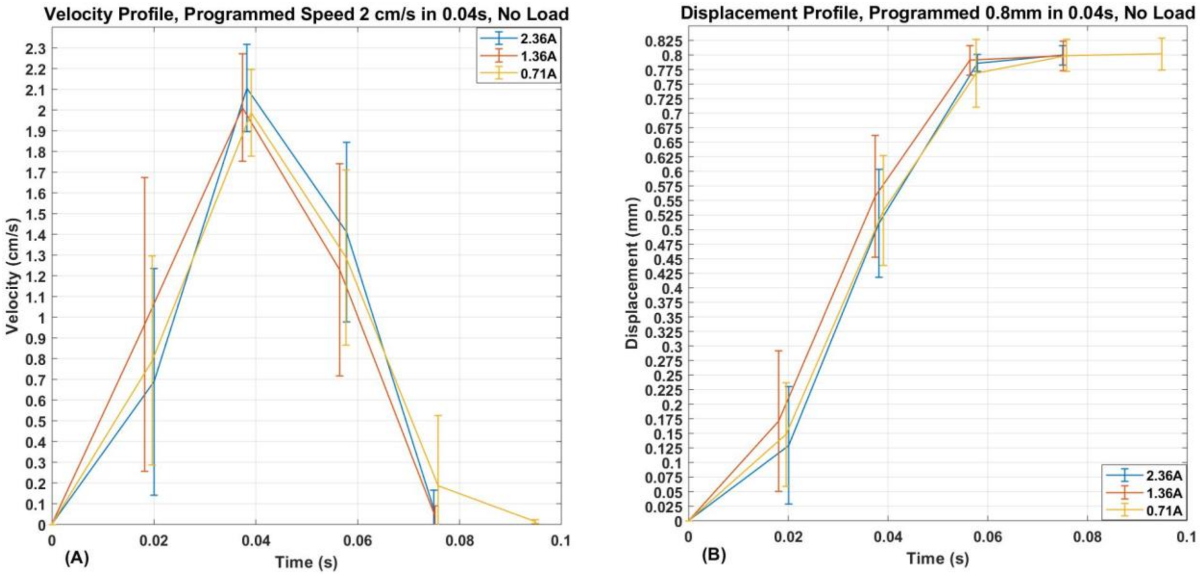

Figure 7.6: Encoder Results – Configuration 1 to 3 (No Load), Table 7.3. Average velocity Profile is depicted on the left (A) and Displacement profile on the right (B). Velocity is expressed in *cm/s*, Displacement in *mm* and time in *s*.

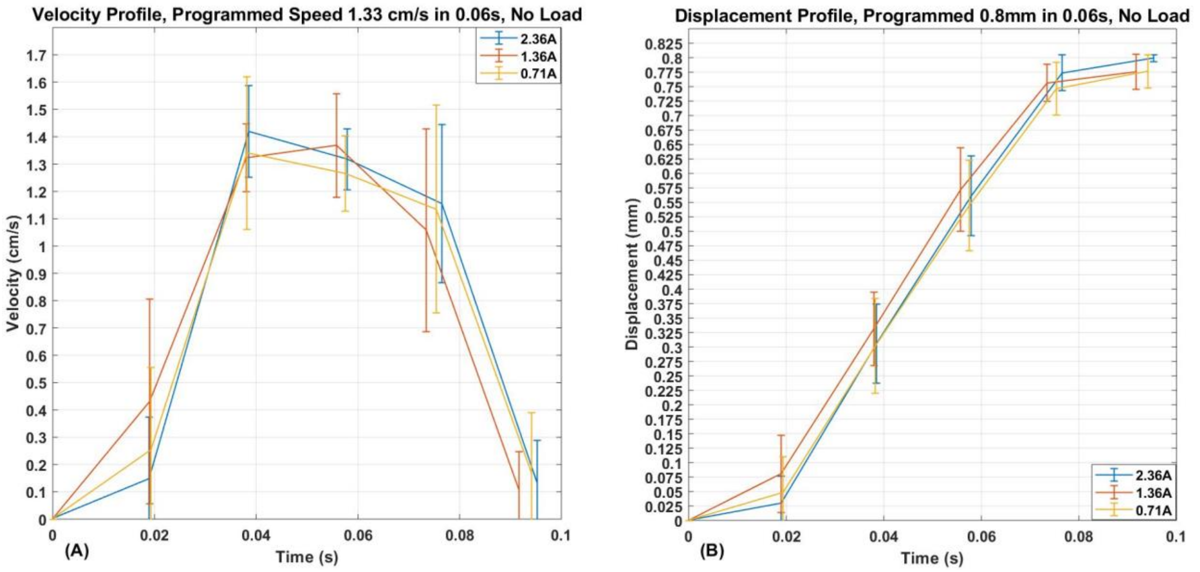

Figure 7.7: Encoder Results – Configuration 4 to 6 (No Load), Table 7.3. Velocity Profile is depicted on the left (A) and Displacement profile on the right (B). Velocity is expressed in *cm/s*, Displacement in *mm* and time in *s*.

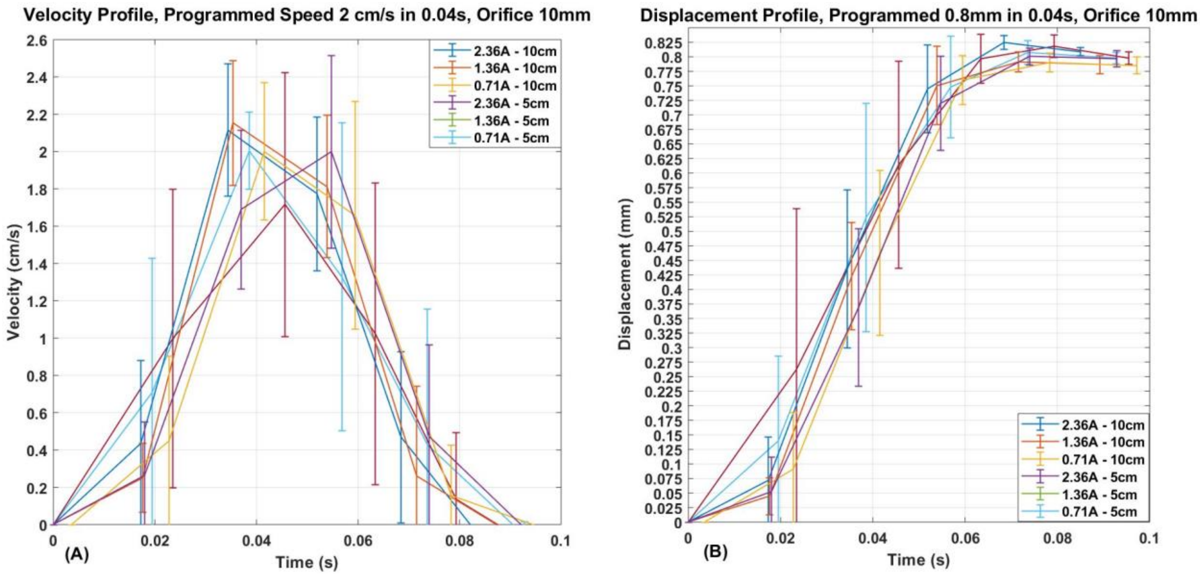

Figure 7.8: Encoder Results – Configuration 7 to 12, Table 7.3. Velocity Profile is depicted on the left (A) and Displacement profile on the right (B). Velocity is expressed in *cm/s*, Displacement in *mm* and time in *s*.

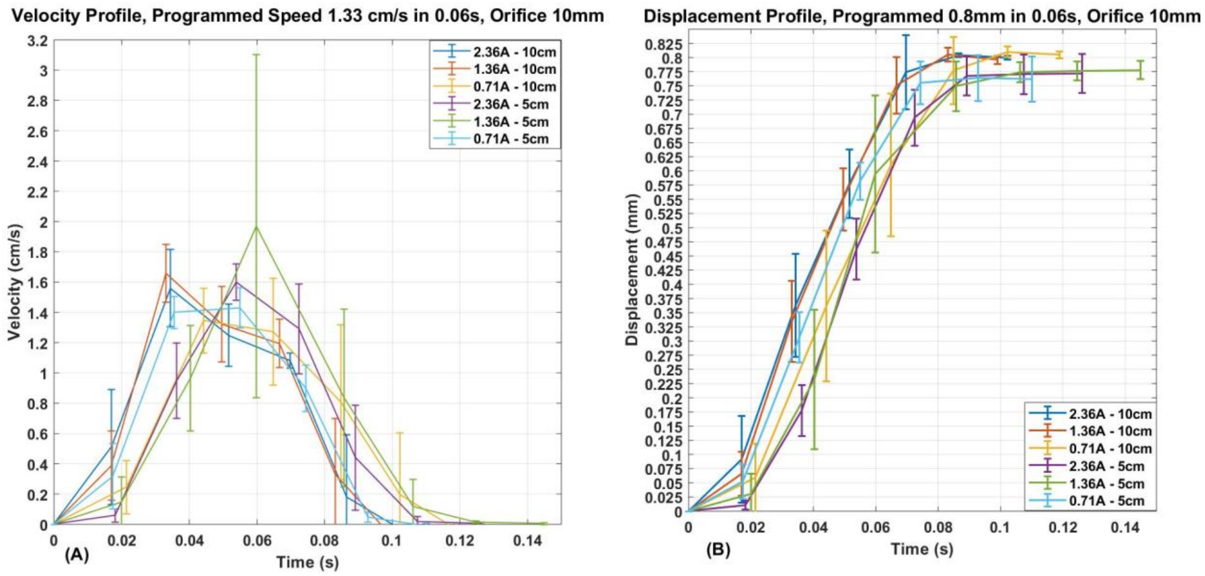

Figure 7.9: Encoder Results – Configuration 13 to 18, Table 7.3. Velocity Profile is depicted on the left (A) and Displacement profile on the right (B). Velocity is expressed in *cm/s*, Displacement in *mm* and time in *s*.

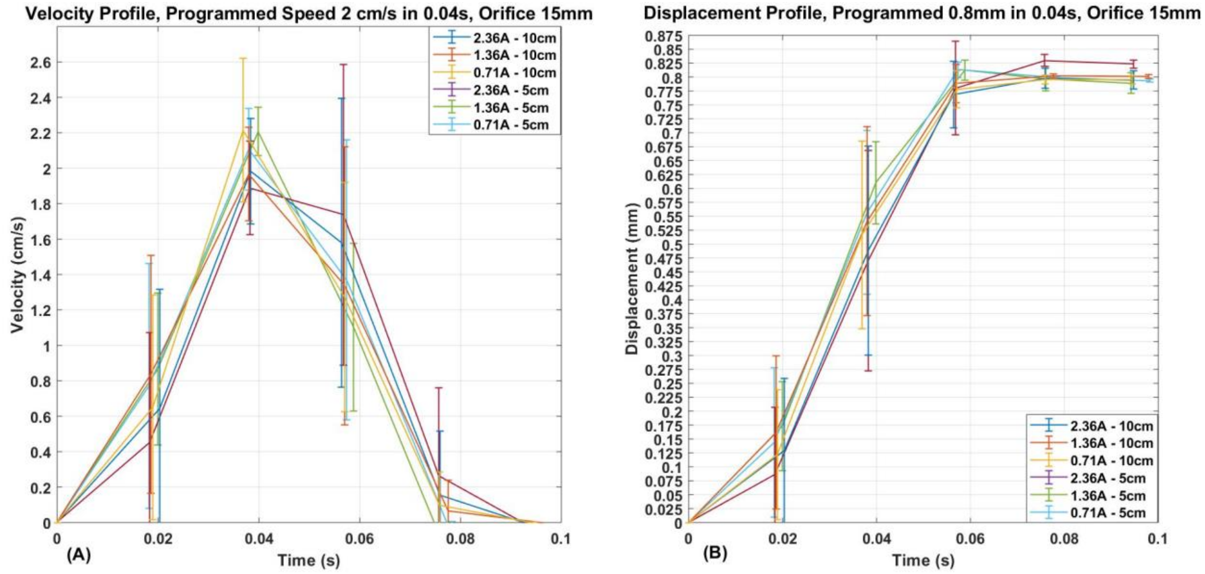

Figure 7.10: Encoder Results – Configuration 19 to 24, Table 7.3. Velocity Profile is depicted on the left (A) and Displacement profile on the right (B). Velocity is expressed in *cm/s*, Displacement in *mm* and time in *s*.

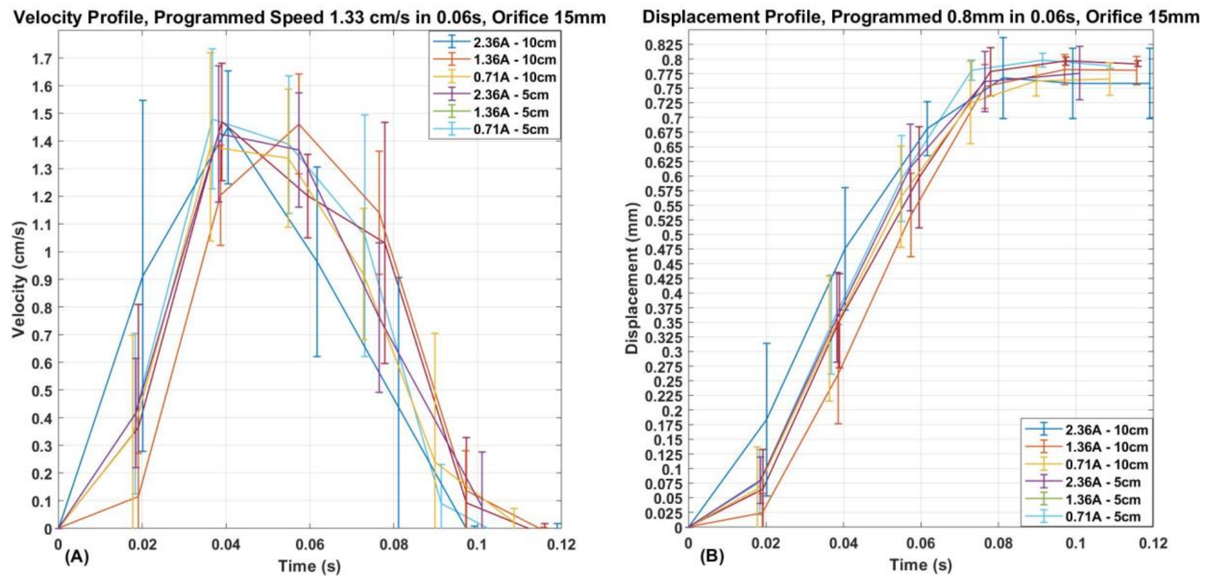

Figure 7.11: Encoder Results – Configuration 25 to 30, Table 7.3. Velocity Profile is depicted on the left (A) and Displacement profile on the right (B). Velocity is expressed in *cm/s*, Displacement in *mm* and time in *s*.

For improved clarity on piston peak velocity and final displacement variability, all the values are summarised in Table 7.4.

Experimental Configuration – Encoder Data	Orifice (mm)	Piston Velocity (programmed) (cm/s)	Piston Distance from the orifice (cm)	RMS Current (A)	Power (W)	Peak Velocity (cm/s)	Final Displacement (mm)
1	No Load	2	x	0.71	25.56 (26%)	1.98+/-0.21 (+/-10%)	0.802+/-0.028 (+/-3%)
2	No Load	2	x	1.36	48.96 (50%)	2.01+/-0.26 (+/-13%)	0.798+/-0.025 (+/-3%)
3	No Load	2	x	2.36	84.69 (87%)	2.1+/-0.21 (+/-10%)	0.799+/-0.016 (+/-2%)
4	No Load	1.33	x	0.71	25.56 (26%)	1.34+/-0.28 (+/-20%)	0.776+/-0.029 (+/-3%)
5	No Load	1.33	x	1.36	48.96 (50%)	1.37+/-0.19 (+/-13%)	0.776+/-0.030 (+/-3%)
6	No Load	1.33	x	2.36	84.69 (87%)	1.42+/-0.17 (+/-12%)	0.799+/-0.006 (+/-1%)
7	10	2	5	0.71	25.56 (26%)	2.00+/-0.52 (+/-25%)	0.797+/-0.014 (+/-2%)
8	10	2	5	1.36	48.96 (50%)	2.00+/-0.37 (+/-18%)	0.785+/-0.014 (+/-2%)
9	10	2	5	2.36	84.69 (87%)	2.15+/-0.33 (+/-15%)	0.798+/-0.009 (+/-1%)
10	10	2	10	0.71	25.56 (26%)	2.11+/-0.35 (+/-17%)	0.809+/-0.007 (+/-1%)
11	10	2	10	1.36	48.96 (50%)	1.72+/-0.71 (+/-41%)	0.797+/-0.011 (+/-1%)
12	10	2	10	2.36	84.69 (87%)	2.00+/-0.21 (+/-10%)	0.787+/-0.016 (+/-2%)
13	10	1.33	5	0.71	25.56 (26%)	1.43+/-0.13 (+/-9%)	0.768+/-0.040 (+/-5%)
14	10	1.33	5	1.36	48.96 (50%)	1.97+/-1.13 (+/-57%)	0.778+/-0.016 (+/-2%)
15	10	1.33	5	2.36	84.69 (87%)	1.60+/-0.12 (+/-7%)	0.772+/-0.035 (+/-4%)
16	10	1.33	10	0.71	25.56 (26%)	1.35+/-0.21 (+/-16%)	0.805+/-0.006 (+/-1%)
17	10	1.33	10	1.36	48.96 (50%)	1.66+/-0.19 (+/-11%)	0.796+/-0.007 (+/-1%)
18	10	1.33	10	2.36	84.69 (87%)	1.25+/-0.21 (+/-16%)	0.799+/-0.003 (0.3%)
19	15	2	5	0.71	25.56 (26%)	2.21+/-0.41 (+/-18%)	0.795+/-0.007 (+/-1%)
20	15	2	5	1.36	48.96 (50%)	1.97+/-0.26 (+/-13%)	0.801+/-0.004 (+/-0.5%)
21	15	2	5	2.36	84.69 (87%)	1.98+/-0.30 (+/-15%)	0.794+/-0.016 (+/-2%)
22	15	2	10	0.71	25.56 (26%)	1.89+/-0.26 (+/-14%)	0.823+/-0.007 (+/-1%)
23	15	2	10	1.36	48.96 (50%)	2.11+/-0.23 (+/-11%)	0.794+/-0.003 (0.4%)

24	15	2	10	2.36	84.69 (87%)	2.21+/-0.14 (+/-6%)	0.789+/-0.018 (+/-2%)
25	15	1.33	5	0.71	25.56 (26%)	1.42+/-0.24 (+/-17%)	0.776+/-0.045 (+/-6%)
26	15	1.33	5	1.36	48.96 (50%)	1.38+/-0.34 (+/-25%)	0.766+/-0.028 (+/-4%)
27	15	1.33	5	2.36	84.69(87%)	1.46+/-0.18 (+/-12%)	0.780+/-0.024 (+/-3%)
28	15	1.33	10	0.71	25.56 (26%)	1.45+/-0.20 (+/-14%)	0.758+/-0.060 (+/-8%)
29	15	1.33	10	1.36	48.96 (50%)	1.47+/-0.21 (+/-14%)	0.792+/-0.004 (+/-0.5%)
30	15	1.33	10	2.36	84.69 (87%)	1.48+/-0.25 (+/-17%)	0.789+/-0.004 (0.5%)

Table 7.4: Experimental configurations – Encoder Data – piston Peak velocity (*cm/s*) and total displacement (*mm*) estimated.

Average peak velocity values are always within +/- 20 % for 26 configurations tested.

Exceptions were:

- Orifice 10 mm - Piston Velocity 1.33 cm/s - piston placed at 5 cm from orifice – Motor input power 48.96 W - Variability +/- 57 %;
- Orifice 10 mm - Piston Velocity 2 cm/s - piston placed at 10 cm from orifice - Motor input power 48.96 W - Variability +/- 41 %;
- Orifice 10 mm - Piston Velocity 2 cm/s - piston placed at 5 cm from orifice – Motor input power 25.56 W - Variability +/- 26 %;
- Orifice 15mm - Piston Velocity 1.33cm/s - piston placed at 5cm from orifice – Motor input power 48.96 W -> Variability +/- 25 %;

Average final displacement variability was within +/- 5 % for 28 configurations tested. A maximum variability of +/- 8 % was found for the configuration with Orifice 15 mm - Piston Velocity 1.33 cm/s - piston placed at 10 cm from the orifice - Motor input power 25.56 W and a variability of +/- 6 % for the configuration with Orifice 15 mm - Piston Velocity 1.33 cm/s - piston placed at 5 cm from the orifice - Motor input power 25.56 W.

7.3.4 Results – Correlation Plots

For each configuration listed in Table 7.3, peak velocity and final displacement data was plotted versus increasing piston load and increasing motor input power for each vortex ring. Figure 7.12 illustrates plots of piston peak velocity values versus increasing piston load (two different output orifice diameters and two different piston positions) for programmed piston speed of 2 cm/s and motor input power of 96.84 W, 84.96 W, 48.96 W and 25.56 W. Figure 7.13 illustrates plots of piston final displacement values versus increasing piston load for equivalent input conditions. Similarly, Figure 7.14 and Figure 7.15 show plots of piston peak velocity and final displacement values versus increasing piston load for programmed piston speed of 1.33 cm/s and motor input power of 84.96W, 48.96W and 25.56 W, respectively. Unfortunately, data were not available for programmed piston speed of 1.33 cm/s and motor input power of 96.84 W.

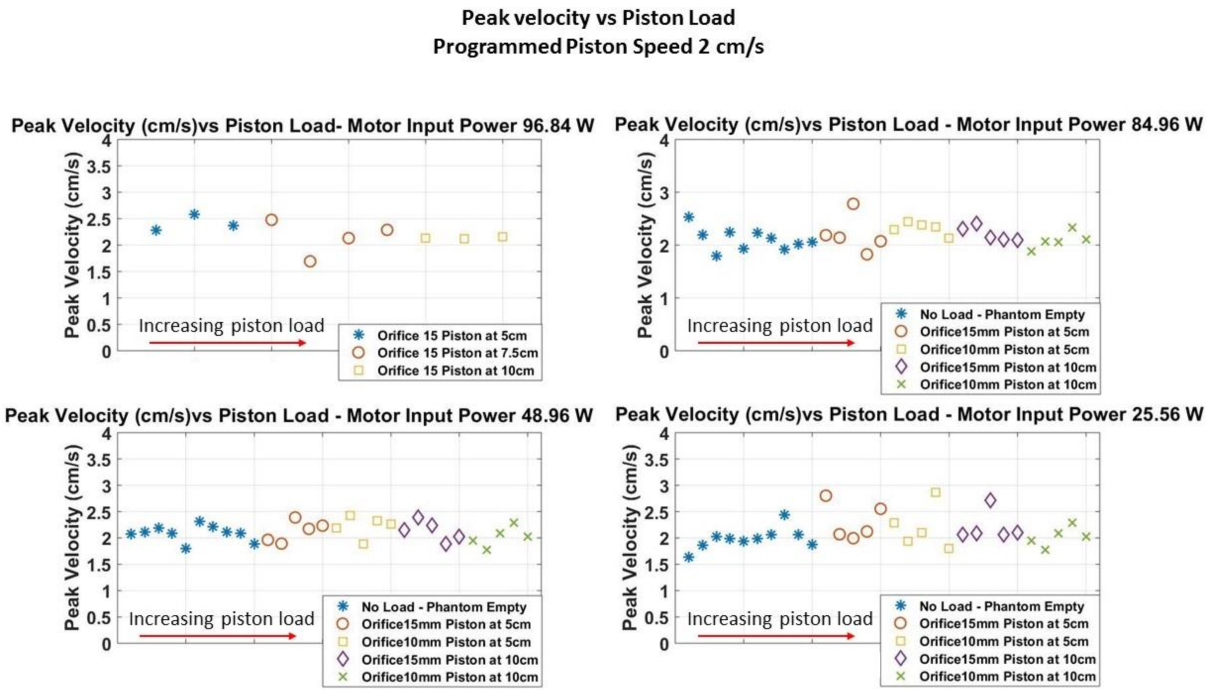

Figure 7.12: Encoder results – Piston peak velocity values plotted versus increasing piston load (two different orifices and two different piston positions) for four different motor input power (96.84 W, 84.96 W, 48.96 W and 25.56 W) and a programmed piston speed of 2 cm/s.

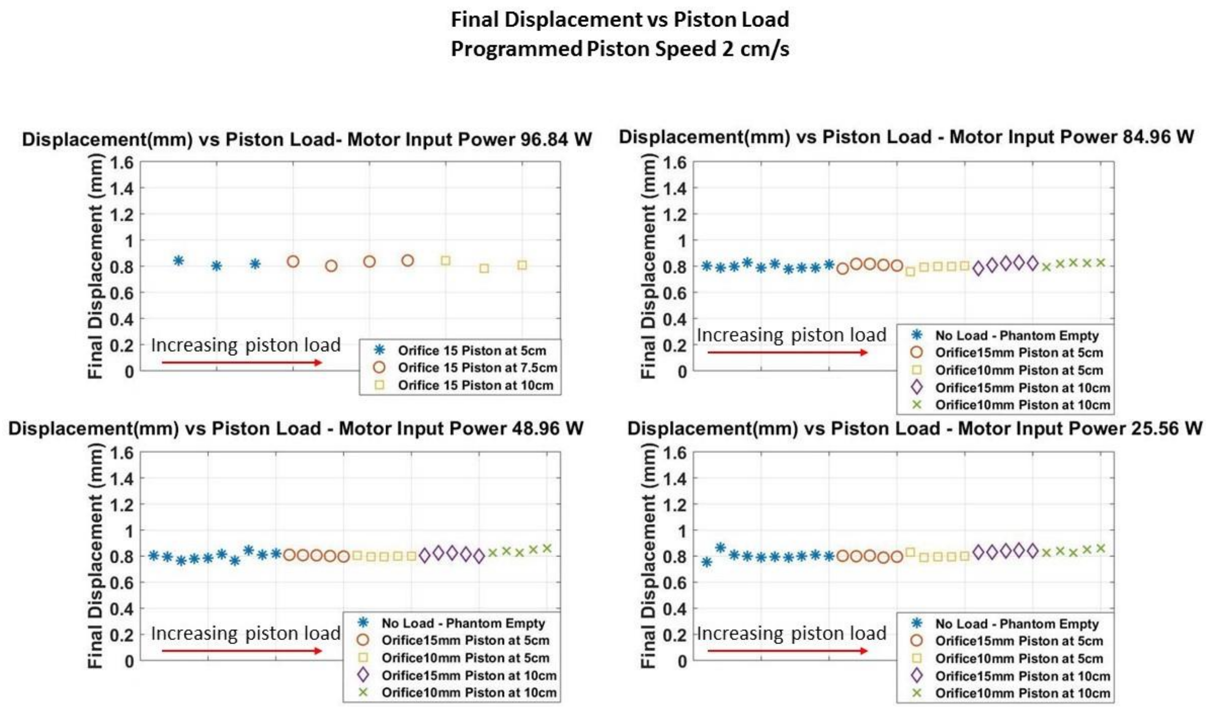

Figure 7.13: Encoder results – Piston final displacement values plotted versus increasing piston load (two different orifices and two different piston positions) for four different motor input power (96.84 W, 84.96 W, 48.96 W and 25.56 W) and a programmed piston speed of 2 cm/s.

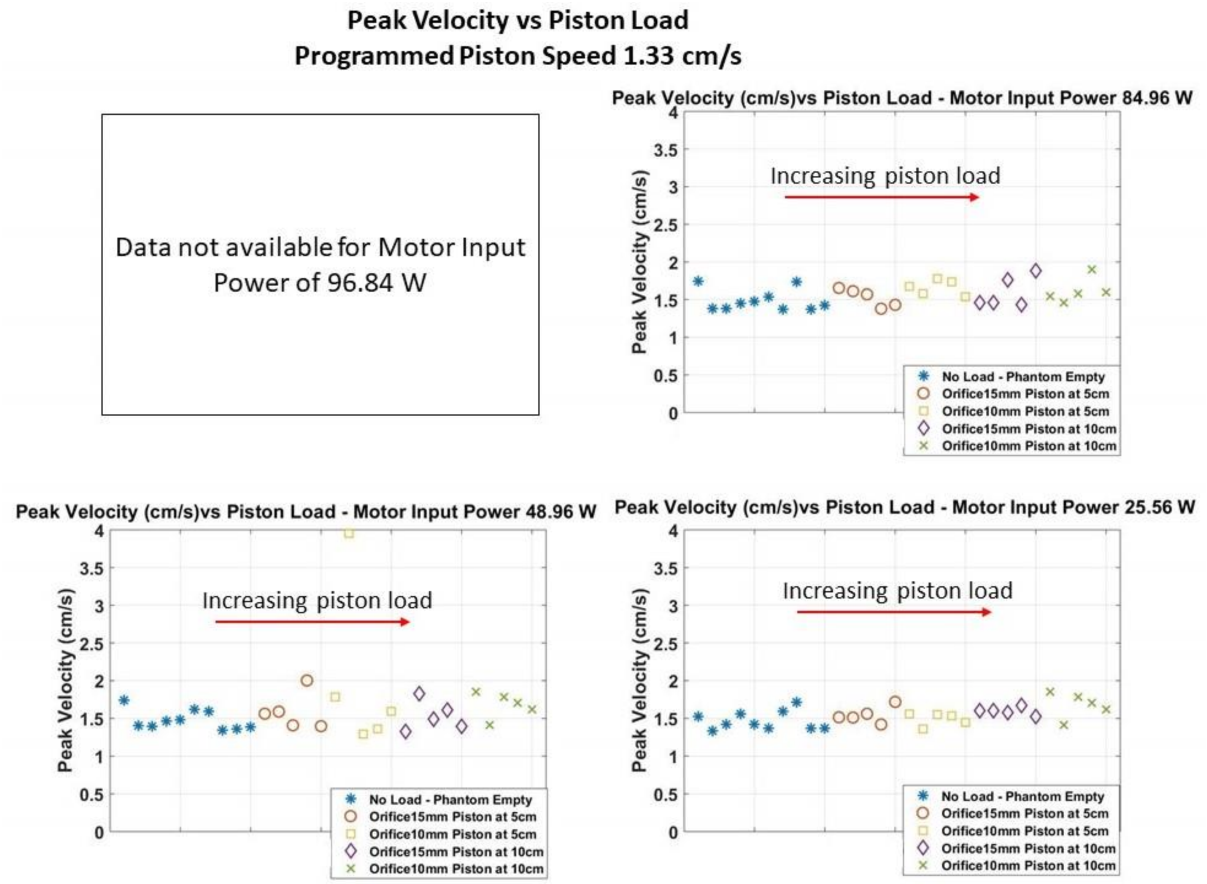

Figure 7.14: Encoder results – Piston peak velocity values plotted versus increasing piston load (two different orifices and two different piston positions) for three different motor input power (84.96 W, 48.96 W and 25.56 W) and a programmed piston speed of 2 cm/s.

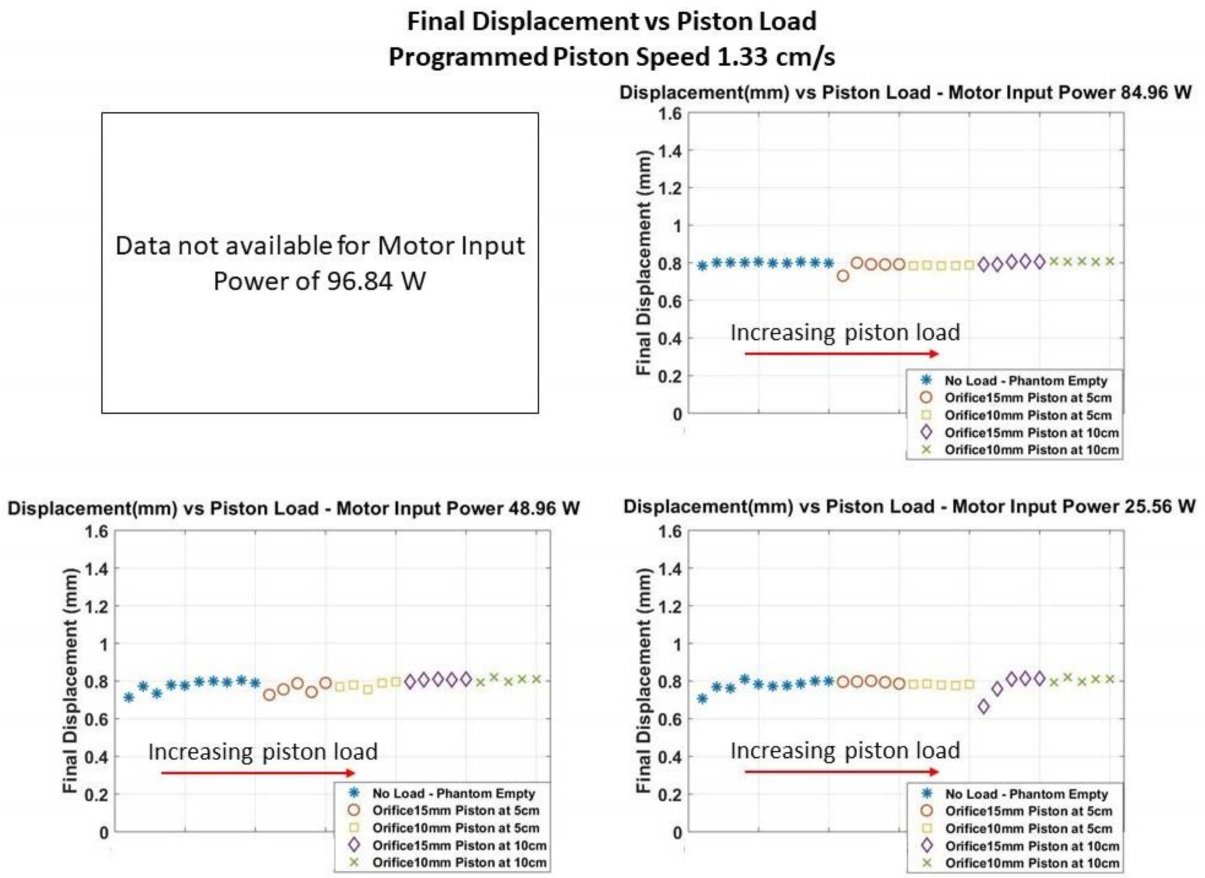

Figure 7.15: Encoder results – Piston final displacement values plotted versus increasing piston load (two different orifices and two different piston positions) for four different motor input power (84.96 W, 48.96 W and 25.56 W) and a programmed piston speed of 2 cm/s.

Plots of Figure 7.14, Figure 7.15, Figure 7.16 and Figure 7.17 show that, for all the tested configurations, there was no dependency of piston peak velocity and final displacement values on the load. Data dispersion is randomly allocated and comparable for all the configurations. There is no need to depict a regression line because it is evident that the slope would be very close to zero and would be swamped by the typical reproducibility error of +/-10 %. Consequently, there is not a significant correlation between the variables.

Finally, all the piston peak velocity and final displacement data were collected and plotted versus increasing motor input power and neglecting the piston load (piston position and orifice output diameter). Figure 7.16 illustrates the results for the four input powers (96.84 W, 84.96 W, 48.96 W and 25.56 W) and two piston speed (2 cm/s and 1.33 cm/s) tested.

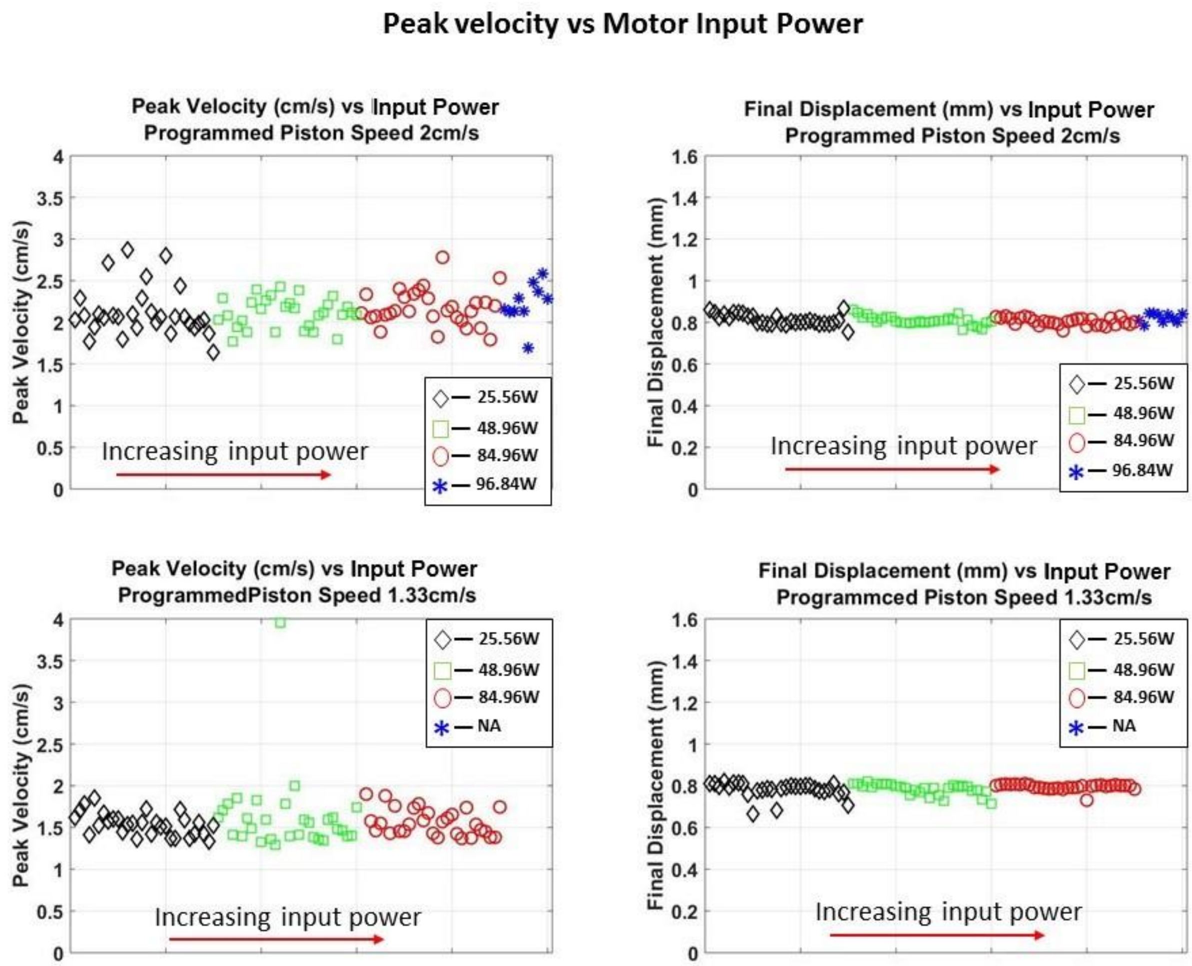

Figure 7.16: Encoder results – Piston peak velocity and final displacement values plotted versus increasing motor input power (84.96 W, 48.96 W and 25.56 W) and programmed piston speed of 2 cm/s and 1.33 cm/s.

The condition (Orifice 10 mm - Piston Velocity 1.33 cm/s - piston placed at 5 cm from orifice – Motor input power 48.96 W) that showed higher variability (+/-57 %) in peak velocity shows a peak velocity value of 3.9 cm/s, that clearly moves away from the other values and increases the variability calculation. The two cases that showed higher variabilities in piston final displacements (Orifice 15 mm - Piston Velocity 1.33 cm/s - piston placed at 10 cm from the orifice - Motor input power 25.56 W – Variability +/- 8 % and Orifice 15 mm - Piston Velocity 1.33 cm/s - piston placed at 5 cm from the orifice - Motor input power 25.56 W- +/- 6 %) shows a distinct lower value on the first acquisition. This suggests that it might be worth considering ignoring the first acquisition and performing measurements using subsequent vortex rings. However, only three outliers were observed out of a total of 175 vortex ring acquisitions.

7.3.5 Discussion

Previous experiments have demonstrated that piston peak and average velocity variability do not significantly influence the vortex ring generation. This was validated for a configuration involving orifice output diameter of 15 mm, programmed piston speed of 2 cm/s, motor input power of 96.84 W, and three different initial piston positions (different piston loads). Stepper motor overheating is an important limitation of the phantom since it restricts the use of the system over prolonged experiments. Three different motor inputs power (84.96 W, 48.96 W and 25.56 W) were tested in a combination of two different piston positions and two different output orifice diameters. The piston position and the output orifice diameter determines the load during piston action. Data collected in previous experiments (Section 7.1) was also used for the analysis. Encoder data was collected, following methods described in the previous chapter (Chapter 6), from the acquisitions of ten consecutive vortex rings generated under thirty different combinations of input power and piston load (Table 7.3). Average and standard deviation values were calculated for piston peak velocity and piston final displacement data for each configuration. Peak velocity values showed variability within +/- 20 % for 26 configurations tested. Bigger variability was found for four particular configurations and three of these were with input power of 48.96 W. Measurements could be performed again to assess if these errors were just random or if these configurations (Configuration 7, 11, 14 and 26 – Table 7.3) are particularly problematic for the motor. A marked distinct value in peak velocity was found for Configuration 14, when the single acquisition was plotted as function of the piston load (Figure 7.14). This might be a false reading that significantly increases the average variability. Final displacement variability was within +/- 5 % for 28 configurations tested. The worst case of +/- 8 % was found for a configuration involving orifice diameter of 15 mm, programmed piston velocity of 1.33 cm/s, motor input power of 25.56 W and the piston placed at 10 cm from orifice. This configuration shows a distinct lower value on the first acquisition (Figure 7.15) that increases the variability. Although this distinct lower value is exhibited just for two acquisition on 175 vortex ring generated, it might be worth considering to start measurements from the generation of the second vortex ring to avoid systematic errors. However, such variation also needs to be related to ring performance. Big variations might influence the vortex ring reproducibility which is not ideal for the calibration of medical imaging, however, the instrumentation pack allows detection of such anomalies in real-time.

Piston peak velocity and final displacement values have been plotted as a function of increasing input power and increasing piston load, for all the different combinations listed in Table 7.3. Results show that the data dispersion is random and it is independent of the combination of input power and piston load. For all the configurations, plots of piston peak velocity and final piston displacement values do not show a significant dependency on the piston load or the motor input power. The data suggests that there is no significant relationship between the variables. Consequently, the piston can be positioned randomly during Vortex Ring based Complex Flow Phantom applications and any provided orifice diameter (Figure 4.4, Chapter 4) can be used without introducing systematic errors. In addition, the lowest selectable motor power of 25.56 W can be used during the phantom applications without affecting the performance of the system. This reduces drastically the motor overheating during prolonged applications. A detailed calculation of pressures and loads involved for each configuration was not needed, since all the combinations of input power and piston loads showed consistent results and there is not a particular challenging condition for the system.

7.3.6 Conclusion

Experiments have assessed potential dependency of the piston velocity and piston displacement profile on motor input powers and piston loads. For all the configuration tested, variability was quantified, average and standard deviation values were provided. Three configurations were anomalous with considerable variability (up to +/- 57 % for peak velocity, although there was a clear false reading) and further tests need to be conducted to clarify if those input settings are critical. There is no significant dependency of piston velocity and piston displacement profile on motor input power and different piston loads. Correlation plots clearly demonstrate that variables are not correlated. The phantom can be used at reduced motor power (which reduces noticeably motor overheating) and placing the piston randomly without affecting its performance.

7.4 Different combination Piston/Loads – Motor input power – Laser Diodes/Photodiodes acquisitions

7.4.1 Introduction

Section 7.2 clarified that variability up to +/- 15 % in peak piston velocity and average piston velocity do not significantly affect the vortex ring production with translational velocity variability lower than +/- 6 %. This experiment was conducted for re-examining this hypothesis and for obtaining useful reference values for the system. The piston used the modified design described in Chapter 6. Consequently, vortex ring translational velocity reference values provided by the Laser PIV experimental session (Chapter 5) may not be relevant anymore. Video camera acquisitions were performed for the tested configuration and results were referred to each other to assess the rigour of the approach. Previous data, gathered in the experimental sessions described in Section 7.2, were also cross-referenced with new data to verify the reproducibility of the method.

7.4.2 Method

Data was collected with the Laser Diodes/photodiodes instrumentation pack system for all of the configuration listed in Table 7.5. Laser Diodes/Photodiodes acquisitions require the introduction of dark food colourant dye into the piston/cylinder system. The dark colour progressively mixes with the volume of water into the imaging tank and over time it makes the Laser Diodes/Photodiodes acquisitions challenging or impossible. In order to test all the listed configurations (Configuration 1 to 19, Table 7.5) in a reasonable amount of time and without moving the experimental set up, acquisitions were performed on the generation of five consecutive vortex rings.

Vortex ring translational velocities were measured for the experimental set up listed in Table 7.5. These configurations are the same as those used in previous experiments described in Section 7.3. Motor performance and piston profile are not influenced by different motor input powers or piston loads (Section 7.3).Consequently, optical acquisitions (Laser Diodes/Photodiodes and video camera acquisitions) were performed with random initial piston positions. Laser Diodes/Photodiodes acquisitions were performed following the method described in Section 6.3.5 (Chapter 6). As an additional test of the reliability of the Laser Diodes/Photodiodes system, optical/video (Section 5.2.2, Chapter 5) acquisitions were also performed on three configurations and results were compared. Also results obtained in the early experiments (Table 7.5, Configuration 13, "*OLD acquisition 1*") and in another experiment performed independently on a different day (Table 7.5, "*OLD acquisition 2*") were also compared.

Experimental Configuration – Optical Data	Modality	Orifice	Piston Velocity	RMS Current	Power
1	Laser diode/Photodiode	10mm	2cm/s	0.71A	25.56W (26%)
2	Laser diode/Photodiode	10mm	2cm/s	1.36A	48.96W (50%)
3	Laser diode/Photodiode	10mm	2cm/s	2.36A	84.69W (87%)
4	Laser diode/Photodiode	10mm	1.33cm/s	0.71A	25.56W (26%)
5	Laser diode/Photodiode	10mm	1.33cm/s	1.36A	48.96W (50%)
6	Laser diode/Photodiode	10mm	1.33cm/s	2.36A	84.69W (87%)
7	Laser diode/Photodiode	15mm	2cm/s	0.71A	25.56W (26%)
8	Laser diode/Photodiode	15mm	2cm/s	1.36A	48.96W (50%)
9	Laser diode/Photodiode	15mm	2cm/s	2.36A	84.69W (87%)
10	Laser diode/Photodiode	15mm	1.33cm/s	0.71A	25.56W (26%)
11	Laser diode/Photodiode	15mm	1.33cm/s	1.36A	48.96W (50%)
12	Laser diode/Photodiode	15mm	1.33cm/s	2.36A	84.69W (87%)
13	Laser diode/Photodiode (OLD acquisition 1)	15mm	2cm/s	2.69A	96.84W (100%)
14	Laser diode/Photodiode (OLD acquisition 2)	15mm	2cm/s	2.69A	96.84W (100%)
15	Optical/video camera	15mm	1.33cm/s	0.71A	25.56W (26%)
16	Optical/video camera	15mm	1.33cm/s	1.36A	48.96W (50%)
17	Optical/video camera	15mm	1.33cm/s	2.36A	84.69W (87%)

Table 7.5: Experimental configurations – Laser Diode/photodiodes acquisitions – five rings evaluated for each configuration.

7.4.3 Results

Vortex ring translational velocities were plotted as a function of position in the imaging tank. Average values and error bars (+/- 1 SD) were calculated from the acquisition of five consecutive vortex ring for each configuration listed in Table 7.5. Figure 7.17 and Figure 7.18 illustrate vortex ring translational velocities for configurations involving a 10 mm orifice size, different motor input powers (25.56 W, 48.96 W and 84.69 W), and piston programmed velocities of 2 cm/s and 1.33 cm/s, respectively (Configuration 1 to 6, Table 7.5). Standard deviation values indicate variability up to +/- 20 % for the configurations that generate fastest vortex rings (Configuration 1 to 3, Table 7.5). The variability drops to +/- 12 % for Configurations 4 to 6, which produce vortex rings with slightly lower translational velocities. All the error bars overlap, demonstrating that maximum percentage different between average values is within expected limits of uncertainty.

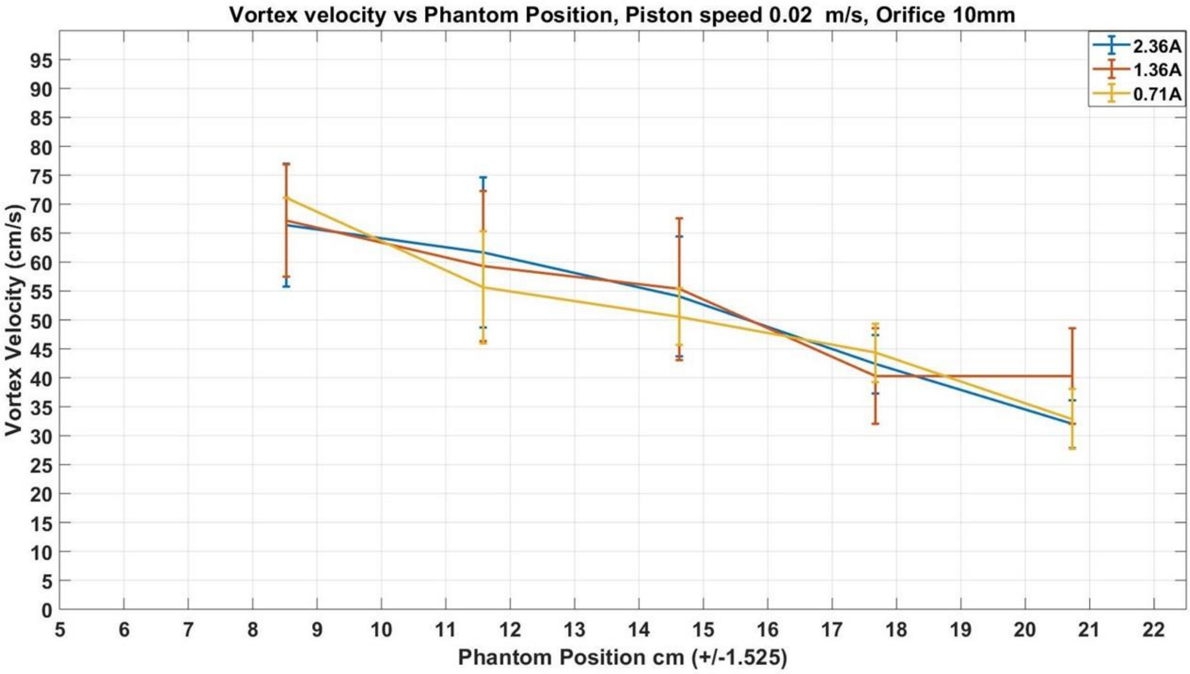

Figure 7.17: Vortex Ring translational velocity as a function of position and motor current (A = amps) in the imaging tank – Laser Diodes/Photodiodes acquisitions for Configuration 1 to 3, Table 7.5.

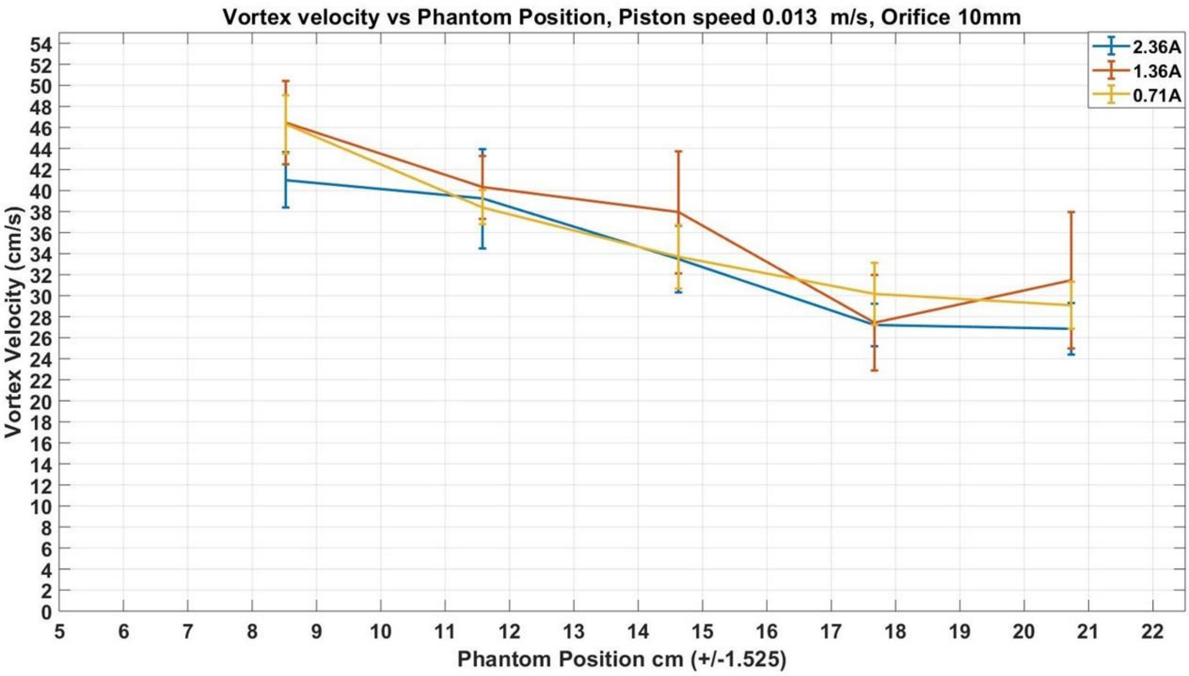

Figure 7.18: Vortex Ring translational velocity as a function of position in the imaging tank – Laser Diodes/Photodiodes acquisitions for Configuration 4 to 6, Table 7.5. Different colours refer to different motor currents (A = amps).

Figure 7.19 and Figure 7.20 illustrate vortex ring translational velocities for configurations involving a 15 mm orifice size, different motor powers (25.56 W, 48.96 W and 84.69 W), and piston programmed velocities of 2 cm/s and 1.33 cm/s, respectively (Configuration 7 to 17, Table 7.5). Old Laser diodes/photodiodes acquisitions (different experimental day), performed with a motor input power of 96.84 W, were also compared and are illustrated in Figure 7.19. Optical/video acquisition results, performed for configurations involving a 15 mm orifice, different motor input powers, and programmed piston velocity of 1.33 cm/s are also illustrated in Figure 7.20. Error bar values (+/- 1SD) indicate variability always lower than +/- 10 %. Independent measurement methods (optical/video) and acquisitions performed with the same method on a different day are in good agreement. Percentage differences between average values were always lower than 10 %.

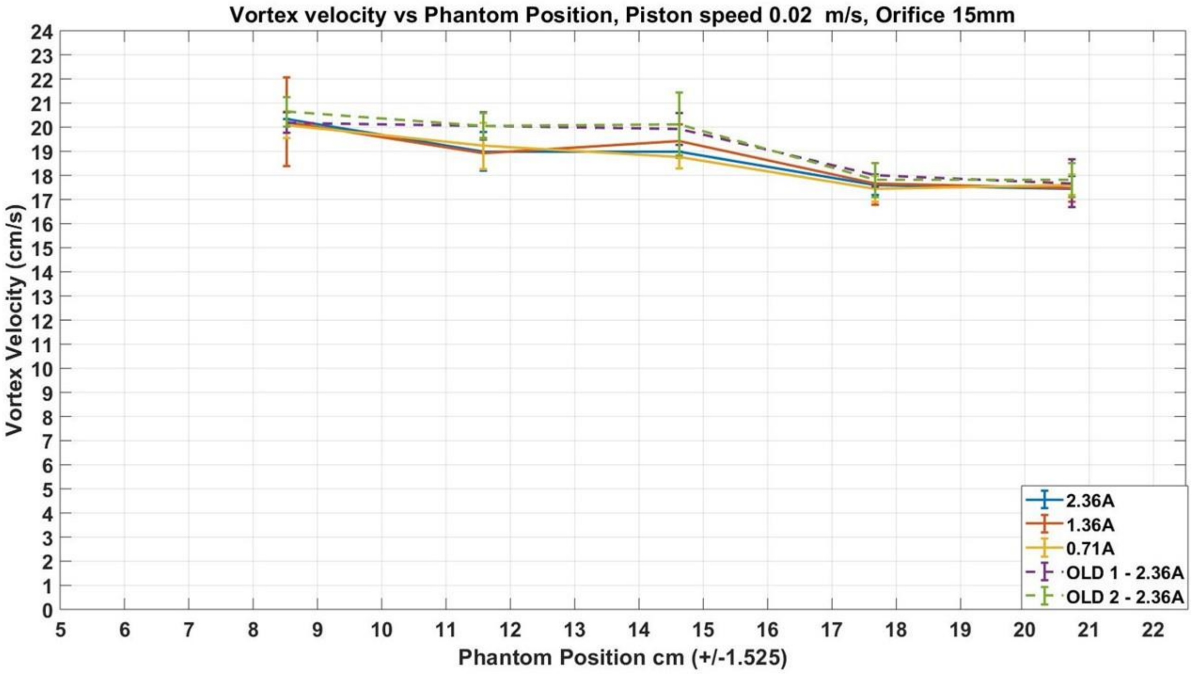

Figure 7.19: Vortex Ring translational velocity as a function of position in the imaging tank – Laser Diodes/Photodiodes acquisitions compared with "*old*" (different experimental day, different motor input powers) acquisitions. Configuration 7 to 9 and Configuration 13-14, Table 7.5. Old acquisitions are depicted with dash lines while Laser Diodes/Photodiodes acquisitions are depicted with solid lines. Different colours refer to different motor currents (A = amps).

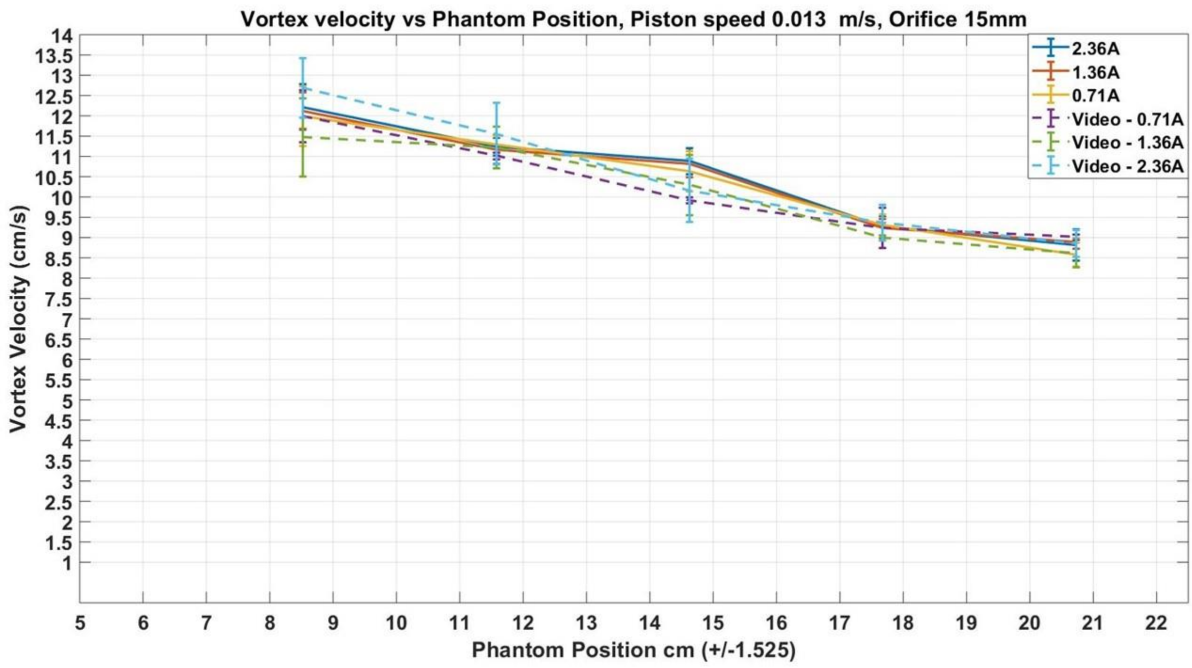

Figure 7.20: Vortex Ring translational velocity as a function of position in the imaging tank – Laser Diodes/Photodiodes acquisitions compared with optical/acquisitions. Configuration 10 to 12 and Configuration 15-17, Table 7.5. Optical/video acquisition are depicted with dash lines while Laser Diodes/Photodiodes acquisitions are depicted with solid lines.

7.4.4 Discussion

Measurements were performed with the Laser Diodes/Photodiodes system in order to obtain new reference values on vortex ring translational velocities. Optical/video acquisitions, performed simultaneously, and *"OLD"* acquisitions, performed independently with the same method on different days, were used to add rigour to the method. Results obtained were all in good agreement. High variability was found for the piston/orifice configuration that generated vortex rings with the highest translational velocities. However, the variability drops drastically from +/- 20 % to +/- 12 % for slightly lower velocities and to values always lower +/- 10 % for all the other configurations tested. Possibly the higher variability for the configuration generating fastest vortex rings is related to the measurement method rather than the phantom itself. Laser PIV acquisitions on fast configurations (piston speed 2 cm/s and orifice 10 mm, Figure 5.2.5) in previous experiments exhibited variability always lower than +/- 6 %. It might be that the combination of a very fast vortex ring with a small ring size is particularly challenging for Laser Diodes/Photodiodes acquisitions. No significant difference was found between translational velocities of vortex rings generated with different motor input powers. This confirms the findings of previous experiments (Section 7.3): the phantom can be used with lower input powers without significantly affecting the performance.

7.4.5 Conclusion

The reliability of the Laser Diodes/Photodiodes was tested with independent measurement methods. The system seems to struggle to measure the translational velocity of vortex rings produced with very high velocities and small ring diameters (Figure 7.17). However, variability lower than +/- 10 % was accurately assessed for most of the configuration tested and new phantom reference values have been established.

7.5 Energetics

7.5.1 Introduction

The instrumentation pack offers valuable information for characterising the flow and the phantom. The combination of piston profile data and vortex ring translational velocities can also clarify aspects of the energetics involved in the vortex ring generation and propagation. This might add micro-flow information to the macro-flow characteristics already characterised. Our earlier experiments have demonstrated that vortex rings with translational velocity errors lower than +/- 10 % can be generated. Analysis of the energies involved in the vortex ring formation might support analysis of aspects of the generation process that are not yet fully appreciated. The energetics analysis involves characterising energies associated which each stage of ring vortex generation and propagation.

7.5.2 Mass moved by the motor (Piston plus Water)

A CAD drawing of the new piston design is shown in Figure 6.1 (Chapter 6). The piston is manufactured from PMMA (Perspex), which has a density of 1.19 g/cm^3, and it is composed from two main components: the stem, which is comparable to a parallelepiped, and the piston cap, which has a cylinder shape. Consequently, the mass (volume x density) of the piston can be calculated as the sum of the mass of a parallelepiped plus the the mass of the cylinder. The volume of the stem is 91 cm^3 (2.5 cm x 2.5 cm x 14.560 cm) while the volume of the piston cap is 192.325 cm^3 ((r^2 π) x h -> 3.5^2 cm x 3.14 x 5 cm). Hence, the mass of the piston is 337.16g. The motor pushes the mass of the piston plus the water through the cylinder. With a fixed displacement of 0.8 mm, the mass of water pushed out of the cylinder is ~ 3.1 x 10^{-6} m^3 (~3.1 g). The mass of fluid into the cylinder is about 0.38 kg (Figure 7.17).

7.5.3 Method - Energy delivered by the motor in pulse

The energy delivered in pulses by the motor can be calculated from the motor input power. The delivered motor energy (Joules) corresponds to the motor input power (Watt) multiplied by the amount of time (Seconds) that it is applied (Energy = Power x Time). Selected motor input powers (Power = Voltage x Current) in previous experiments were 96.84 W, 84.96 W, 48.96 W and 25.56 W. Energy limits delivered in a pulse by the motor were calculated for the two piston speeds commonly used (2 cm/s and 1.33 cm/s), and as summarised in Table 7.6.

Piston Speed (cm/s)	Pulse length (s)	Input Current (A)	Max Delivered Energy (J)
2	0.04	2.69	3.87
1.33	0.06	2.69	5.81
2	0.04	2.36	3.39
1.33	0.06	2.36	5.09
2	0.04	1.36	1.95
1.33	0.06	1.36	2.93
2	0.04	0.71	1.02
1.33	0.06	0.71	1.53

Table 7.6: Limit energies for each pulse delivered by the motor with the main configurations tested.

The motor pushes the piston plus the amount of water into the cylinder. The water is forced through the narrow orifice and gains velocity, thus kinetic energy. The kinetic energy (Joule) is the energy possessed by an object due to its motion and it is calculated as:

$$\boldsymbol{E = \frac{1}{2}\, m\, v^{2}} \qquad \textbf{Joule = kg (m}^{2}\textbf{/s}^{2}\textbf{)} \qquad \textbf{(1)}$$

Where *m* is the mass of the object and *v* is its velocity.

This kinetic energy is provided by the external work (Joule) applied by the motor. Assuming that dissipative forces are negligible and that the fluid flows with no losses through the cylinder and at the orifice interface (laminar flow), the piston energy is entirely transferred to the fluid and ejected from the orifice.

Piston Energy → Fluid Energy → Ejected From the Orifice

The motor pushes the piston and the amount of water contained in the cylinder through the orifice. The external work (Joule) needed to complete the action is:

$$\boldsymbol{W_{external} = E_{final} - E_{initial} = \frac{1}{2}\, m_{final}\, v_{final}^{2} - \frac{1}{2}\, m_{initial}\, v_{initial}^{2}}$$

If the case of 15 mm orifice and 2 cm/s piston velocity is considered, the amount of energy needed is about 0.4 mJ. This is illustrated with simple calculations depicted in the schematic block of Figure 7.21. Technically the motor also has to stop the flow, so maybe an additional energy (~0.14 mJ) needs to be considered.

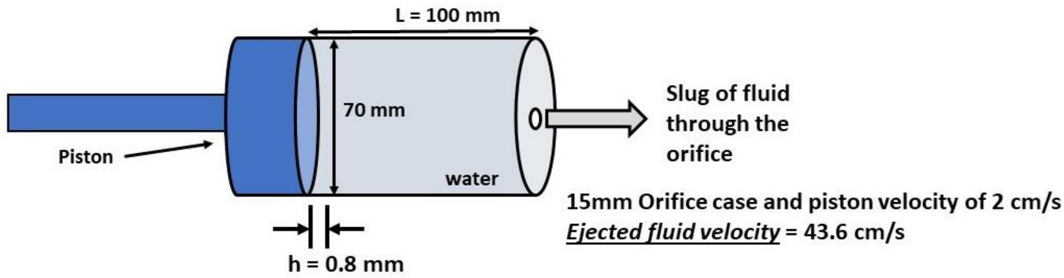

<u>*Swept volume*</u> = $\pi r^2 h = 3.14 \times 0.035^2 \times 0.0008 = 3.1 \times 10^{-6}$ m^3
<u>*Volume of fluid in cylinder*</u> = $\pi r^2 L = 3.14 \times 0.035^2 \times 0.1 = 0.38 \times 10^{-3}$ m^3
<u>*Mass of fluid in cylinder*</u> = $0.38 \times 10^{-3} \times 10^3 = 0.38$ kg

<u>*Energy to move water into cylinder + piston*</u> = $\frac{1}{2}(m_{water} + m_{piston})v^2 = 0.5 \times (0.38+0.34) \times 0.02^2 = 1.44 \times 10^{-4} = 0.14$ mJ

<u>*Energy of slug*</u> = $\frac{1}{2} m v^2 = \frac{1}{2}$ (volume x density) x $v^2 = 0.5 \times (3.1 \times 10^{-6} \times 1000) \times 0.43^2 = 0.29$ mJ

<u>*Total energy per ring*</u> = 0.29 mJ + 0.14 mJ = 0.43 mJ

Figure 7.21: Schematic diagram illustrating piston kinetic and ejected fluid kinetic energy. Please note that this is a schematic representation and elements are not to scale.

These simple calculations indicate that the motor/piston combination is capable of delivering several joules during the pump pulse, but the vortex ring only requires a fraction of a millijoule (mJ). Clearly the actuator has far more power than required for effective ring generation.

7.5.4 Method – Energy transferred into the Vortex Ring

Evidence from the experimental work performed with the introduction of food colourant dye suggests that all the colourant goes into the ring core and there is very little left behind the translating vortex ring. The behaviour can be idealised assuming no losses so that the energy delivered by the piston is totally transferred to the fluid and, consequently, into the vortex ring.

Piston Energy → Fluid Energy → Vortex Ring Energy

The programmed piston displacement was always 0.8 mm. This value has been experimentally assessed to be fairly repeatable with variability lower than +/- 5 %. Furthermore, the final displacement was found to be independent from the different motor input powers, initial piston position and output orifice diameter. Consequently, it has been demonstrated that the energy delivered by the motor is always sufficiently high to produce stable vortex rings and a detailed analysis of pressures involved is not needed. With a cylinder diameter of 70 mm and a displacement of 0.8 mm, the piston ejects ~3.1×10^3 mm^3 (or ~3.1×10^{-6} m^3) of fluid at velocities dependent on the output orifice diameters and on the piston programmed velocity. For example, considering the configuration of a 15 mm diameter orifice and an average piston velocity of 2 cm/s, the ejected fluid possesses a kinetic energy ($E=1/2\ mv^2$) of ~0.3 mJ (0.29 mJ, Figure 7.21). Ideally, this energy is completely transferred into the vortex ring. This process is illustrated in the schematic block of Figure 7.22.

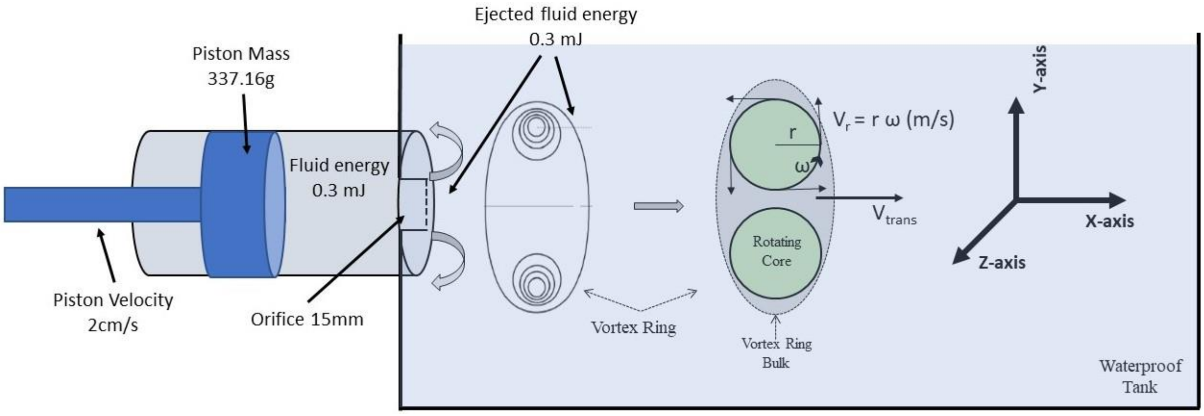

Figure 7.22: Schematic block of the kinetic energy transferred from the piston to the fluid into the cylinder and into the vortex ring. Please note that this is a schematic representation and elements are not to scale.

Laser PIV experiments for this configuration, described in Chapter 5, have reported a ratio of 3 to 2 between measured peak rotational velocity (V_{rot} = 42.3 cm/s) and translational velocity (V_{trans} = 27.8 cm/s) at a distance travelled of 8.5 cm into the phantom imaging tank. The energy is proportional to velocity squared, therefore it can be assumed that it is partitioned approximately 55 % - 45 % between the translational and the rotational velocity. Assuming that the vortex travels through the tank with minimal (zero) losses, $E_{rotational}$ = 0.165 mJ and $E_{translational}$ = 0.135 mJ, as shown in Figure 7.23 with this partition.

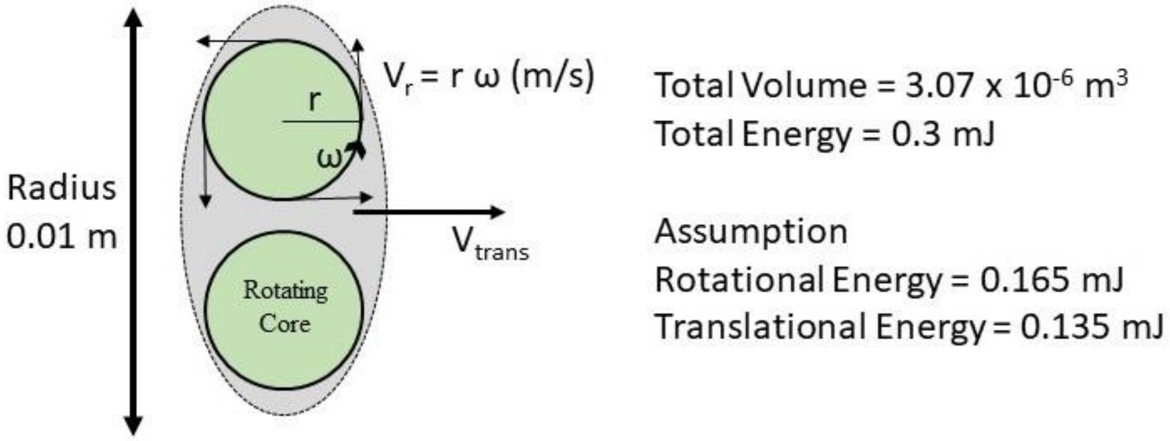

Figure 7.23: Schematic diagram of the energy transferred from the piston to the fluid into the cylinder and into the vortex ring. Please note that this is a schematic representation and elements are not to scale.

Consequently, the vortex ring translational velocity can be calculated as:

$$E = \frac{1}{2}\, m\, v^{2} \quad \rightarrow \quad V = \sqrt{\frac{2E}{m}} \quad \rightarrow \quad V_{translational} = 0.2782\ m/s\ \approx 28\ cm/s$$

This value was calculated assuming no losses, partition of energy V_{trans}/ V_{rot} (45 % / 55 %) and that all the volume ejected from the orifice forms the vortex ring bulk. Clearly this constitutes an idealisation and an upper bound. Technically, the rotating core pulls in additional fluid while the vortex ring is travelling which adds extra mass. For a configuration of 15 mm orifice, piston velocity of 2 cm/s, and piston displacement of 0.8 mm, a value of about one fourth of extra mass addition has been calculated from Laser PIV acquisitions. Assuming the ring has added one fourth of extra mass when it has travelled 8.5 cm into the phantom, the translational velocity calculated above (28 cm/s) decreases by about 10 % (25.2 cm/s). The translational velocity calculate with Laser Diodes/Photodiodes acquisitions is 20 cm/s, which corresponds to kinetic energy of ~0.07mJ.

7.5.5 Results - Energy delivered by the motor

Following assumptions described in Section 7.5.3, kinetic energies of the piston/fluid and of the fluid ejected from the orifice were calculated and are summarised in Table 7.7.

Orifice (mm)	Piston Velocity (m/s)	Energy Of Ejected slug of fluid (mJ)	Energy to move piston + water (mJ)	W required (mJ)
10	0.02	1.49	0.14	1.63
10	0.013	0.66	0.14	0.80
15	0.02	0.29	0.14	0.43
15	0.013	0.13	0.14	0.27

Table 7.7: Energy delivered by the motor for the different configuration tested.

The motor is able to provide energies in pulses of the order of few joules while external work required for the fluid ejection is ~1.63 mJ in the worst case scenario. Although losses were neglected in the calculation, these values differ by a factor of 10^3. This might explain why vortex ring results were insensitive to different combinations of piston loads and motor input powers on piston velocity profile, piston final displacement and vortex ring translational velocity.

7.5.6 Results – Energy delivered by the motor - Limitations

To create the vortex ring, the motor needs to overcome the inertia of the fluid in the cylinder and it needs to accelerate the ejected slug of fluid (0.43 mJ). Ideal and real motor (piston) velocity profiles are depicted in schematic block of Figure 7.24. Basic calculations to identify motor limits for different power settings (Section 7.3) are provided in Table 7.8.

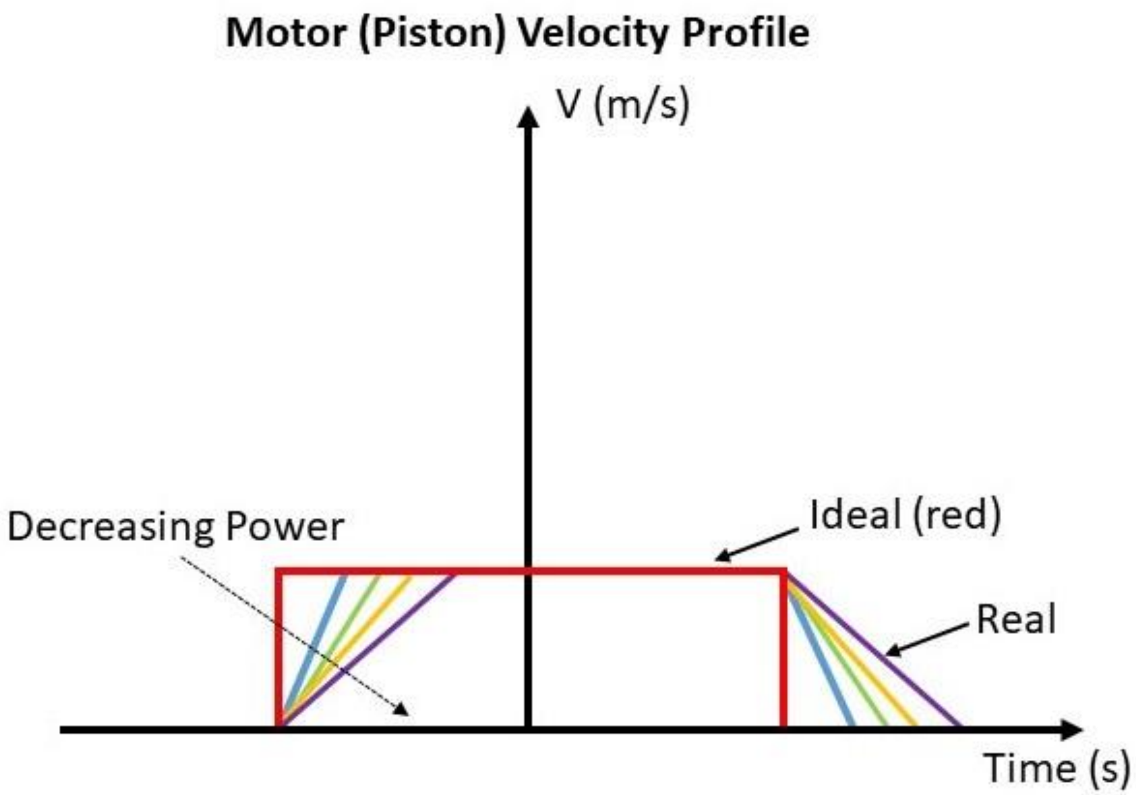

Figure 7.24: Schematic block of ideal (red) and real (other colours) piston velocity profiles.

Power (W)	Energy (mJ)	Time to deliver the energy (μs)
96.84	0.43	4.44
84.69	0.43	5.07
48.96	0.43	8.78
25.56	0.43	16.82

Table 7.8: Motor limitations – time needed for the motor to deliver 0.43 mJ for different power settings. These values should be compared with the typical pulse length of 0.04s (40000μs).

7.5.7 Results – Energy transferred into the Vortex Ring

Following the idealisation described in previous section, values were calculated for each condition tested and are summarised in Table 7.9. Higher energy losses (%) are estimated for vortex rings generated with lower translational velocities. Estimated energy losses are listed in the last column of the table (in %) and refers to the difference between the energy of the ejected fluid (at orifice interface) and the energy when the vortex has travelled 8.5 cm into the phantom imaging tank. The kinetic energy of the ejected fluid is subdivided between rotational and translational velocity components. Ratios of approximately 50 % - 50 % (10 mm orifice) and 45 % - 55 % (15 mm orifice) were estimated from Laser PIV acquisitions (Section 5.2.5, Chapter 5). The second last column provides absolute values of energy dissipation. The assumption that the vortex ring has added about one fourth of extra mass while travelling into the phantom is not valid for the 10 mm configurations. This can be appreciated in two Laser PIV acquisition frames illustrated in Figure 7.25: the vortex ring size remains approximately constant after it has travelled 8.5 cm into the water tank.

Orifice (mm)	Piston Velocity (m/s)	Kinetic Energy Ejected Fluid (mJ)	Kinetic energy Rotational/Translational Ratio estimated from Laser PIV acquisitions (%)	Vortex Ring Velocity estimated assuming no losses (m/s)	Estimated velocity with Laser Diode/Photodiodes (m/s) - Average (+/- 5 %)	Kinetic Energy Estimated from Laser Diode/Photodiodes data (mJ)	Translational velocity energy losses calculated (mJ)	Energy losses calculated (%)
10	0.02	1.49	50-50	0.69	0.68	0.90	0.02	1.5
10	0.013	0.66	50-50	0.46	0.43	0.36	0.04	5.8
15	0.02	0.29	55-45	0.29	0.20	0.08	0.05	18
15	0.013	0.13	55-45	0.24	0.12	0.03	0.03	23

Table 7.9: Energetics involved in vortex ring generation and propagation. The kinetic energy ratio between rotational and translational velocity has been calculated from Laser PIV acquisitions. Kinetic energy estimated from Laser Diode/Photodiodes acquisitions with the 15 mm orifice assumes that the vortex ring has added one fourth of extra mass when it has travelled 8.5 cm into the phantom imaging tank.

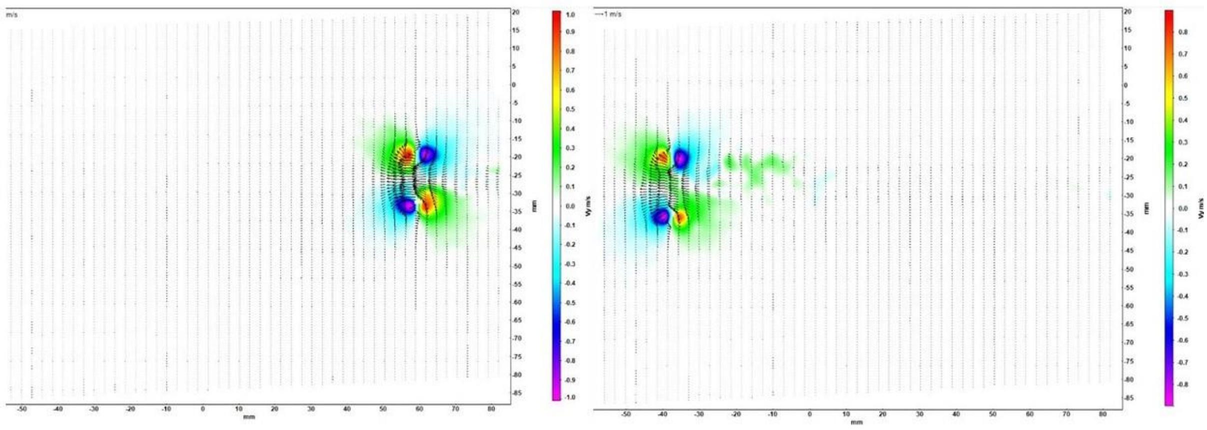

(a) (b)

Figure 7.25: Frame 1 (a) and Frame 3 (b) – Laser PIV acquisition for a configuration with a 10 mm orifice and piston speed of 2 cm/s. The vortex size remains approximately the same while the vortex has travelled 8.5 cm into the phantom.

7.5.8 Discussion

A simple energetic analysis has been conducted with the available data to highlight the potential of the instrumentation pack. Simple approximations allowed basic calculations on the energetics and losses involved with the system. If a simple energetics analysis is sufficiently accurate, it should be possible to predict the vortex ring behaviour with the sorts of straightforward calculations described above. The motor is able to deliver energies of few Joules while the energy required to push the piston and a column of ~3.1 x 10^3 mm^3 of fluid through the orifice requires a meagre 1.63 mJ. This explains why the motor can be used at reduced input powers and with different piston loads (piston position, orifice output diameter) without significantly affecting phantom performance. The process of vortex ring formation is complex, therefore, it is not clear how much energy and fluid volume are transferred into the ring and how much is lost during the formation. However, simple relationships were found assuming that all the ejected volume forms the vortex ring with calculation of the partition of energy between translational velocity component and rotational velocity. Vortex rings generated with higher translational velocities exhibit lower energy losses (in percentage terms), calculated when the vortex has travelled 8.5 cm into the phantom imaging tank. Beyond the formation step, it can be assumed that main energy losses are purely viscous. Intuitively, if the flow is ejected with lower velocity, the Reynolds number is lower, consequently viscous forces are higher and energy loss is higher. In addition, the configuration that involves 10 mm diameter exhibits a stroke ratio (*L/D*) of 3.92 (Table 5.1, Chapter 5). This value is optimal for vortex ring formation (Table 2.1, Chapter 2) and better approximates the assumption that all the energy and all the volume of ejected fluid forms the vortex ring (Garib *et al* 1998, "*for 3.6 < L/D < 4.5, there is a clear separation between the formed vortex ring and the trailing jet region behind it*. *All the discharged fluid has entrained into the vortex ring*"). Conversely, the configuration of 15 mm diameter is characterised by a stroke ratio (*L/D*) of 1.16. Under this condition, vortex rings generated exhibit a thick core and a diffusive vorticity distribution tending to the Hill's fat-limit (Table 2.1, Chapter 2; Shariff & Krueger, 2018).

The energetic analysis conducted is not exhaustive and several approximations have been made for simplifying the problem. However, results help with the interpretation of previous experiments and theoretical models (Gharib et al, 1998; Shariff & Krueger, 2018) and give an idea of the potentiality of the instrumentation pack system. This is valuable in helping to optimise the phantom design. Motor limits have been identified with these simple calculations.

7.5.9 Conclusion

A basic analysis has been conducted exploiting data already obtained in previous experimental sessions. The energetic analysis is informative for previous experimental studies and highlights the potential of the instrumentation pack in characterising the phantom at a more detailed level. Further analysis might further clarify vortex ring formation and propagation processes. Finally, energetic analysis allows to predict the effect of future design changes and optimise them (e.g. for an MRI compatible design, Chapter 8).

7.6 Discussion

The instrumentation pack offers advanced characterisation of phantom and flow performance. Details, described in Chapter 6, demonstrated the functionality of the system. A number of additional experiments reported in this chapter illustrate the potential and advantages of such instrumentation.

Early experiments assessed the variability of the motor and how this affects the reproducibility of the vortex ring translational velocity. Average piston peak velocity, piston average velocity (calculated as final displacement divided by time) and piston final displacement showed variability lower than +/- 13 %, +/- 14% and +/- 3 %, respectively. However, this variation did not affect the average vortex ring translational velocity which exhibited variability always lower than +/- 6 %. These values relied on simultaneous acquisition, with linear encoder and Laser Diodes/Photodiodes monitoring ten consecutive vortex rings generated at different piston initial positions (which corresponds to different motor loads). For the selected motor input power of 96.84 W, no correlation was found between the vortex ring translation velocity, different piston peak velocities, different piston average velocities or different piston positions (loads).

Performance of the phantom was also tested under a combination of 30 different motor input powers (84.96 W, 48.96 W and 25.56 W) and different piston loads (two different orifice diameters and two different piston positions). Average peak velocity values showed variability within +/- 20 % for 26 configurations tested. Greater variability was found for four particular configurations. Average final displacement variability was within +/- 5 % for 28 configurations tested. The worst case of +/- 8 % showed a distinct lower value on the acquisition (Figure 7.15) of the first vortex ring generated. This was true for only two of 175 acquisitions, but it might be prudent to start measurements from the generation of the second vortex ring to avoid systematic errors. Piston peak velocity and final displacement values were plotted as a function of increasing motor input power and increasing piston load (combination of orifice diameter and initial piston position) for all the 175 performed acquisitions. Correlation plots show that there is no a dependency between the variables, suggesting that the piston can be randomly positioned, operating with any orifice diameter (Figure 4.4, Chapter 4), and the lowest selectable motor input power of 25.56 W can be used without significantly affecting the performance of the system.

Validity of the Laser Diode/Photodiode measurement method was tested by comparing the results with simultaneous optical/video acquisitions and with measurements performed with the same method on two different days. Measurements proved to be challenging for the configuration producing the smallest vortex ring size and the fastest vortex ring translational velocities. Average translational velocity variability for this particular configuration was +/- 20 %, although previous Laser PIV acquisitions on the same configurations showed variability always lower than +/- 6 %. Variability drastically dropped to values around +/- 10 % or lower with slower rings, demonstrating the utility of the system in providing vortex ring translational velocity reference values for most of the available settings. Again, there was no significant difference between translational velocities of vortex rings generated with different motor input powers.

Finally a simple energetic analysis was conducted with the available data to further highlight the potential of the instrumentation pack in clarifying features of the system and of the flow. Energies needed to push a column of fluid (~3.1x 10^{-6} m^3) through the orifices are of the order of 1 mJ, and explains why phantom performance is not affected by motor input power or different piston loads. Although a number of idealisations were made to carry out basic calculations, results approximated theoretical predictions and experimental analyses as described in Table 2.1, Chapter 2. Vortex rings generated by a stroke ratio (*L/D*) of 3.92, which corresponds to the optimal vortex ring formation, encouragingly approximated the idealisation that all of the volume of ejected fluid and all of the energy is incorporated into the vortex ring bulk. Vortex rings generated by stroke ratio (*L/D*) of 1.16 are known to be more diffusive, more dissipative and possibly do not absorb all the energy and volume of the ejected fluid (Section 2.4, Chapter 2).

7.7 Conclusion

These experiments have been conducted with the instrumentation pack described in the previous chapter (Chapter 6). The analysis conducted was not exhaustive and more experiments would enable greater characterisation of the system and the flow. However, the experiments highlight the value of an instrumentation pack and provide an idea of the amount of useful information that can be readily obtained. Surprisingly, piston peak variability up to +/- 20 % and piston displacement variability up to +/- 8 % do not significantly affect the vortex ring translational velocity reproducibility. Indeed, the instrumentation pack would naturally alert the user to any anomalous ring behaviour. It is appropriate that the Vortex Ring based Complex Flow Phantom can be used with the lowest selectable motor input power (25.56 W), placing the piston at any position and installing any orifice provided without affecting results. The methods have been validated by cross referencing the results with independent measurement methods or with previous experiments found in literature.

In conclusion, the instrumentation pack is a reliable, cost-effective, simple and fast tool to assess the performance of the phantom and to clarify physical relationships that regulate flow generation and propagation. In addition, reference values can be calculated on a number of different parameters (i.e. vortex ring translational velocity, volume ejected and piston velocity profile) without resorting to the use of expensive and time-consuming measurement methods, such as Laser PIV. The real-time feedback of the instrumentation pack enables the user to trust the phantom, and be made aware immediately if it is not performing as expected.

CHAPTER 8

Magnetic Resonance Compatible Vortex Ring based Complex Flow Phantom design – Proof of concept

8.1 Introduction

The Vortex Ring based Complex Flow Phantom prototype, described in Chapter 4, is naturally compatible with Ultrasound imaging and X-ray-CT. For Magnetic Resonance Imaging (MRI) compatibility, significant modifications of the design must be introduced. Notably, the stepper motor is ferromagnetic and it is not compatible with the Magnetic Resonance (MR) environment. An MRI compatible version of the complex flow phantom is proposed and described in this chapter. The prototype has been tested in a laboratory environment to prove the working principles. Long-term ambition of the design anticipates MRI imaging with advanced 4D Phase Contrast and comparison with Doppler Vector Flow Imaging.

The complex flow phantom currently is entirely manufactured from Perspex (PMMA). Other small parts, such as the pegs that fix the water tank to the base, are manufactured from other plastics or nylon. However, the mechanism of action of the piston relies on an external linear stepper motor (Nema 23 external linear actuator, 1.8 degrees, 36V, 3A, OMC Corporation Limited, Nanjing, China). When a DC current is applied to the terminals of the motor, it moves and develops torque (Section 4.4.4, Chapter 4). The motor is not compatible with the Magnetic Resonance environment (described below) because it contains ferromagnetic materials. Furthermore, the MR scanner relies on a very homogeneous magnetic field; electromagnets interact with the electromagnetic field of the scanner and introduce artefacts in the image.

Material restrictions in the Magnetic Resonance environment, health and safety regulations and an MRI compatible version of the Vortex Ring based Complex Flow Phantom prototype are described in this chapter.

8.2 Magnetic Resonance Units – Materials restrictions

8.2.1 Introduction

Several regulations must be observed when introducing materials near to strong magnetic fields. Generally speaking, materials in proximity to MRI machines require accurate labelling and are classified as listed in Table 8.1 (American Society for Testing Materials 2013):

Sign	Definition	Label
MR SAFE **(this item can be taken in the scanner)**	*"To obtain the new MR safe designation, objects must be completely free of all metallic components. It must be completely non-metallic, non-conductive, and not RF reactive. Everything that receives the new MR safe designation must be equally safe at all field strengths, gradients and sequences. Objects getting the new designation will have to be fabricated very carefully from non-conductive materials such as rubber, plastics, ceramics, select polymers, wood and fiberglass."* (American Society for Testing Materials 2013)	
MR CONDITIONAL **(caution – some of these items can be taken in the scanner, some cannot)**	*"The bulk of objects, including most contemporary medical implants and devices, will receive the MR conditional designation. This means that the object or device is safe under certain tested conditions, and those conditions should be enumerated on the product, its packaging or in the enclosed literature. Nearly everything that carries either the current MR safe or MR compatible designations would be switched to MR conditional under the new standard".* (American Society for Testing Materials 2013)	
MR UNSAFE **(danger – this object cannot be taken in the scanner)**	*"MR unsafe – an item that is known to pose hazards in all MRI environments. MR unsafe items include magnetic items such as a pair of ferromagnetic scissors."* (American Society for Testing Materials 2013) Every material that has not been previously tested must be classified as MR unsafe.	

Table 8.1: Classification and labelling of materials in MR Units – (American Society for Testing Materials 2013).

Forces acting on different materials, types of materials, and delineated safety zones of typical Magnetic Resonance Units are described in detail in following sections.

8.2.2 Diamagnetic, Paramagnetic and Ferromagnetic materials

Magnetic Resonance Imaging (MRI) relies on strong magnetic fields and radiofrequency coils. The main magnet, commonly designated as B (or B_0), is "always on" and constitutes the major source of risk. In clinical applications, the magnetic fields are usually 1.5 T or 3 T. For context, the Earth's magnetic field is ~ 50 µT. How objects behave when they are in the proximity of such large magnetic fields, depends on what they are made of and on their shape (Panych, 2018).

The volume magnetic susceptibility is a dimensionless parameter (χ), which quantifies the degree to which a material becomes magnetised in response to an external magnetic field. The volume magnetic susceptibility is defined as the ratio between the magnetic moment per unit volume (M) to the intensity of the externally applied magnetic field (H). If χ is negative and small, the material is diamagnetic and the magnetic field within the material is weakened by the induced magnetisation (examples are water, plastic, wood, biological tissues). If χ is positive and small, the material is paramagnetic. If an external magnetic field is applied (i.e. gadolinium for MRI contrast enhanced imaging, deoxyhemoglobin for MRI bold signal) to a paramagnetic material or fluid, the internal magnetic field is enhanced. If χ is large and positive, the material is ferromagnetic (examples at room temperature are iron, nickel and cobalt). Ferromagnetic materials are strongly attracted to magnets and form magnetic fields even if an external magnetic field is not applied. This category of materials constitutes the principal safety concern in presence of Magnetic Resonance (MR) magnetic field. Diamagnetic and paramagnetic materials are also affected by external magnetic fields, but these effects are valuable for imaging and do not pose a projectile hazard like ferromagnetic materials.

Typically, a material is considered (general rule) MR safe if the gravitational forces on the object are significantly higher than the magnetic forces. Accurate guidelines and standard test methods, to assess the compatibility of materials with the MR environment, are provided by the American Society for Testing Materials (American Society for Testing Materials 2010; American Society for Testing Materials 2011).

8.2.3 Forces involved with strong magnetic fields

Ferromagnetic materials are not compatible with the MR environment. It is reasonable to think that most metals are ferromagnetic; however, metals such as copper, titanium, aluminium or some stainless steel are not ferromagnetic and are compatible with the MR room (assuming that they are pure).

When a ferromagnetic material is moved close to the MR scanner, it experiences a translational (attractive) and a rotational (torque) force. The attractive force depends on the magnetic susceptibility of the material, on the field strength (B) and on the spatial gradient of the magnetic field (change of the magnetic field with respect to distance, *dB/dz*, *T/m*) (Medicines and Healthcare Products Regulatory Agency 2014; Panych, 2018). It is reasonable to think that the closer a ferromagnetic material gets to the scanner the stronger is the attractive force. Typically, the force produced is maximum just at the opening of the magnet (max gradient near the bore entry) and is zero (uniform field, zero gradient) in the centre of the scanner (Schenck 2005).

MR scanners are designed to have a uniform magnetic field in the imaging region, which is near the centre. For this reason, the magnetic field strength is very high in the centre but the gradient forces are essentially zero (Schenck 2005). The magnetic forces decay rapidly to zero as a function of the distance from the scanner. Small changes in distances can have a substantial impact on attractive forces. When the force of attraction on a ferromagnetic object exceeds a critical value, the object moves and continues to accelerate towards the magnet. The object effectively becomes a "projectile" (projectile effect). The magnetic field *B* (red), magnetic gradient (blue) and force product (green) along the axis of a 4 T MR scanner are shown in Figure 8.1.

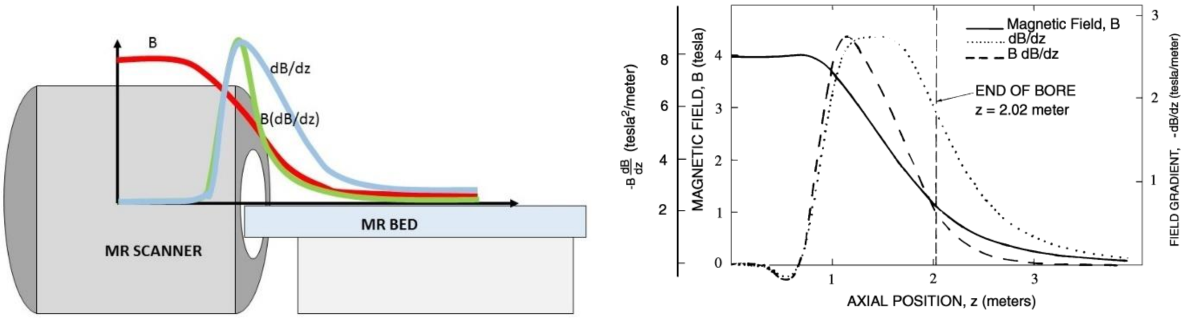

Figure 8.1: Field, gradient and force product along the axis of a 4T MR scanner.
Figure 1: Schenck, J. F. (2005). Physical Interactions of Static Magnetic Fields with Living Tissues, in: *Progress in Biophysics and Molecular Biology*.

Additionally, ferromagnetic objects also experience a rotational force when moved close to an MR scanner. The rotational force, which is proportional to *B*, is due to the tendency of ferromagnetic objects to align with the direction of the magnetic field. The torque is also dependent on the shape of the object and its angle in relation to the static magnetic field. The torque vanishes if the induced magnetisation is parallel to *B* (Schenck 2005). The maximum of the torque force occurs near the isocentre of the magnet.

8.2.4 Magnetic Resonance Zones

The American College of Radiology (ACR) defines standards for safe practices in clinical and research MR environments. The ACR MR Safe practice guidelines (Kanal et al 2013) divides conceptually the MR site into four Zones:

- Zone I: area accessible to the general public. This area is outside the MR environment;
- Zone II: interface between the accessible zone (Zone I) and the strictly controlled zones (Zone III and Zone IV);
- Zone III: zone close to the MR room where gradients and RF magnetic fields are sufficiently strong to present a hazard to unscreened or non-MR personnel (visitors, patients, untrained staff). Access to this zone, which is for example the control room, is authorised under the supervision of MR personnel;
- Zone IV: synonymous with the MR scanner magnet room itself. It is always placed within the Zone III. Non-MR personnel should be accompanied by people who have been extensively trained and educated in broad aspects of MR safety issues.

An MRI functional diagram that illustrates the different area is shown in Figure 8.2. By way of example, the layout of an MRI unit is shown in Figure 8.3.

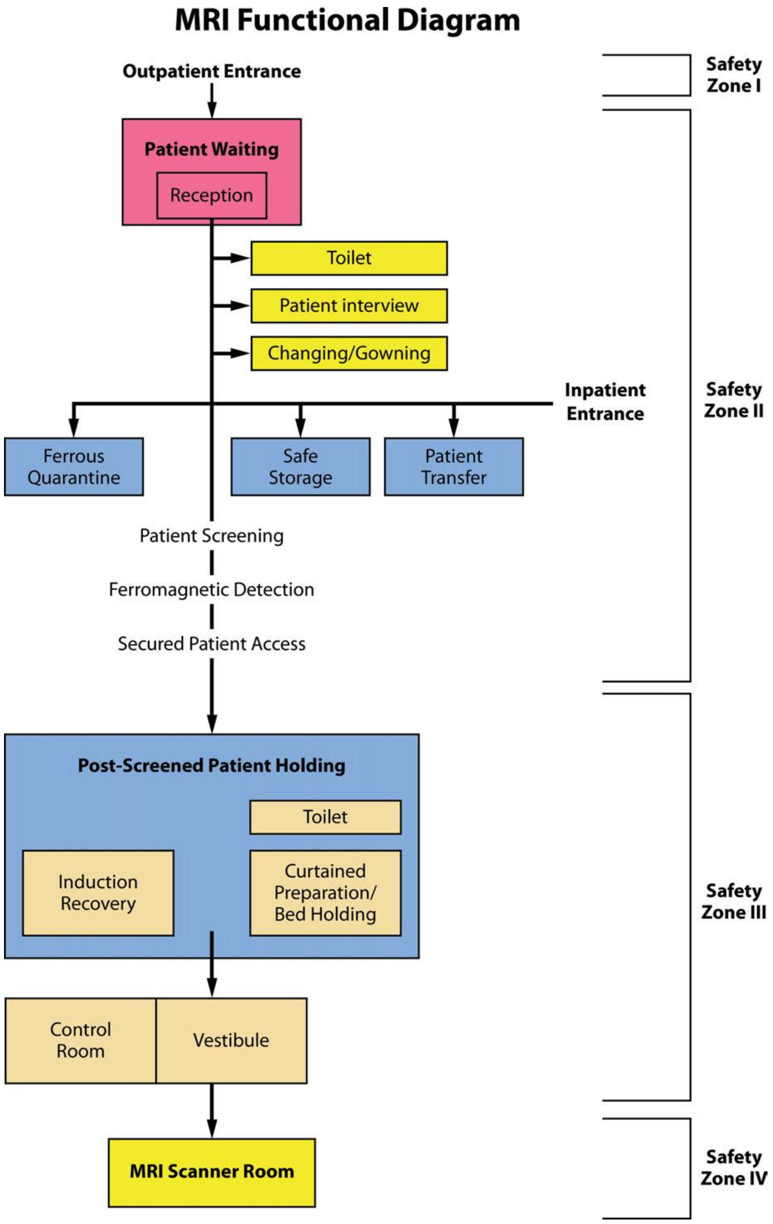

Figure 8.2: MRI functional diagram of the four different zones.

Figure 1 : Kanal, E., Barkovich, A. J., Bell, C., Borgstede, J. P., Bradley, W. G., Froelich, J. W., Gimbel, J. R., Gosbee, J. W., Kuhni-Kaminski, E., Larson, P. A., Lester, J. W., Nyenhuis, J., Schaefer, D. J., Sebek, E. A., Weinreb, J., Wilkoff, B. L., Woods, T. O., Lucey, L. & Hernandez, D. (2013). ACR Guidance Document on MR Safe Practices: 2013. *Journal of Magnetic Resonance Imaging*.

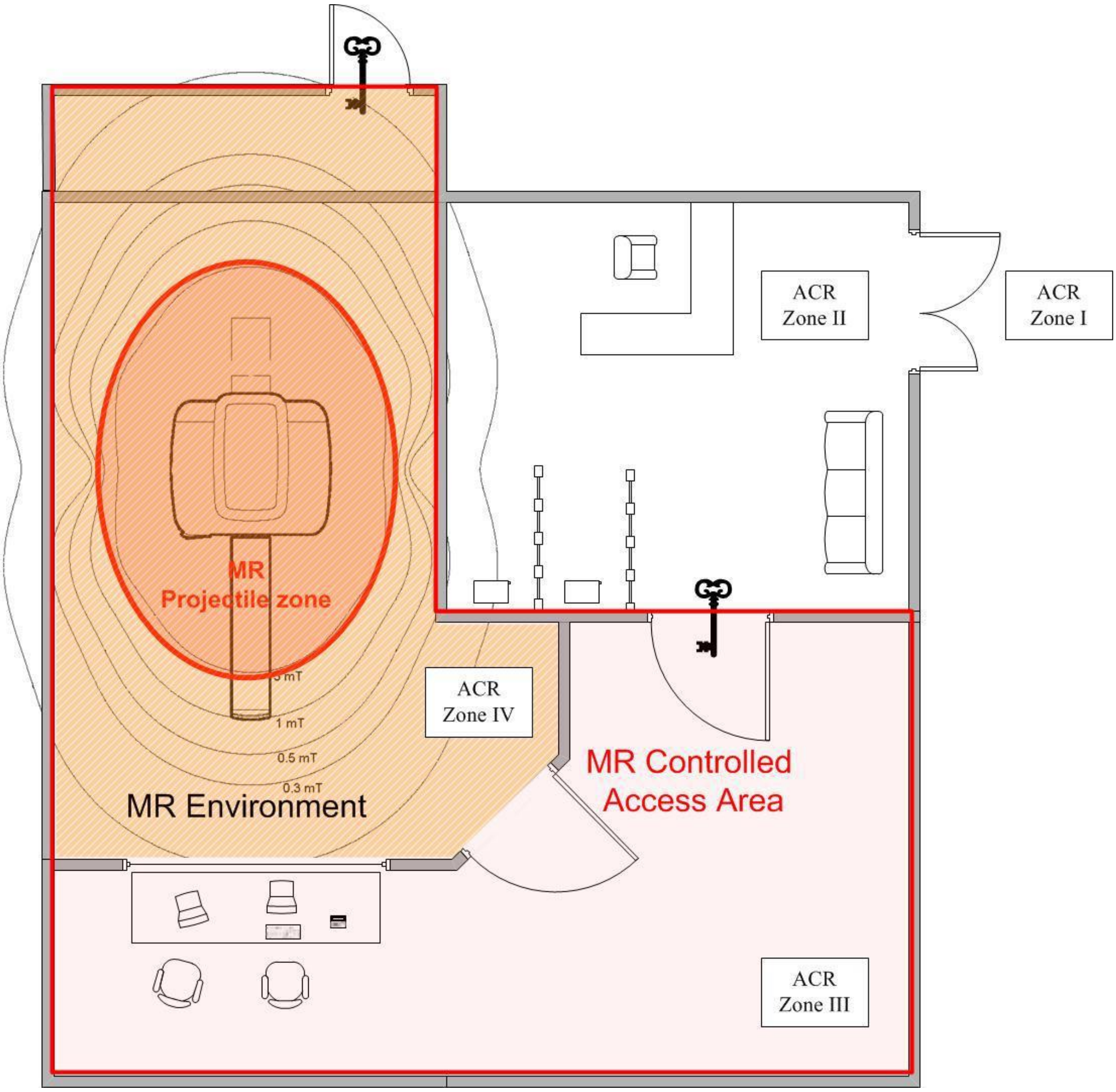

Figure 8.3: Example of MRI unit layout.

Figure 1: Medicines and Healthcare Products Regulatory Agency (2014). *Safety Guidelines for Magnetic Resonance Imaging Equipment in Clinical Use*.

It is appropriate to clarify numerous technical terms:

- The static magnetic field, *B*, is measured in *Tesla* (*T*).
- The spatial gradient, which is the strength of the magnetic field with respect to distance, is measured in *Tesla/meter* or in *Gauss/cm* (*1T/m = 100 G/cm*).
- The magnetic force product (attractive magnetic force) is measured in T^2/m.
- The *MR environment* is the "*three dimensional volume of space surrounding the MR magnet that contains both the Faraday shielded volume and the 0.50 mT field contour (5 Gauss line). This volume is the region in which an item might pose hazard from exposure to the electromagnetic fields produced by the MR equipment and accessories*" (American Society for Testing Materials 2013).
- The *control area* incorporates the inner controlled area (Zone IV), the control room (Zone III) and typically patient preparation or changing room.

- The <u>*projectile zone*</u> is "*the volume containing the full extent of the 3 mT magnetic field contour, or other appropriate measure around the MRI scanner"* (Medicines and Healthcare Products Regulatory Agency 2014). The field strength limit of 3 *mT* has been chosen by the Physical Agents (electromagnetic fields) of The European Parliament and The Council of The European Union Directive (European Union Directive 2013). Outside the *3 mT* line, there is no risk of projectile effects.

8.2.5 Introduction of ferromagnetic objects into the MR environment

Technically, a ferromagnetic material (such as a stepper motor) might be introduced in Zone IV and kept beyond the projectile zone with no major safety concerns. However, for the majority of MRI units, the introduction of ferromagnetic objects is not allowed both in the MR controlled access area nor the MR environment area (Figure 8.3). MR personnel, which act under the authority of the MR medical director (or designated physician of the day), are responsible for ensuring that MR safe practice guidelines are strictly adhered to. Therefore, they rarely allow the introduction of ferromagnetic objects in Zone IV.

Supposing that a stepper motor is allowed to be introduced to an MR environment area, there are issues related to the creation of image artefacts. MR scanners are manufactured with very homogenous magnet fields. Although the magnet is manufactured with the most rigorous of tolerances, the magnetic field is distorted when anything magnetic is placed into the imaging suite. Pipes, wires, ducts, iron elements in walls or in the floor, fringe fields, introduce further distortions. Small pieces of metal with known magnetic qualities are added near the permanent magnet or currents are driven by specific coils to improve the homogeneity of the magnetic field. The first process is known as passive shimming, the second process as active shimming. The presence of a stepper motor introduces a further magnetic field that was not considered in the shimming process, producing shimming disturbances. Moreover, MRI measures radiofrequency response at an atomic level. Power supply, transformer, digital stepper driver, stepper motor currents and magnetic fields may interfere with the MRI electronics and create artefacts in the image (or vice versa). Instabilities in the magnetic field and radiofrequency emissions of external objects must be low in order not to be detected by the MR system and to not produce image reconstruction errors or artefacts (American Society for Testing Materials 2013). Because of potential shimming disturbances and electromagnetic interference, it is inadvisable to introduce ferromagnetic elements or electric components into the MR environment.

Conversely, for specific purposes (e.g. research, quality control) and under controlled circumstances, MR personnel may allow the introduction of ferromagnetic objects and motors into the Zone III for two main reasons:

1) Zone IV is radiofrequency shielded (typically with a Faraday cage) to prevent external electromagnetic radiation from distorting the MR signal and to prevent interference between the MR scanner and nearby medical devices. Consequently, there is unlikely to be interference between the stepper motor (and the dedicated electronic chain) and the MR signal;
2) the magnetic field is below 0.3 mT and there is little risk of projectile hazards from the ferromagnetic material.

8.2.6 Summary

Magnetic Resonance Imaging relies on strong magnetic fields that are *"always ON"*. Several restrictions apply to non-authorised persons and materials introduced into the Magnetic Resonance controlled zones (from Zone II to Zone 4). Zone II (Figure 8.3) is the area that interfaces between the zone accessible to the public (Zone I) and the strictly controlled zones. MR unsafe materials are (commonly) ferromagnetic and strictly forbidden into the MR Zone III and Zone IV (Figure 8.3). Ferromagnetic materials experience a projectile effect when positioned within magnetic fields higher than 3 mT. Although a stepper motor (which is ferromagnetic) might be introduced in Zone IV and kept at a distance beyond the 3 mT threshold with minimum risk, the electronic components (i.e. power supply, transformer, currents, magnetic fields) may introduce distortion into the homogeneous magnetic field, generating artefact into the image. Ideally, the electronic and ferromagnetic components must be kept outside Zone IV. A complex flow phantom design that deliver this flexibility is described in following section.

8.3 Magnetic Resonance Compatible Vortex Ring based Complex Flow Phantom - Design

8.3.1 Introduction

As discussed, numerous restrictions are in operation when working with MRI units. The stepper motor (and related electronics), that are used to drive the piston of the phantom, constitute a critical issue for Magnetic Resonance compatibility. As noted in Chapter 1, there are MRI compatible linear motion systems available on the commercial market, but the cost is significant (over 10000 GBP). Notably, Shelley Medical Imaging Technologies (Shelley Medical Imaging Technologies, Ontario, Canada) provides an MRI compatible multimodality motion controller unit for diagnostic imaging (i. e. http://www.simutec.com/Docs/MRI%20Compatible%20Multimodality%20Motion%20Stage%20V2%20LR.pdf). Companies like Physik Instrumente L.P. (PI L.P., MA, USA) and Micromo (MICROMO, FL, USA) are manufacturers of piezo linear actuators. However, these are very limited in maximum achievable speed, maximum achievable range of motion and maximum actuation force. They are designed for micro application and are not compatible with the working requirements of the Vortex Ring based Complex Flow Phantom. Furthermore, they are also expensive and custom-designed products would have a price much higher than the whole test object itself. Finally, there is poor or no evidence in literature that these motors do not create electromagnetic interference with the MRI signal. For these reasons, replacement of the stepper motor for MR applications is undesirable. It might be considered in the future if new technologies were available and if the competition of the market ultimately lowered the average price.

It is desirable that modification of the Vortex Ring based Complex Flow Phantom design exploits the existing components as much as possible, to minimise escalating manufacturing costs. Since the critical part is the stepper motor (and related electronics), the most intuitive strategy was to create a design where the motor can remain in Zone III while the phantom operates in Zone IV (effectively in the scanner). This can be realised with the creation of a hydraulic piston/cylinder arrangement. The piston, driven by the motor, constitutes the generator side of the hydraulic system and delivers a regulated flow to the hydraulic cylinder. The vortex ring generation requires displacement of fluid, therefore, a piston chamber and a cylinder chamber can be simply connected by a pipe (Figure 8.11).

For MRI compatibility the piston/cylinder arrangement, manufactured with the technology described in Section 6.2.2 (Chapter 6), is coupled to the water-tank ("Imaging Tank", Figure 4.3, Chapter 4) through a connection with a reinforced PVC pipe hose. Assuming that the mass of an incompressible fluid is always conserved regardless of the pipeline complexity or flow direction (incompressibility assumption), the volume of fluid displaced into the piston/cylinder is the same volume displaced at the phantom orifice interface ("Interchangeable Output Orifices", Figure 4.5, Chapter 4). Neglecting pipe wall compliance, frictional losses and microscopic effects, mean fluid velocities in a system of equal areas are equal for each cross-section. If the area changes, the velocity is inversely proportional to the cross-sectional area (where ρ is the density of the fluid, A is the cross-sectional area and V the velocity of the fluid):

$$\rho_1 A_1 V_1 = \rho_2 A_2 V_2 = \rho_3 A_3 V_3 = \ldots\ldots$$

assuming that ρ (density) stays constant

$$A_1 V_1 = A_2 V_2 = A_3 V_3 = \ldots\ldots$$

8.3.2 Design - Motor Base and Piston/Cylinder support blocks

In the MRI compatible design a new support base was designed to align the piston/cylinder assembly with the motor. The component, designated the "Motor Base" and shown in the technical drawing in Figure 8.4, was manufactured from white PMMA (Perspex). It has dimensions of 513 mm (Length) x 170 mm (Width) x 5 mm (Thickness) and hosts a square block of PMMA of dimensions 65 cm (Length) x 65 cm (Width) x 25 mm (Thickness). Length and width dimensions have tolerance +/- 0.25 mm. Wall thicknesses have a production tolerance of +/- 10 % plus additional 0.4 mm, in agreement with the ISO 7823-1:2003 (ISO 7823-1:2003).

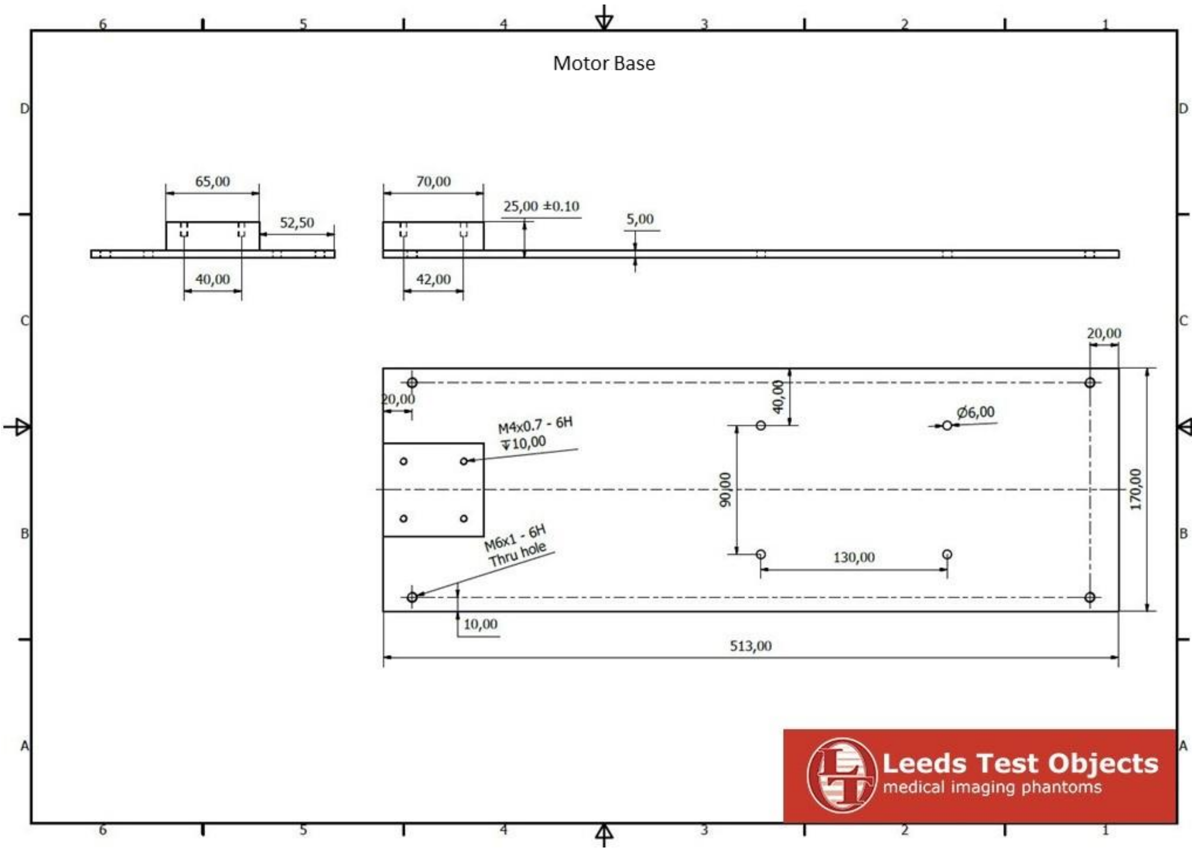

Figure 8.4: MRI Compatible Vortex Ring based Complex Flow Phantom – "Motor Base".

The motor base has four marginal (in the four corners) holes that permit fixing to another base, if more rigidity or different angulation of the piston are required. Finally, it has four additional internal holes that are designed to match the threaded holes of two support blocks ("Support Block Back" and "Support Block Front). The support blocks screw into the base and secure the piston/cylinder system to prevent movement. Technical drawings of the "Support Block Back" and "Support Block Front" are shown in Figure 8.5 and Figure 8.6, respectively. The support block "Support Block Back" part has dimensions 130 mm (Length) x 15 mm (Width) x 59 mm (Height). A semicircle of radius 45 mm has been cut from the top part of the block to host the piston/cylinder. The support block "Support Block Front" part has same length and height of the "Support Block Back" part (130 mm x 59 mm) but it is wider (25 mm) to accommodate two semicircles of different radius and widths have been cut from the top part. A semicircle of radius 45 mm and width 12.5 mm hosts the front part of the piston/cylinder while a semicircle of radius 40 mm and width 10 mm prevents the piston/cylinder moving forward during the piston pushing action. Moreover, the piston/cylinder is glued into the "Support Block Front" component to ensure stronger locking and to impede the movement in the opposite direction (when the piston moves backward). All the dimensions specified in this section have the same tolerances indicated in Section 8.3.2.

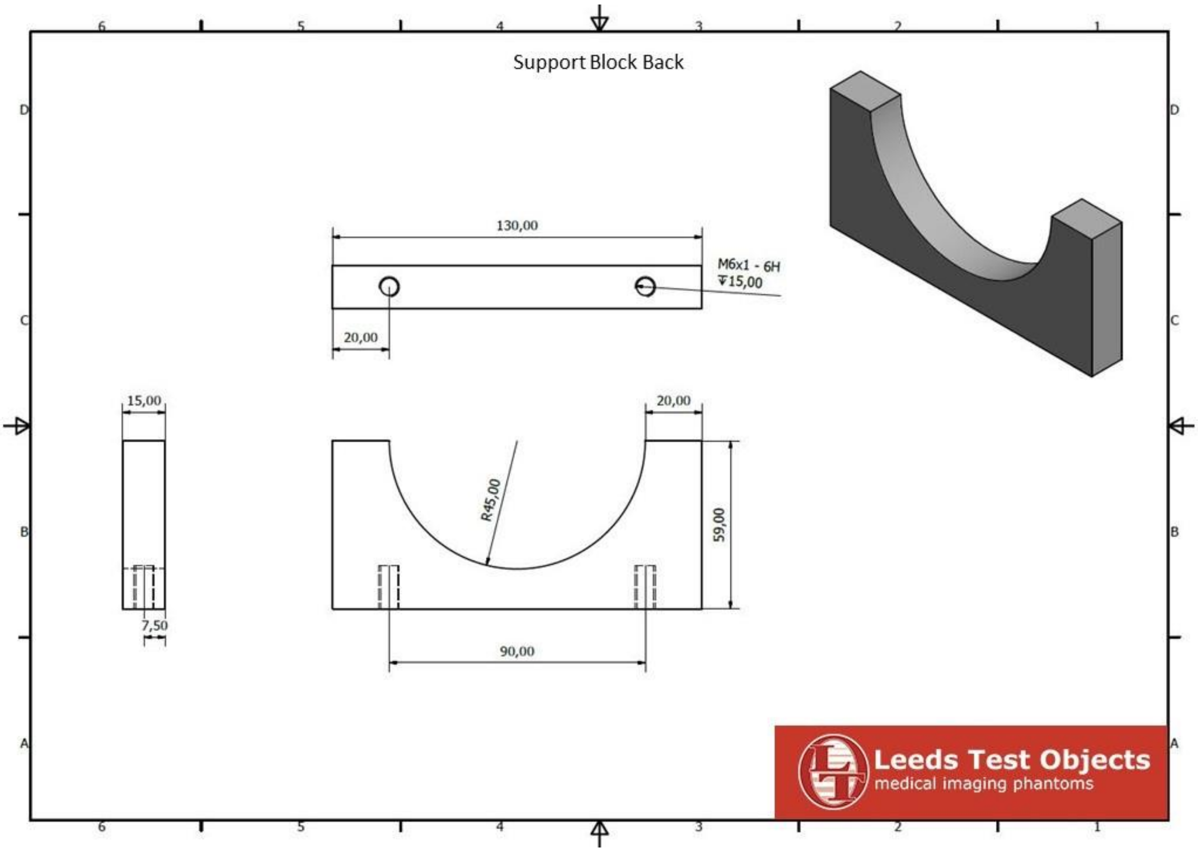

Figure 8.5: MRI Compatible Vortex Ring based Complex Flow Phantom - “Support Block Back”.

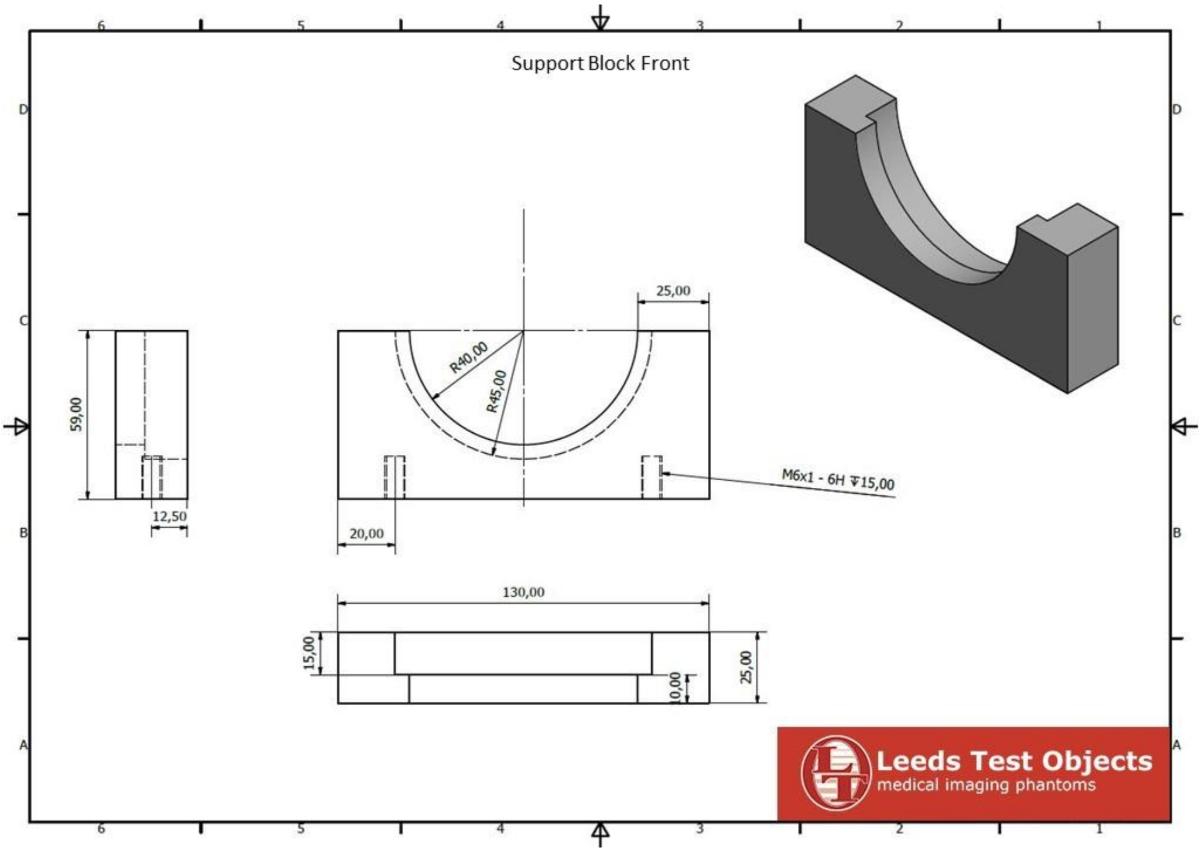

Figure 8.6: MRI Compatible Vortex Ring based Complex Flow Phantom - “Support Block Front”.

8.3.3 Design - Piston/Cylinder system

The piston was manufactured following the procedure described in Section 6.2.2 (Chapter 6). A cylinder, of internal diameter 70 mm (tolerance of +/- 0.10 mm), was manufactured from clear PMMA (Perspex). The cylinder (“MR Cylinder”, Figure 8.7) has an internal length of 144 mm +/- 0.25 mm. The rear part of the cylinder is threaded and matches the piston guide (“Piston Guide”, Figure 4.4, Chapter 4). The front part of the cylinder has a ½ inch thread hole to match a ½ inch British Standard Pipe Taper (BSPT) male connector (RS Components Ltd, Stock No 795-203). The connector is straight and matches the internal dimensions of a reinforced PVC pipe hose (RS Components Ltd, Stock No 330-0858). The PVC pipe hose is used to transfer the volume of fluid from the “MR Cylinder” (Figure 8.7) to the “Tank Cylinder” (Figure 8.8), which is connected to the “Imaging Tank” (Figure 4.3, Chapter 4). An M8 threaded hole has been cut from the top part of the MR cylinder. The threaded hole matches with a HDPE metric threaded O-ring plug M8 x 1. The plug allows the water to flow from the “Imaging Tank” to “MR Cylinder” (through the PVC hose pipe) and vice versa. “MR Cylinder” technical drawing is shown in Figure 8.7.

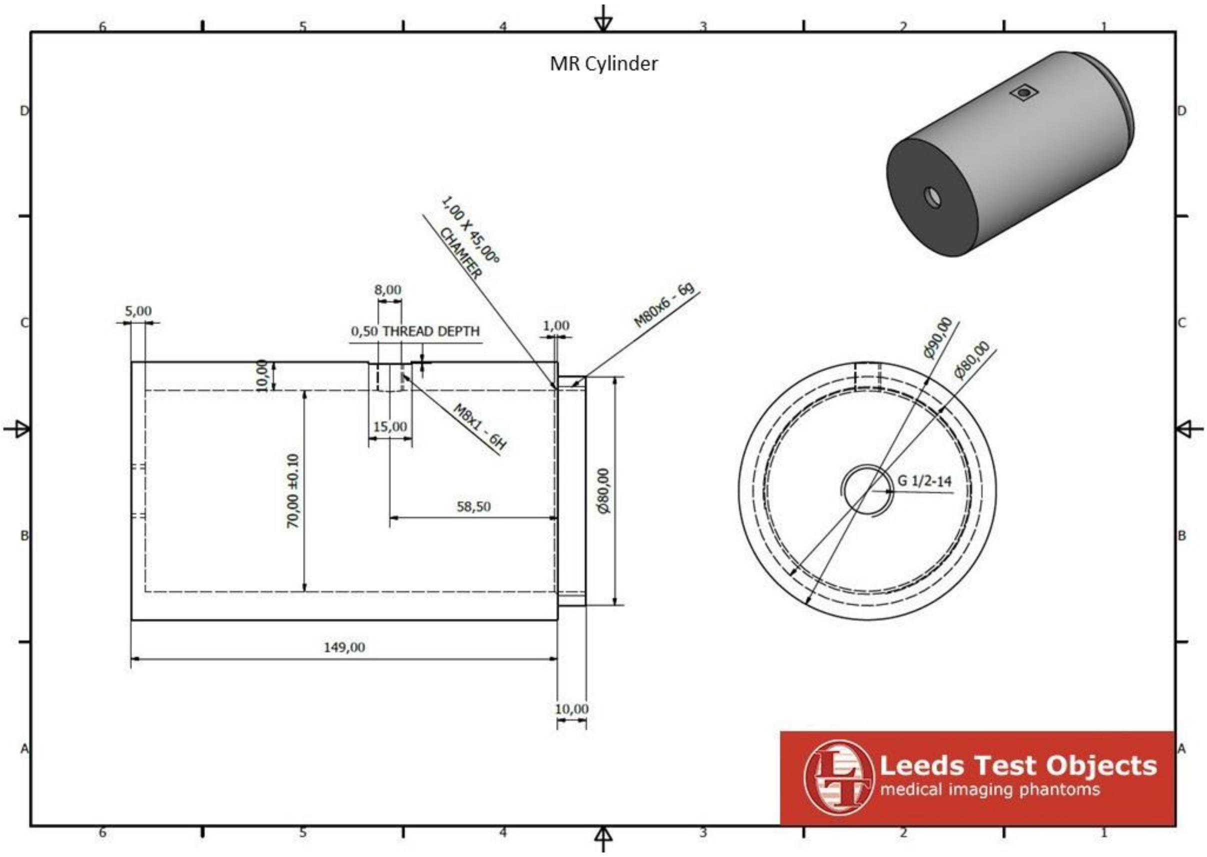

Figure 8.7: MRI Compatible Vortex Ring based Complex Flow Phantom – “MR Cylinder”.

8.3.4 Design - Tank Cylinder

The original component "Cylinder" (from Figure 4.4, Chapter 4) has been re-designed to support connection to the PVC pipe hose. The new component, designated "Tank Cylinder" (Figure 8.8), has the same internal and external diameter, and the same front thread as the original "Cylinder" ("Cylinder", Figure 4.4, Chapter 4). The posterior part connects to the "MR Cylinder" assembly through the PVC pipe hose. Similarly the front part of the "MR Cylinder" ("MR Cylinder", Figure 8.9) component, it has a ½ inch thread hole to match a ½ inch British Standard Pipe Taper (BSPT) male connector (RS Components Ltd, Stock No 795-203). Technical drawing of the "Tank Cylinder" is shown in Figure 8.8.

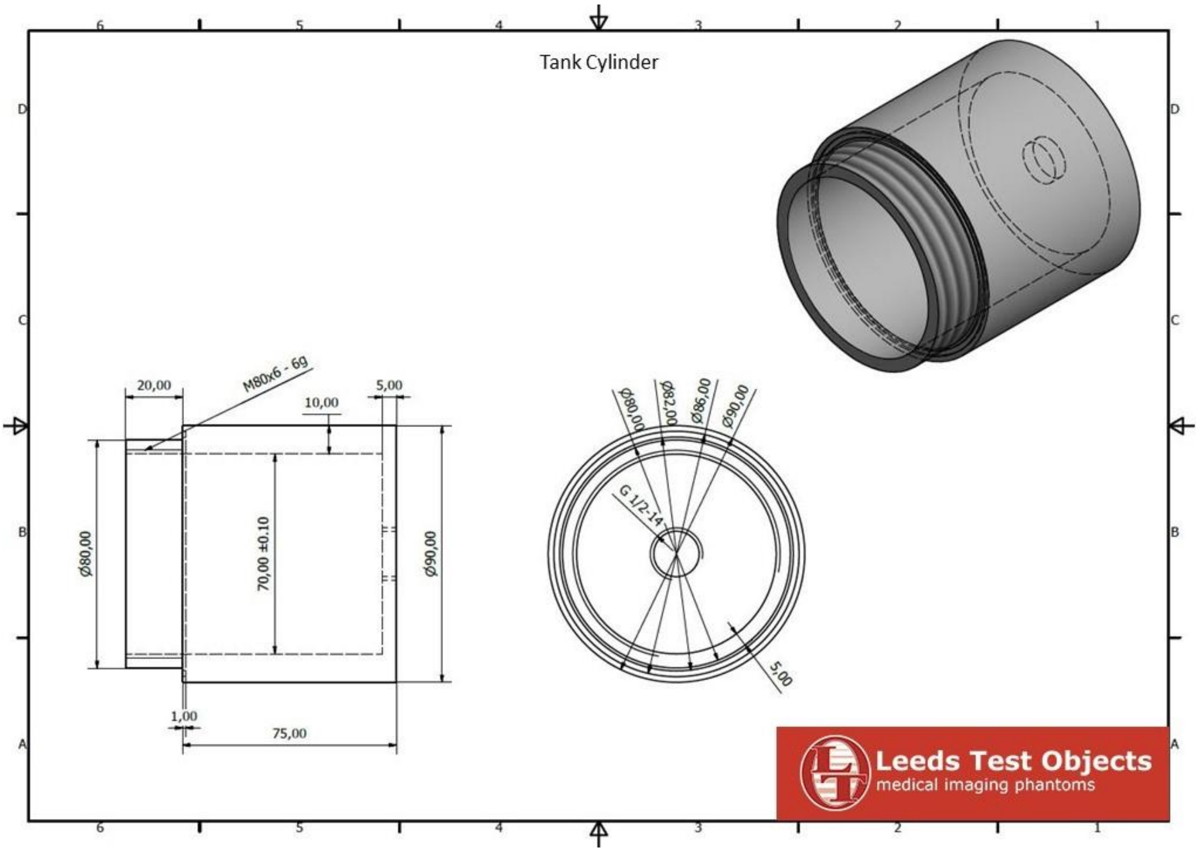

Figure 8.8: MRI Compatible Vortex Ring based Complex Flow Phantom – "Tank Cylinder".

The "Tank Cylinder" has a length of 75 mm (tolerances specified in Section 6.4.2). The length is a critical component for vortex ring generation. The PVC hose pipe has an internal diameter of 12 mm cut to a length of 10 m to allow easy remote positioning of the phantom within the MR environment. Considering that this is a narrow pipe over a long length, energy losses and Reynolds number might be critical. Turbulence in the pipes is expected for Re > 2000. Therefore, the "Tank Cylinder" (Figure 8.8) should be long enough to avoid such turbulence (introduced by the pipe) affecting the vortex ring formation at the orifice ("Interchangeable Output Orifices", Figure 4.5, Chapter 4) interface. On the other hand, the "Tank Cylinder" (Figure 8.8) cannot be too long for not loading with excessive weight the leak-proof coupling with the water tank ("Imaging Tank", Figure 4.3, Chapter 4).

8.3.5 Assembled System

All the components depicted in Figure 8.4, Figure 8.5, Figure 8.6 and Figure 8.7 were assembled for testing, and produced the system presented in Figure 8. 9. The PVC pipe hose is also visible, secured to the BSPT connector with a Nylon 6.6 plastic hose clip (RS Components Ltd, Stock No 291-650). A schematic diagram of the design is illustrated in Figure 8.10, the stepper motor assembly remains in MRI Zone III while the phantom imaging tank is placed into the scanner (MRI Zone IV).

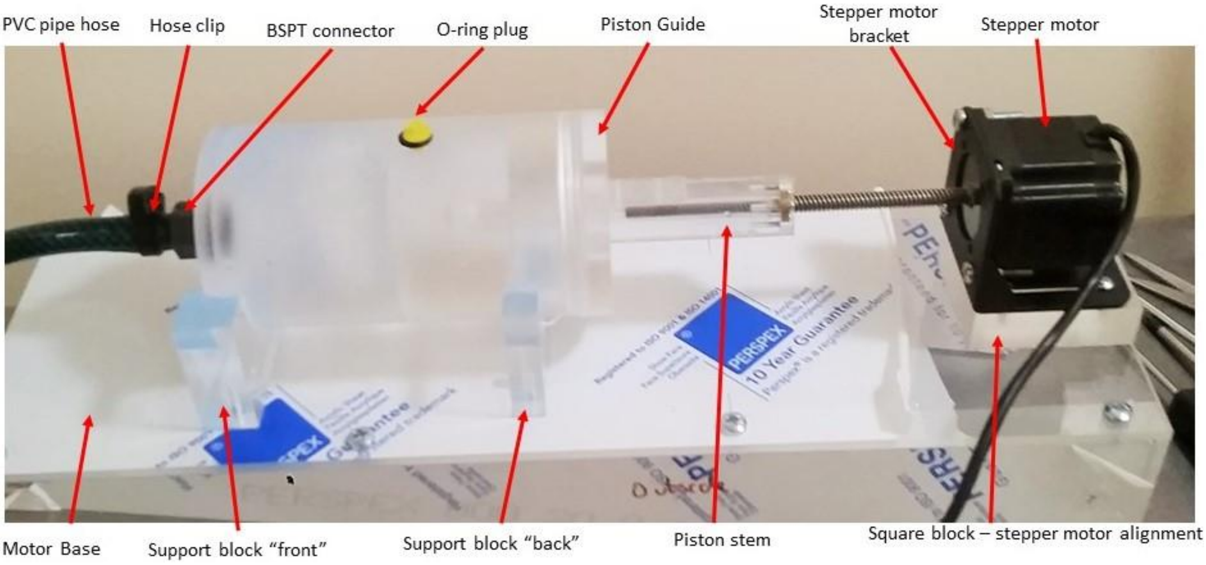

Figure 8.9: MRI Compatible Complex Flow Phantom – Stepper Motor assembly.

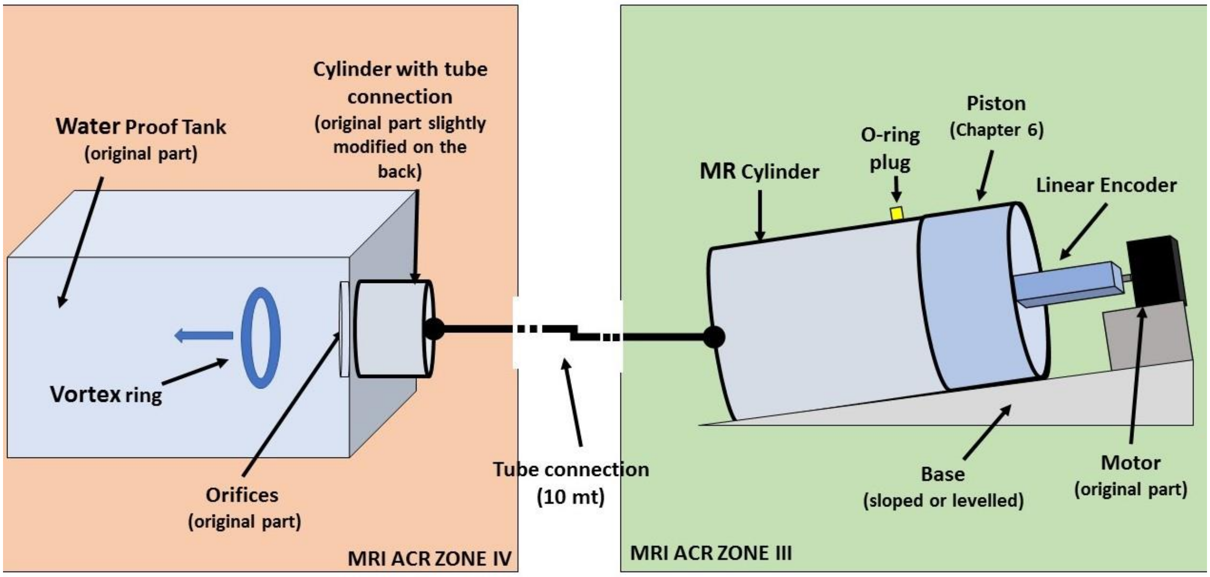

Figure 8.10: Schematic diagram of the MRI compatible Vortex Ring based Complex Flow Phantom design – the stepper motor assembly is placed in MRI ACR Zone III while the phantom imaging tank is placed into the MR scanner. Please note that this is a schematic representation and elements are not to scale.

8.3.6 Demonstration and Application

Early applications have been performed to test the MRI Compatible Vortex Ring based Complex Flow Phantom prototype. Videos have been acquired for demonstration purposes and two frames are shown in Figure 8.11. The test was conducted at Leeds Test Objects Ltd (Leeds Test Objects Ltd, Boroughbridge, United Kingdom) and proved the working principles of the phantom design.

The stepper motor assembly (Figure 8.9) was positioned at a distance of approximately 9 m from the water-proof tank ("Imaging Tank", Figure 4.3, Chapter 4). The two systems were connected with the 10 m PVC pipe hose. Connections were secured on both parts with Nylon 6.6 plastic hose clips for minimising the risk of leakage (particularly important if the phantom is operating near MR electronics). The piston stem (Figure 8.9) was pulled back and the tank was filled with water. The stepper motor assembly was initially positioned at a lower height than the imaging tank so that when the HDPE O-ring plug was removed from the cylinder, the water flowed from the imaging tank into the piston cylinder assembly. This configuration is particularly helpful because it removes air-bubbles within the system. When the "MR Cylinder" ("MR Cylinder", Figure 8.7) was full, the HDPE O-ring plug was replaced and the stepper motor assembly was positioned at the same height as the imaging tank. Clearly, any difference in height between the imaging tank and the piston-cylinder assembly results in different loads placed on the motor due to gravitational force. Initially the two systems were kept at the same height for simplicity.

The "Tank Cylinder" (Figure 8.8) was filled with blue DYE food colourant, for vortex ring visibility with video cameras, and a 15 mm orifice ("Interchangeable Output Orifices", Figure 4.5, Chapter 4) was inserted. As expected, the vortex ring forms at the 15 mm orifice interface and travels with self-induced velocity across the whole phantom. Obviously, using equivalent settings of Table 5.1 (Chapter 5) or Table 7.3 (Chapter 7), vortex rings produced had considerably slower velocities. The motor load increases considerably, since it is displacing the fluid through a very long and narrow pipe. However, the instrumentation pack described in Chapter 6 can be used on the new prototype and new reference values can be easily established. Although some design limitations were found and are discussed in detail in the following section (Section 8.4), the phantom performed as expected and demonstrated that it is ready to be tested in clinical MRI units. The Nylon 6.6 plastic hose clips guarantee a secure coupling between pipes and BSPT connectors, particularly important when the phantom operates in a clinical MR scanner.

Figure 8.11: MRI Compatible Complex Flow Phantom – test with blue DYE food colourant within Leeds Test Objects Ltd facilities.

8.4 Magnetic Resonance Compatible Vortex Ring based Complex Flow Phantom – Design Limitations

8.4.1 Introduction

Design limitations rapidly became apparent in this prototype. Specifically, the motor struggles to deliver enough energy to generate fast vortex rings (i.e. translational velocities higher than 30 cm/s). The long and narrow pipe also has a tendency to introduce turbulence into the flow that is visibly transferred into the vortex ring. Pressures generated by the system are insufficient to create water leakage at the piston cylinder interface. Limitations and potential alternatives are discussed in the following sections.

8.4.2 Design Limitations – Motor energy

A simple energetic analysis clarifies why the motor struggles to generate fast vortex rings. The motor moves the piston and the water contained within the “MR Cylinder” (Figure 8.7), the “Tank Cylinder” (Figure 8.8) and the pipe. The kinetic energy needed to generate a vortex ring with energy of ~0.3 mJ (Section 7.5.3, Chapter 7) is:

$$E = \frac{1}{2}\, mv^2 = \frac{1}{2}\, m_{piston}\, V_{piston}^2 + m_{water/MR\ cylinder} V_{water/MR\ cylinder}^2 + m_{water/pipe} V_{water/pipe}^2 + m_{water/tank\ cylinder} V_{water/tank\ cylinder}^2 + 0.3\ \text{mJ} \quad (1)$$

Calculations are summarised in Table 8.2:

	Radius (m)	**Length (m)**	**Volume (m^3)**	**Mass (kg)**
pipe	0.006	10	0.0011304	1.1304
tank cylinder	0.035	0.095	0.000365418	0.3654175
mr cylinder	0.035	0.1	0.00038465	0.38465
piston				0.33716*
Energy = 0.068 + 0.077 + 261.776 + 0.731 + 0.3 = 262.95 mJ = 0.263 J				

Table 8.2: summary of kinetic energy calculations to generate a vortex ring with 0.3 mJ with the MRI compatible complex flow phantom.
* value calculated in Section 7.5.2, Chapter 7.

When the flow is pushed through a pipe there is a resistance (analogue to electrical resistance $V = IR$) between the fluid and the vessel wall that generates negative work. For this case the resistance is assumed constant and it is defined as the ratio between the pressure difference (ΔP) and the rate of change of mass or volume (ΔQ).

$$R = \frac{\Delta P}{\Delta Q} \qquad (2)$$

The flow through the pipe is affected by tube diameter, tube length and fluid viscosity (Equation 3). Flow is directly proportional to the fourth power of the tube radius (r^4) and inversely proportional to the length of the tube. Viscosity is a measure of frictional forces within the fluid layers, therefore, the flow is also inversely proportional to viscosity. All these variables are brought together by the Hagan-Poiseuille equation:

$$Q = \frac{P\pi r^4}{8\eta L} \qquad (3)$$

Where Q is the flow rate (*Litres/seconds*), η is the viscosity (*Pascals x seconds*), P is the pressure (*Pascals*), r is the radius of the tube *(meters)*, L is the length of the tube (*meters*). From equation (3), it is possible to calculate the pressure difference between the two ends of the pipe.

$$\Delta \mathrm{P} = \frac{8\eta \mathrm{LQ}}{\pi \mathrm{r}^4} \qquad (4)$$

Consequently, the pressure difference needed to push a column of fluid of ~3.07 x 10^{-3} litres, in 0.04 seconds, within a tube of 10 m length and 12 mm diameter, is 1.34 x 10^6 Pa. This calculation is based on assumptions of incompressible flow, laminar flow within the pipe, no deformation of the pipe walls, no acceleration of flow through the pipe and constant circular pipe cross-section. Under these assumptions, Bernoulli's equation stated that (block scheme in Figure 8.12):

$$P_1 + \frac{1}{2}\rho v_1^2 + \rho g h_1 = P_2 + \frac{1}{2}\rho v_2^2 + \rho g h_2 \qquad (5)$$

Where P_1 is the pressure within the MR cylinder, ρ the density of the water, v_1 the fluid velocity within the MR cylinder, g the gravitational constant, h_1 the height of the fluid within the MR cylinder. P_2, v_2 and h_2 are equivalent values within the Tank cylinder (Figure 8.12). Placing "MR cylinder" (Figure 8.7) and “Tank cylinder” (Figure 8.8) at the same level $h_1 = h_2$, consequently, there is no variation of potential energy.

$$P_1 = P_2 + \frac{1}{2}\rho(v_2^2 - v_1^2) \qquad (6)$$

Assuming that no further work (J) is needed to push the fluid from the tube-end to the orifice (it is less than 1 mJ*,* Table 7.7, Chapter 7), 1.34 x 10^6 Pa. The work (Joule = Pascal/m^3) needed to push a column of ~3.07 x 10^{-3} litres through the pipe in 0.04 s is:

$$W = \frac{P_1}{m^3} = \frac{P_2 + \frac{1}{2}\rho\left(v_2^2 - v_1^2\right)}{m^3} = 4.12\,Joule \qquad (7)$$

The total kinetic energy needed to generate a vortex ring with 0.3 mJ energy is 4.12 J plus 0.263 J (E_{tot} ~ 4.38 J). In the real case, there are losses within the tube, the fluid is turbulent at that speed (Reynolds number ~ 6000) and the tube walls are deformable. In a circular pipe with smooth internal surface and uniform diameter the pressure loss due to viscous forces can be calculated with the Darcy-Weisbach equation:

$$\frac{\Delta p}{L} = f_D\,\frac{\rho}{2}\,\frac{\langle v\rangle^2}{D} \qquad (8)$$

Where *Δp/L* is the pressure loss per unit of length, *p* the density of the fluid, *D* the hydraulic diameter of the pipe, $<v>^2$ the mean flow velocity and f_D the Darcy-friction factor. Consequently, the work (J) needed is higher than the motor can supply in 0.04 seconds (Table 7.6, Chapter 7). Selecting the maximum input power of 96.84W, the motor is capable of delivering 4.38 J in 0.045s. The suggestion is to significantly increase the pipe diameter and reduce the length (where possible) or to control two motors with the same Arduino Board.

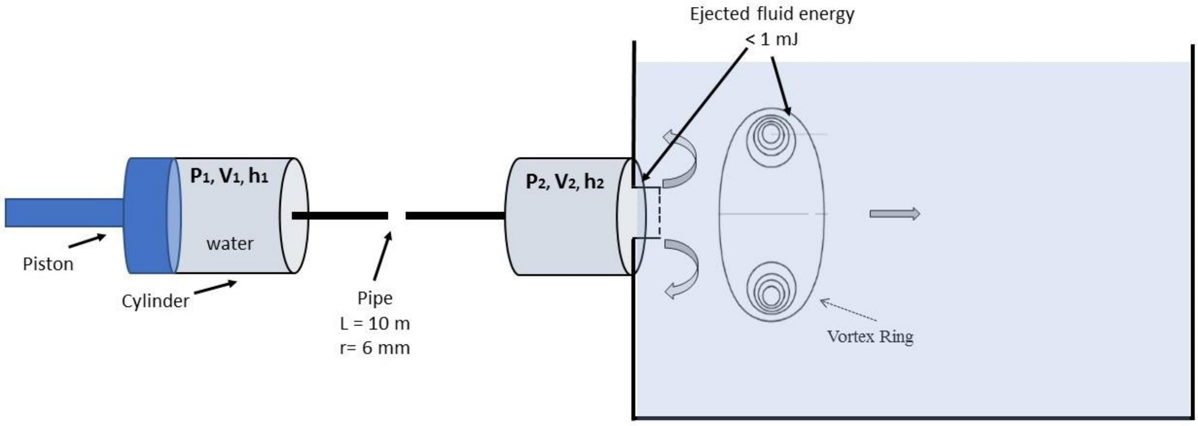

Figure 8.12: Schematic block of the MRI compatible Vortex Ring based Complex Flow Phantom design – quantities involved in Bernoulli’s equation (Equation 3). Please note that this is a schematic representation and elements are not to scale.

8.4.3 Design Limitations – Turbulence

The flow within the pipe has a Reynolds number of ~6000. Consequently, the flow is turbulent and this is reflected in the generation of turbulent vortex rings. This effect is clearly visible from visual inspection. Turbulent flow is not convenient for a test object because it is characterised by chaotic fluid motion with random changes in pressure and velocity. Three potential alternatives were identified to overcome this problem. The "Tank Cylinder" might be manufactured big enough to avoid turbulence without compromise of vortex ring generation (option 1). However, a bigger "Tank Cylinder" implies a heavier weight needs to be sustained by the screw coupling and a compromise should be chosen. A flow straightener might be added into the "Tank Cylinder" to stabilise the flow before vortex ring generation (option 2). A flow straightener is a component, often based on a honeycomb or a circular structure, which minimises the lateral velocity components (caused by swirling motion and turbulence) of the flow. By way of an example, a simple flow straightener prototype was built using two laser-cut PMMA (Perspex) bases and (about) two hundred plastic mini cocktail straws of 3 mm diameter (Figure 8.13). Number of straws and dimensions should be chosen to create minimal resistance to the flow.

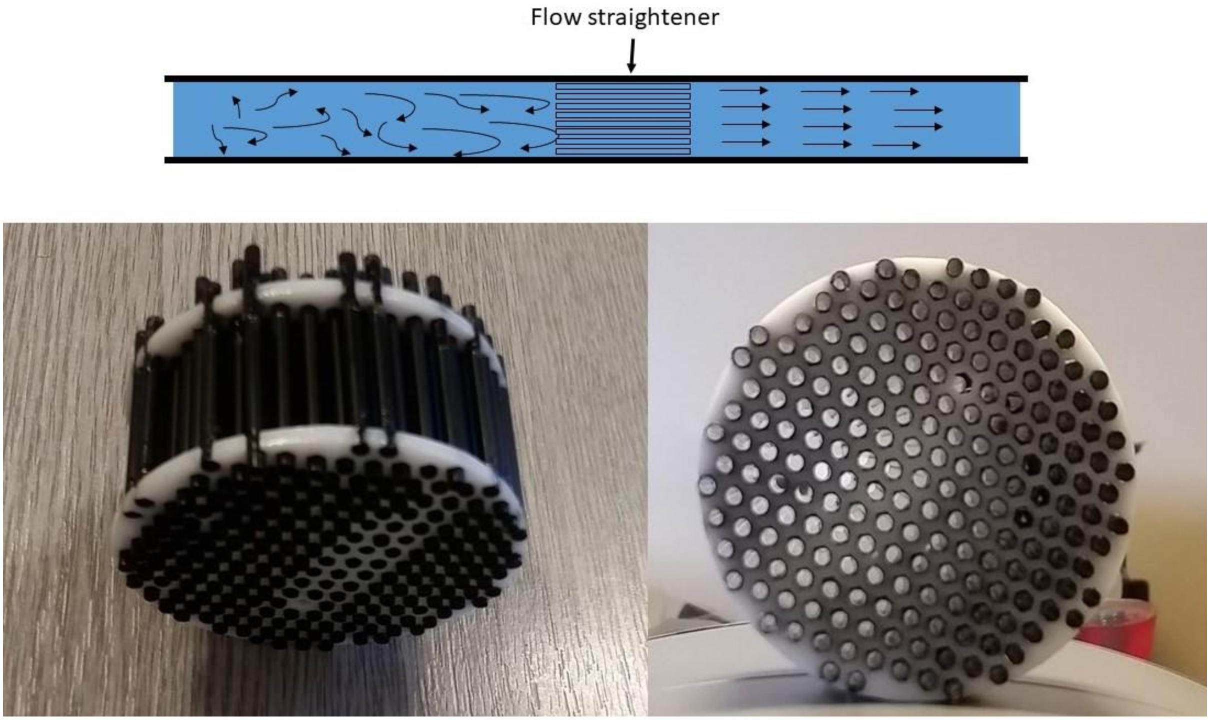

Figure 8.13: MRI Compatible Vortex Ring based Complex Flow Phantom – Flow Straightener (simple prototype).

Alternatively, the hydraulic piston (option 3) could be designed as shown in schematic block in Figure 8.14. A cylindrical block of Perspex can be manufactured with low tolerances following the method described in Section 6.2.2 (Chapter 6). Sucking fluid from the "Tank Cylinder" cylinder allows the piston to retract while routing pressurised fluid into the "Tank Cylinder" allows the piston to extend.

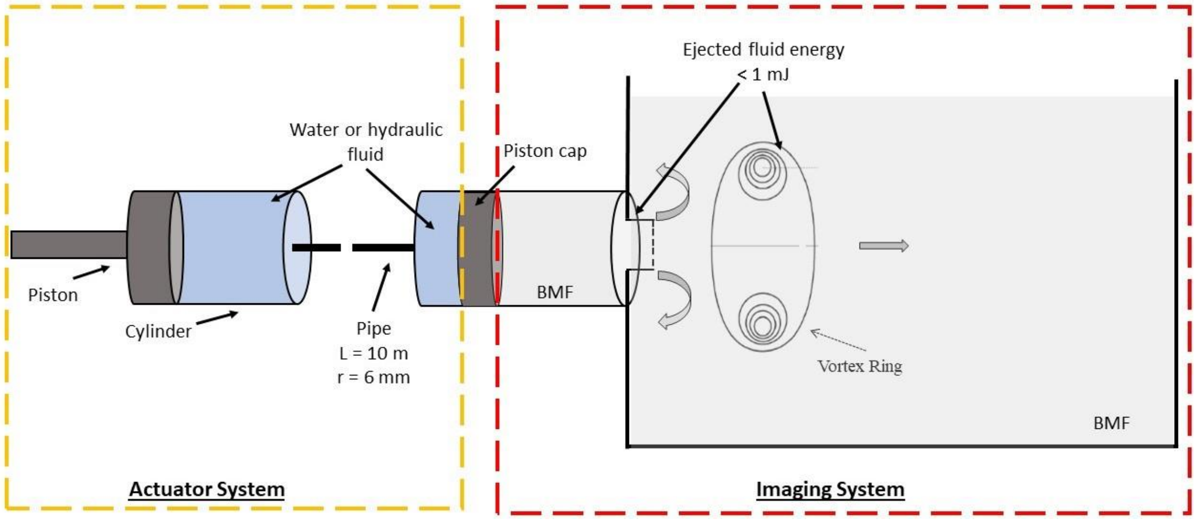

Figure 8.14: Schematic block MRI Compatible Vortex Ring based Complex Flow Phantom – hydraulic piston. The piston connected to the pump hydraulically displaces the piston at the tank. Please note that this is a schematic representation and elements are not to scale.

Obviously, the introduction of a flow straightener or of a further Perspex block (hydraulic piston) implies further negative work (i.e. viscous losses of the fluid through the straightener, friction of the hydraulic piston) that needs to be considered for the choice of the actuator system (motor).

8.4.4 Design Limitations – Piston leakage

A negligible leakage (about 30 ml in 2 hours) was noticed from the piston cylinder composing the actuator system. The piston cap (Figure 6.1, Chapter 6) manufactured from Perspex with low (+/- 0.10 mm) tolerance offered optimal sealing properties and smooth coupling. However, the pressure difference exerted by the new system pushes the water around the piston cap, provoking a tiny leakage. Since the leakage is negligible, PTFE thread seal tape could be placed on the "Piston Guide" (Figure 8.9) internal screw to avoid any discharge. However, the best option is probably to design a hydraulic piston, as discussed in Section 8.4.3. The piston cap contained within the "Tank Cylinder" separates the hydraulic fluid that drives the actuator system ("Actuator System", Figure 8.14) from the fluid needed for the vortex ring generation ("Imaging System", Figure 8.14). Lubricants can be used because they do not interact with components contained in blood mimicking fluids that are compatible with medical imaging. Consequently, the piston design proposed in Chapter 4 ("Plunger", Figure 4.4, Chapter 4) can be used. The rubber O-ring delivers optimal sealing properties while the lubricant facilitates smooth coupling during dynamic applications.

8.5 Summary

Hazards and safety regulations for Magnetic Resonance Units have been described in detail in Section 6.3. Ferromagnetic materials cannot be used because, beyond certain limits (*3 mT*), they experience a projectile effect. In addition, MR scanners are manufactured with very homogeneous magnetic fields and the introduction of electrical motors produces distortion of the magnetic field and artefacts in the images. MRI compatible piezo linear actuators are available on the market but are expensive and limited in terms of power, velocity and displacement extent.

Slight modifications were made to the Vortex Ring based Complex Flow Phantom (described in Chapter 4) to adapt the design for the MR Environment. The component “Tank Cylinder” (Figure 8.8) was manufactured to be compatible with the “Imaging Tank” (Figure 4.3, Chapter 4) and with a BSPT connector. The piston cylinder system was manufactured following the method described in Chapter 6. Distinct from the previous design, the output of the cylinder provides coupling with a BSPT connector. A new base and further Perspex blocks were manufactured to secure an aligned connection between stepper motor, piston and cylinder. The “Imaging Tank” (Figure 4.3, Chapter 4), manufactured exclusively from plastic components, can be placed in the scanner while the piston cylinder unit remains outside the MR Environment (Zone IV). The two systems are connected through a PVC pipe hose which is secured with Nylon 6.6 plastic hose clips. Functionality and application of the system were demonstrated by generating vortex rings at Leeds Test Objects Ltd (Section 8.3.6).

As expected from the manufacturing of a first prototype, limitations were identified and potential alternatives were proposed. Particularly, the pipe that connects the two systems is narrow (12 cm diameter) and very long (10 m), causing noticeable pressure difference between the extremities. The energy (J) needed to overcome this pressure difference is very close to the maximum energy the motor can deliver. The chosen stepper motor was one of the most powerful on the market (36 V, 3 A) at the time of writing (2018). Unless other technologies are released in the future, larger pipes (pressure inversely proportional to the forth power of the pipe radius) or the connection of two identical motors to the same Arduino Board are possible solutions. The narrow pipe also introduces other limitations. The flow within it is turbulent (Re ~ 6000) and affects the generation of laminar vortex rings. From experimental observations it was noted that most of the vortex rings produced exhibited a turbulent core. Potential alternatives are to increase the pipe diameter, increase the “Tank Cylinder” length, or introduce a flow straightener into the “Tank Cylinder”, or the manufacture of a hydraulic piston system (as shown in Figure 8.14). Fortunately, the pressure difference caused by the pipe generates negligible piston leakage. The manufacturing of a hydraulic piston system guarantees separation between the two systems (actuator system and imaging system, Figure 8.14), consequently, the piston design proposed in Chapter 4 could be used. The O-ring delivers waterproof sealing and a lubricant can be introduced to guarantee smooth piston displacement profiles.

Overall, the system has demonstrated reliability, and generated vortex rings as expected. Despite its limitations it is certainly capable of challenging clinical MRI Units. The instrumentation pack can be applied to the system and new reference flow values can be easily calculated following the methods described in Chapter 6.

8.6 Conclusion

A number of restrictions apply when working with MR Units. Notably, electrical motors and ferromagnetic materials cannot be included within the MRI Environment (Zone IV). New components were manufactured from Perspex and a cost-effective Magnetic Resonance Compatible Vortex Ring based Complex Flow Phantom design is proposed. Being just a first prototype, some limitations were identified but these have been discussed in detail and potential cost-effective alternatives were suggested. Overall, the phantom performed adequately and is in a form that can be scanned in a clinical environment.

CHAPTER 9

Conclusion and future work

This chapter consolidates the work of the PhD and clarifies key outcomes whilst addressing opportunities for future work.

9.1 Thesis Overview

The motivation for this PhD was the lack of cost-effective and reliable flow phantom technologies available on the market. Current flow test objects are not able to clarify the performance of innovative medical imaging technologies (i.e. Vector Doppler Ultrasound and 4D Flow MRI) designed to provide quantitative interpretation of blood flow. Current phantom technologies are expensive, they lack specifications relating to accuracy and performance, and they struggle to reproduce stable complex flow pattern characteristics associated with physiological blood flow. We hypothesised that the ring vortex was a suitable flow candidate for use in a complex flow phantom, leading to the following aim.

Aim: the aim of the PhD was the design, construction, testing and validation of a novel, cost-effective, robust, portable, multimodal complex flow phantom for diagnostic imaging based on the ring vortex flow.

Chapter 1 introduced various medical imaging technologies for blood flow assessment and discussed in detail the role of phantoms in Quality Control for medical imaging (with a focus on flow phantoms). A literature and market analysis was conducted to provide an update on the current flow phantom technologies available on the market for Doppler Ultrasound and MRI, main medical imaging technologies for blood flow assessment.

An early challenge identified for a complex flow test object was the need for a complex flow that was physiologically relevant, stable, reproducible, predictable and controllable. The literature analysis conducted within **Chapter 2** highlighted such a flow. The vortex ring was identified as a good candidate because it is a fluid dynamics phenomenon that has been extensively studied *in vitro* and it is physiologically relevant. Vortex rings are implicated in the efficiency of cardiac output and simple parameters (i.e. left ventricle valve diameter) can be used as quantitative index of cardiac health. The literature also provided evidence that vortex rings can be produced in the laboratory with encouraging reproducibility.

After having identified the best flow candidate, two systems were built in the laboratory to test vortex ring credibility before the construction of a complex flow phantom prototype. An Air-Based Vortex Ring Generator was first investigated for proof of concept. Results obtained from Computational Fluid Dynamic (CFD) analysis and optical/video acquisitions matured with theoretical predictions to provide the motivation for construction of a programmable Liquid-Based Vortex Ring Generator. Equivalent analysis (CFD and optical/video) were performed on the liquid-based prototype to asses reliability and robustness of the system. Reproducibility of generated vortex rings was promising, but discrepancies were found between experimental data and CFD simulations. CFD characterised the main characteristics of the flow, but was insufficiently accurate to constitute a flow reference standard when calibrating the phantom. PIV was used as an alternative. Vortex ring generator designs, experiments, methods and results are supported by the publication of a journal article (Ferrari et al 2017) and a conference proceeding article (Ferrari et al 2018), and are described in detail in **Chapter 3**.

The two prototypes informed the construction of a Vortex Ring Based Complex Flow Phantom prototype. This relied on an actuator system, consisting of a computer controlled stepper motor, a piston/cylinder system (controlled by the motor) and a water-proof imaging tank for the vortex ring generation and propagation. Technical drawings and design specifications, are supported by the publication of a journal article (Ambrogio et al 2019), and are described in detail in **Chapter 4**. Considering the reliability and the novelty of the design, three prototypes were built and multiple measurement methods were undertaken to independently validate the performance. Laser PIV was performed on a phantom prototype providing a sophisticated and reliable measurement method useful for cross validating the other results. Optical/video measurements were performed on a second prototype and ultrasound acquisitions on the third prototype. Optical/video results matched well with the Laser PIV results as well as PW Spectral Doppler Ultrasound. Optical/video and Laser PIV measurements are described in a published journal article (Ambrogio et al 2019) while ultrasound results were presented in a poster presentation (Appendix 2) at "The 50th Annual Scientific Meeting of the British Medical Ultrasound Society". State of the art Vector Doppler Ultrasound imaging technique was also successfully performed on a prototype manufactured for CREATIS (Lyon, France), as a beneficiary partner of the VPH-CaSE training network. The study is reported in a published journal article (Appendix 3). All the experiments, methods and results are described in **Chapter 5**.

The piston arrangement proved to be a crucial part of the phantom design, which needed to be modified for delivering an optimal balance between sealing properties and the coefficient of friction. Taking advantage of the design modifications, adaptation for a linear encoder was introduced. An instrumentation pack, comprising a linear magnetic encoder and a Laser diodes/photodiodes array, was manufactured and installed on a prototype. The linear encoder provides valuable information about the piston velocity profile, on which mainly the vortex ring generation depends. The Laser diodes/photodiodes array provides real-time information on vortex ring translational velocity as function of time. The instrumentation pack design, data collection methods and demonstration of functionality are described in **Chapter 6**.

The value of the instrumentation pack is demonstrated through several experiments, which are reported in **Chapter 7**. Information such as motor input power required, vortex ring variability, correlation between piston velocity profile and vortex ring variability and vortex ring energetics were collected in real-time without resorting to expensive and time-consuming measurement methods (i.e. Laser PIV). The instrumentation pack proved to be a valuable and reliable tool for characterising and promoting confidence in the phantom and the flow during applications. Ultimately, it offers the possibility of calibrating the phantom before applications.

Chapter 8 explored concepts and technical specifications for adaptation of our design for the Magnetic Resonance Environment. Hazards and safety rules impose numerous restrictions and application of the design in the laboratory is provided. Overall, the phantom performed according to expectation and is capable of being tested in a clinical setting. Additional design limitations were identified and potential improvements were suggested.

PhD success: in respect of this PhD, its success can be measured by the extent to which it addresses the hypothesis. To that end, this thesis has provided detailed technical specifications for the construction of a credible, novel, robust, cost-effective and portable complex flow phantom for medical imaging based on the vortex ring.

The phantom can be obtained from Leeds Test Objects Ltd, which owns the intellectual property, or can be built in any laboratory. Price of components and manufacturing was less than 2,000.00 GBP (including VAT) at the time of working (2019).

9.2 Current limitations and future work - Phantom design

The complex flow phantom design has proven to be reliable when tested with different and independent measurement methods under a number of different generating conditions. Extensive experimental studies have also identified limitations and set the scene for future work and design improvements.

The design offers great flexibility because the programmable actuator is open-source. This constitutes both an advantage and a limitation. The phantom offers pre-set parameters that can be easily varied (following the detailed instructions provided) in an Arduino Software (IDE) environment. However, not all the users (i.e. clinical scientists, medical physicists, biomedical engineers) will be familiar with programming and very often installation of new software is limited by IT administration teams. The open-source platform is an advantage for research laboratories but it constitutes a disadvantage for the clinically oriented market. Ideally, the phantom should come with both pre-programmed user-friendly modes and open-source option. The device would benefit from being capable to work as a standalone device without requiring connection to a Laptop. This can be realised by flashing a ROM for the Arduino and through the installation of accessories, such as touch screen, push buttons and LED indicators. These accessories are easy to buy on the market, to install, and to program. Not only they are cost effective (sometimes very cheap), they are stylish and make the design more appealing. The Arduino is well established but it might be prudent to guard against obsolescence in the future.

The stepper motor proved to be insufficiently powerful to generate fast vortex rings (i.e. 80 cm/s) in the MRI compatible design configuration. The long and narrow pipe generates considerable pressure differences. Consequently, multiple stepper motors could be connected to the same Arduino Board to simultaneously push the piston. Limitations of the MRI compatible Complex Flow Phantom design were discussed in detail and potential alternatives were suggested, but it is clear that an MR compatible phantom based on the vortex ring is achievable, without being excessively expensive. Important work needs to be done here to refine the design and confirm that key characteristics such as stability, reproducibility, predictability and controllability remain.

9.3 Current limitations and future work - Study

The vortex ring complex flow phantom offers stable complex three-dimensional flow patterns that are physiologically relevant, controllable, reproducible, stable and predictable. This is a unique design that offers the possibility of performing validation and optimisation of flow imaging methods and calibration and Quality Control of clinical scanners. The phantom is almost entirely manufactured with transparent materials, offering visual assessment via optical measurement techniques (i.e. Laser PIV, video etc.). The instrumentation pack is valuable in providing real-time feedback on the phantom performance. Limitation of commercially available phantoms (flow and string phantoms) have been discussed in Chapter 4 (Section 4.5).

Vector Doppler Flow Imaging is currently available on clinical scanners and 4D flow MRI is performed at research level in a number of research institutions. Cross-validation of the results obtained from Vector Doppler Flow Imaging, 4D Flow MRI and Laser PIV provides an interesting opportunity to clarify how these different modalities quantitatively interpret the flow. Arguably, comparable but different results are likely to be obtained between different imaging modalities and between different vendors of the same imaging modality. This has implications for the definition of new universally accepted standards for Quality Control, definition of guidelines for calibration, improvement of scanner designs and flow reconstruction algorithms. Unfortunately, the time-scale of the PhD did not allow evaluation using a 4D flow MRI scan on the phantom in a clinical environment. However, design and technical specification are in the public domain (Ambrogio et al 2019), the phantom can be built/improved/modified in any lab. The design is flexible and offers the possibility to operate in a free field or to embed tissue mimicking materials (TMMs) compatible with the medical technology of interest. The advent of innovative 3D printed techniques allows image segmentation and direct or indirect printing of TMMs with anthropomorphic shapes. This is valuable for the definition of patient specific treatment protocols and for the research and development of new techniques.

9.4 Current limitations and future work - Laser PIV raw data

The Laser PIV is a powerful and sophisticated tool but its use within the thesis is restricted to the extraction of bulk flow velocity and size of the ring. The PIV provides information on the micro-flow environment, and the acquisition has been made to provide data for three early stage researchers (Simone Ambrogio, Simone Ferrari and Emilia Badescu) within the VPH-CaSE Training Network (https://www.vph-case.eu/).

Flow reproducibility is crucial for the development of a test object, and this concept is emphasised within the thesis. Vortex ring macro-flow features were characterised within the thesis, and the assumption that the typical +/- 10 % macro-flow variability reflects in the variability of the micro-flow environment has been made. This has big implications for the utility of the phantom and for the interpretation of scanner performance. Consequently, raw Laser PIV data on vector velocity fields along the X-axis and Y-axis have been analysed for one piston speed and each orifice size. Combinations of orifice size and piston speed (L/D ratio) have been chosen to include best case (lower macro-flow variability, Configuration 2-Table 5.1, Chapter 5) and worst case (larger macro-flow variability, Configuration 10-Table 5.1, Chapter 5). Calculations and results, reported in Appendix 6, show that the variability is always within +/- 5 % for Configurations 3 and Configuration 7 in the region of interest between 5 and 11 cm into the phantom. This value complies with the BS EN 61685:2002 – IEC 61685:2001, International Standard for the design of a flow Doppler test object. Configuration 7 showed larger variability, however, values were always within +/- 10 %. As expected from the macro-flow analysis (Chapter 5), Configuration 10 showed a larger variability with values typically within +/- 20 %. In accordance with theory (Tinaikar et al 2018) and ultrasound acquisitions (Section 5.3.6, Chapter 5), high correlation with R^2 values ranging from 0.89 (Configuration 10) to 0.99 (Configuration 7) was found between the two velocity components. This confirms that if the macro-flow variability is known, equivalent behaviour can be expected for the micro-flow environment.

9.5 PhD contribution and final message

An innovative complex flow test object design compatible with Doppler Ultrasound and MRI is provided. The tool has been extensively tested and reference values provided. Design, experiments and results are supported with strong scientific background complemented by journal articles and conference proceedings publications, poster and oral presentation in international conferences.

Limitations of the design have been identified and suggestions for future works presented.

The phantom constitutes a credible tool for carrying out Quality Control tests of Doppler Ultrasound modalities in a clinical environment and for validating advanced flow estimation algorithms at research level. Suggestions have been provided to Leeds Test Objects Ltd (owner of the design intellectual property) to make the design more appealing and to launch it on the market. Furthermore, a student of the University of Sheffield was recently (May 2019) awarded a grant scholarship (EPSRC) for improving the design and validating the phantom in a clinical MRI environment. This highlights the attractiveness of the design and its potential in clinical practice and in research.

Currently three complex flow phantom prototypes are in circulation owned by Leeds Test Objects Ltd, the University of Sheffield and CREATIS (CNRS, Lyon, France), respectively. The University of Sheffield and Leeds Test Objects are continuing their cooperation for design improvements and further validation studies. The CREATIS consortium continues to perform research and development of innovative high frame rate Ultrasound flow imaging methods.

References

1) Akhmetov, D. G. & Kisarov, O. P. (1969). Hydrodynamic Structure of a Vortex Ring. *Journal of Applied Mechanics and Technical Physics*, 7(4), 87–90.
2) Akhmetov, D. G. (2001). Formation and Basic Parameters of Vortex Rings. *Journal of Applied Mechanics and Technical Physics*, 42(5), 794–805. Retrieved from http://link.springer.com/10.1023/A:1017992426213%0Ahttp://dx.doi.org/10.1023/A:1017992426213
3) Akhmetov, D. G. (2009). *Vortex Rings*. Retrieved from http://www.annualreviews.org/doi/10.1146/annurev.fl.24.010192.001315.
4) Al-Ghathian, M., F. M.T. & S., M. (2005). Friction Forces in O-Ring Sealing. *American Journal of Applied Sciences*.
5) American Society for Testing and Materials. (2010). Standard Test Method for Measurement of Magnetically Induced Displacement Force on Medical Devices in the Magnetic Resonance Environment (F2052-06). *Annual Book of ASTM Standards*.
6) American Society for Testing and Materials. (2011). Standard Test Method for Measurement of Magnetically Induced Torque on Medical Devices in the Magnetic Resonance Environment (F2213-06). *Annual Book of ASTM Standards*.
7) American Society for Testing and Materials. (2013). Standard Practice for Marking Medical Devices and Other Items for Safety in the Magnetic Resonance Environment (F2503-13). *Annual Book of ASTM Standards*.
8) Anavekar, N. S. & Oh, J. K. (2009). Doppler Echocardiography: A Contemporary Review. *Journal of Cardiology*, 54(3), 347–358.
9) Archer, P. J., Thomas, T. G. & Coleman, G. N. (2008). Direct Numerical Simulation of Vortex Ring Evolution from the Laminar to the Early Turbulent Regime. *Journal of Fluid Mechanics*, 598, 201–226.
10) Arvidsson, P. M., Kovács, S. J., Töger, J., Borgquist, R., Heiberg, E., Carlsson, M. & Arheden, H. (2016). Vortex Ring Behavior Provides the Epigenetic Blueprint for the Human Heart. *Scientific Reports*, 6.
11) Badescu, E., Petrusca, L., Garcia, D., Friboulet, D. & Liebgott, H. (2017-a). Towards 3-D Tissue Doppler Ultrafast Echocardiography: An in Vitro Study, in: *IEEE International Ultrasonics Symposium, IUS*.
12) Badescu, E., Bujoreanu, D., Petrusca, L., Friboulet, D. & Liebgott, H. (2017-b). Multi-Line Transmission for 3D Ultrasound Imaging: AN Experimental Study, in: *IEEE International Ultrasonics Symposium, IUS*.
13) Badescu, E., Ambrogio, S., Fenner, J., Liebgott, H., Friboulet, D. & Garcia, D. (2018). Vortex Ring Phantom for Invetigation of Ultrasound Vector Flow Imaging, in: *IEEE International Ultrasonic Symposium*, *IUS.*
14) Bale-Glickman, J., Selby, K., Saloner, D. & Savaş, O. (2003). Experimental Flow Studies in Exact-Replica Phantoms of Atherosclerotic Carotid Bifurcations Under Steady Input Conditions. *Journal of Biomechanical Engineering*, 125(1), 38. Retrieved from http://biomechanical.asmedigitalcollection.asme.org/article.aspx?articleid=1409355
15) Bollache, E., Ooij, P., Powell, A., Carr, J., Markl, M. & Barker, A. (2016). Comparison of 4D flow and 2D velocity-encoded phase contrast MRI sequences for the evaluation of aortic hemodynamics. *Int J Cardiovasc Imaging*, 32(10):1529-1541.
16) Boone, J. M. et al (2012). Radiation Dose and Image-Quality Assessment in Computed Tomography. *Journal of the ICRU*.
17) Bradway, D. P., Hansen, K. L., Nielsen, M. B. & Jensen, J. A. (2015). Transverse Oscillation Vector Flow Imaging for Transthoracic Echocardiography, in: *Proc. SPIE*, (pp. 941902–7). Retrieved from http://proceedings.spiedigitallibrary.org/proceeding.aspx?doi=10.1117/12.2081145

18) BHF. (2018). Cardiovascular Disease Statistics - BHF UK Factsheet. *British Heart Foundation*, (February). Retrieved from https://www.bhf.org.uk/research/heart-statistics [Accesed 01 Feb 2018].
19) Brewin, M. P., Pike, L. C., Rowland, D. E. & Birch, M. J. (2008). The Acoustic Properties, Centered on 20 MHZ, of an IEC Agar-Based Tissue-Mimicking Material and Its Temperature, Frequency and Age Dependence. *Ultrasound in Medicine and Biology*.
20) Brown, R. W., Cheng, Y.-C. N., Haacke, E. M., Thompson, M. R. & Venkatesan, R. (2014). *Magnetic Resonance Imaging: Physical Principles and Sequence Design*. Retrieved from http://books.google.com/books?id=BnOvQgAACAAJ&pgis=1
21) Browne, J. E., Ramnarine, K. V., Watson, A. J. & Hoskins, P. R. (2003). Assessment of the Acoustic Properties of Common Tissue-Mimicking Test Phantoms. *Ultrasound in Medicine and Biology*, 29(7), 1053–1060.
22) Browne, J. E. (2014). A Review of Doppler Ultrasound Quality Assurance Protocols and Test Devices. *Physica Medica*, 30(7), 742–751.
23) Bryant, D., Payne, J., Firmin, D. and Longmore, D. (1984). Measurement of flow with NMR imaging using a gradient pulse and phase difference technique. *J Comput Assist Tomogr*, 9:139-149.
24) BS EN 61685:2002, IEC 61685:2001. Title: Ultrasonics. Flow measurement systems. Flow test object. Published: 14th February 2002.
25) Campbell-Washburn, A. E., Rogers, T., Stine, A. M., Khan, J. M., Ramasawmy, R., Schenke, W. H., McGuirt, D. R., Mazal, J. R., Grant, L. P., Grant, E. K., Herzka, D. A. & Lederman, R. J. (2018). Right Heart Catheterization Using Metallic Guidewires and Low SAR Cardiovascular Magnetic Resonance Fluoroscopy at 1.5 Tesla: First in Human Experience. *Journal of Cardiovascular Magnetic Resonance*.
26) Cannon, L. M., Fagan, A. J. & Browne, J. E. (2011). Novel Tissue Mimicking Materials for High Frequency Breast Ultrasound Phantoms. *Ultrasound in Medicine and Biology*.
27) Capineri, L., Scabia, M. & Masotti, L. (2002). A Doppler System for Dynamic Vector Velocity Maps. *Ultrasound in Medicine and Biology*, 28(2), 237–248.
28) Chu, K. C. & Rutt, B. K. (1997). Polyvinyl Alcohol Cryogel: An Ideal Phantom Material for MR Studies of Arterial Flow and Elasticity. *Magnetic Resonance in Medicine*.
29) CIRS (2018). *Doppler String Phantom*. Available at: http://www.cirsinc.com/products/all/69/doppler-string-phantom/
30) Cournane, S., Cannon, L., Browne, J. E. & Fagan, A. J. (2010). Assessment of the Accuracy of an Ultrasound Elastography Liver Scanning System Using a PVA-Cryogel Phantom with Optimal Acoustic and Mechanical Properties. *Physics in Medicine and Biology*.
31) Cournane, S., Fagan, A. J. & Browne, J. E. (2014). An Audit of a Hospital-Based Doppler Ultrasound Quality Control Protocol Using a Commercial String Doppler Phantom. *Physica Medica*, 30(3), 380–384.
32) Crandon, S., Elbaz, M., Westenberg, J., van der Geest, R., Plein, S. & Garg, P. (2017). Clinical applications of intra-cardiac four-dimensional flow cardiovascular magnetic resonance: A systematic review. *International Hournal of Cardiology*, 249:486-493.
33) Culjat, M. O., Goldenberg, D., Tewari, P. & Singh, R. S. (2010). A Review of Tissue Substitutes for Ultrasound Imaging. *Ultrasound in Medicine and Biology*.
34) Currie, P. J., Hagler, D. J., Seward, J. B., Reeder, G. S., Fyfe, D. A., Bove, A. A. & Taji, A. J. (1986). Instantaneous Pressure Gradient: A Simultaneous Doppler and Dual Catheter Correlative Study. *Journal of the American College of Cardiology*, 7(4), 800–806.
35) Dabiri, J. O. & Gharib, M. (2004). Fluid Entrainment by Isolated Vortex Rings. *Journal of Fluid Mechanics*, 511, 311–331.
36) de Isla, L. P., Vivas, D. & Zamorano, J. (2008). Three-Dimensional Speckle Tracking. *Current Cardiovascular Imaging Reports*, 1(1), 25–29.
37) Didden, N. (1979). On the Formation of Vortex Rings: Rolling-up and Production of Circulation. *Zeitschrift f??r angewandte Mathematik und Physik ZAMP*, 30(1), 101–116.

38) Dineley, J., Meagher, S., Poepping, T. L., McDicken, W. N. & Hoskins, P. R. (2006). Design and Characterisation of a Wall Motion Phantom. *Ultrasound in Medicine & Biology*.
39) Domenichini, F., Pedrizzetti, G. & Baccani, B. (2005). Three-Dimensional Filling Flow into a Model Left Ventricle. *Journal of Fluid Mechanics*, 539, 179–198.
40) Domenichini, F. & Pedrizzetti, G. (2011). Intraventricular Vortex Flow Changes in the Infarcted Left Ventricle: Numerical Results in an Idealised 3D Shape. *Computer Methods in Biomechanics and Biomedical Engineering*.
41) Dudley, N. & McKenna, M. (2017). Options for assuring Doppler velocity accuracy, in: *IPEM - The Physics & Technology of Medical Ultrasound*.
42) Dyverfeldt, P. et al (2015). 4D flow cardiovascular magnetic resonance consensus statement. *Journal of Cardiovascular magnetic Resonance*, 17:72.
43) Ebbers, T. (2011). Flow Imaging: Cardiac Applications of 3D Cine Phase-Contrast MRI. *Current Cardiovascular Imaging Reports*, 4(2), 127–133.
44) European Union Directive. (2013). Directive No. 2013/35/EU, of 26 June 2013, on the Minimum Health and Safety Requirements Regarding the Exposure of Workers to the Risks Arising from Physical Agents (Electromagnetic Fields). *Official Journal of the European Union*.
45) Evans, D. H., Jensen, J. A. & Nielsen, M. B. (2011). Ultrasonic Colour Doppler Imaging. *Interface Focus*, 1(4), 490–502. Retrieved from http://rsfs.royalsocietypublishing.org/cgi/doi/10.1098/rsfs.2011.0017
46) Ferrari, S., Ambrogio, S., Walker, A., Verma, P., Narracott, A. J., Wilkinson, I. & Fenner, J. W. (2017). The Ring Vortex: Concepts for a Novel Complex Flow Phantom for Medical Imaging. *Open Journal of Medical Imaging*, 7(1), 28–41. Retrieved from http://www.scirp.org/journal/doi.aspx?DOI=10.4236/ojmi.2017.71004
47) Ferrari, S., Ambrogio, S., Walker, A., Narracott, A. J. & Fenner, J. W. (2018). The Ring Vortex: A Candidate for a Liquid-Based Complex Flow Phantom for Medical Imaging. *Lecture Notes in Computational Vision and Biomechanics*, 27, 893–902.
48) Firmin, D., Nayler, G., Kilner, P. & Longmore, D. (1990). The application of phase shift in NMR for flow measurements. *Magn Reson Med*, 14(2):230-241.
49) Fleming, A. D., McDicken, W. N., Sutherland, G. R. & Hoskins, P. R. (1994). Assessment of Colour Doppler Tissue Imaging Using Test-Phantoms. *Ultrasound in Medicine and Biology*.
50) Fraenkel, L. E. (1972). Examples of Steady Vortex Rings of Small Cross-Section in an Ideal Fluid. *Journal of Fluid Mechanics*, 51(1), 119–135.
51) Garcia, J., Barker, A. Markl, M. (2019). The Role of Imaging of Flow Patterns by 4D Flow MRI in Aortic Stenosis. *JACC: Cardiovascular Imaging*, 12(2):252-266.
52) Garcia, D., Juan, J. C., Tanné., D., Yotti, R., Cortina, C., Bertrand, É., Antoranz, J. C., Pérez-David, E., Rieu, R., Fernández-Avilés, F. & Bermejo, J. (2010). Two-Dimensional Intraventricular Flow Mapping by Digital Processing Conventional Color-Doppler Echocardiography Images. *IEEE Transactions on Medical Imaging*, 29(10), 1701–1713.
53) Garg, P. et al (2017). Comparison of Fast Acquisition Strategies in Whole-Heart Four-Dimensional Flow Cardiac MR: Two-Center, 1.5 Tesla, Phantom and In Vivo Validation Study. *J Magn Reson Imaging*, 47(1):272-281.
54) Garg, P. et al (2018). Comparison of fast acquisition strategies in whole-heart four-dimensional flow cardiac MR: two-center, 1.5 Tesla, phantom and in vivo validation study. *J Mang Reson Imaging*, 47(1):272-281.
55) GE Healthcare (2018). *BSI (Blood Speckle Imaging)*. Fig 3. Retrieved from http://www3.gehealthcare.com/~/media/documents/us-global/products/ultrasound/vivid/blood_speckle_imaging_whitepaper_v3.pdf?Parent=%7BFFE4E8B5-6E64-4833-A3F6-A777E6FAF790%7D.
56) Ger, R. B. et al (2017). A Multi-Institutional Comparison of Dynamic Contrast-Enhanced Magnetic Resonance Imaging Parameter Calculations. *Scientific Reports*.

57) Gerhard-Herman, M., Gardin, J. M., Jaff, M., Mohler, E., Roman, M., Naqvi, T. Z., American Society of Echocardiography & Society for Vascular Medicine and Biology. (2006). Guidelines for Noninvasive Vascular Laboratory Testing: A Report from the American Society of Echocardiography and the Society for Vascular Medicine and Biology. *Vasc Med*, 11(3), 183–200. Retrieved from file://localhost/Users/aamato/Sente/My Vascular Library.sente6lib/Contents/Attachments/Gerhard-Herman/2006/Guidelines for noninvasive vascular laboratory tes.pdf
58) Gharib, M., Rambod, E. & Shariff, K. (1998). Universal Time Scale for Vortex Ring Formation. *Journal of Fluid Mechanics*, 360, 121–140. Retrieved from http://dx.doi.org/10.1017/S0022112097008410
59) Gharib, M., Rambod, E., Kheradvar, A., Sahn, D. J. & Dabiri, J. O. (2006). Optimal Vortex Formation as an Index of Cardiac Health. *Proceedings of the National Academy of Sciences*, 103(16), 6305–6308. Retrieved from http://www.pnas.org/cgi/doi/10.1073/pnas.0600520103
60) Gomez, A., Pushparajah, K., Simpson, J. M., Giese, D., Schaeffter, T. & Penney, G. (2013). A Sensitivity Analysis on 3D Velocity Reconstruction from Multiple Registered Echo Doppler Views. *Medical Image Analysis*, 17(6), 616–631.
61) Grant, I. (1997). Particle Image Velocimetry: A Review. *Proceedings of the Institution of Mechanical Engineers, Part C (Journal of Mechanical Engineering Science) Publ: Mech. Eng. Publications for IMechE*, 211(1), 55–76. Retrieved from http://pic.sagepub.com/content/211/1/55.abstract
62) Hansen, K. L., Udesen, J., Oddershede, N., Henze, L., Thomsen, C., Jensen, J. A. & Nielsen, M. B. (2009-a). In Vivo Comparison of Three Ultrasound Vector Velocity Techniques to MR Phase Contrast Angiography. *Ultrasonics*, 49(8), 659–667.
63) Hansen, K. L., Udesen, J., Thomsen, C., Jensen, J. A. & Nielsen, M. B. (2009-b). In Vivo Validation of a Blood Vector Velocity Estimator with MR Angiography. *IEEE Transactions on Ultrasonics, Ferroelectrics, and Frequency Control*, 56(1), 91–100.
64) Hansen, K. L., Nielsen, M. B. & Jensen, J. A. (2017-a). Vector Velocity Estimation of Blood Flow – A New Application in Medical Ultrasound. *Ultrasound*, 25(4).
65) Hansen, K. L., Møller-Sørensen, H., Kjaergaard, J., Jensen, M. B., Lund, J. T., Pedersen, M. M., Olesen, J. B., Jensen, J. A. & Nielsen, M. B. (2017-b). Vector Flow Imaging Compared with Conventional Doppler Ultrasound and Thermodilution for Estimation of Blood Flow in the Ascending Aorta. *Ultrasonic Imaging*, 39(1), 3–18.
66) Hemmsen, M. C., Rasmussen, J. H. & Jensen, J. A. (2014). Tissue Harmonic Synthetic Aperture Ultrasound Imaging. *The Journal of the Acoustical Society of America*, 136(4), 2050–2056. Retrieved from http://asa.scitation.org/doi/10.1121/1.4893902
67) Heng, H. G. & Widmer, W. R. (2010). Appearance of Common Ultrasound Artifacts in Conventional vs. Spatial Compound Imaging. *Veterinary Radiology and Ultrasound*, 51(6), 621–627.
68) Hill, M. J. M. (1894). On a Spherical Vortex VI. On a Spherical Vortex. *Source Philosophical Transactions of the Royal Society of London. A*, 185, 213–245. Retrieved from http://www.jstor.org/stable/90670%0Ahttp://about.jstor.org/terms
69) Hitachi (2018). *VFM Technology*. Retrieved from http://social-innovation.hitachi/us/solutions/life_economy/improving-the-understanding-of-hemodynamics/index.html.
70) Ho, C. K., Chee, A. J. Y., Yiu, B. Y. S., Tsang, A. C. O., Chow, K. W. & Yu, A. C. H. (2017). Wall-Less Flow Phantoms with Tortuous Vascular Geometries: Design Principles and a Patient-Specific Model Fabrication Example. *IEEE Transactions on Ultrasonics, Ferroelectrics, and Frequency Control*.
71) Hong, G.-R., Kim, M., Pedrizzetti, G. & Vannan, M. a. (2013). Current Clinical Application of Intracardiac Flow Analysis Using Echocardiography. *Journal of cardiovascular ultrasound*, 21(4), 155–162. Retrieved from http://www.pubmedcentral.nih.gov/articlerender.fcgi?artid=3894365&tool=pmcentrez&rendertype=abstract

72) Hoskins, P. R. (2008). Simulation and Validation of Arterial Ultrasound Imaging and Blood Flow. *Ultrasound in Medicine and Biology*.
73) Hoskins, P. R. (2010). Haemodynamics and Blood Flow Measured Using Ultrasound Imaging. *Proceedings of the Institution of Mechanical Engineers, Part H: Journal of Engineering in Medicine*.
74) Hoskins, P. R. (2015). Recent Developments in Vascular Ultrasound Technology. *Ultrasound*, 23(3), 158–165.
75) Hoskins, P. R., Lawford, P. V. & Doyle, B. J. (2017). *Cardiovascular Biomechanics*.
76) Hoskins, P.R., Martin, K. & Thrush, A. (2019). *Diagnostic Ultrasound, Third Edition*. Boca Raton:CRC Press.
77) ICRU. (2012). *ICRU Report 87 - Radiation Dose and Image-Quality Assessment in Computed Tomography*.
78) IEC. (2013). *IEC 61675-1:2013 – Characteristics and test conditions – Part 1: Positron emission tomographs.*
79) Institute for Health Matrics and Evaluation. (2010). Global Burden of Diseases, Injuries, and Risk Factors Study 2010. *Global Burden Of Disease*, 2010(Gbd). Retrieved from http://www.healthdata.org/sites/default/files/files/country_profiles/GBD/ihme_gbd_country_report_nigeria.pdf
80) Institute of Physics and Engineering in Medicine 2010 *Report 102 - Quality Assurance of Ultrasound Imaging Systems* (Manchester: Stephen Russell).
81) International Standards Organization. (ISO 7823-1:2003). *Plastics – Poly(methyl methacrylate) sheets – Types, dimensions and characteristics.*
82) International Standards Organization. (ISO 9000:2015). *Quality Management Systems – Fundamentals and Vocabulary*.
83) Jensen. (1996). Estimation of Blood Velocities Using Ultrasound: A Signal Processing Approach. *Cambridge, UK : Cambridge University Press*. Retrieved from http://www.ncbi.nlm.nih.gov/entrez/query.fcgi?db=pubmed&cmd=Retrieve&dopt=AbstractPlus&list_uids=2pZOAAAAIAAJ%0Apapers://3417802c-d225-4431-ae35-ca17933cab09/Paper/p230
84) Jensen, J. A. & Munk, P. (1998). A New Method for Estimation of Velocity Vectors. *IEEE Transactions on Ultrasonics, Ferroelectrics, and Frequency Control*, 45(3), 837–851.
85) Jensen, J. A. (2001). A New Estimator for Vector Velocity Estimation. *IEEE transactions on ultrasonics, ferroelectrics, and frequency control*, 48(4), 886–894.
86) Jensen, J.A. *et al* (2013). New developments in Vector Velocity Imaging using the Transverse Oscillation Approach. *Proceedings of SPIE,* 8675, 86750F. Retrieved from http://orbit.dtu.dk/files/55238022/New_Developments_in_Vector_Velocity.pdf
87) Jensen, J. A., Pihl, M.J., Olesen, J.B., Moller-Hansen, P., Lindskov-Hansen, K. & Bachman-Nielsen, M. (2013). New Developments in Vector Velocity Imaging using the Transverse Oscillation Approach. *In Proceedings of SPIE: Medical Imaging 2013: Ultrasonic Imaging, Tomography, and Therapy*, 8675, 86750F.
88) Jensen, J. A., Brandt, A. H. & Nielsen, M. B. (2015). Convex Array Vector Velocity Imaging Using Transverse Oscillation and Its Optimization. *IEEE Transactions on Ultrasonics, Ferroelectrics, and Frequency Control*, 62(12), 2043–2053.
89) Jensen, J. A., Nikolov, S. I., Yu, A. C. H. & Garcia, D. (2016). Ultrasound Vector Flow Imaging-Part I: Sequential Systems. *IEEE Transactions on Ultrasonics, Ferroelectrics, and Frequency Control*, 63(11), 1704–1721.
90) Jones, A. K., Heintz, P., Geiser, W., Goldman, L., Jerjian, K., Martin, M., Peck, D., Pfeiffer, D., Ranger, N. & Yorkston, J. (2015). Ongoing Quality Control in Digital Radiography: Report of AAPM Imaging Physics Committee Task Group 151. *Medical Physics*, 42(11), 6658–6670.
91) Kanal, E., Barkovich, A. J., Bell, C., Borgstede, J. P., Bradley, W. G., Froelich, J. W., Gimbel, J. R., Gosbee, J. W., Kuhni-Kaminski, E., Larson, P. A., Lester, J. W., Nyenhuis, J., Schaefer, D. J., Sebek,

E. A., Weinreb, J., Wilkoff, B. L., Woods, T. O., Lucey, L. & Hernandez, D. (2013). ACR Guidance Document on MR Safe Practices: 2013. *Journal of Magnetic Resonance Imaging*.
92) Kaplanski, F. & Rudi, U. (1999). Dynamics of a Viscous Vortex Ring. *International Journal of Fluid Mechanics Research*, 26(5), 618-630. Retrieved from http://www.dl.begellhouse.com/journals/71cb29ca5b40f8f8,5e12a65502d5a022,73e1111467f626e3.html
93) Kenwright, D. A., Anderson, T., Moran, C. M. & Hoskins, P. R. (2015-a). Assessment of Spectral Doppler for an Array-Based Preclinical Ultrasound Scanner Using a Rotating Phantom. *Ultrasound in Medicine and Biology*, 41(8), 2232–2239.
94) Kenwright, D. A., Laverick, N., Anderson, T., Moran, C. M. & Hoskins, P. R. (2015-b). Wall-Less Flow Phantom for High-Frequency Ultrasound Applications. *Ultrasound in Medicine and Biology*.
95) Ketterling, J. A., Aristizabal, O., Yu, A. C. H., Yiu, B. Y. S., Turnbull, D. H., Phoon, C. K. L. & Silverman, R. H. (2017). High-Speed, High-Frequency, Vector-Flow Imaging of in Utero Mouse Embryos, in: *IEEE International Ultrasonics Symposium, IUS*.
96) Kheradvar, A., Milano, M. & Gharib, M. (2007). Correlation between Vortex Ring Formation and Mitral Annulus Dynamics during Ventricular Rapid Filling. *ASAIO Journal*, 53(1), 8–16.
97) Kheradvar, A. & Gharib, M. (2007). Influence of Ventricular Pressure Drop on Mitral Annulus Dynamics through the Process of Vortex Ring Formation. *Annals of Biomedical Engineering*, 35(12), 2050–2064.
98) Kheradvar, A. & Gharib, M. (2009). On Mitral Valve Dynamics and Its Connection to Early Diastolic Flow. *Annals of Biomedical Engineering*, 37(1), 1–13.
99) Kheradvar, A. (2010). Correlation between Transmitral Vortex Formation and Mitral Valve's Leaflet Length. *Circulation*, 122(21). Retrieved from http://circ.ahajournals.org/content/122/Suppl_21/A20561
100) Kheradvar, A., Assadi, R., Falahatpisheh, A. & Sengupta, P. P. (2012). Assessment of Transmitral Vortex Formation in Patients with Diastolic Dysfunction. *Journal of the American Society of Echocardiography*, 25(2), 220–227.
101) Kheradvar, A. & Pedrizzetti, G. (2012). *Vortex Formation in the Cardiovascular System*. London: *Springer-Verlag*.
102) Kim, W.Y. *et al* (1995). A quantitative analysis by three-dimensional Magnetic Resonance Velocity Mapping. *Journal of the American College of Cardiology*, 26(1), 224-238.
103) Kisslo, J.A. & Adams, D.B. (1987). *Principles of Doppler Echocardiography and the Doppler examination #1*. London: *Ciba-Geigy*.
104) Kokkalis, E., Cookson, A. N., Stonebridge, P. A., Corner, G. A., Houston, J. G. & Hoskins, P. R. (2015). Comparison of Vortical Structures Induced by Arteriovenous Grafts Using Vector Doppler Ultrasound. *Ultrasound in Medicine and Biology*.
105) Kraft, K., Fei, D. & Fautouros, P. (1992). Quantitative phase-velocity MR imaging of in-plane laminar flow: effect of fluid velocity, vessel diameter, and slice thickness. *Medical Physics*, 19(1):79-85.
106) Kripfgans, O. D., Rubin, J. M., Hall, A. L. & Fowlkes, J. B. (2006). Vector Doppler Imaging of a Spinning Disc Ultrasound Doppler Phantom. *Ultrasound in Medicine and Biology*.
107) Krueger, P. S. & Gharib, M. (2003). The Significance of Vortex Ring Formation to the Impulse and Thrust of a Starting Jet. *Physics of Fluids*, 15(5), 1271–1281.
108) Kruskal, J. B., Newman, P. a, Sammons, L. G. & Kane, R. a. (2004). Optimizing Doppler and Color Flow US: Application to Hepatic Sonography. *Radiographics : a review publication of the Radiological Society of North America, Inc*, 24(3), 657–675.
109) Kwong R., Jerosch-Herold M. & Heydari B. (2008). Cardiovascular Magnetic Resonance Imaging. Contemporary Cardiology. Springer, New York, NY.
110) Lamb, H. (1932). *Hydrodynamics*. Cambridge: *Cambridge University Press.*

111) Lang, R.M. *et al* (2012). EAE/ASE Recommendations for Image Acquisition and Display Using Three-Dimensional Echocardiography. *European Heart Journal- Cardiovascular Imaging*, 13, -46. Retrieved form https://www.escardio.org/static_file/Escardio/Subspecialty/EACVI/position-papers/EAE-ASE-recommendation-image-acquisition-3D-echo.pdf
112) Logason, K., Bärlin, T., Jonsson, M. L., Boström, A., Hårdemark, H. G. & Karacagil, S. (2001). The Importance of Doppler Angle of Insonation on Differentiation between 50-69% and 70-99% Carotid Artery Stenosis. *European Journal of Vascular and Endovascular Surgery*, 21(4), 311–313.
113) Lotz, H., Meier, C., Leppert, A. & Galanski, M. (2002). Cardiovascular Flow Measurement with Phase-Contrast MR Imaging: Basic Facts and Implementation. *RadioGraphics*, 22:651-671.
114) Lubbers, J. & Graaff, R. (1998). A Simple and Accurate Formula for the Sound Velocity in Water. *Ultrasound in Medicine and Biology*.
115) Madsen, E. L., Zagzebski, J. A. & Frank, G. R. (1982). Oil-in-Gelatin Dispersions for Use as Ultrasonically Tissue-Mimicking Materials. *Ultrasound in Medicine and Biology*.
116) Maier, S., Meier, D., Boesinger, P., Moser, U. & Vieli, A. (1989). Human abdominal aorta: comparative measurements of blood flow with MR imaging and multigated Doppler US. *Radiolgy,* 171:487-492.
117) Markl M. (2019). Techniques in the Assessment of Cardiovascular Blood Flow and Velocity. In: Kwong, R., Jerosh-Herold, M. & Heydary, B. (eds) Cardiovascular Magnetic Resonance Imaging. Contemporary Cardio
118) Markl, M., Schnell, S. & Barker, A. J. (2014). 4D Flow Imaging: Current Status to Future Clinical Applications. *Current Cardiology Reports*, 16(5):481.
119) Maulik, D. (2005). Spectral Doppler: Basic Principles and Instrumentation, in: *Doppler Ultrasound in Obstetrics and Gynecology: 2nd Revised and Enlarged Edition*, (pp. 19–34).
120) Maxworthy, T. (1972). The Structure and Stability of Vortex Rings. *Journal of Fluid Mechanics*, 51(1), 15–32.
121) Maxworthy, T. (1977). Some Experimental Studies of Vortex Rings. *Journal of Fluid Mechanics*, 81(3), 465–495.
122) McDicken, W. N., Morrison, D. C. & Smith, D. S. A. (1983). A Moving Tissue-Equivalent Phantom for Ultrasonic Real-Time Scanning and Doppler Techniques. *Ultrasound in Medicine and Biology*.
123) McDicken, W. N. & Anderson, T. (2002). The Difference between Colour Doppler Velocity Imaging and Power Doppler Imaging. *European Journal of Echocardiography*, 3(3), 240–244.
124) Medicines and Healthcare Products Regulatory Agency. (2014). *Safety Guidelines for Magnetic Resonance Imaging Equipment in Clinical Use*.
125) Mendis, S., Puska, P. & Norrving, B. (2011). Global Atlas on Cardiovascular Disease Prevention and Control. *World Health Organization*, 2–14.
126) Mindray (2016). *V Flow (A novel visualization of blood flow)*. Retrieved from http://res.mindray.com/Documents/2016-09-21/b6402778-6c85-4231-8d22-994da3d76f28/WP_V%20Flow_V2.0.pdf.
127) Moran, P., Moran, R. & Karstaedt, M. (1985). Verification and evaluation of internal flow and motion. *Radiology*, 154(2).
128) Moulinier, L., Venet, T., Schiller, N. B., Kurtz, T. W., Curtis Morris, R. & Sebastian, A. (1991). Measurement of Aortic Blood Flow by Doppler Echocardiography: Day to Day Variability in Normal Subjects and Applicability in Clinical Research. *Journal of the American College of Cardiology*, 17(6), 1326–1333.
129) Murphy, D. J., Aghayev, A. & Steigner, M. L. (2018). Vascular CT and MRI: A Practical Guide to Imaging Protocols. *Insights into Imaging*, 9(2), 215–236.
130) National Radiological Protection Board (1992). *Protection of the Patient in X-ray computed tomography*. London: *HMSO* (ISBN 0 85951 345 8).

131) Nayak, K. S., Nielsen, J. F., Bernstein, M. A., Markl, M., Gatehouse, P. D., Botnar, R. M., Saloner, D., Lorenz, C., Wen, H., Hu, B. S., Epstein, F. H., Oshinski, J. N. & Raman, S. V. (2015). Cardiovascular Magnetic Resonance Phase Contrast Imaging. *Journal of Cardiovascular Magnetic Resonance*.
132) NEMA. (2007). *Publication NU 2-2007- Performance Measurements of Positron Emission Tomographs*.
133) Newbould, R. D., Skare, S. T., Alley, M. T., Gold, G. E. & Bammer, R. (2010). Three-Dimensional T1, T2 and Proton Density Mapping with Inversion Recovery Balanced SSFP. *Magnetic Resonance Imaging*.
134) Norbury, J. (1973). A Family of Steady Vortex Rings. *Journal of Fluid Mechanics*, 57(3), 417–431.
135) O'Donnel M (1985). NMR blood flow using multiecho, phase contrast sequences. *Med Phys*, 12:59-64.
136) Ohtsuki, S. & Tanaka, M. (2006). The Flow Velocity Distribution from the Doppler Information on a Plane in Three-Dimensional Flow. *Journal of Visualization*, 9(1), 69–82.
137) Panych, L. P. & Madore, B. (2018). The Physics of MRI Safety. *Journal of Magnetic Resonance Imaging*.
138) Papadofrangakis, E., Engeler, W.E., & Fakiris, J.A. (1981). *Measurement of true blood velocity by an ultrasound system*, US4265126A.
139) Pastorelli, A., Torricelli, G., Scabia, M., Biagi, E. & Masotti, L. (2008). A Real-Time 2-D Vector Doppler System for Clinical Experimentation. *IEEE Transactions on Medical Imaging*, 27(10), 1515–1524.
140) Pedersen, M. M., Pihl, M. J., Haugaard, P., Hansen, J. M., Hansen, K. L., Nielsen, M. B. & Jensen, J. A. (2012). Comparison of Real-Time In Vivo Spectral and Vector Velocity Estimation. *Ultrasound in Medicine and Biology*, 38(1), 145–151.
141) Pedersen, M. M., Pihl, M. J., Haugaard, P., Hansen, K. L., Lange, T., Lönn, L., Nielsen, M. B. & Jensen, J. A. (2014). Novel Flow Quantification of the Carotid Bulb and the Common Carotid Artery with Vector Flow Ultrasound. *Ultrasound in Medicine and Biology*, 40(11), 2700–2706.
142) Pedrizzetti, G., La Canna, G., Alfieri, O. & Tonti, G. (2014). The Vortex—an Early Predictor of Cardiovascular Outcome? *Nature Reviews Cardiology*, 11(9), 545–553. Retrieved from http://www.nature.com/doifinder/10.1038/nrcardio.2014.75.
143) Pelc, N., Sommer, F., Li, K., Herfkens, R. & Ezmann, D (1994). Quantitative magnetic resonance flow imaging. *Magn Reson Q*, 10(3):125-147.
144) Pelc, N., Bernstein, M., Shimakawa, A. & Glover, G. (1991). Encoding strategies for three-direction phase-contrast MR Imaging of flow. *JMRI*, 4(1):405-413.
145) Pellikka, P. A. et al (2013). American Society of Echocardiography Cardiovascular Technology and Research Summit: A Roadmap for 2020. *Journal of the American Society of Echocardiography*, 26(4), 325–338.
146) Peppas, N. A. & Stauffer, S. R. (1991). Reinforced Uncrosslinked Poly (Vinyl Alcohol) Gels Produced by Cyclic Freezing-Thawing Processes: A Short Review. *Journal of Controlled Release*.
147) Petrusca, L., Varray, F., Souchon, R., Bernard, A., Chapelon, J.-Y., Liebgott, H., N'Djin, W. & Viallon, M. (2018). Fast Volumetric Ultrasound B-Mode and Doppler Imaging with a New High-Channels Density Platform for Advanced 4D Cardiac Imaging/Therapy. *Applied Sciences*.
148) Pierrakos, O. & Vlachos, P. P. (2006). The Effect of Vortex Formation on Left Ventricular Filling and Mitral Valve Efficiency. *Journal of Biomechanical Engineering*, 128(4), 527. Retrieved from http://biomechanical.asmedigitalcollection.asme.org/article.aspx?articleid=1415670
149) Pihl, M. & Jensen, J. (2014). A Transverse Oscillation Approach for Estimation of Three-Dimensional Velocity Vectors, Part I: Concept and Simulation Study. *IEEE Transactions on Ultrasonics, Ferroelectrics, and Frequency Control*, 61(10), 1599–1607.
150) Prevrhal, S., Forsythe, C. H., Harnish, R. J., Saeed, M. & Yeh, B. M. (2011). CT Angiographic Measurement of Vascular Blood Flow Velocity by Using Projection Data. *Radiology*.

151) Querzoli, G., Fortini, S. & Cenedese, A. (2010). Effect of the Prosthetic Mitral Valve on Vortex Dynamics and Turbulence of the Left Ventricular Flow. *Physics of Fluids*.
152) Quiñones, M. A., Otto, C. M., Stoddard, M., Waggoner, A. & Zoghbi, W. A. (2002). Recommendations for Quantification of Doppler Echocardiography: A Report from the Doppler Quantification Task Force of the Nomenclature and Standards Committee of the American Society of Echocardiography. *Journal of the American Society of Echocardiography : official publication of the American Society of Echocardiography*, 15(2), 167–184.
153) Rajagopal, S., Sadhoo, N. & Zeqiri, B. (2015). Reference Characterisation of Sound Speed and Attenuation of the IEC Agar-Based Tissue-Mimicking Material Up to a Frequency of 60MHz. *Ultrasound in Medicine and Biology*.
154) Ramnarine, K. V., Nassiri, D. K., Hoskins, P. R. & Lubbers, J. (1998). Validation of a New Blood-Mimicking Fluid for Use in Doppler Flow Test Objects. *Ultrasound in Medicine and Biology*.
155) Ramnarine, K. V., Anderson, T. & Hoskins, P. R. (2001). Construction and Geometric Stability of Physiological Flow Rate Wall-Less Stenosis Phantoms. *Ultrasound in Medicine and Biology*.
156) Ramnarine, K. V., Garrard, J. W., Dexter, K., Nduwayo, S., Panerai, R. B. & Robinson, T. G. (2014). Shear Wave Elastography Assessment of Carotid Plaque Stiffness: Invitro Reproducibility Study. *Ultrasound in Medicine and Biology*.
157) Rebergen, S., van der Wall, E., Doornbos, J. & de Roos, A. (1993). Magnetic resonance measurement of velocity and flow: technique, validation, and cardiovascular applications. *Am Heart J*, 126(6):1439-1456.
158) Ressner, M., Brodin, L. A., Jansson, T., Hoff, L., Ask, P. & Janerot-Sjoberg, B. (2006). Effects of Ultrasound Contrast Agents on Doppler Tissue Velocity Estimation. *Journal of the American Society of Echocardiography*.
159) Reynolds, O. (1876). On the resistance encountered by vortex rings and the relation between vortex rings and the stream-lines of a disc. *Nature*, 14, 477-479.
160) Rickey, D. W., Picot, P. A., Christopher, D. A. & Fenster, A. (1995). A Wall-Less Vessel Phantom for Doppler Ultrasound Studies. *Ultrasound in Medicine and Biology*.
161) Rosenfeld, M., Rambod, E. & Gharib, M. (1998). Circulation and Formation Number of Laminar Vortex Rings. *Journal of Fluid Mechanics*, 376, 297–318.
162) Rosenfeld, M., Katija, K. & Dabiri, J. O. (2009). Circulation Generation and Vortex Ring Formation by Conic Nozzles. *Journal of Fluids Engineering*, 131(9), 91204. Retrieved from http://fluidsengineering.asmedigitalcollection.asme.org/article.aspx?articleid=1434454
163) Saffman, P. G. (1970). The Velocity of Viscous Vortex Rings. *Studies in Applied Mathematics*, 49(4), 371–380.
164) Saffman, P. G. (1978). The Number of Waves on Unstable Vortex Rings. *Journal of Fluid Mechanics*, 84(4), 625–639.
165) Schenck, J. F. (2005). Physical Interactions of Static Magnetic Fields with Living Tissues, in: *Progress in Biophysics and Molecular Biology*.
166) Sengupta, P. P., Pedrizzetti, G., Kilner, P. J., Kheradvar, A., Ebbers, T., Tonti, G., Fraser, A. G. & Narula, J. (2012). Emerging Trends in CV Flow Visualization. *JACC: Cardiovascular Imaging*, 5(3), 305–316.
167) Shariff, K. & Krueger, P. S. (2018). Advective Balance in Pipe-Formed Vortex Rings. *Journal of Fluid Mechanics*.
168) Smith, R. F., Rutt, B. K. & Holdsworth, D. W. (1999). Anthropomorphic Carotid Bifurcation Phantom for MRI Applications. *Journal of Magnetic Resonance Imaging*.
169) Ståhlberg, F., Nordell, B., Ericsson, A., Greitz, T., Persson, B. & Sperber, G. (1986). Quantitative Study of Flow Dependence in NMR Images at Low Flow Velocities. *Journal of Computer Assisted Tomography*.
170) Stankovic, Z., Allen, B. D., Garcia, J., Jarvis, K. B. & Markl, M. (2014). 4D Flow Imaging with MRI. *Cardiovascular diagnosis and therapy*, 4(2), 173–92. Retrieved from

http://www.ncbi.nlm.nih.gov/pubmed/24834414%5Cnhttp://www.pubmedcentral.nih.gov/articlerender.fcgi?artid=PMC3996243
171) Stauffer, S. R. & Peppast, N. A. (1992). Poly(Vinyl Alcohol) Hydrogels Prepared by Freezing-Thawing Cyclic Processing. *Polymer*.
172) Sun, C., Pye, S. D., Browne, J. E., Janeczko, A., Ellis, B., Butler, M. B., Sboros, V., Thomson, A. J. W., Brewin, M. P., Earnshaw, C. H. & Moran, C. M. (2012). The Speed of Sound and Attenuation of an IEC Agar-Based Tissue-Mimicking Material for High Frequency Ultrasound Applications. *Ultrasound in Medicine and Biology*.
173) Sun Nuclear (2018). *Doppler 403 Mini-Doppler 1430 Flow Phantoms*. Available at: http://www.cirsinc.com/products/all/69/doppler-string-phantom/
174) Surry, K. J. M., Austin, H. J. B., Fenster, A. & Peters, T. M. (2004). Poly(Vinyl Alcohol) Cryogel Phantoms for Use in Ultrasound and MR Imaging. *Physics in Medicine and Biology*.
175) Teirlinck, C. J. P. M., Bezemer, R. A., Kollmann, C., Lubbers, J., Hoskins, P. R., Fish, P., Fredfeldt, K. E. & Schaarschmidt, U. G. (1998). Development of an Example Flow Test Object and Comparison of Five of These Test Objects, Constructed in Various Laboratories. *Ultrasonics*.
176) Tinaikar, A., Advaith, S. & Basu, S. (2018). Understanding Evolution of Vortex Rings in Viscous Fluids. *Journal of Fluid Mechanics*, 836, 873–909.
177) Töger, J., Carlsson, M., Söderlind, G., Arheden, H. & Heiberg, E. (2011). Volume Tracking: A New Method for Quantitative Assessment and Visualization of Intracardiac Blood Flow from Three-Dimensional, Time-Resolved, Three-Component Magnetic Resonance Velocity Mapping. *BMC Medical Imaging*.
178) Töger, J., Bidhult, S. L., Revstedt, J., Carlsson, M., Arheden, H. & Heiberg, E. (2015). Phantom Validation of 4D Flow: Independent Validation of Vortex Ring Volume Quantification Using Planar Laser-Induced Fluorescence. *Journal of Cardiovascular Magnetic Resonance*.
179) Töger, J., Kanski, M., Arvidsson, P. M., Carlsson, M., Kovács, S. J., Borgquist, R., Revstedt, J., Söderlind, G., Arheden, H. & Heiberg, E. (2016-a). Vortex-Ring Mixing as a Measure of Diastolic Function of the Human Heart: Phantom Validation and Initial Observations in Healthy Volunteers and Patients with Heart Failure. *Journal of Magnetic Resonance Imaging*.
180) Töger, J., Bidhult, S., Revstedt, J., Carlsson, M. & Heiberg, E. (2016-b). Independent Validation of Four-Dimensional Flow MR Velocities and Vortex Ring Volume Using Particle Imaging Velocimetry and Planar Laser-Induced Fluorescence. *Magnetic Resonance in Medicine*, 75(3), 1064–1075.
181) Udesen, J. & Jensen, J. A. (2006). Investigation of Transverse Oscillation Method. *IEEE Transactions on Ultrasonics, Ferroelectrics, and Frequency Control*, 53(5), 959–971.
182) Udesen, J., Nielsen, M. B., Nielsen, K. R. & Jensen, J. A. (2007). Examples of In Vivo Blood Vector Velocity Estimation. *Ultrasound in Medicine and Biology*, 33(4), 541–548.
183) van der Geest, R.J. & Garg, P. (2016). Advanced analysis techniques for Intra-cardiac Flow evaluation from 4D Flow MRI. *Cur Radiol Rep,* 4:38.
184) Walker, A., Henriksen, E., Ringqvist, I. & Ask, P. (2009). A Rotating Cylinder Phantom for Flow and Tissue Color Doppler Testing, in: *IFMBE Proceedings*, (pp. 788–791).
185) Weigand, A. & Gharib, M. (1997). On the Evolution of Laminar Vortex Rings. *Experiments in Fluids*, 22(6), 447–457.
186) Weir, A. J., Sayer, R., Wang, C. X. & Parks, S. (2015). A Wall-Less Poly(Vinyl Alcohol) Cryogel Flow Phantom with Accurate Scattering Properties for Transcranial Doppler Ultrasound Propagation Channels Analysis, in: *Proceedings of the Annual International Conference of the IEEE Engineering in Medicine and Biology Society, EMBS*.
187) Westerdale, J., Belohlavek, M., McMahon, E. M., Jiamsripong, P., Heys, J. J. & Milano, M. (2011). Flow Velocity Vector Fields by Ultrasound Particle Imaging Velocimetry. *Journal of Ultrasound in Medicine*.

188) Westerweel, J., Elsinga, G. E. & Adrian, R. J. (2013). Particle Image Velocimetry for Complex and Turbulent Flows. *Annual Review of Fluid Mechanics*, 45(1), 409–436. Retrieved from http://www.annualreviews.org/doi/10.1146/annurev-fluid-120710-101204

189) Wieneke, B. (2005). Stereo-PIV Using Self-Calibration on Particle Images, in: *Experiments in Fluids*, (pp. 267–280).

190) Yan, X., Carriveau, R. & Ting, D.S.K. (2018). Laminar to Turbulent Buoyant Vortex Ring Regime in Terms of Reynolds Number, Bond Number, and Weber Number. *Journal of Fluids Engineering*, 140(5), 054502.

191) Yang, X., Sun, C., Anderson, T., Moran, C. M., Hadoke, P. W. F., Gray, G. A. & Hoskins, P. R. (2013). Assessment of Spectral Doppler in Preclinical Ultrasound Using a Small-Size Rotating Phantom. *Ultrasound in Medicine and Biology*.

192) Yiu, B. Y. S. & Yu, A. C. H. (2017). Spiral Flow Phantom for Ultrasound Flow Imaging Experimentation. *IEEE Transactions on Ultrasonics, Ferroelectrics, and Frequency Control*, 64(12), 1840–1848.

193) Zhang, J., et al (2018). Comparison of image acquisition techniques in four-dimensional flow cardiovascular MR on 3 Tesla in volunteers and tetralogy of fallot patients. *2018 40th Annual International Conference of the IEEE Engineering in Medicine and Biology Society (EMBC)*, Honolulu, HI, pp 1115-1118.

194) Zeqiri, B., Scholl, W. & Robinson, S. P. (2010). Measurement and Testing of the Acoustic Properties of Materials: A Review. *Metrologia*.

195) Zhou, X., Kenwright, D. A., Wang, S., Hossack, J. A. & Hoskins, P. R. (2017). Fabrication of Two Flow Phantoms for Doppler Ultrasound Imaging. *IEEE Transactions on Ultrasonics, Ferroelectrics, and Frequency Control*.

Appendices

Appendix 1: Arduino Code that drives the Vortex Ring based Complex Flow Phantom

```
int pulPin = 9; // Pin 9 ->> Pull +

int dirPin = 10; // Pin 10 ->> DIR +

int enblPin = 11; // Pin 11 ->> ENA + Pin

int buttonPin = 7;

int triggerpin = 5;


// ENA-, Pull- and DIR- linked to the ground for our configuration ( Arduino works just on positive
voltages)


int revolution = 0;

int buttonState = 0;


//set up --> Set displacement, Set How many rings you want to produce, Set Speed


int StepDisplacement = 40; // Set which is the entity of the displacemet (in other words, how many
pulses you want to send) -> 400 = 8mm

int HowManyRings = 100; // Set how many rings do you want to produce

int SetSpeed =500;//in microseconds -> 0.8 mm / 500*2*40(microseconds)/ = 0.01 m/s

//in microseconds, Minimum for square wave is 200 (sometimes overrun, better working from 250
or more


//piston diameter =70mm




void setup() {

  // put your setup code here, to run once:

  pinMode(pulPin, OUTPUT);

  pinMode(dirPin, OUTPUT);
```

```
  pinMode(enblPin, OUTPUT);

  pinMode(buttonPin, INPUT);
  pinMode(triggerpin, OUTPUT);

  digitalWrite(enblPin, LOW);
  delayMicroseconds(6);

  digitalWrite(dirPin, HIGH); // High --> piston forward =, LOW--> piston backward
  delayMicroseconds(6);

  digitalWrite(pulPin, LOW);

  delay(1000);
  digitalWrite(enblPin, HIGH);// initialise and then switch off

}

void loop() {
    buttonState = digitalRead(buttonPin);

    if (buttonState == HIGH){
         delay(10); //delay for the button

        while (revolution < HowManyRings) {

        digitalWrite(enblPin, HIGH);
        delay (18000);// 1 ring each 25 seconds in order not to overheat the motor. Don't go below 20
sec, it overheats.

        digitalWrite(enblPin, LOW);
```

```
        delayMicroseconds(6);

        digitalWrite(dirPin, HIGH); // High --> piston forward =, LOW--> piston backward
        delayMicroseconds(6);

        digitalWrite(pulPin, LOW);
        delay (2000);
        digitalWrite(triggerpin, HIGH);

   for (int i = 0; i <=  StepDisplacement; i++) {

     digitalWrite(pulPin, HIGH);
     delayMicroseconds (SetSpeed);
     digitalWrite(pulPin, LOW);
     delayMicroseconds(SetSpeed);
  }
   revolution++;
 digitalWrite(triggerpin, LOW);
 }
    }
}
```

Appendix 2: Flow phantoms limitation – Inlet length calculation for having parabolic flow within a pipe.

In order to have well-known flow conditions at the measuring point, the tube shall be straight and the inner diameter should be uniform along the pipe over an inlet length *L.* The inlet length should not include connectors that disturb the flow. Assuming that the flow profile at the beginning of the inlet length is flat, the pipe inlet length *L* for having laminar flow (*Re* < *2000*) can be calculated by the equation:

$$L = 0.03\ D\ Re$$

These concepts are described within the BS EN 61685:2002-IEC 61685:2001, International Standard for the design of a flow Doppler test object.

Simple calculations have been made for two commercial flow phantoms, Doppler 403™ and Mini-Doppler 1430™, manufactured by Sun Nuclear Corporation - Gammex (Sun Nuclear Corporation, FL, USA). Datasheets declare that the Doppler 403™ Flow Phantom has internal diagonal pipe at 40 degrees from 2 to 16 cm depth, with 5 mm inner diameter; while the Mini-Doppler 1430™ Phantom has internal diagonal pipe at 35 degrees from 2 to 9 cm depth, with 4 mm inner diameter. Simple trigonometry calculations indicate that the vessel inlet lengths are 21.78 cm and 12.20 cm for the Doppler 403™ and the Mini-Doppler 1430™, respectively. Reynolds numbers (*Re*) have been calculated for a range of typical velocities indicated by the devices. Results are reported in Table 1-Appendix 2. Critical peak velocities are 2 m/s and 1.7 m/s for the Doppler 403™ and the Mini-Doppler 1430™, respectively. This calculation assumes that the pump motor does not introduce turbulence into the flow, there are no connectors and the pipe diameter remains constant under the influence of the flow pressure. Although the critical velocity for the Mini-Doppler 1430™ is 1.7 m/s, bubbles start to be introduced when the pump is set for velocity higher than 0.7 m/s (peak).

V (m/s) - Mean	V (m/s) - Peak	Doppler 403™- *Re*	Mini-Doppler 1430™ - *Re*	Doppler 403™- *L* (cm)	Mini-Doppler 1430™ - L2(cm)
0.1	0.2	139.47	111.58	2.09	1.34
0.15	0.3	209.21	167.37	3.14	2.01
0.2	0.4	278.95	223.16	4.18	2.68
0.25	0.5	348.68	278.95	5.23	3.35
0.3	0.6	418.42	334.74	6.28	4.02
0.35	0.7	488.16	390.53	7.32	4.69
0.4	0.8	557.89	446.32	8.37	5.36
0.45	0.9	627.63	502.11	9.41	6.03
0.5	1	697.37	557.89	10.46	6.69
0.55	1.1	767.11	613.68	11.51	7.36
0.6	1.2	836.84	669.47	12.55	8.03
0.65	1.3	906.58	725.26	13.60	8.70
0.7	1.4	976.32	781.05	14.64	9.37
0.75	1.5	1046.05	836.84	15.69	10.04
0.8	1.6	1115.79	892.63	16.74	10.71
0.85	1.7	1185.53	948.42	17.78	11.38
0.9	1.8	1255.26	1004.21	18.83	12.05
0.95	1.9	1325.00	1060.00	19.88	12.72
1	2	1394.74	1115.79	20.92	13.39
1.05	2.1	1464.47	1171.58	21.97	14.06
1.1	2.2	1534.21	1227.37	23.01	14.73
1.15	2.3	1603.95	1283.16	24.06	15.40
1.2	2.4	1673.68	1338.95	25.11	16.07
1.25	2.5	1743.42	1394.74	26.15	16.74

Table 1- Appendix 2. Inlet length, *L*, and Reynolds number, *Re*, calculations for the Doppler 403™ and the Mini-Doppler 1430™. Fluid viscosity for *Re* calculations is assumed 3.8 x 10^{-3} *Pa s*, as indicated in the datasheet. Peak velocity has been calculated assuming parabolic flow.

Appendix 3: Poster Presentation BMUS 2018. A Novel Complex Flow Phantom for Doppler Ultrasound

Leeds Test Objects
medical imaging phantoms

The University Of Sheffield.

A Novel Complex Flow Phantom for Doppler Ultrasound

Simone Ambrogio[1,2], Adrian Walker[1], Simone Ferrari[2], Prashant Verma[3], Andrew Narracott[2], John Fenner[2]

[1] Leeds Test Objects Ltd, Boroughbridge, United Kingdom

[2] Medical Physics, Mathematical Modelling in Medicine Group, Department of Cardiovascular Disease, University Of Sheffield, United Kingdom

[3] Medical Imaging & Medical Physics, Sheffield Teaching Hospital NHS Foundation Trust, Sheffield, United Kingdom

simone@leedstestobjects.com

Background

Traditional Doppler Ultrasound methods and newer Ultrasound technologies, including vector flow imaging and volume quantification, are used to measure blood flow in cardiovascular systems exhibiting complexities such as recirculation, turbulence, jets and vortices. Existing Doppler phantoms struggle to confirm the accuracy of Ultrasound methods in measuring complex flow. A novel phantom, designed to produce complex flows that are physiologically relevant, stable, predictable, controllable and reproducible, is presented. A vortex ring is chosen as the reference flow for the development of the proposed phantom.

Methods

A vortex ring forms when a column of fluid is pushed through a smaller orifice into a neighbouring fluid environment. The fluid "rolls up" at the orifice face, forming a toroidal vortex that (for specific Reynolds numbers) propagates along its axisymmetric axis. The phantom design proposed uses a piston/cylinder system to propel a slug of fluid through an orifice that connects to an open tank full of fluid. Different orifices diameters can be provided on demand. Main vortex parameters, which are related to the piston displacement and piston speed, can be controlled by a programmable microcontroller and a linear stepper motor. Orgasol® particles (10um) were chosen to provide a scattering signal for vortex visualisation using Ultrasound.

Results

The assembled phantom is shown in Figure 1. Laser-PIV (particle image velocimetry) measurements have shown that vortex ring velocities ranging from 8cm/s to 80cm/s can be produced with reproducibility better than +/-8% (Figure 2). Figure 3 shows the Ultrasound scans of the ring vortex with examples of B-mode (3a), Colour Flow Doppler (3b), Pulsed Wave Doppler spectrum (3c) and Echo-PIV (3d) images.

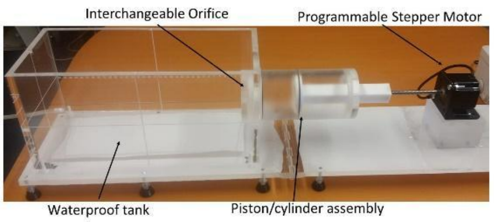

Figure 1. Complex Flow Phantom – Assembled system

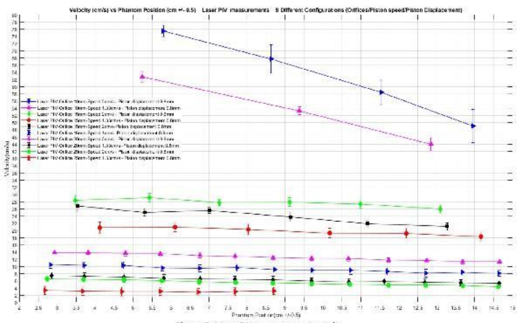

Figure 2. Laser-PIV measurement results

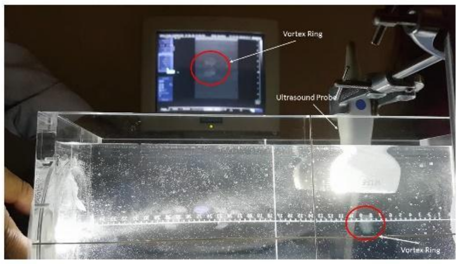

Figure 3. Ultrasound scan with examples of B-mode imaging (3a), Colour Flow Doppler imaging (3b), Pulsed Wave Spectral Doppler imaging (3c) and Echo-PIV (3d).

Figure 3.a B-mode imaging

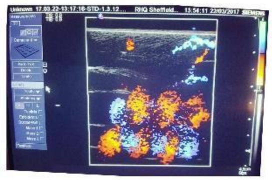

Figure 3.b Colour Flow Doppler imaging

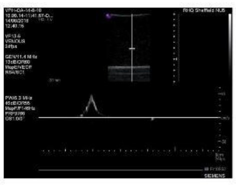

Figure 3.c Pulsed Wave Spectral Doppler imaging

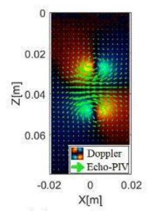

Figure 3.d Echo-PIV applied in post-processing

Conclusion

A novel, cost-effective, vortex ring flow phantom has been presented. Early results point to its potential as an Ultrasound flow phantom that can test scanners operating in standard Doppler modes and advanced flow mapping modes.

Acknowledgements

This work is funded by the European Commission through the H2020 Marie Sklodowska-Curie European VPH-CaSE Training Network (www.vph-case.eu), GA No. 642612.

COORDINATED BY THE UNIVERSITY OF SHEFFIELD MSCA ITN 2014 ETN

Appendix 4: Instrumentation Pack - Arduino code Laser diodes/Photodiodes system

LASER DIODES PROGRAM

```
int analogPin0 = 0;    // potentiometer wiper (middle terminal) connected to analog pin 3
int analogPin1 = 1;
int analogPin2 = 2;
int analogPin3 = 3;
int analogPin4 = 4;
int analogPin5 = 5;// outside leads to ground and +5V
int analogPin15= 15;
int val0 = 0;
int val1 = 0;
int val2 = 0;
int val3 = 0;
int val4 = 0;
int val5 = 0;// variable to store the value read
int control=0;
void setup()
{
  Serial.begin(9600);          //  setup serial
}

void loop()
{
  //control=analogRead(analogPin15);
  //if (control > 900)
  //{
  val0 = analogRead(analogPin0);
  val1 = analogRead(analogPin1);
  val2 = analogRead(analogPin2);
  val3 = analogRead(analogPin3);
  val4 = analogRead(analogPin4);
```

```
val5 = analogRead(analogPin5);// read the input pin
Serial.println(val0);
Serial.println(val1);
Serial.println(val2);
Serial.println(val3);
Serial.println(val4);
Serial.println(val5);
delay(20);//}
}
```

Appendix 5: Instrumentation Pack - MATLAB code for Encoder Reading

```
lassdef E2019Q
    methods(Static)
        %%%%%%%%%%%%%%%% OPEN/CLOSE COM port functions %%%%%%%%%%%%%%%%%%%%
        % Open COM  Port for E201-9Q
        function FID = Open_COM_Port(ComString)
            FID = serial(ComString);
            FID.Terminator = '';
            fopen(FID);
        end

        % Close COM Port for E201-9Q
        function Close_COM_Port(FID)
            fclose(FID);
        end
        %%%%%%%%%%%%%%%%%%%%%%%%%%%%%%%%%%%%%%%%%%%%%%%%%%%%%%%%%%%%%%%%%%%%

        %%%%%%%%%%%%%%%%%%%%%%% Status functions %%%%%%%%%%%%%%%%%%%%%%%%%%
        % Read software version of E201-9Q
        function data = GetSoftwareVersion(FID)
            fprintf(FID,'v');
            data = [];
            start = clock;
            while(isempty(strfind(data, 13)))
                if FID.BytesAvailable > 0
                    data = [data fscanf(FID,'%c',FID.BytesAvailable)];
                end
                if etime(clock,start) > 3
                    disp('Timeout occurs while reading COM port');
                    break
                end
            end
        end

        % Read serial number of E201-9Q
        function data = GetSerialNumber(FID)
            fprintf(FID,'s');
            data = [];
            start = clock;
            while(isempty(strfind(data, 13)))
                if FID.BytesAvailable > 0
                    data = [data fscanf(FID,'%c',FID.BytesAvailable)];
                end
                if etime(clock,start) > 3
                    disp('Timeout occurs while reading COM port');
                    break
                end
            end
        end

        % Read encoder supply status, voltage and current consumption
        function data = GetEncSupply(FID)
            fprintf(FID,'e');
            data = [];
            start = clock;
            while(isempty(strfind(data, 13)))
                if FID.BytesAvailable > 0
                    data = [data fscanf(FID,'%c',FID.BytesAvailable)];
                end
```

```
        if etime(clock,start) > 3
            disp('Timeout occurs while reading COM port');
            break
        end
    end
end

% Read status of hardware input pins on interface
function data = GetInputPinStatus(FID)
    fprintf(FID,'p');
    data = [];
    start = clock;
    while(isempty(strfind(data, 13)))
        if FID.BytesAvailable > 0
            data = [data fscanf(FID,'%c',FID.BytesAvailable)];
        end
        if etime(clock,start) > 3
            disp('Timeout occurs while reading COM port');
            break
        end
    end
end
%%%%%%%%%%%%%%%%%%%%%%%%%%%%%%%%%%%%%%%%%%%%%%%%%%%%%%%%%%%%%%%%%%%

%%%%%%%%%%%%%%%%%% Power management functions %%%%%%%%%%%%%%%%%%%%%
% Turn ON power supply to encoder
function data = EncSupply_ON(FID)
    fprintf(FID,'n');
    data = [];
    start = clock;
    while(isempty(strfind(data, 13)))
        if FID.BytesAvailable > 0
            data = [data fscanf(FID,'%c',FID.BytesAvailable)];
        end
        if etime(clock,start) > 3
            disp('Timeout occurs while reading COM port');
            break
        end
    end
end

% Turn OFF power supply to encoder
function data = EncSupply_OFF(FID)
    fprintf(FID,'f');
    data = [];
    start = clock;
    while(isempty(strfind(data, 13)))
        if FID.BytesAvailable > 0
            data = [data fscanf(FID,'%c',FID.BytesAvailable)];
        end
        if etime(clock,start) > 3
            disp('Timeout occurs while reading COM port');
            break
        end
    end
end
%%%%%%%%%%%%%%%%%%%%%%%%%%%%%%%%%%%%%%%%%%%%%%%%%%%%%%%%%%%%%%%%%%%

%%%%%%%%%%%% Functions related to the encoder position %%%%%%%%%%%%
% Read encoder position (string, decimal)
```

```
function data = GetEncPosition(FID)
    fprintf(FID,'?');
    data = [];
    start = clock;
    while(isempty(strfind(data, 13)))
        if FID.BytesAvailable > 0
            data = [data fscanf(FID,'%c',FID.BytesAvailable)];
        end
        if etime(clock,start) > 3
            disp('Timeout occurs while reading COM port');
            break
        end
    end
end

% Read encoder position (string, decimal) with timestamp
function data = GetEncPosition_Timestamp(FID)
    fprintf(FID,'!');
    data = [];
    start = clock;
    while(isempty(strfind(data, 13)))
        if FID.BytesAvailable > 0
            data = [data fscanf(FID,'%c',FID.BytesAvailable)];
        end
        if etime(clock,start) > 3
            disp('Timeout occurs while reading COM port');
            break
        end
    end
end

% Read encoder position (string, HEX)
function data = GetEncPositionHEX(FID)
    fprintf(FID,'>');
    data = [];
    start = clock;
    while(isempty(strfind(data, 13)))
        if FID.BytesAvailable > 0
            data = [data fscanf(FID,'%c',FID.BytesAvailable)];
        end
        if etime(clock,start) > 3
            disp('Timeout occurs while reading COM port');
            break
        end
    end
end

% Read encoder position (string, HEX) with timestamp
function data = GetEncPositionHEX_Timestamp(FID)
    fprintf(FID,'<');
    data = [];
    start = clock;
    while(isempty(strfind(data, 13)))
        if FID.BytesAvailable > 0
            data = [data fscanf(FID,'%c',FID.BytesAvailable)];
        end
        if etime(clock,start) > 3
            disp('Timeout occurs while reading COM port');
            break
        end
    end
```

```
        end

        % Clear reference status flag
        function ClearReferenceFlag(FID)
            fprintf(FID,'c');
        end

        % Set current count value to zero (also affects reference mark)
        function ResetCurrentCount(FID)
            fprintf(FID,'z');
        end

                % Set current count value to zero (also affects reference
mark)
        function Auto(FID)
            fprintf(FID,'1');
        end


        % Clear zero offset value stored by "ResetCurrentCount" function
        function ClearZeroOffset(FID)
            fprintf(FID,'a');
        end
        %%%%%%%%%%%%%%%%%%%%%%%%%%%%%%%%%%%%%%%%%%%%%%%%%%%%%%%%%%%%%%%%%%%

        %%%%%%%%%%%%%%% String to Double converting functions %%%%%%%%%%%%%
        % Get encoder count in double precision format
        function data = GetEncCountDOUBLE(FID)
            temp = E2019Q.GetEncPosition(FID);
            data = str2double(temp(2:min(strfind(temp,':')-1)));
        end

        % Get encoder reference mark in double precision format
        function data = GetEncReferenceDOUBLE(FID)
            temp = E2019Q.GetEncPosition(FID);
            data =
str2double(temp(min(strfind(temp,':'))+2:max(strfind(temp,':'))-1));
        end

        % Get timestamp of position in double precision format
        function data = GetTimestampDOUBLE(FID)
            temp = E2019Q.GetEncPosition_Timestamp(FID);
            data = str2double(temp(max(strfind(temp,':'))+2:end-1));
        end
        %%%%%%%%%%%%%%%%%%%%%%%%%%%%%%%%%%%%%%%%%%%%%%%%%%%%%%%%%%%%%%%%%%%
    end
end

clear all
close all
clc


E2019Q_ID = E2019Q.Open_COM_Port('COM17');

Power_Supply = E2019Q.EncSupply_ON(E2019Q_ID); % turn on
%Power_Supply = E2019Q.EncSupply_OFF(E2019Q_ID); % turn off
%SW_Version = E2019Q.GetSoftwareVersion(E2019Q_ID);
%Serial_Num = E2019Q.GetSerialNumber(E2019Q_ID);
```

```
Enc_Supply = E2019Q.GetEncSupply(E2019Q_ID);
Pin_Status = E2019Q.GetInputPinStatus(E2019Q_ID);

Counter = zeros(200,1);
Time = zeros(200,1);
%Velocity1=zeros(1,200);
i = 1;

%clock1 = tic;

while i<200
Enc_Count = E2019Q.GetEncCountDOUBLE(E2019Q_ID);
Pos_Timestamp= E2019Q.GetTimestampDOUBLE(E2019Q_ID);
Counter(i) = Enc_Count;
Time (i) = Pos_Timestamp;
%Velocity1(i) = Enc_Count/Pos_Timestamp;
Enc_Reference=E2019Q.GetEncReferenceDOUBLE(E2019Q_ID);
E2019Q.ClearReferenceFlag(E2019Q_ID);
E2019Q.ResetCurrentCount(E2019Q_ID);
E2019Q.ClearZeroOffset(E2019Q_ID);
i= i+1;
end


Power_Supply = E2019Q.EncSupply_OFF(E2019Q_ID); % turn off
%E2019Q.Close_COM_Port(E2019Q_ID); % before disconnecting
E2019Q.Close_COM_Port(E2019Q_ID); % before disconnecting
```

Appendix 6: How the macro-flow variability reflects on the micro-flow environment.

The macro-flow reproducibility reflects on the micro-flow environment. This concept is crucial for promoting the utility of the Vortex Ring based Complex Flow Phantom and has been demonstrated extracting vector flow fields from Laser PIV acquisitions on Configurations 2, 3, 7 and 10, Table 5.1-Chapter 5. Results are reported in following Tables. Axis reference, Quiver Plot, Velocity flow fields along X-Axis and Y-Axis reconstructed in Matlab are also illustrated in Figures 1, 2, 3 and 4 – Appendix 6.

Configuration - 2 - Table 5.1- Chapter 5						
Phantom Position (cm +/-0.5)	Vx (cm/s) - Average	Vx (cm/s) – Standard Dev (+/-)	Vx (cm/s) – Error (+/- %)	Vy (cm/s) - Average	Vy (cm/s) – Standard Dev (+/-)	Vy (cm/s) – Error (+/- %)
5.25	-158.06	8.34	5.28	81.65	5.91	7.23
9.24	-133.72	11.24	8.41	65.47	4.60	7.03
12.8	-114.77	11.30	9.84	61.87	5.85	9.45

Table 1- Appendix 6. Configuration 2-Table 5.1-Chapter 5 – vortex velocity flow fields along X-axis and Y-Axis. Average values and standard deviations (+/- 1SD) were calculated from the acquisition of 10 vortex rings.

Configuration - 3 - Table 5.1- Chapter 5						
Phantom Position (cm +/-0.5)	Vx (cm/s) - Average	Vx (cm/s) – Standard Dev (+/-)	Vx (cm/s) – Error (+/- %)	Vy (cm/s) - Average	Vy (cm/s) – Standard Dev (+/-)	Vy (cm/s) – Error (+/- %)
3.5	-88.92	4.12	4.63	51.25	3.83	7.47
5.5	-85.14	3.77	4.43	50.00	2.65	5.29
7.25	-82.20	4.08	4.97	48.01	2.35	4.88
9.25	-79.19	2.79	3.52	44.31	1.50	3.37
11	-75.62	1.30	1.71	41.46	1.37	3.30
13.25	-71.62	2.82	3.93	38.32	2.45	6.39

Table 2- Appendix 6. Configuration 3-Table 5.1-Chapter 5 – vortex velocity flow fields along X-axis and Y-Axis. Average values and standard deviations (+/- 1SD) were calculated from the acquisition of 10 vortex rings.

Configuration - 7 - Table 5.1- Chapter 5						
Phantom Position (cm +/-0.5)	Vx (cm/s) - Average	Vx (cm/s) – Standard Dev (+/-)	Vx (cm/s) – Error (+/- %)	Vy (cm/s) - Average	Vy (cm/s) – Standard Dev (+/-)	Vy (cm/s) – Error (+/- %)
2.75	-41.31	1.78	4.31	23.77	2.14	9.01
3.75	-39.85	1.97	4.95	22.79	1.04	4.56
4.75	-38.86	1.15	2.95	21.43	1.62	7.56
5.75	-37.54	0.99	2.64	20.82	0.99	4.77

6.75	-36.66	1.19	3.24	20.02	0.84	4.20
7.75	-35.66	1.38	3.87	19.19	0.85	4.44
8.75	-34.50	1.22	3.55	18.35	0.77	4.20
9.75	-33.86	1.14	3.35	17.35	0.85	4.90
10.75	-33.28	1.14	3.44	16.85	0.78	4.62
11.75	-32.65	0.93	2.85	16.43	0.95	5.77
12.75	-32.03	1.16	3.63	15.49	0.89	5.73
13.75	-31.18	1.28	4.11	15.07	0.89	5.94
14.75	-30.42	1.68	5.54	14.40	1.09	7.54

Table 3- Appendix 6. Configuration 7-Table 5.1-Chapter 5 – vortex velocity flow fields along X-axis and Y-Axis. Average values and standard deviations (+/- 1SD) were calculated from the acquisition of 10 vortex rings.

Configuration - 10 - Table 5.1- Chapter 5						
Phantom Position (cm +/-0.5)	Vx (cm/s) - Average	Vx (cm/s) – Standard Dev (+/-)	Vx (cm/s) – Error (+/- %)	Vy (cm/s) - Average	Vy (cm/s) – Standard Dev (+/-)	Vy (cm/s) – Error (+/- %)
2.75	-1.52	0.25	16.15	5.37	1.00	18.61
3.75	-1.38	0.26	18.46	5.29	0.96	18.18
4.75	-1.42	0.15	10.71	4.97	0.97	19.60
5.75	-1.29	0.23	17.68	4.87	0.88	18.15
6.75	-1.22	0.18	14.88	4.66	0.88	18.91
7.75	-1.13	0.21	18.33	4.62	0.88	19.13
8.75	-1.22	0.18	15.18	4.49	0.87	19.44
9.75	-1.15	0.15	12.96	4.22	0.77	18.29
10.75	-1.03	0.17	16.36	4.09	0.76	18.51
11.75	-1.02	0.11	10.68	4.05	0.74	18.34
12.75	-1.15	0.25	21.49	3.89	0.76	19.60
13.75	-1.59	0.20	12.49	5.74	1.19	20.77
14.75	-1.12	0.24	21.59	3.82	0.64	16.65
15.75	-0.99	0.19	19.61	3.68	0.68	18.50
16.75	-0.97	0.14	14.71	3.59	0.66	18.37
17.75	-1.05	0.10	9.07	3.57	0.66	18.43

18.75	-0.99	0.13	13.66	3.54	0.64	18.04
19.75	-1.05	0.17	15.99	3.48	0.65	18.59
20.75	-0.93	0.08	9.05	3.36	0.68	20.32

Table 4- Appendix 6. Configuration 10-Table 5.1-Chapter 5 – vortex velocity flow fields along X-axis and Y-Axis. Average values and standard deviations (+/- 1SD) were calculated from the acquisition of 10 vortex rings.

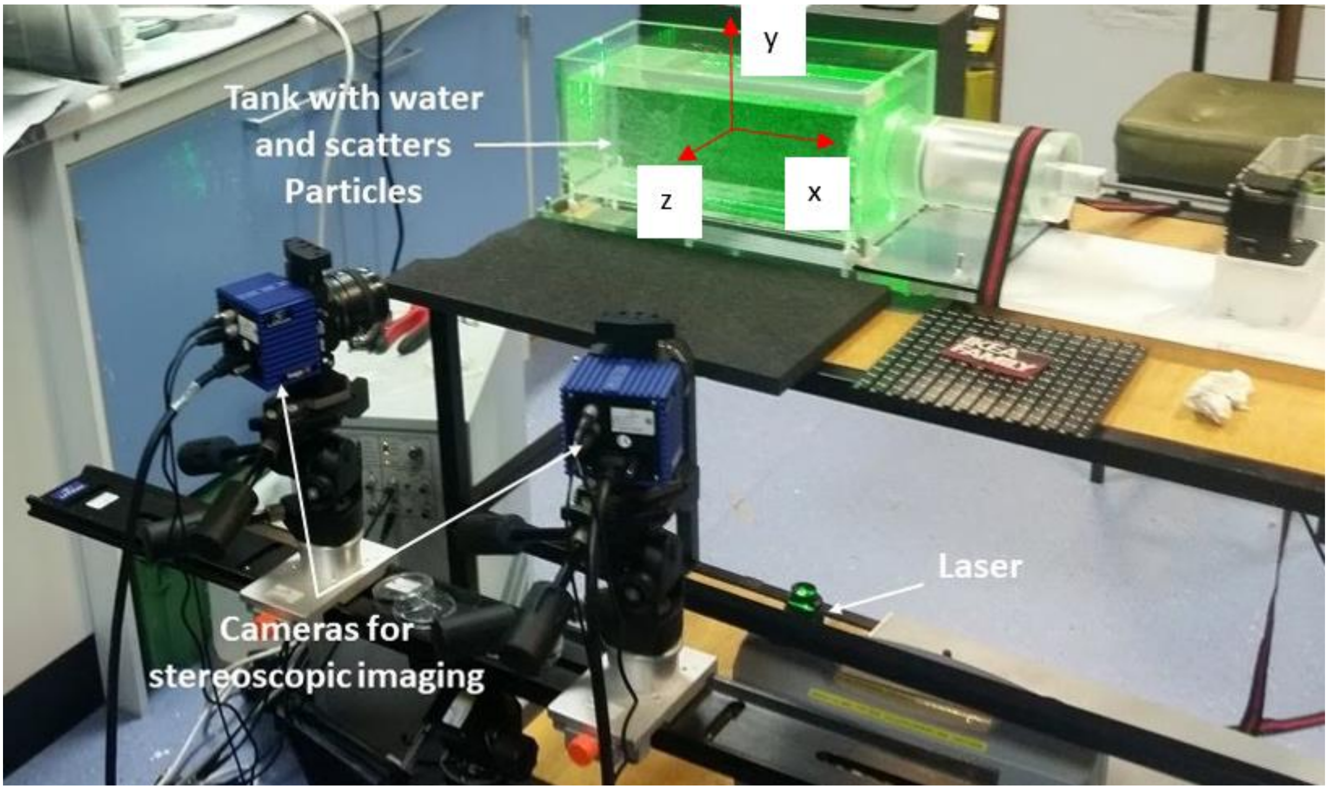

Figure 1- Appendix 6. Image illustrating axis references during Laser PIV acquisitions.

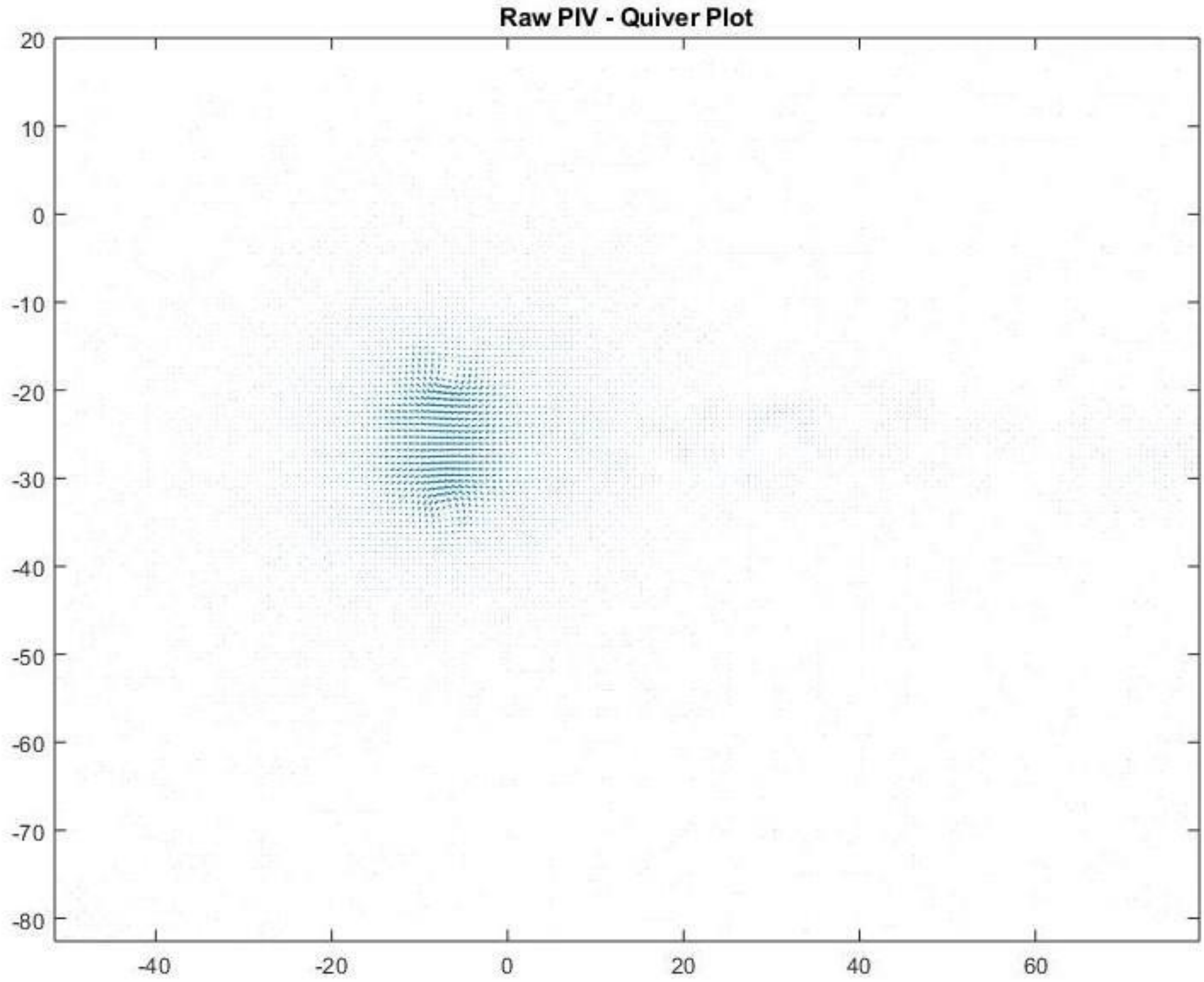

Figure 2- Appendix 6. Quiver Plot reconstructed in Matlab from Laser PIV raw data – Configuration 2, Table 5.1, Chapter 5.

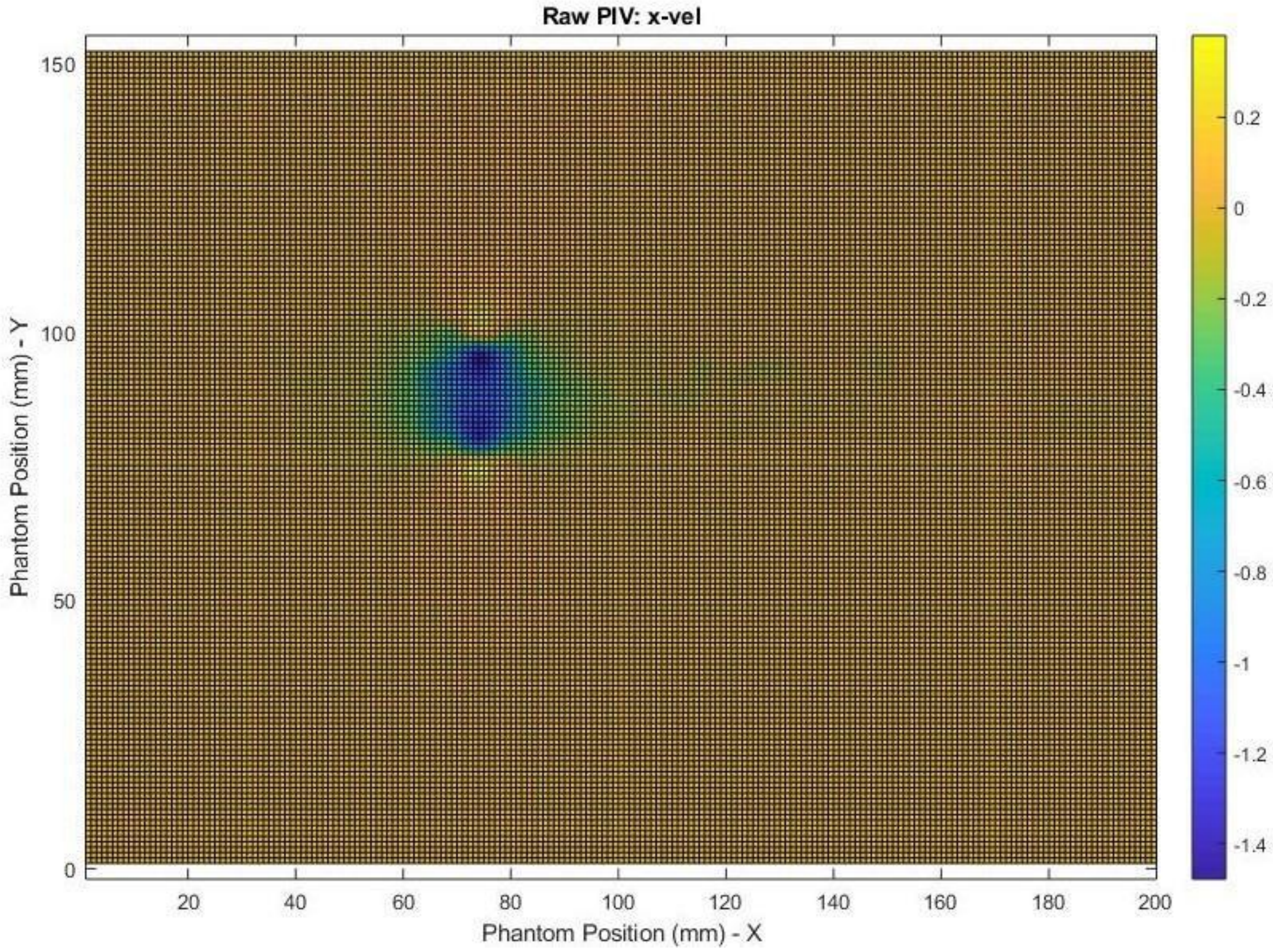

Figure 3- Appendix 6. Velocity along X-axis (Vx) reconstructed in Matlab from Laser PIV raw data – Configuration 2, Table 5.1, Chapter 5.

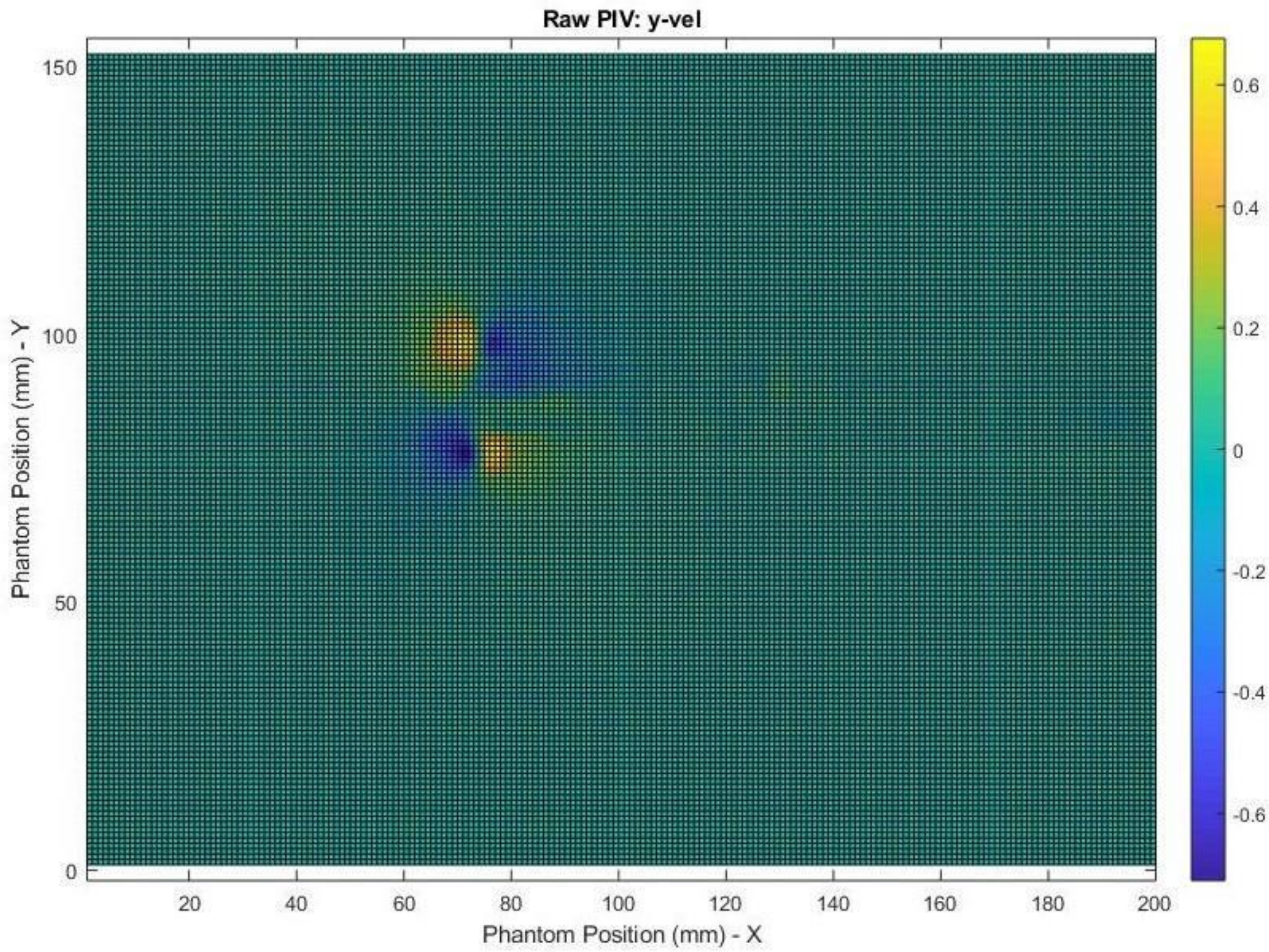

Figure 4- Appendix 6. Velocity along Y-axis (Vy) reconstructed in Matlab from Laser PIV raw data – Configuration 2, Table 5.1, Chapter 5.

Since Laser PIV data were not available at the time that echo-PIV and vector Doppler were performed a quantitative comparative analysis is not feasible. The two acquisitions were performed with different vortex ring generating conditions (piston speed and piston displacement). However, by comparing Figure 5-Appendix 6 with figures 2-, 3- and 4-Appendix 6, it is possible to appreciate qualitatively the similarity between the velocity flow fields reconstructed with the two techniques.

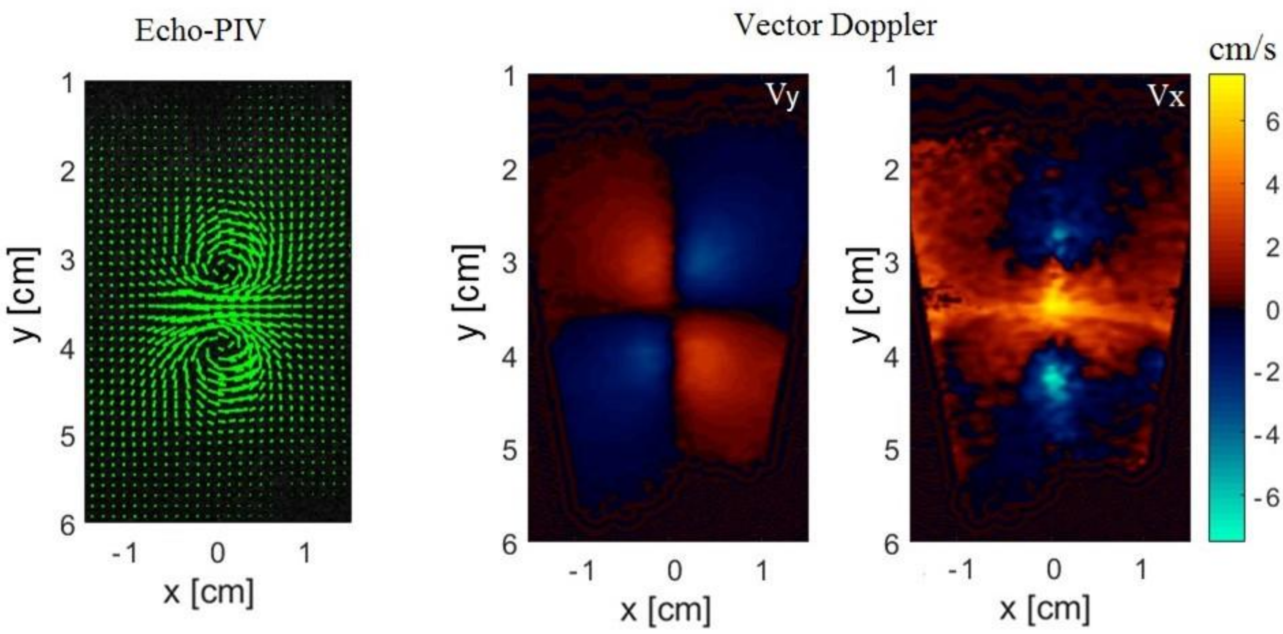

Figure 5- Appendix 6. Vortex ring velocity flow fields reconstructed with echo-PIV (a) and Vector Doppler (b).

In agreement with Tinaikar et al 2018 and ultrasound acquisitions (Section 5.3.6, Chapter 5), high correlation with R^2 values ranging from 0.89 (Configuration 10) to 0.99 (Configuration 7) was found between the two velocity components. Linearised plots are shown in Figure 6-Appendix 6, Figure 7-Appendix 6, Figure 8-Appendix 6 and Figure 9-Appendix 6 for Configuration 2, Configuration 3, Configuration 7 and Configuration 10, respectively.

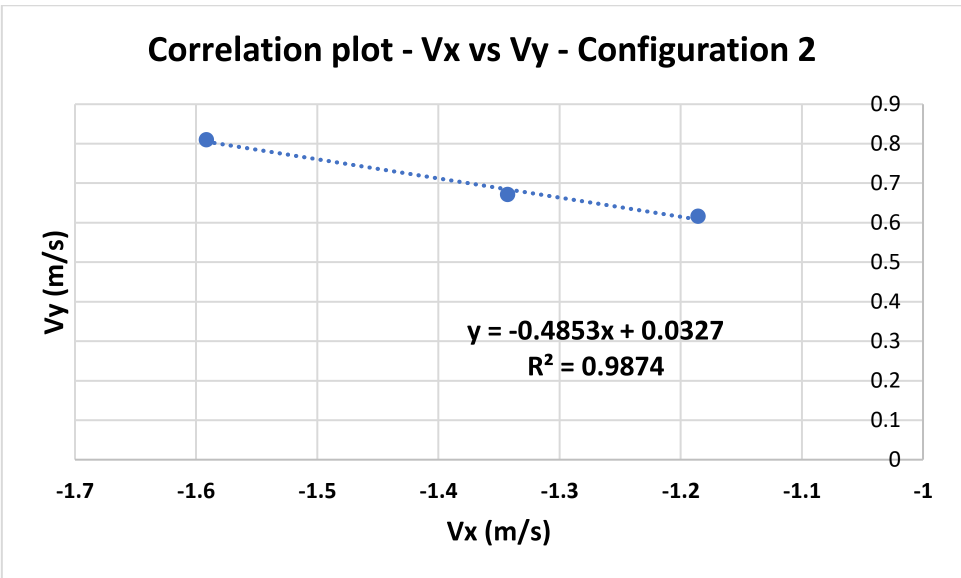

Figure 6 - Appendix 6. Linear relationship between the rotational and the translational velocities – Configuration 2

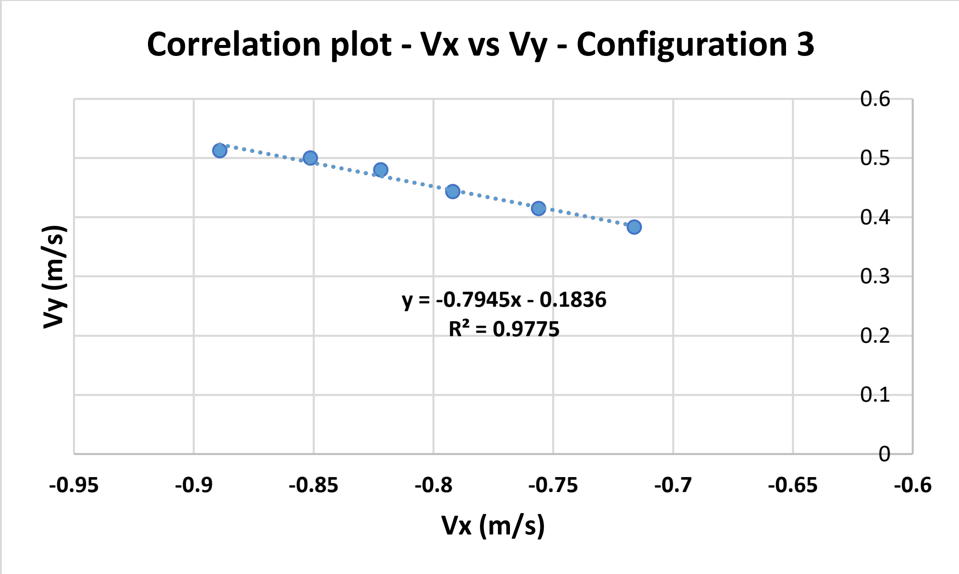

Figure 7 - Appendix 6. Linear relationship between the rotational and the translational velocities – Configuration 3

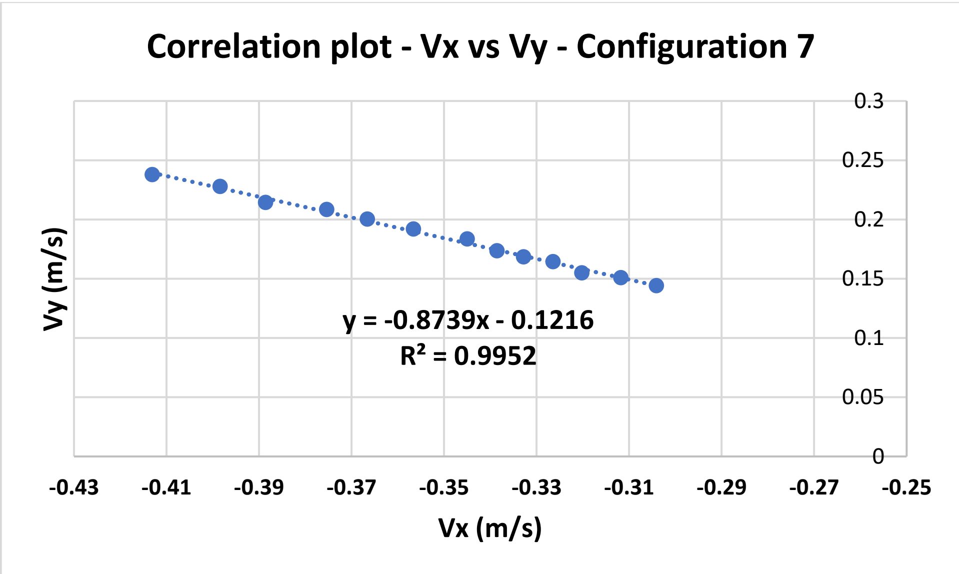

Figure 8 - Appendix 6. Linear relationship between the rotational and the translational velocities – Configuration 7

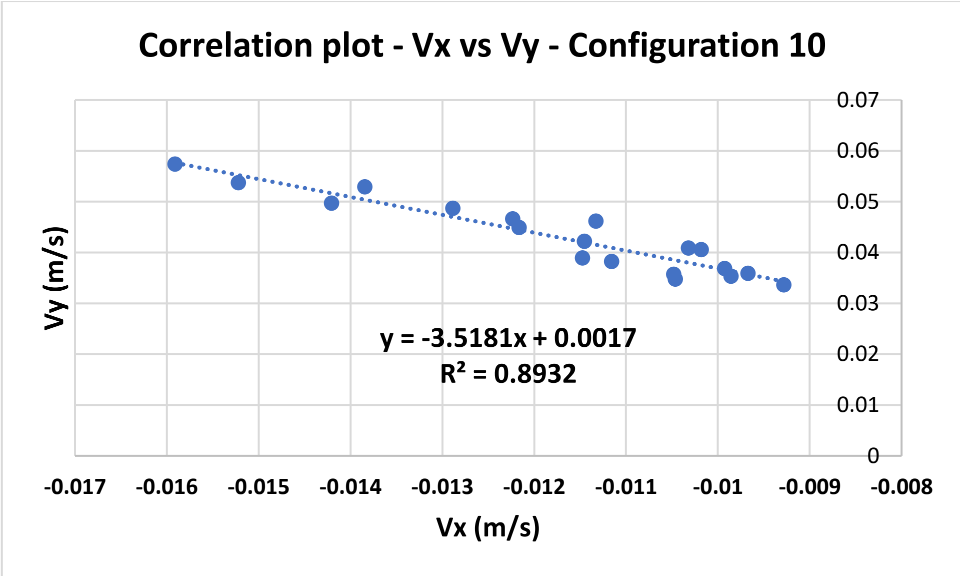

Figure 9 - Appendix 6. Linear relationship between the rotational and the translational velocities – Configuration 10